Electroweak processes in nucleons and nuclei at intermediate energies

En Wang

Departamento de Física Teórica

Universidad de Valencia

TESIS DOCTORAL

VALENCIA 2014

Dr. Luis Alvarez Ruso, Investigador Ramón y Cajal del Consejo Superior de Investigaciones Científicas,
Dr. Juan Miguel Nieves Pamplona, Investigador Científico del Consejo Superior de Investigaciones Científicas

CERTIFICAN: Que la presente Memoria *Electroweak processes in nucleons and nuclei at intermediate energies* ha sido realizada bajo su dirección en el Departamento de Física Teórica de la Universidad de Valencia por D. En Wang y constituye su tesis doctoral para optar al grado de Doctor en Física.

Y para que así conste, en cumplimiento con la legislación vigente, presentan ante el Departamento de Física Teórica, la referida memoria, firmando el presente certificado en Burjassot (Valencia) a 14 de Octubre de 2014

Luis Alvarez Ruso **Juan Miguel Nieves Pamplona**

Contents

Acknowledgments

It is a pleasure to thank all the people whose support and advice have helped me to complete this dissertation. First of all, I wish to express my deep gratitude to my supervisors Drs. Juan Nieves and Luis Alvarez-Ruso, whose expertise, understanding, and patience, added considerably to my graduate experience. I also thank them for the continuous guidance, encouragement, and support, but also for giving me much assistance during the last four years. A very special thanks goes out to Dr. Ju-Jun Xie for countless fruitful and inspiring discussions and his valuable advice.

I am especially grateful to Prof. Eulogio Oset for providing me the opportunity to work on such a fascinating group, and much assistance in work and life during my graduate experience. Also, and thanks to him, I have visited several beautiful valencian villages and learned much about certain aspects of the spanish culture, such as bull-fighting, bull-running and Fallas.

I also thank Prof. Manuel Jose Vicente Vacas for his assistance in my quotidian life, for sharing with me his extraordinary computing skills and many entertaining discussions in front of a beer and some *tapas* after work.

I am obliged to all my colleagues of the group, C. Hidalgo, F. Aceti, C.W. Xiao, E. Javier Garzón, T. Ledwig, T. Uchino, A. Hiller Blin and J. Morais Dias, who have made possible multitude of entertaining lunches, coffee breaks and extra-academic parties. I will always remenber all these good moments...

I would also like to thank all my friends in Valencia, particularly, Profs. B.X. Sun, L.R. Dai, W.H. Liang and H.X. Chen, and Drs. J. Lu and Y. Duan, with whom I have shared lots of parties, visited many beautiful places in Spain, and gone for hiking, boating and riding. All

this has made my life in Valencia more colorful.

Above all, I would like to thank my wife, Dr. L.J. Liu for her tolerance and permanent encouragement, and I am deeply indebted to my parents and my sister for the constant support and for believing in me and my work.

Chapter 1

Introduction

1.1 Neutrino nucleon and neutrino-nucleus interactions

In 1930, Wolfgang Pauli postulated a neutral and undetected particle in order to explain how beta decay could conserve energy, momentum and angular momentum (spin) [1]. In 1956, Clyde Cowan, Frederick Reines, F.B. Harrison, H.W. Kruse and A.D. McGuire published the confirmation that they had detected the neutrinos through the inverse beta decay [2]. Since then, we have learned much about this elusive particle, which only interacts weakly with matter. There are at least three different flavor neutrinos, all of them chargeless and with spin 1/2.

Recently, it has been observed that neutrinos can change their flavor and have non-zero masses, which is in contrast to the predictions of the Standard Model of particle physics. To address these questions, there have been, are currently running, and are planned for the short future, several experiments disseminated around the world, aimed at obtaining a precise determination of the mass-squared differences and the flavor-mixing angles. Neutrino beams are not monochromatic, and the ability to reconstruct the neutrino energy is crucial in all these studies. Taking as an example the T2K experiment [3], the probability for electron neutrino appearance, from a muon neutrino beam with energy $E_\nu \sim 1$ GeV propagating over a baseline $L \sim 300$ km, is dominated by the

term

$$P_{\nu_\mu \to \nu_e} \approx \sin^2\theta_{23}\sin^2 2\theta_{13}\sin^2\frac{\Delta m^2_{32}L}{4E_\nu} \tag{1.1}$$

depending on the neutrino energy E_ν, which is not known for broad fluxes, and on the oscillation parameters θ_{23}, θ_{13} and Δm^2_{32}. A reliable determination of the neutrino energies in nuclear targets requires a good understanding of the reaction mechanisms and a precise simulation of final state interactions. There are also irreducible backgrounds, for example from neutral current π^0 or γ production when these particles produce showers that are misidentified as electrons from $\nu_e n \to e^- p$.

Besides the neutrino oscillation, neutrino interactions also play an important role in:

- Astrophysical phenomena In particular, the dynamics of core-collapse supernovae is controlled by neutrino interactions. The neutron rich environment of supernovae is a candidate site for r-process nucleosynthesis [4] because radiated neutrinos convert neutrons into protons. To address these questions a good knowledge of low energy neutrino production and detection cross sections is also required.

- Physics beyond the Standard Model Non-standard neutrino interactions leading, for example, to deviations from universality in the weak couplings or flavor violation in neutral current processes could affect neutrino production, propagation, and detection processes as sub-leading effects (see Ref. [5] for a recent review). Long and short baseline experiments allow to set bounds on these interactions.

- Hadronic physics Neutrino cross section measurements allow to investigate the axial structure of the nucleon and baryon resonances, enlarging our views of hadron structure beyond what is presently known from experiments with hadronic and electromagnetic probes, not forgetting about lattice QCD. Another fundamental and open question is the strangeness content of the nucleon spin which can be best unraveled in $\nu p(n) \to \nu p(n)$ studies.

- Nuclear physics Modern neutrino experiments are performed with nuclear targets. For nuclear physics this represents a challenge and an opportunity. A challenge because the precise knowledge of neutrino and baryon properties can only be achieved if nuclear effects are under control. An opportunity because neutrino cross sections incorporate richer information than electron-scattering ones, providing an excellent testing ground for nuclear structure, many-body mechanisms and reaction models.

As we know, neutrinos only interact with matter through weak interactions, and the cross sections are tiny, so it is very challenging to detect the neutrino. To increase the neutrino cross section, the targets often contain a large atomic mass number (A) nucleus. Neutrino-nuclear interactions readily separate into three distinct topical areas that can be classified as low, medium, and high energy. At low energy, $\mathcal{O}$ (MeV), the wavelength scale of the interaction is greater than the nuclear diameter so that the initial and final states are specific nuclear levels. These are the interactions of greatest interest to solar and reactor neutrino oscillation experiments. In the medium-energy regime, $\mathcal{O}$ (1 GeV), which will be studied in this thesis, the interaction length is hadronic $\sim$ (1 fm), and the interactions are strongly modified by nuclear effects. These are the interactions of greatest interest to atmospheric and accelerator-based neutrino oscillation experiments. At high energies, $\mathcal{O}$ (100 GeV), the scale for deep-inelastic scattering (DIS) becomes partonic ($\sim$ 0.1 fm), and nuclear effects, although present, are less significant.

In the medium-energy regime, particles produced in neutrino interactions can re-interact before leaving the nucleus and can be absorbed, change their kinematics or even change charge before being detected. Nuclear re-interactions limit our ability to identify the reaction channel and they change the topology of the measured hadronic final state. Consequently, the detected rates on nuclei are changed significantly compared to the ones on free nucleons.

Our present knowledge of neutrino-nucleus interactions has been significantly improved by a new generation of oscillation and cross section experiments. Quasielastic (QE) scattering measurements have been published by MiniBooNE [6–8] at neutrino energies $E_\nu \sim 1$ GeV, by MINERνA [9, 10] at $E_\nu \sim 3.5$ GeV and by NOMAD at high (3-

100 GeV) energies [11]. Detailed single pion production data have become available from MiniBooNE [12–14] for different reaction channels including the coherent one, which has also been studied by SciBooNE [15, 16] at $E_\nu \sim 1$ GeV and NOMAD [17]. Finally, new inclusive cross section results have been reported by T2K [18], SciBooNE [19], MINOS [20] and NOMAD [21] Collaborations. These results challenge our understanding of neutrino interactions with matter and have triggered a renewed theoretical interest [22]. Quasielastic scattering has been investigated with a local Fermi gas [23–26], realistic spectral functions [27, 28], different models to describe the interaction of the knocked-out nucleon with the residual nucleus [29–31] and using the information from electron scattering data encoded in the scaling function [32]. The importance of two-nucleon contributions for the proper understanding of QE-like and inclusive cross sections has emerged in different studies [26, 33, 34], and their impact in the kinematic neutrino-energy reconstruction has been stressed [35–37]. Incoherent pion production has also been scrutinized using microscopic models for the reaction mechanism on the nucleon [38–43], with special attention paid to pion final state interactions in nuclei [43–47]. New microscopic models have been developed for coherent pion production [48–52] while traditional ones, based on the partial conservation of the axial current (PCAC), have been updated [53–56].

One of the possible reaction channels is photon emission induced by neutral current (NC) interactions (NCγ), which can occur on single nucleons and on nuclear targets. Weak photon emission has a small cross section compared, for example, with pion production, the most important inelastic mechanism. In spite of this, NC photon emission turns out to be one of the largest backgrounds in $\nu_\mu \to \nu_e$ ($\bar{\nu}_\mu \to \bar{\nu}_e$) oscillation experiments where electromagnetic showers instigated by electrons (positrons) and photons are not distinguishable. Thus, NC events producing single photons become an irreducible background to the charge-current (CC) QE signatures of ν_e ($\bar{\nu}_e$) appearance. This is precisely the case of the MiniBooNE experiment that was designed to test an earlier indication of a $\bar{\nu}_\mu \to \bar{\nu}_e$ oscillation signal observed at LSND [57, 58]. The MiniBooNE experiment finds an excess of events with respect to the predicted background in both ν and $\bar{\nu}$ modes. In the $\bar{\nu}$ mode, the data are found to be consistent with $\bar{\nu}_\mu \to \bar{\nu}_e$ oscillations and have

some overlap with the LSND result [59]. MiniBooNE data for ν_e appearance in the ν_μ mode show a clear (3σ) excess of signal-like events at low reconstructed neutrino energies ($200 < E_\nu^{\rm QE} < 475$ MeV) [59–61]. However, the $E_\nu^{\rm QE}$ distribution of the events is only marginally compatible with a simple two-neutrino oscillation model [59]. While several exotic explanations for this excess have been proposed, it could be related to unknown systematics or poorly understood backgrounds in the experimental analysis. In a similar way, NCγ is a source of misidentified electron-like events in the ν_e appearance measurements at T2K [62]. Even if the NCγ contribution to the background is relatively small, it can be critical in measurements of the CP-violating phase. It is therefore very important to have a robust theoretical understanding of the NC photon emission reaction, which cannot be unambiguously constrained by data. The study of the NCγ processes relevant for the MiniBooNE and T2K experiments is the first objective of the present thesis.

1.2 Hadron resonances

1.2.1 Meson resonances and SU(6) spin–flavor symmetry

Chiral symmetry and its pattern of spontaneous and explicit breaking plays a major role when dealing with most hadron processes involving pions and kaons (Goldstone bosons). Chiral Perturbation Theory (ChPT) [63], provides a model independent scheme where a multitude of low-energy nonperturbative strong-interaction phenomena can be understood. It has been successfully applied to study different processes, both in the meson-meson and in the meson-baryon sectors, involving light (u and d) or strange (s) quarks. However, by construction, ChPT is only valid at low energies, and it cannot describe the nature of hadron resonances. In recent years, it has been shown that by unitarizing the ChPT amplitudes, one can greatly extend the region of applicability of ChPT. This approach, is referred as unitary chiral perturbation theory (UChPT) [64, 65], and it has received much attention and provided many interesting results. In particular, many

meson-meson and meson-baryon resonances and bound states appear naturally within UChPT. These states are then interpreted as having a "dynamical nature". In other words, they are not genuine $q\bar{q}$ or qqq states, but are mainly built out of their meson-meson or meson-baryon components.

Heavy Quark Spin Symmetry (HQSS) is a proper QCD spin-flavor symmetry [66, 67] when the quark masses become much larger than the typical confinement scale, $\Lambda_{\rm QCD}$. HQSS predicts that all types of spin interactions vanish for infinitely massive quarks: the dynamics is unchanged under arbitrary transformations of the heavy quark spin. Consequently, the spin of the light degrees of freedom $\vec{S}_l = \vec{J} - \vec{S}_Q$ is conserved in that limit. Thus, heavy hadrons come in doublets (unless $s_l = 0$, with $\vec{S}_l^2 = s_l(s_l+1)$) containing states with total spin $j_\pm = s_l \pm 1/2$ obtained by combining the spin of the light degrees of freedom with the spin of the heavy quark $s_Q = 1/2$. These doublets are degenerated in the $m_Q \to \infty$ limit. For finite charm quark mass, there exist corrections, but the symmetry is still quite accurate.

In the Chapter 6, we will work within a model proposed in [68], where SU(6) spin-flavor symmetry is invoked to extend the SU(3) flavor UChPT framework of Refs. [64, 65] to include the dynamics of the low lying vector mesons belonging to the ρ-nonet. The approximate spin-flavor symmetry scheme of Ref. [68] provides a unified framework to deal with the lowest-lying mesons, implementing the required symmetry-breaking patterns and, in particular, fulfilling low-energy theorems derived from chiral symmetry. This scheme is of special relevance, because if it is extended to include heavier quark flavors, the approximate QCD HQSS will also be naturally accommodated in this spin-flavor approach through a suitable flavor-breaking pattern.

We will derive an extension of the model of Ref. [68] aiming to better accommodate the abundant existing phenomenology in the SU(3) flavor sector, particularly in what concerns to the vector meson–vector meson interaction. We will study the S-wave interaction of two members of the 35 (π-octet + ρ-nonet) SU(6) multiplet by means of an enlarged Weinberg-Tomozawa meson Lagrangian to accommodate vector mesons. We will firstly recover most of the results published in Ref. [68], where most of the low-lying even-parity meson resonances, especially in the spin-parity 0^+ and 1^+ sectors were dynamically gener-

ated and classified according to multiplets of the spin-flavor symmetry group SU(6). Next, we will re-examine the pattern of spin symmetry breaking advocated in Ref. [68] and propose two new symmetry breaking terms. Such terms neither affect the interaction of Nambu-Goldstone bosons between themselves, nor the interaction with vector mesons, but however they could improve the spin-parity 2^+ sector of the model of Ref. [68]. Indeed, the model used in Ref. [68] for the vector meson–vector meson interaction does not provide a satisfactory description of the main features of the 2^+ $f_2(1270)$, $K_2(1430)$ and $a_2(1320)$ resonances, which existence is experimentally well established. With the inclusion of these new terms, we find a much better description of these unstable mesons, without disturbing the results obtained in the spin-parity 0^+ and 1^+ sectors.

1.2.2 Baryon resonances: an effective Lagrangian approach

The baryon spectrum and baryon couplings studied from experimental data are two of the most important issues in hadronic physics and they are attracting great attention (see Ref. [69] for a general review). Nucleon excited states below 2.0 GeV have been extensively studied, from both the experimental and the theoretical points of view [70]. Thus, there exists abundant information on most of their parameters, such as masses, total and partial decay widths, and decay modes. However, the current knowledge on the properties of states around or above 2.0 GeV is still in its infancy [70]. On the other hand, in this region of energies, many theoretical predicted *missing N^* states*, within the constituent quark [71] or chiral unitary [72–76] approaches, have so far not been observed. Because a large number of effective degrees of freedom will induce a great number of excited states, the *missing N^* states* problem seems to favor diquark configurations, which could lead to reduced numbers of degrees of freedom. Such schemes would naturally predict a smaller number of excited N^* states [77]. Thus, the study of the possible role played by the 2.0 GeV region nucleon resonances in the available new accurate data from the LEPS [78, 79] and CLAS [80] Collaborations is timely and could shed light on the complicated dynamics that governs the highly excited nucleon (or in general baryon)

spectrum.

The associated strangeness production reaction $\gamma p \to K^+\Lambda(1520)$ might be thus an adequate tool to study the N^* resonances around 2.0 GeV, as long as they have significant couplings to the $K\Lambda(1520)$ pair. This is because the $K\Lambda(1520)$ is a pure isospin 1/2 channel and the threshold is about 2.0 GeV ($m_K + M_{\Lambda(1520)} \simeq 2.0$ GeV). Besides, this reaction requires the creation of an $\bar{s}s$ quark pair. Thus, a thorough and dedicated study of the strangeness production mechanism in this reaction has the potential to achieve a deeper understanding of the interaction among strange hadrons and, also, of the nature of the baryon resonances.

The effective Lagrangian approach is a straightforward method for systems where there is not enough information to provide a fundamental description of some of its properties. The idea is to parametrize the corresponding effects by introducing new interactions with coefficients to be determined phenomenologically. Experimental limits or the measurement of these parameters provide the information needed to achieve an accurate description. A standard procedure consists in first determining the relevant dynamical degrees of freedom involved and the exact (or partially) symmetries obeyed, and then construct the most general Lagrangian consistent with them.

In the Chapters 7 and 8, we will study the reaction $\gamma p \to K^+\Lambda(1520)$ within the effective Lagrangian approach, and will discuss some features of the $N^*(2120)$ resonance that can be inferred from recent data taken in Spring8 [78, 79] and CLAS [80].

1.3 Outline

This thesis is organized as follows. In the Chapter 2, we introduce some basic theoretical background on electroweak interactions, which will be used in the rest of the work. In the Chapters 3-5, the study of photon emission in NC reactions in nucleons and nuclei is presented. The microscopic model derived in the first of these three chapters is used to predict the number of NCγ events for the specific conditions of the MiniBooNE and T2K experiments. Results are presented in Chapters 4 and 5, respectively. The comparisons with the MiniBooNE

in situ estimate and the results obtained with the NEUT Monte Carlo generator, used by the T2K collaboration, are also discussed in these two chapters.

The second part of this thesis comprises the Chapters 6-8. The first chapter of this part is devoted to the study of meson resonances with a generalized Weinberg-Tomozawa interaction extended to the spin-flavor SU(6) symmetry group. As mentioned, we will present a through analysis of the low-lying even parity meson resonances dynamically generated within this approach in the 0^+ and 2^+ sectors. In the following two chapters, the $\Lambda(1520)$ photo-production reaction $\gamma p \to K^+\Lambda(1520)$ is analyzed in detail. In the Chapter 7, we investigate the $\Lambda(1520)$ photo-production off the proton using an effective Lagrangian approach and the isobar model, paying an special attention to the role played by the $J^P = 3/2^-$ $N^*(2120)$ resonance in this process. In the next chapter, possible Regge signatures in the recent CLAS data for this reaction are discussed and a hybrid approach is presented.

Finally, the main conclusions of our work are collected in Chapter 9. Besides, the are four appendices that include some technical details.

Chapter 2

Electroweak interactions

According to the Standard Model of particle physics, there are three mass-less neutrinos, ν_e, ν_μ and ν_τ. Neutrinos appear only left-handed, i.e., have spin anti-parallel to their momentum, while anti-neutrinos are right-handed. The electroweak interaction of leptons and nucleons is the first step to derive a model to describe neutrino-nucleus interactions. In this chapter, we will present a brief introduction to the electroweak interactions [81].

2.1 Lagrangian of the electroweak interaction

The Standard Model of electromagnetic and weak interactions is based on the local $SU(2) \times U(1)$ gauge symmetry [82–84]. After spontaneous symmetry breaking via the Higgs mechanism we get for the interaction part of the Lagrangian,

$$\mathcal{L}_{\text{int}} = -e\mathcal{J}^{\mu}_{\text{EM}}A_{\mu} - \frac{g}{2\sqrt{2}}\left(\mathcal{J}^{\mu}_{\text{CC}}W^{\dagger}_{\mu} + \text{h.c.}\right) - \frac{g}{2\cos\theta_W}\mathcal{J}^{\mu}_{\text{NC}}Z_{\mu}\,, \quad (2.1)$$

with,

- $\mathcal{J}^{\mu}_{\text{EM}}$, the electromagnetic current (EM) which couples to the photon field A_μ, as shown in Fig. 2.1(a).
- $\mathcal{J}^{\mu}_{\text{CC}}$, the weak charged current (CC) which couples to the charged W-boson field W_μ, as shown in Fig. 2.1(b).

- $\mathcal{J}^{\mu}_{\rm NC}$, the weak neutral current (NC) which couples to the neutral Z^0-boson field Z_μ, as shown in Fig. 2.1(c).

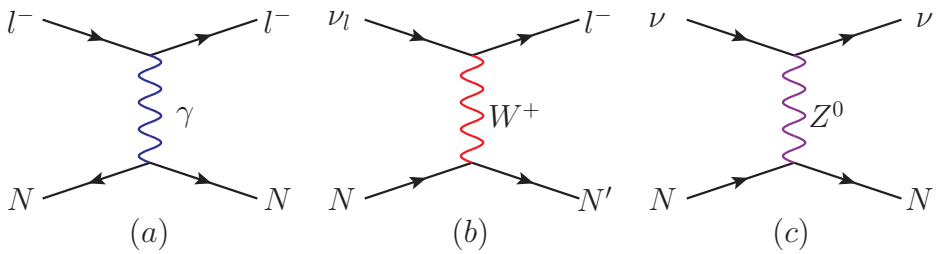

Figure 2.1: The interactions of leptons and nucleons. (a) EM scattering, (b) CC scattering, (c) NC scattering.

For the electromagnetic and weak coupling, we have:

$$\sin\theta_W = \frac{e}{g}\,, \quad \cos\theta_W = \frac{M_W}{M_Z}\,, \tag{2.2}$$

$$\frac{G}{\sqrt{2}} = \frac{g^2}{8M_W^2}\,, \tag{2.3}$$

where θ_W is the Weinberg angle, G is the Fermi coupling constant, M_W and M_Z are the masses of the W and Z bosons, respectively. At present, the values of these parameters are [70],

$$G = 1.1663787 \pm 0.0000006 \times 10^{-5}\ \text{GeV}^{-2}\,, \tag{2.4}$$

$$\sin^2\theta_W = 0.23116 \pm 0.00012\,, \tag{2.5}$$

$$M_W = 80.385 \pm 0.015\ \text{GeV}\,, \tag{2.6}$$

$$M_Z = 91.1876 \pm 0.0021\ \text{GeV}. \tag{2.7}$$

The electroweak currents in Eq. (2.1) include sums over all quarks and leptons, which will denote as j^μ and J^μ, for the leptonic and quark contributions, respectively. Next, we will give explicit expressions for the leptonic and quark currents.

2.2 Leptonic and quark currents

2.2.1 Leptonic currents

The leptonic electromagnetic current [Fig. 2.1(a)] couples to photons and it reads,

$$j^{\mu}_{\rm EM} = \bar{l}\gamma^{\mu} l\,, \tag{2.8}$$

where the Dirac matrices γ^{μ} and some of their properties are discussed in Appendix A.1.

As shown in Fig. 2.1(b), the CC couples to a charged $W^{\pm}$ boson. It does not change the lepton flavor but turns a charged lepton into a neutrino or viceversa. The coupling involves only left-handed fields leading to a vector–axial structure in the currents, which is given by

$$j^{\mu}_{\rm CC} = \bar{\nu}_l\gamma^{\mu}(1-\gamma_5) l\,. \tag{2.9}$$

Finally, the NC couples to the neutral Z^0 boson as depicted in Fig. 2.1(c), does not change the flavor and even keeps the identity of the lepton. In the case of the neutrinos, it is only possible the coupling to the left handed fields, while for the case of charged leptons both left and right handed fields are involved, but with different couplings,

$$j^{\mu}_{\rm NC} = \frac{1}{2}\bar{\nu}_l\gamma^{\mu}(1-\gamma_5)\nu_l + \frac{1}{2}\bar{l}\gamma^{\mu}(g_V - g_A\gamma_5) l\,, \tag{2.10}$$

$$g_V = -\frac{1}{2} - 2\sin^2\theta_W, \qquad g_A = -\frac{1}{2}. \tag{2.11}$$

The interaction Lagrangian of course includes all lepton flavors, therefore a sum over all flavors is understood implicitly in these expressions.

2.2.2 Quark Currents

We now specify the quark currents $J^{\mu}_{\rm EM}$, $J^{\mu}_{\rm CC}$ and $J^{\mu}_{\rm NC}$. We will restrict the discussion only to three flavors. The u, d and s quarks are the building blocks of a fundamental representation of the unitary flavor group $SU(3)_f$. Together they form a triplet field $\Psi(x)$:

$$\Psi(x) = \begin{pmatrix} \psi_u(x) \\ \psi_d(x) \\ \psi_s(x) \end{pmatrix}, \tag{2.12}$$

where $x \equiv x^\mu = (t, \vec{x})$ represents time and space coordinates. Each of the spin 1/2 quark fields $\psi_u(x)$, $\psi_d(x)$ and $\psi_s(x)$ is a four-component Dirac field which annihilates a quark or creates a antiquark of a given flavor. In this thesis, color plays no role and we shall drop explicitly color labels. However, it is noted that all electroweak currents, being color blind, involve a color trace.

Electromagnetic Quark Currents

The electromagnetic current reads,

$$J^\mu_{\rm EM} = \bar{\Psi} Q \gamma^\mu \Psi \tag{2.13}$$

$$= \frac{2}{3}\bar{\psi}_u \gamma^\mu \psi_u - \frac{1}{3}(\bar{\psi}_d \gamma^\mu \psi_d + \bar{\psi}_s \gamma^\mu \psi_s). \tag{2.14}$$

where the charge matrix for the u, d and s quarks is defined as,

$$Q = \begin{pmatrix} 2/3 & 0 & 0 \\ 0 & -1/3 & 0 \\ 0 & 0 & -1/3 \end{pmatrix}, \tag{2.15}$$

in electron charge $e > 0$ units. The u and d quarks alone form an isospin $I = 1/2$ doublet. When the s quark is included, the charge operator is,

$$Q = \frac{Y}{2} + I_3, \tag{2.16}$$

where $Y = B + S$ (with B and S, the baryon and the strangeness quantum numbers) is the hypercharge and I_3 is the third component of quark isospin. We have,

$$Y = \frac{\lambda_8}{\sqrt{3}} = \begin{pmatrix} 1/3 & 0 & 0 \\ 0 & 1/3 & 0 \\ 0 & 0 & -2/3 \end{pmatrix}, \tag{2.17}$$

$$I_3 = \frac{\lambda_3}{2} = \begin{pmatrix} 1/2 & 0 & 0 \\ 0 & -1/2 & 0 \\ 0 & 0 & 0 \end{pmatrix}. \tag{2.18}$$

The matrices λ_i are the Gell-Mann matrices, given in Appendix A.1. Thus, the electromagnetic current can be written,

$$\begin{aligned} J^{\mu}_{\rm EM} &= \bar{\Psi}(\frac{Y}{2} + I_3)\gamma^{\mu}\Psi \\ &= \bar{\Psi}(\frac{\lambda_8}{2\sqrt{3}} + \frac{\lambda_3}{2})\gamma^{\mu}\Psi \\ &= \frac{1}{2}V^{\mu}_{Y} + V^{\mu}_{3}\,, \end{aligned} \tag{2.19}$$

where the isospin (isovector) V^{μ}_3 and the hypercharge Y^{μ} currents read,

$$V^{\mu}_3 = \frac{1}{2}(\bar{\psi}_u\gamma^{\mu}\psi_u - \bar{\psi}_d\gamma^{\mu}\psi_d)\,, \tag{2.20}$$

$$Y^{\mu} = \frac{1}{3}(\bar{\psi}_u\gamma^{\mu}\psi_u + \bar{\psi}_d\gamma^{\mu}\psi_d) - \frac{2}{3}\bar{\psi}_s\gamma^{\mu}\psi_s\,. \tag{2.21}$$

Weak Quark Currents

In the case of the CC, we should consider that the mass eigenstates with third component of weak isospin $-1/2$ (the d and s quarks) are not the weak eigenstates. However, both sets of eigenstates are connected through a unitary transformation determined by the Cabbibo mixing angle, [1]

$$\begin{pmatrix} \psi'_d \\ \psi'_s \end{pmatrix} = \begin{pmatrix} \cos\theta_C & \sin\theta_C \\ -\sin\theta_C & \cos\theta_C \end{pmatrix} \begin{pmatrix} \psi_d \\ \psi_s \end{pmatrix}\,, \tag{2.22}$$

where $\cos\theta_C = 0.9745$ is the Cabbibo mixing angle. With the weak eigenstates given in Eq. (2.22), the CC then reads,

$$\begin{aligned} J^{\mu}_{\rm CC} &= \bar{\Psi}\gamma^{\mu}(1-\gamma^5)\Psi' \\ &= \bar{\psi}_u\gamma^{\mu}(1-\gamma^5)(\cos\theta_C\psi_d + \sin\theta_C\psi_s)\,. \end{aligned} \tag{2.23}$$

The term proportional to $\cos\theta_C$, responsible for the beta decay of the neutron, is

$$J^{\mu}_{\rm CC} = \cos\theta_C(V^{\mu}_{\rm CC} - A^{\mu}_{\rm CC})\,, \tag{2.24}$$

[1] For the weak isospin $-1/2$ quarks (i.e d, s and b), the mass eigenstates are obtained by a unitary transformation involving the CKM matrix. For practical purposes, the mixing angles θ_2 and θ_3 are small, and we can ignore both of them and thus we use only the Cabibbo angle $\theta_C = -\theta_1$ through this thesis [81].

$$\begin{aligned} V^{\mu}_{\rm CC} &= \bar{\psi}_u \gamma^{\mu} \psi_d = \bar{\Psi} \gamma^{\mu} \frac{\lambda_1 + i\lambda_2}{2} \Psi \\ &= \bar{\Psi} \gamma^{\mu} \frac{\lambda_+}{2} \Psi = V^{\mu}_1 + i V^{\mu}_2 \,, \end{aligned} \tag{2.25}$$

$$\begin{aligned} A^{\mu}_{\rm CC} &= \bar{\psi}_u \gamma^{\mu} \gamma^5 \psi_d = \bar{\Psi} \gamma^{\mu} \gamma^5 \frac{\lambda_1 + i\lambda_2}{2} \Psi \\ &= \bar{\Psi} \gamma_{\mu} \gamma^5 \frac{\lambda_+}{2} \Psi = A^{\mu}_1 + i A^{\mu}_2 . \end{aligned} \tag{2.26}$$

The NC is diagonal in flavor and it can be written as,

$$\begin{aligned} J^{\mu}_{\rm NC} &= \bar{\Psi} \gamma^{\mu} \left[(t_3 - Q \times \sin^2\theta_W)(1 - \gamma^5) - Q \times \sin^2\theta_W (1 + \gamma^5) \right] \Psi \\ &= \bar{\psi}_u \gamma^{\mu} \left(\frac{1}{2} - \frac{4}{3} \sin^2\theta_W - \frac{1}{2}\gamma^5 \right) \psi_u \\ &\quad + \bar{\psi}_d \gamma^{\mu} \left(-\frac{1}{2} - \frac{2}{3} \sin^2\theta_W + \frac{1}{2}\gamma^5 \right) \psi_d \\ &\quad + \bar{\psi}_s \gamma^{\mu} \left(-\frac{1}{2} - \frac{2}{3} \sin^2\theta_W + \frac{1}{2}\gamma^5 \right) \psi_s \,, \end{aligned} \tag{2.27}$$

where t_3 is the third component of the weak isospin. For the up quark $t_3 = 1/2$, and for down and strange quarks $t_3 = -1/2$. The NC can be expressed in the $(V - A)$ structure,

$$J^{\mu}_{\rm NC} = V^{\mu}_{\rm NC} - A^{\mu}_{\rm NC} \,, \tag{2.28}$$

$$\begin{aligned} V^{\mu}_{\rm NC} &= \bar{\Psi} \gamma^{\mu} \left[I_3 (1 - 2\sin^2\theta_W) \right] \Psi \\ &\quad - 2\sin^2\theta_W \bar{\Psi} \gamma^{\mu} \frac{Y}{2} \Psi + \bar{\Psi} \gamma^{\mu} t_{3(s)} \Psi \\ &= (1 - 2\sin^2\theta_W) V^{\mu}_3 - \sin^2\theta_W V^{\mu}_Y - \frac{1}{2} V^{\mu}_s , \end{aligned} \tag{2.29}$$

$$\begin{aligned} A^{\mu}_{\rm NC} &= \bar{\Psi} \gamma_{\mu} t_3 \gamma^5 \Psi \\ &= \bar{\Psi} \gamma_{\mu} (I_3 + t_{3(s)}) \gamma^5 \Psi \\ &= \bar{\Psi} \gamma_{\mu} \frac{\lambda_3}{2} \gamma^5 \Psi + \bar{\Psi} \gamma_{\mu} t_{3(s)} \gamma^5 \Psi \\ &= A^{\mu}_3 + \frac{1}{2} A^{\mu}_s \,. \end{aligned} \tag{2.30}$$

As shown in Eqs. (2.19), (2.25) and (2.29), V^{μ}_1, V^{μ}_2 and V^{μ}_3 are components of the same isospin vector current, V^{μ}_Y and V^{μ}_s are the isoscalar

hypercharge and strange currents, respectively. In Eqs. (2.26) and (2.30), A_1^μ, A_2^μ and A_3^μ form a vector in the isospin space, and A_s^μ is the isoscalar strange axial current. Therefore, we define the currents as,

$$\boldsymbol{V}^\mu = (\mathcal{V}_1^\mu, \mathcal{V}_2^\mu, \mathcal{V}_3^\mu) = \mathcal{V}^\mu \frac{\boldsymbol{t}}{2}, \tag{2.31}$$

$$\boldsymbol{A}^\mu = (\mathcal{A}_1^\mu, \mathcal{A}_2^\mu, \mathcal{A}_3^\mu) = \mathcal{A}^\mu \frac{\boldsymbol{t}}{2}, \tag{2.32}$$

where $\boldsymbol{t} = \boldsymbol{\tau}$ ($\boldsymbol{t} = \boldsymbol{T}^\dagger$) is the transition operator for isospin $1/2 \to 1/2$ ($1/2 \to 3/2$). The operator of the $1/2 \to 1/2$ transition is defined as,

$$\boldsymbol{\tau} = (\tau_1, \tau_2, \tau_3), \tag{2.33}$$

$$\tau_\pm = \frac{\tau_1 \pm i\tau_2}{2}, \quad \tau_0 = \tau_3, \tag{2.34}$$

$$\tau_-|p\rangle = |n\rangle, \quad \tau_+|n\rangle = |p\rangle, \tag{2.35}$$

$$\tau_+|p\rangle = \tau_-|n\rangle = 0, \tag{2.36}$$

where τ_i are the Pauli matrices given in Appendix A.1. And for transition of $1/2 \to 3/2$, the operator $\boldsymbol{T}^\dagger$ is defined by,

$$\boldsymbol{T}^\dagger = (T_1^\dagger, T_2^\dagger, T_3^\dagger), \tag{2.37}$$

$$\langle \frac{3}{2} M | T_\lambda^\dagger | \frac{1}{2} m \rangle = \left(\frac{1}{2} m 1 \lambda | \frac{3}{2} M \right), \tag{2.38}$$

$$T_{\pm 1}^\dagger = \mp \frac{T_1^\dagger \pm i T_2^\dagger}{\sqrt{2}}, \quad T_0^\dagger = T_3^\dagger. \tag{2.39}$$

2.2.3 $1/2 \to 1/2$ isospin transitions

For the $1/2 \to 1/2$ isospin transition, the EM matrix element reads,

$$\begin{aligned} \langle N^{*+} \mid J_{\rm EM}^\mu \mid p \rangle &= \langle N^{*+} \mid \frac{1}{2} V_Y^\mu + V_3^\mu \mid p \rangle \\ &= \langle N^{*+} \mid \mathcal{V}_Y^\mu \frac{I}{2} + \mathcal{V}^\mu \frac{\tau_3}{2} \mid p \rangle \\ &= \frac{\mathcal{V}_Y^\mu + \mathcal{V}^\mu}{2} \equiv \mathcal{V}_p^\mu, \end{aligned} \tag{2.40}$$

and, analogously,

$$\langle N^{*0} \mid J_{\rm EM}^\mu \mid n \rangle = \frac{\mathcal{V}_Y^\mu - \mathcal{V}^\mu}{2} \equiv \mathcal{V}_n^\mu. \tag{2.41}$$

For the vector part of the CC, the transition matrix element is,

$$\begin{aligned}\langle N^{*+} \mid V^{\mu}_{\rm CC} \mid n\rangle &= \langle N^{*+} \mid V^{\mu}_1 + iV^{\mu}_2 \mid n\rangle \\ &= \langle N^{*+} \mid \mathcal{V}^{\mu}\tau_+ \mid n\rangle \\ &\equiv \mathcal{V}^{\mu} = \mathcal{V}^{\mu}_p - \mathcal{V}^{\mu}_n\,, \end{aligned} \tag{2.42}$$

and for the NC on protons, we find,

$$\begin{aligned} & \langle N^{*+} \mid V^{\mu}_{\rm NC} \mid p\rangle \\ = \;& \langle N^{*+} \mid (1-2\sin^2\theta_W)V^{\mu}_3 - \sin^2\theta_W V^{\mu}_Y - \frac{1}{2}V^{\mu}_s \mid p\rangle \\ = \;& \langle N^{*+} \mid (1-2\sin^2\theta_W)\mathcal{V}^{\mu}\frac{\tau_3}{2} - \sin^2\theta_W \mathcal{V}^{\mu}_Y I - \mathcal{V}^{\mu}_s\frac{I}{2} \mid p\rangle \\ = \;& \left(\frac{1}{2} - \sin^2\theta_W\right)\mathcal{V}^{\mu} - \sin^2\theta_W\mathcal{V}^{\mu}_Y - \frac{1}{2}\mathcal{V}^{\mu}_s \\ = \;& \left(\frac{1}{2} - 2\sin^2\theta_W\right)\mathcal{V}^{\mu}_p - \frac{1}{2}\mathcal{V}^{\mu}_n - \frac{1}{2}\mathcal{V}^{\mu}_s\,, \end{aligned} \tag{2.43}$$

and for the NC transition on neutrons,

$$\begin{aligned}\langle N^{*0} \mid V^{\mu}_{\rm NC} \mid n\rangle &= -\left(\frac{1}{2} - \sin^2\theta_W\right)\mathcal{V}^{\mu} - \sin^2\theta_W\mathcal{V}^{\mu}_Y - \frac{1}{2}\mathcal{V}^{\mu}_s \\ &= \left(\frac{1}{2} - 2\sin^2\theta_W\right)\mathcal{V}^{\mu}_n - \frac{1}{2}\mathcal{V}^{\mu}_p - \frac{1}{2}\mathcal{V}^{\mu}_s\,. \end{aligned} \tag{2.44}$$

For the CC axial part, we have,

$$\begin{aligned}\langle N^{*+} \mid A^{\mu}_{\rm CC} \mid n\rangle &= \langle N^{*+} \mid A^{\mu}_1 + iA^{\mu}_2 \mid n\rangle \\ &= \langle N^{*+} \mid \mathcal{A}^{\mu}\tau_+ \mid n\rangle = \mathcal{A}^{\mu}\,, \end{aligned} \tag{2.45}$$

and for the NC,

$$\begin{aligned}
\langle N^{*+} \mid A^\mu_{\rm NC} \mid p\rangle &= \langle N^{*+} \mid A^\mu_3 + \frac{1}{2}A^\mu_s \mid p\rangle \\
&= \langle N^{*+} \mid \mathcal{A}^\mu \frac{\tau_3}{2} + \mathcal{A}^\mu_s \frac{I}{2} \mid p\rangle \\
&= \frac{\mathcal{A}^\mu + \mathcal{A}^\mu_s}{2}\,, \qquad (2.46)\\
\langle N^{*0} \mid A^\mu_{\rm NC} \mid n\rangle &= \langle N^{*0} \mid A^\mu_3 + \frac{1}{2}A^\mu_s \mid n\rangle \\
&= \langle N^{*0} \mid \mathcal{A}^\mu \frac{\tau_3}{2} + \mathcal{A}^\mu_s \frac{I}{2} \mid n\rangle \\
&= \frac{-\mathcal{A}^\mu + \mathcal{A}^\mu_s}{2}\,. \qquad (2.47)
\end{aligned}$$

2.2.4 $1/2 \to 3/2$ isospin transitions

For the transition between isospin 1/2 to isospin 3/2 states, the currents should be purely isovector. First, the EM transition matrix elements read,

$$\begin{aligned}
\langle \Delta^+ \mid J^\mu_{\rm EM} \mid p\rangle &= \langle \Delta^+ \mid V^\mu_3 \mid p\rangle \\
&= \langle \Delta^+ \mid \mathcal{V}^\mu \frac{T^\dagger_0}{2} \mid p\rangle \\
&= \mathcal{V}^\mu \left(\frac{1}{2}\ \frac{1}{2}\ 1\ 0\ \mid\ \frac{3}{2}\ \frac{1}{2}\right) = \sqrt{\frac{2}{3}}\mathcal{V}^\mu\,, \qquad (2.48)
\end{aligned}$$

$$\langle \Delta^0 \mid J^\mu_{\rm EM} \mid n\rangle = \mathcal{V}^\mu \left(\frac{1}{2}\ -\frac{1}{2}\ 1\ 0\ \mid\ \frac{3}{2}\ -\frac{1}{2}\right) = \sqrt{\frac{2}{3}}\mathcal{V}^\mu\,. \qquad (2.49)$$

For the vector part of the CC, the transition matrix elements are given by,

$$\begin{aligned}
\langle \Delta^+ \mid V^\mu_{\rm CC} \mid n\rangle &= \langle \Delta^+ \mid V^\mu_1 + iV^\mu_2 \mid n\rangle \\
&= -\sqrt{2}\langle \Delta^+ \mid \mathcal{V}^\mu T^\dagger_{+1} \mid n\rangle \\
&= -\sqrt{2}\mathcal{V}^\mu \left(\frac{1}{2}\ -\frac{1}{2}\ 1\ 1\ \mid\ \frac{3}{2}\ \frac{1}{2}\right) \\
&= -\sqrt{\frac{2}{3}}\mathcal{V}^\mu\,, \qquad (2.50)
\end{aligned}$$

$$\begin{aligned}\langle \Delta^{++} \mid V^\mu_{\rm CC} \mid p\rangle &= \langle \Delta^{++} \mid V^\mu_1 + iV^\mu_2 \mid p\rangle \\ &= -\sqrt{2}\langle \Delta^{++} \mid \mathcal{V}^\mu T^\dagger_{+1} \mid p\rangle \\ &= -\sqrt{2}\mathcal{V}^\mu \left(\frac{1}{2}\ \frac{1}{2}\ 1\ 1 \ \mid\ \frac{3}{2}\ \frac{3}{2}\right) \\ &= -\sqrt{2}\mathcal{V}^\mu\,. \end{aligned} \tag{2.51}$$

And for the axial part of the CC, we find

$$\begin{aligned}\langle \Delta^{+} \mid A^\mu_{\rm CC} \mid n\rangle &= \langle \Delta^{+} \mid A^\mu_1 + iA^\mu_2 \mid n\rangle \\ &= -\sqrt{\frac{2}{3}}\mathcal{A}^\mu\,, \end{aligned} \tag{2.52}$$

$$\begin{aligned}\langle \Delta^{++} \mid A^\mu_{\rm CC} \mid p\rangle &= \langle \Delta^{++} \mid A^\mu_1 + iA^\mu_2 \mid p\rangle \\ &= -\sqrt{2}\mathcal{V}^\mu\,. \end{aligned} \tag{2.53}$$

For the NC, we have

$$\begin{aligned}\langle \Delta^{+} \mid V^\mu_{\rm NC} \mid p\rangle &= \langle \Delta^{+} \mid \left(1-2\sin^2\theta_W\right)\mathcal{V}^\mu_3 \mid p\rangle \\ &= \langle \Delta^{+} \mid \left(1-2\sin^2\theta_W\right)\mathcal{V}^\mu T^+_0 \mid p\rangle \\ &= \left(1-2\sin^2\theta_W\right)\mathcal{V}^\mu \left(\frac{1}{2}\ \frac{1}{2}\ 1\ 0 \ \mid\ \frac{3}{2}\ \frac{1}{2}\right) \\ &= \left(1-2\sin^2\theta_W\right)\sqrt{\frac{2}{3}}\mathcal{V}^\mu\,, \end{aligned} \tag{2.54}$$

$$\begin{aligned}\langle \Delta^{0} \mid V^\mu_{\rm NC} \mid n\rangle &= \langle \Delta^{0} \mid \left(1-2\sin^2\theta_W\right)\mathcal{V}^\mu_3 \mid n\rangle \\ &= \langle \Delta^{0} \mid \left(1-2\sin^2\theta_W\right)\mathcal{V}^\mu T^+_0 \mid n\rangle \\ &= \left(1-2\sin^2\theta_W\right)\mathcal{V}^\mu \left(\frac{1}{2}\ -\frac{1}{2}\ 1\ 0 \ \mid\ \frac{3}{2}\ -\frac{1}{2}\right) \\ &= \left(1-2\sin^2\theta_W\right)\sqrt{\frac{2}{3}}\mathcal{V}^\mu\,, \end{aligned} \tag{2.55}$$

and for the axial part of the NC,

$$\begin{aligned}\langle \Delta^{+} \mid A^\mu_{\rm NC} \mid p\rangle &= \langle \Delta^{+} \mid \mathcal{A}^\mu_3 \mid p\rangle \\ &= \langle \Delta^{+} \mid \mathcal{A}^\mu T^+_0 \mid p\rangle \\ &= \mathcal{A}^\mu \left(\frac{1}{2}\ \frac{1}{2}\ 1\ 0 \ \mid\ \frac{3}{2}\ \frac{1}{2}\right) = \sqrt{\frac{2}{3}}\mathcal{A}^\mu\,, \end{aligned} \tag{2.56}$$

$$\langle \Delta^0 \mid A^\mu_{\rm NC} \mid n \rangle \;=\; \sqrt{\frac{2}{3}} \mathcal{A}^\mu \,. \tag{2.57}$$

Chapter 3

Photon emission in neutral current (NCγ) interactions at intermediate energies

3.1 Introduction

A good understanding of (anti)neutrino cross sections is crucial to reduce the systematic uncertainties in oscillation experiments aiming at a precise determination of neutrino properties [85]. Our present knowledge of neutrino-nucleus interactions has been significantly improved by a new generation of oscillation and cross section experiments [6–21]. These results challenge our understanding of neutrino interactions with matter and have triggered a renewed theoretical interest [22–56].

As mentioned in the general introduction of the thesis, one of the possible reaction channels is photon emission induced by NC interactions (NCγ), which can occur on single nucleons and on nuclear targets. Weak photon emission has a small cross section compared, for example, with pion production, the most important inelastic mechanism. In spite of this, NC photon emission turns out to be one of the largest backgrounds in $\nu_\mu \to \nu_e$ ($\bar{\nu}_\mu \to \bar{\nu}_e$) oscillation experiments where electromagnetic showers instigated by electrons (positrons) and photons are not distinguishable. Thus, NC events producing single photons become an irreducible background to the CC QE signatures of ν_e ($\bar{\nu}_e$) appearance. This is precisely the case of the MiniBooNE experiment

that was designed to test an earlier indication of a $\bar{\nu}_\mu \to \bar{\nu}_e$ oscillation signal observed at LSND [57, 58]. The MiniBooNE experiment finds an excess of events with respect to the predicted background in both ν and $\bar{\nu}$ modes. In the $\bar{\nu}$ mode, the data are found to be consistent with $\bar{\nu}_\mu \to \bar{\nu}_e$ oscillations and have some overlap with the LSND result [59]. MiniBooNE data for ν_e appearance in the ν_μ mode show a clear (3σ) excess of signal-like events at low reconstructed neutrino energies ($200 < E_\nu^{\rm QE} < 475$ MeV) [59, 60]. However, the $E_\nu^{\rm QE}$ distribution of the events is only marginally compatible with a simple two-neutrino oscillation model [59]. While several exotic explanations for this excess have been proposed, it could be related to unknown systematics or poorly understood backgrounds in the experimental analysis. In a similar way, NCγ is a source of misidentified electron-like events in the ν_e appearance measurements at T2K [62]. Even if the NCγ contribution to the background is relatively small, it can be critical in measurements of the CP-violating phase. It is therefore very important to have a robust theoretical understanding of the NC photon emission reaction, which cannot be unambiguously constrained by data. This is the goal of the present work.

The first step torwards a realistic description of NC photon emission on nuclear targets of neutrino detectors is the study of the corresponding process on the nucleon. Theoretical models for the $\nu N \to \nu N \gamma$ reaction have been presented in Refs. [42, 86]. They start from Lorentz-covariant effective field theories with nucleon, pion, $\Delta(1232)$ but also scalar (σ) and vector (ρ, ω) mesons as the relevant degrees of freedom, and exhibit a nonlinear realization of (approximate) $SU(2)_L \otimes SU(2)_R$ chiral symmetry. The single mechanism of $\Delta(1232)$ excitation followed by its decay $\Delta \to N\gamma$ was considered in Ref. [87], where a consistent treatment of the Δ vertices and propagator is adopted. Several features of the previous studies, in particular the approximate chiral symmetry and the dominance of the $\Delta(1232)$ mediated mechanism are common to the model derived in our work. In Ref. [42], a special attention is paid to the power counting, which is shown to be valid for neutrino energies below 550 MeV. However, the neutrino fluxes of most neutrino experiments span to considerably higher energies. Thus, in Ref. [88], the power counting scheme was abandoned, and the model of [42] was phenomenologically extended to the intermediate energies

($E_\nu \sim 1$ GeV) relevant for the MiniBooNE ν flux, by including phenomenological form factors. Though the extension proposed for the Δ and the nucleon Compton-like mechanisms seems reasonable, the one for the contact terms notably increases the cross section above ~ 1 GeV (they are more significant for neutrinos than for antineutrinos). Since the contact terms and the associated form factors are not well understood so far, the model predictions for $E_\nu > 1$ GeV should be taken cautiously, as explicitly acknowledged in Ref. [88].

In nuclear targets, the reaction can be incoherent when the final nucleus is excited (and fragmented) or coherent, when it remains in the ground state. It is also possible that, after nucleon knockout, the residual excited nucleus decays emitting low-energy γ rays. This mechanism has been recently investigated [89] and shall not be discussed here. The model of Ref [86] has been applied to incoherent photon production in an impulse approximation that ignores nuclear corrections [90]. These are also neglected in the coherent case, which is calculated by treating the nucleus as a scalar particle and introducing a form factor to ensure that the coherence is restricted to low-momentum transfers [86]. More robust is the approach of Refs. [52, 91] based on a chiral effective field theory for nuclei, again extended phenomenologically to higher energies [88]. In addition to Pauli blocking and Fermi motion, the Δ resonance broadening in the nucleus, is also taken into account. The latter correction causes a very strong reduction of the resonant contribution to the cross section, in variance with our results, as will be shown below. The ratio of the Δ to photon and Δ to π^0 decay rates is enhanced in the nuclear medium by an amount that depends on the resonance invariant mass, momentum and also production position inside the nucleus, as estimated with a transport model [92, 93]. The coherent channel has also been studied in Refs. [94, 95] at high energies. A discussion about these works can be found in Section V.E of Ref. [86].

It is worth mentioning that both the models of Ref. [86] and Refs [42, 52, 88, 91] have been used to calculate the NCγ events at MiniBooNE with contradicting conclusions [88, 90]. While in Ref. [90] the number of these events were calculated to be twice as many as expected from the MiniBooNE in situ estimate, much closer values were predicted in Ref. [88]. The result that NCγ events give a significant contribution to

the MiniBooNE low-energy excess [86] could have its origin in the lack of nuclear effects and rather strong detection efficiency correction.

Here we present a realistic model for NC photon emission in the $E_\nu \sim 1$ GeV region that extends and improves certain relevant aspects of the existing descriptions. The model is developed in the line of previous work on weak pion production on nucleons [39] and nuclei for both incoherent [43] and coherent [50, 96] processes. The model for free nucleons satisfies the approximate chiral symmetry incorporated in the non-resonant terms and includes the dominant $\Delta(1232)$ excitation mechanism, with couplings and form factors taken from the available phenomenology. Moreover, we have extended the validity of the approach to higher energies by including intermediate excited states from the second resonance region [$P_{11}(1440)$, $D_{13}(1520)$ and $S_{11}(1535)$]. Among them, we have found a considerable contribution of the $D_{13}(1520)$ for (anti)neutrino energies above 1.5 GeV. When the reaction takes place inside the nucleus, we have applied a series of standard medium corrections that have been extensively confronted with experiment in similar processes such as pion [97, 98], photon [99] and electron [100, 101] scattering with nuclei, or coherent pion photo [102] and electroproduction [103].

This chapter is based on Ref. [104] and it is organized as follows. The model for NC production of photons off nucleons is described in Sec. 3.2. After discussing the relevant kinematics, we evaluate the different amplitudes in Subsec. 3.2.2. In the first place, the dominant $\Delta(1232)$ and non-resonant contributions are studied (Subsec. 3.2.2). Next, we examine the contributions driven by N^* resonances from the second resonance region (Subsec. 3.2.2). The relations between vector form factors and helicity amplitudes, and the off-diagonal N^*N Goldberger-Treiman (GT) relations are discussed in Appendices B.1 and B.2, respectively. NCγ reactions in nuclei are studied in Sec. 3.3. First, in Subsec. 3.3.1, we pay attention to the incoherent channel driven by one particle–one hole (1p1h) nuclear excitations. Next, in Subsec. 3.3.2, the coherent channel is studied. We present the results of this chapter in Sec. 3.4, where we also compare some of our predictions with the corresponding ones from Refs. [86, 88]. This section is split in two subsections, where the results for NCγ on single nucleons (Subsec. 3.4.1) and on nuclei (Subsec. 3.4.2) are discussed. Predictions

for nuclear incoherent and coherent reactions are presented in Subsec. 3.4.2. Finally the main conclusions of this work are summarized in Sec. 3.5.

3.2 Neutral current photon emission off nucleons

In this section, we describe the model for NC production of photons off nucleons,

$$\begin{aligned} \nu(k) + N(p) &\rightarrow \nu(k') + N(p') + \gamma(k_\gamma), \\ \bar{\nu}(k) + N(p) &\rightarrow \bar{\nu}(k') + N(p') + \gamma(k_\gamma)\,. \end{aligned} \tag{3.1}$$

3.2.1 Kinematics and general definitions

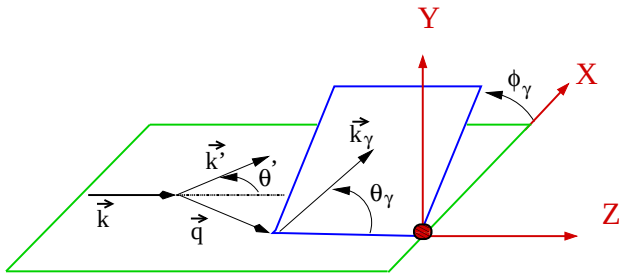

Figure 3.1: Representation of the different LAB kinematical variables used through this work.

The unpolarized differential cross section with respect to the photon kinematical variables (kinematics is sketched in Fig. 3.1) is given in the Laboratory (LAB) frame by

$$\frac{d^3\sigma_{(\nu,\bar{\nu})}}{dE_\gamma d\Omega(\hat{k}_\gamma)} = \frac{E_\gamma}{|\vec{k}|}\frac{G^2}{16\pi^2}\int \frac{d^3k'}{|\vec{k}'|} L^{(\nu,\bar{\nu})}_{\mu\sigma} W^{\mu\sigma}_{\mathrm{NC}\gamma}\,. \tag{3.2}$$

As we neglect the neutrino masses, $E_\nu = |\vec{k}|$, $E' = |\vec{k}'|$ and $E_\gamma = |\vec{k}_\gamma|$, where $\vec{k}$, $\vec{k}'$ and $\vec{k}_\gamma$ are the incoming neutrino, outgoing neutrino and outgoing photon momenta in LAB, in this order; $G = 1.1664 \times 10^{-11}$

MeV^{-2} is the Fermi constant, while $L^{(\nu,\bar{\nu})}$ and $W_{\mathrm{NC}\gamma}$ stand for the leptonic and hadronic tensors, respectively. The leptonic tensor[1]

$$\begin{aligned} L^{(\nu,\bar{\nu})}_{\mu\sigma} &= (L_s)_{\mu\sigma} + \mathrm{i}(L^{(\nu,\bar{\nu})}_a)_{\mu\sigma} \\ &= k'_\mu k_\sigma + k'_\sigma k_\mu + g_{\mu\sigma}\frac{q^2}{2} \pm \mathrm{i}\epsilon_{\mu\sigma\alpha\beta}k'^\alpha k^\beta, \\ &\qquad (+ \to \nu,\ - \to \bar{\nu}) \end{aligned} \tag{3.3}$$

is orthogonal to the four momentum transfer $q_\mu = k_\mu - k'_\mu$, with $q^2 = -2k\cdot k' = -4EE'\sin^2\theta'/2$. The hadronic tensor includes the non-leptonic vertices and reads

$$\begin{aligned} W^{\mu\sigma}_{\mathrm{NC}\gamma} &= \frac{1}{4M}\overline{\sum_{\mathrm{spins}}}\int \frac{d^3p'}{(2\pi)^3}\frac{1}{2E'_N}\delta^4(p' + k_\gamma - q - p) \\ &\quad \times \langle N\gamma|j^\mu_{\mathrm{nc}\gamma}(0)|N\rangle\langle N\gamma|j^\sigma_{\mathrm{nc}\gamma}(0)|N\rangle^*, \end{aligned} \tag{3.4}$$

with M the nucleon mass[2] and E'_N the energy of the outgoing nucleon. The bar over the sum of initial and final spins denotes the average over the initial ones. The one particle states are normalized as $\langle\vec{p}|\vec{p}'\rangle = (2\pi)^3 2p_0\delta^3(\vec{p}-\vec{p}')$. Then, the matrix element $\langle N\gamma|j^\mu_{\mathrm{NC}\gamma}(0)|N\rangle$ is dimensionless. For the sake of completeness, we notice that the NC, j^μ_{nc} and electromagnetic (EM), J^μ_{EM} currents at the quark level are given by (note a change of normalization and here $j^\mu_{\mathrm{NC}}/2 = J^\mu_{\mathrm{NC}}$, as defined in Eq. (2.27))

$$\begin{aligned} j^\mu_{\mathrm{NC}} &= \bar{\Psi}_u\gamma^\mu(1 - \frac{8}{3}\sin^2\theta_W - \gamma_5)\Psi_u - \bar{\Psi}_d\gamma^\mu(1 - \frac{4}{3}\sin^2\theta_W - \gamma_5)\Psi_d \\ &\quad -\bar{\Psi}_s\gamma^\mu(1 - \frac{4}{3}\sin^2\theta_W - \gamma_5)\Psi_s, \\ &= \bar{\Psi}_q\gamma^\mu(1-\gamma_5)\tau^1_0\Psi_q - 4\sin^2\theta_W J^\mu_{\mathrm{EM}} - \bar{\Psi}_s\gamma^\mu(1-\gamma_5)\Psi_s \qquad (3.5) \\ J^\mu_{\mathrm{EM}} &= \frac{2}{3}\bar{\Psi}_u\gamma^\mu\Psi_u - \frac{1}{3}\bar{\Psi}_d\gamma^\mu\Psi_d - \frac{1}{3}\bar{\Psi}_s\gamma^\mu\Psi_s, \qquad (3.6) \end{aligned}$$

where Ψ_u, Ψ_d and Ψ_s are the quark fields and θ_W the weak angle ($\sin^2\theta_W \sim 0.231$). The zeroth spherical component of the isovector operator $\tau^{(1)}$ is equal to the third component of the isospin Pauli matrices $\vec{\tau}$.

[1] Our conventions are such that $\epsilon_{0123} = +1$ and $g^{\mu\nu} = (+,-,-,-)$.

[2] We take the average of the neutron and proton masses.

By construction, the hadronic tensor accomplishes

$$W^{\mu\sigma}_{\mathrm{NC}\gamma} = W^{(s)\mu\sigma}_{\mathrm{NC}\gamma} + iW^{(a)\mu\sigma}_{\mathrm{NC}\gamma}\,, \tag{3.7}$$

in terms of its real symmetric, $W^{(s)}_{\mathrm{NC}\gamma}$, and anti-symmetric, $W^{(a)}_{\mathrm{NC}\gamma}$, parts. Both lepton and hadron tensors are independent of the neutrino flavor and, therefore, the cross section for the reaction of Eq. (3.1) is the same for electron, muon or tau incident (anti)neutrinos.

Let us define the amputated amplitudes $\Gamma^{\mu\rho}$, as

$$\langle N\gamma|j^{\mu}_{\mathrm{NC}\gamma}(0)|N\rangle = \bar{u}(p')\Gamma^{\mu\rho}u(p)\epsilon^{*}_{\rho}(k_\gamma)\,, \tag{3.8}$$

where the spin dependence of the Dirac spinors (normalized such that $\bar{u}u = 2M$) for the nucleons is understood, and $\epsilon(k_\gamma)$ is the polarization vector of the outgoing photon. To keep the notation simple we do not specify the type of nucleon ($N = n$ or p) in $\Gamma^{\mu\rho}$. In terms of these amputated amplitudes, and after performing the average (sum) over the initial (final) spin states, we find

$$\begin{aligned} W^{\mu\sigma}_{\mathrm{NC}\gamma} &= -\frac{1}{8M}\int \frac{d^3p'}{(2\pi)^3}\frac{1}{2E'_N}\delta^4(p'+k_\gamma-q-p) \\ &\quad\times \mathrm{Tr}\left((\not{p}'+M)\Gamma^{\mu\rho}(\not{p}+M)\gamma^0(\Gamma^{\sigma}_{\cdot\rho})^{\dagger}\gamma^0\right). \end{aligned} \tag{3.9}$$

After performing the d^3p' integration, there is still a $\delta(p'^0 + E_\gamma - q^0 - p^0)$ left in the hadronic tensor, which can be used to perform the integration over $|\vec{k}'|$ in Eq. (3.2).

3.2.2 Evaluation of the $\Gamma^{\mu\rho}$ amputated amplitudes

The $\Delta(1232)$ contribution, chiral symmetry and non-resonant terms

Just as in pion production [39], one expects the NCγ reaction to be dominated by the excitation of the $\Delta(1232)$ supplemented with a non-resonant background. In our case, the leading non-resonant contributions are nucleon-pole terms built out of Z^0NN and γNN vertices that respect chiral symmetry. The q^2 dependence of the amplitudes is introduced via phenomenological form factors. We also take into account the sub-leading mechanism originated from the anomalous $Z^0\gamma\pi$

vertex, that involves a pion exchange in the $t-$channel. Thus, in a first stage we consider the five diagrams depicted in Fig. 3.2 (see the caption of this figure to clarify the notation). The corresponding amputated amplitudes are

$$\begin{aligned}\Gamma_N^{\mu\rho} &= \Gamma_{NP}^{\mu\rho} + \Gamma_{CNP}^{\mu\rho} \\ &= ie\, J_{EM}^{\rho}(-k_\gamma)\frac{\not p + \not q + M}{(p+q)^2 - M^2 + i\epsilon} J_{NC}^{\mu}(q) \\ &\quad + ie\, J_{NC}^{\mu}(q)\frac{(\not p' - \not q + M)}{(p'-q)^2 - M^2 + i\epsilon} J_{EM}^{\rho}(-k_\gamma), \end{aligned} \tag{3.10}$$

$$\begin{aligned}\Gamma_{\pi Ex}^{\mu\rho} &= eC_N \frac{M g_A}{4\pi^2 f_\pi^2}(1 - 4\sin^2\theta_W)\frac{\gamma_5 \epsilon^{\mu\rho\sigma\alpha} q_\sigma k_{\gamma\alpha}}{(q-k_\gamma)^2 - m_\pi^2}, \\ &\quad (C_N = +1 \to p,\, C_N = -1 \to n) \end{aligned} \tag{3.11}$$

$$\begin{aligned}\Gamma_\Delta^{\mu\rho} &= \Gamma_{\Delta P}^{\mu\rho} + \Gamma_{C\Delta P}^{\mu\rho} \\ &= ie\,\gamma^0 \left[J_{EM}^{\alpha\rho}(p', k_\gamma)\right]^\dagger \gamma^0 \frac{P_{\alpha\beta}(p_\Delta = p+q)}{(p+q)^2 - M_\Delta^2 + iM_\Delta \Gamma_\Delta(p_\Delta^2)} J_{NC}^{\beta\mu}(p,q) \\ &\quad + ie\,\gamma^0 \left[J_{NC}^{\alpha\mu}(p', -q)\right]^\dagger \gamma^0 \frac{P_{\alpha\beta}(p_\Delta = p'-q)}{(p'-q)^2 - M_\Delta^2 + iM_\Delta \Gamma_\Delta(p_\Delta^2)} \\ &\quad \times J_{EM}^{\beta\rho}(p, -k_\gamma), \end{aligned} \tag{3.12}$$

with $e > 0$ the electron charge, such that $\alpha = e^2/4\pi \approx 1/137$, $f_\pi = 92.4$ MeV the pion decay constant and $g_A = 1.267$ the axial nucleon charge; m_π and $M_\Delta (\sim 1232\,\text{MeV})$ are the pion and Δ masses, respectively. As it will be clear in the following, each of the building blocks of the model is gauge invariant by construction $\bar u(p')\,\Gamma_{N,\Delta,\pi Ex}^{\mu\rho}\,u(p)(k_\gamma)_\rho = 0$. The vector parts of these amplitudes are also conserved (CVC) $\bar u(p')\,V_{N,\Delta,\pi Ex}^{\mu\rho}\,u(p) q_\mu = 0$.

- The nucleon NC and EM currents are given by

$$J_{NC}^{\mu}(q) = \gamma^\mu \tilde F_1(q^2) + \frac{i}{2M}\sigma^{\mu\beta} q_\beta \tilde F_2(q^2) - \gamma^\mu\gamma_5 \tilde F_A(q^2), \tag{3.13}$$

$$J_{EM}^{\mu}(k_\gamma) = \gamma^\mu F_1(0) + \frac{i}{2M}\sigma^{\mu\nu}(k_\gamma)_\nu F_2(0), \tag{3.14}$$

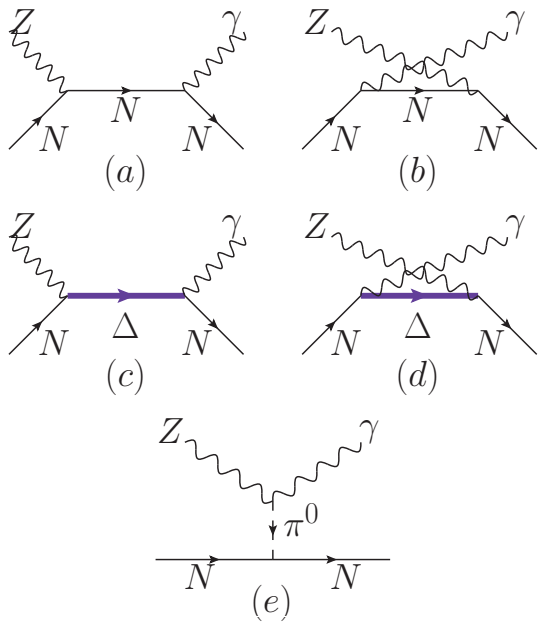

Figure 3.2: Model for photon emission off the nucleon; direct and crossed nucleon-pole terms (a,b), direct and crossed $\Delta(1232)$-pole terms (c,d) and the anomalous $t-$channel pion exchange term (e). Throughout this work, we denote these contributions as NP, CNP, ΔP, $C\Delta P$ and πEx, respectively.

where $\tilde{F}_{1,2}$ and $\tilde{F}_A$ are the NC vector and axial form factors[3] while $F_{1,2}$ are the EM ones. These form factors take different values for protons and neutrons. For $F_{1,2}$, we have that

$$F_1^{(N)} = \frac{G_E^N + \tau G_M^N}{1+\tau},\ F_2^{(N)} = \frac{G_M^N - G_E^N}{1+\tau},\ N = p, n \quad (3.15)$$

with

$$G_E^p = \frac{G_M^p}{\mu_p} = \frac{G_M^n}{\mu_n} = -(1+b\tau)\frac{G_E^n}{\mu_n a\tau} = \left(\frac{1}{1-q^2/M_D^2}\right)^2, \quad (3.16)$$

[3]Note that pseudoscalar ($q^\mu\gamma_5$) terms do not contribute because $q^\mu L_{\mu\sigma}^{(\nu\bar{\nu})} = 0$ when neutrino masses are neglected.

where $\tau = -q^2/4M^2$, $M_D = 0.84$ GeV, $\mu_p = 2.793$, $\mu_n = -1.913$, $b = 4.61$ and $a = 0.942$ [105].

The NC vector form factors $\tilde{F}_{1,2}$ can be referred to the EM ones thanks to isospin symmetry relationships,

$$\tilde{F}_{1,2}^{(p)} = (1 - 4\sin^2\theta_W)F_{1,2}^{(p)} - F_{1,2}^{(n)} - F_{1,2}^{(s)}\,, \qquad (3.17)$$

$$\tilde{F}_{1,2}^{(n)} = (1 - 4\sin^2\theta_W)F_{1,2}^{(n)} - F_{1,2}^{(p)} - F_{1,2}^{(s)}\,, \qquad (3.18)$$

where $F_{1,2}^{(s)}$ are the strange EM form factors. Furthermore, in the axial sector one has that

$$\tilde{F}_A^{(p,n)} = \pm F_A - F_A^{(s)}, \qquad (+ \to p, - \to n)\ , \qquad (3.19)$$

where F_A is the axial form factor that appears in CCQE interactions, for which we adopt a conventional dipole parametrization

$$F_A(q^2) = g_A \left(1 - \frac{q^2}{M_A^2}\right)^{-2} \qquad (3.20)$$

with an axial mass $M_A = 1$ GeV [106]; $F_A^{(s)}$ is the strange axial form factor. At present, the best determinations of the strange form factors are consistent with zero [107], thus they have been neglected in the present study.

- The $t-$channel pion exchange contribution arises from the anomalous ($\pi^0\gamma Z^0$) Lagrangian [86]

$$\mathcal{L}_{\pi^0\gamma Z^0} = \frac{eg}{4\cos\theta_W}\frac{N_C}{12\pi^2 f_\pi}(1 - 4\sin^2\theta_W)\pi^0\epsilon^{\mu\nu\alpha\beta}\partial_\mu Z_\nu \partial_\alpha A_\beta\,, \qquad (3.21)$$

together with the leading order $\pi^0 NN$ interaction term

$$\mathcal{L}_{\pi^0\mathrm{NN}} = \frac{g_A}{f_\pi}\bar{\Psi}\gamma^\mu\gamma_5\frac{\tau_3}{2}(\partial_\mu\pi^0)\Psi\,, \qquad \Psi = \begin{pmatrix} p \\ n \end{pmatrix}\,, \qquad (3.22)$$

where Ψ, π^0, A_β, Z_ν are the nucleon, neutral pion, photon and Z^0 boson fields, respectively. Besides, $g = e/\sin\theta_W$ is related to the Fermi constant G and the W-boson mass as $G/\sqrt{2} = g^2/8M_W^2$; N_C is the number of colors. The Lagrangian of Eq. (3.21) arises from the Wess-Zumino-Witten term [108, 109], which accounts for the axial anomaly of QCD.

- Finally, in the $\Delta-$driven amplitudes of Eq. (3.12), $P^{\mu\nu}$ is the spin 3/2 projection operator, which reads

$$P^{\mu\nu}(p_\Delta) = -(\not{p}_\Delta + M_\Delta)\left[g^{\mu\nu} - \frac{1}{3}\gamma^\mu\gamma^\nu - \frac{2}{3}\frac{p_\Delta^\mu p_\Delta^\nu}{M_\Delta^2} + \frac{1}{3}\frac{p_\Delta^\mu\gamma^\nu - p_\Delta^\nu\gamma^\mu}{M_\Delta}\right]; \quad (3.23)$$

Γ_Δ is the resonance width in its rest frame, given by

$$\Gamma_\Delta(s) = \frac{1}{6\pi}\left(\frac{f^*}{m_\pi}\right)^2\frac{M}{\sqrt{s}}\left[\frac{\lambda^{\frac{1}{2}}(s,m_\pi^2,M^2)}{2\sqrt{s}}\right]^3 \times\Theta(\sqrt{s}-M-m_\pi), \quad s=p_\Delta^2, \quad (3.24)$$

with $f^* = 2.14$, the $\pi N\Delta$ coupling obtained from the empirical $\Delta \to N\pi$ decay width (see Table 3.1); $\lambda(x,y,z) = x^2+y^2+z^2-2xy-2xz-2yz$, and Θ is the step function.

The weak NC and EM currents for the nucleon to Δ transition are the same for protons or neutrons and are given by

$$\begin{aligned}&\frac{1}{2}J_{NC}^{\beta\mu}(p,q)\\ =\ &\left[\frac{\tilde{C}_3^V(q^2)}{M}(g^{\beta\mu}\not{q}-q^\beta\gamma^\mu)+\frac{\tilde{C}_4^V(q^2)}{M^2}(g^{\beta\mu}q\cdot p_\Delta - q^\beta p_\Delta^\mu)\right.\\ &\left.+\frac{\tilde{C}_5^V(q^2)}{M^2}(g^{\beta\mu}q\cdot p - q^\beta p^\mu)\right]\gamma_5+\frac{\tilde{C}_3^A(q^2)}{M}(g^{\beta\mu}\not{q}-q^\beta\gamma^\mu)\\ &+\frac{\tilde{C}_4^A(q^2)}{M^2}(g^{\beta\mu}q\cdot p_\Delta - q^\beta p_\Delta^\mu)+\tilde{C}_5^A(q^2)g^{\beta\mu}\,, \end{aligned} \quad (3.25)$$

$$\begin{aligned}J_{EM}^{\beta\rho}(p,-k_\gamma) = &-\left[\frac{C_3^V(0)}{M}(g^{\beta\rho}\not{k}_\gamma - k_\gamma^\beta\gamma^\rho)\right.\\ &+\frac{C_4^V(0)}{M^2}(g^{\beta\rho}k_\gamma\cdot p_{\Delta c}-k_\gamma^\beta p_{\Delta c}^\rho)\\ &\left.+\frac{C_5^V(0)}{M^2}(g^{\beta\rho}k_\gamma\cdot p - k_\gamma^\beta p^\rho)\right]\gamma_5\,, \end{aligned} \quad (3.26)$$

where $p_\Delta = p + q$ and $p_{\Delta c} = p - k_\gamma$; $\tilde{C}_i^V$, $\tilde{C}_i^A$ and C_i^V are the NC vector, NC axial[4] and EM transition form factors, respectively. As in the nucleon case, the NC vector form factors are related to the EM ones

$$\tilde{C}_i^V(q^2) = (1 - 2\sin^2\theta_W) C_i^V(q^2) \tag{3.27}$$

according to the isovector character of the $N - \Delta$ transition. These EM form factors (and couplings) can be constrained using experimental results on pion photo and electroproduction in the Δ resonance region. In particular, they can be related to the helicity amplitudes $A_{1/2}$, $A_{3/2}$ and $S_{1/2}$ [41, 110] commonly extracted in the analyses of meson electroproduction data. The explicit expressions are given in Appendix B.1. For the helicity amplitudes and their q^2 dependence we have taken the parametrizations of the MAID analysis [111, 112]. [5] In the axial sector, we adopt the Adler model [113, 114]

$$\tilde{C}_3^A(q^2) = 0, \qquad \tilde{C}_4^A(q^2) = -\frac{\tilde{C}_5^A(q^2)}{4}\,, \tag{3.28}$$

for the sub-leading (in a q^2 expansion) form factors and assume a standard dipole for the dominant

$$\tilde{C}_5^A(q^2) = C_5^A(0)\left(1 - \frac{q^2}{M_A^2}\right)^{-2}\,, \tag{3.29}$$

with $C_5^A(0) = 1.00 \pm 0.11$ and $M_A = 0.93$ GeV fixed in a fit to $\nu_\mu d \to \mu^- \Delta^{++} n$ BNL and ANL data [40].

The second resonance region

[4] There is another contribution to the axial current $\tilde{C}_6^A(q^2) q^\beta q^\mu$, which does not contribute to the cross section because $q^\mu L_{\mu\sigma}^{(\nu\bar{\nu})} = 0$ for massless neutrinos.

[5] The set of $N-\Delta(1232)$ vector form factors used in [39], which were taken from Ref. [110], lead to negligible changes in the results compared to those presented below.

[6] In the case of the Δ, we use a $C_5^A(0)$ value obtained in a reanalysis [40] of the $\nu_\mu p \to \mu^- p \pi^+$ ANL and BNL bubble chamber data, which is smaller than the corresponding GT relation by $\sim 20\%$.

Table 3.1: Properties of the resonances included in our model [70]. For each state, we list the Breit-Wigner mass (M_R MeV) , spin (J), isospin (I), parity (P), total decay width (Γ MeV), branching fraction $\Gamma_{R\to N\pi}/\Gamma$ (Br), axial coupling (denoted $F_A(0)$ for spin 1/2 states and $C_5^A(0)$ for spin 3/2 states).

	M_R	J	I	P	Γ	Br	$F_A(0)/C_5^A(0)$
$\Delta(1232)$	1232	3/2	3/2	+	117	100%	1.00 ± 0.11 [6]
$N(1440)$	1440	1/2	1/2	+	300	65%	-0.47
$N(1520)$	1520	3/2	1/2	−	115	60%	-2.14
$N(1535)$	1535	1/2	1/2	−	150	45%	-0.21

Here, we extend the formalism to the second resonance region, which includes three isospin 1/2 baryon resonances $P_{11}(1440)$, $D_{13}(1520)$ and $S_{11}(1535)$ (see Table 3.1). In this way, we extend the validity of the model to higher energies. A basic problem that has to be faced with resonances is the determination of the transition form factors (coupling constants and q^2 dependence). As for the $\Delta(1232)$, we obtain vector form factors from the helicity amplitudes parametrized in Ref. [111]. The equations relating helicity amplitudes and form factors are compiled in Appendix B.1. Our knowledge of the axial transition form factors is much poorer. Some constraints can be imposed from PCAC and the pion-pole dominance of the pseudoscalar form factors. These allow to derive off-diagonal Goldberger-Treiman (GT) relations between the leading axial couplings and the $N^* \to N\pi$ partial decay widths (see Table 3.1 and Appendix B.2 for more details).

For each of the three $P_{11}(1440)$, $D_{13}(1520)$ and $S_{11}(1535)$ states, we have considered the contribution of direct (RP) and crossed (CRP) resonance pole terms as depicted in Fig. 3.3.

$N(1440)$ **and** $N(1535)$**:** The structure of the contribution of these two resonances to the amputated amplitudes is similar to the one of

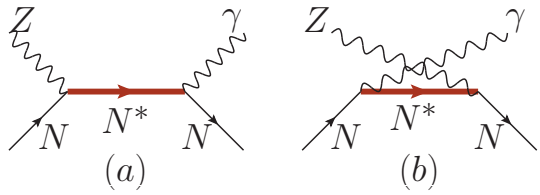

Figure 3.3: Direct (a) and crossed (b) N^* pole contributions to the NC photon emission process. We have considered the three resonances $[N(1440), N(1535), N(1520)]$ right above the $\Delta(1232)$.

the nucleon [Eq. (3.10)]. We have

$$\begin{aligned}\Gamma_R^{\mu\rho} &= \Gamma_{RP}^{\mu\rho} + \Gamma_{CRP}^{\mu\rho} \\ &= ie\, J^{\rho}_{EM(R)}(-k_\gamma)\frac{\not p + \not q + M_R}{(p+q)^2 - M_R^2 + iM_R\Gamma_R} J^{\mu}_{NC(R)}(q) \\ &\quad + ie\, J^{\mu}_{NC(R)}(q)\frac{(\not p' - \not q + M_R)}{(p'-q)^2 - M_R^2 + i\epsilon} J^{\rho}_{EM(R)}(-k_\gamma)\,; \quad (3.30)\end{aligned}$$

the resonance masses M_R are listed in Table 3.1 while the widths Γ_R are discussed in Appendix B.3. The EM and NC currents read

$$\begin{aligned}J^{\mu}_{NC(P_{11})}(q) &= \frac{\tilde F_{1(P_{11})}(q^2)}{(2M)^2}(\not q q^\mu - q^2\gamma^\mu) + \frac{\tilde F_{2(P_{11})}(q^2)}{2M} i\sigma^{\mu\nu}q_\nu \\ &\quad + \tilde F_{A(P_{11})}(q^2)\gamma^\mu\gamma_5\,, \quad (3.31) \\ J^{\mu}_{EM(P_{11})}(k_\gamma) &= \frac{F_{1(P_{11})}(0)}{(2M)^2}\not k_\gamma k_\gamma^\mu + \frac{F_{2(P_{11})}(0)}{2M} i\sigma^{\mu\nu}(k_\gamma)_\nu\,, \quad (3.32)\end{aligned}$$

for the $N(1440)$ and

$$\begin{aligned}J^{\mu}_{NC(S_{11})}(q) &= \left[\frac{\tilde F_{1(S_{11})}(q^2)}{(2M)^2}(\not q q^\mu - q^2\gamma^\mu) + \frac{\tilde F_{2(S_{11})}(q^2)}{2M} i\sigma^{\mu\nu}q_\nu\right]\gamma_5 \\ &\quad + \tilde F_{A(S_{11})}(q^2)\gamma^\mu\,, \quad (3.33) \\ J^{\mu}_{EM(S_{11})}(k_\gamma) &= \left[\frac{F_{1(S_{11})}(0)}{(2M)^2}\not k_\gamma k_\gamma^\mu + \frac{F_{2(S_{11})}(0)}{2M} i\sigma^{\mu\nu}(k_\gamma)_\nu\right]\gamma_5\,, \quad (3.34)\end{aligned}$$

for the $N(1535)$. [7] As in the nucleon case, isospin symmetry implies that

$$\begin{aligned}\tilde{F}^{(p)}_{1,2(R)} &= \left(1-4\sin^2\theta_W\right)F^{(p)}_{1,2(R)} - F^{(n)}_{1,2(R)} - F^{(s)}_{1,2(R)}\,,\\ \tilde{F}^{(n)}_{1,2(R)} &= \left(1-4\sin^2\theta_W\right)F^{(n)}_{1,2(R)} - F^{(p)}_{1,2(R)} - F^{(s)}_{1,2(R)}\,,\end{aligned} \tag{3.35}$$

with $F^{(N)}_{1,2(P_{11},S_{11})}$ expressed in terms of the corresponding helicity amplitudes (see Appendix B.1). The NC axial form factors are

$$\begin{aligned}\tilde{F}^{(p,n)}_{A(R)} &= \pm F_{A(R)} + F^{s}_{A(R)}, \qquad (+\to p, -\to n)\\ F_{A(R)}(q^2) &= F_{A(R)}(0)\left(1-\frac{q^2}{M^{*2}_A}\right)^{-2}.\end{aligned} \tag{3.36}$$

The couplings $F_{A(P_{11},S_{11})}(0)$ are obtained from the GT corresponding relations and have values given in Table 3.1. The q^2 dependence of these form factors is unknown so we have assumed a dipole ansatz with a natural value of $M^*_A = 1.0$ GeV for the axial mass. No information is available about the strange form factors $F^{(s)}_{1,2,A(P_{11},S_{11})}$ but they are likely to be small and to have a negligible impact on the observables, so we set them to zero.

$N(1520)$**:** In this case, the structure of the contribution of this resonance to the amputated amplitudes is similar to that of the $\Delta(1232)$, differing just in the definition of the appropriate form factors and the isospin dependence. Thus, we have

$$\begin{aligned}&\Gamma^{\mu\rho}_{D_{13}} = \Gamma^{\mu\rho}_{D_{13}P} + \Gamma^{\mu\rho}_{CD_{13}P}\\ =\;& ie\gamma^0\left[J^{\alpha\rho}_{EM(D_{13})}(p',k_\gamma)\right]^\dagger\gamma^0\frac{P^{D_{13}}_{\alpha\beta}(p+q)}{(p+q)^2 - M^2_{D_{13}} + iM_{D_{13}}\Gamma_{D_{13}}}\\ &\times J^{\beta\mu}_{NC(D_{13})}(p,q) + ie\,\gamma^0\left[J^{\alpha\mu}_{NC(D_{13})}(p',-q)\right]^\dagger\gamma^0\\ &\times\frac{P^{D_{13}}_{\alpha\beta}(p'-q)}{(p'-q)^2 - M^2_{D_{13}} + i\epsilon}J^{\beta\rho}_{EM(D_{13})}(p,-k_\gamma),\end{aligned} \tag{3.37}$$

[7] Note that by construction gauge invariance and CVC are satisfied. This is also the case for the $N(1520)$ amplitudes that will be discussed next.

where the resonance mass $M_{D_{13}}$ is given in Table 3.1 and the width $\Gamma_{D_{13}}$ is discussed in Appendix B.3; $P^{D_{13}}_{\mu\nu}$ is the spin 3/2 projection operator given also by Eq. (3.23), with the obvious replacement of M_Δ by $M_{D_{13}}$. Besides, the $N - N(1520)$ EM and NC transition currents are given by

$$\begin{aligned} & J^{\beta\mu}_{NC(D_{13})}(p,q) \\ = \; & \frac{\tilde{C}^V_{3(D_{13})}(q^2)}{M}(g^{\beta\mu}\not{q} - q^\beta\gamma^\mu) + \frac{\tilde{C}^V_{4(D_{13})}(q^2)}{M^2}(g^{\beta\mu}q\cdot p_{D_{13}} - q^\beta p^\mu_{D_{13}}) \\ & + \frac{\tilde{C}^V_{5(D_{13})}(q^2)}{M^2}(g^{\beta\mu}q\cdot p - q^\beta p^\mu) + \left[\frac{\tilde{C}^A_{3(D_{13})}(q^2)}{M}(g^{\beta\mu}\not{q} - q^\beta\gamma^\mu)\right. \\ & \left. + \frac{\tilde{C}^A_{4(D_{13})}(q^2)}{M^2}(g^{\beta\mu}q\cdot p_{D_{13}} - q^\beta p^\mu_{D_{13}}) + \tilde{C}^A_{5(D_{13})}(q^2)g^{\beta\mu}\right]\gamma_5\,, \end{aligned} \tag{3.38}$$

$$\begin{aligned} & J^{\beta\rho}_{EM(D_{13})}(p,-k_\gamma) \\ = \; & -\left[\frac{C^V_{3(D_{13})}(0)}{M}(g^{\beta\rho}\not{k}_\gamma - k^\beta_\gamma\gamma^\rho) + \frac{C^V_{4(D_{13})}(0)}{M^2}(g^{\beta\rho}k_\gamma\cdot p_{D_{13}\,c}\right. \\ & \left. - k^\beta_\gamma p^\rho_{D_{13}\,c}) + \frac{C^V_{5(D_{13})}(0)}{M^2}(g^{\beta\rho}k_\gamma\cdot p - k^\beta_\gamma p^\rho)\right], \end{aligned} \tag{3.39}$$

where $p_{D_{13}} = p + q$ and $p_{D_{13}\,c} = p - k_\gamma$; $\tilde{C}^V_{i(D_{13})}$, $\tilde{C}^A_{i(D_{13})}$ and $C^V_{i(D_{13})}$ are the NC vector, NC axial and EM form factors, respectively. The NC vector form factors are related to the EM ones in the same way as for the other isospin 1/2 states considered above, namely

$$\begin{aligned} \tilde{C}^{V(p)}_{i(D_{13})} &= \left(1 - 4\sin^2\theta_W\right)C^{(p)}_{i(D_{13})} - C^{(n)}_{i(D_{13})} - C^{(s)}_{i(D_{13})}\,, \\ \tilde{C}^{V(n)}_{i(D_{13})} &= \left(1 - 4\sin^2\theta_W\right)C^{(n)}_{i(D_{13})} - C^{(p)}_{i(D_{13})} - C^{(s)}_{i(D_{13})}\,, \end{aligned} \tag{3.40}$$

where $C^{(p,n)}_{3-5(D_{13})}$ are obtained from the helicity amplitudes using Eqs. (B.14-B.16). For the axial form factors, one again has that

$$\tilde{C}^{A(p,n)}_{i(D_{13})} = \pm C^A_{i(D_{13})} + C^{sA}_{i(D_{13})}\,, \qquad (+ \to p, - \to n)\,. \tag{3.41}$$

We take a standard dipole form for the dominant axial NC form factor

$$C^A_{5(D_{13})}(q^2) \;=\; C^A_{5(D_{13})}(0)\left(1-\frac{q^2}{M^{*2}_A}\right)^{-2}, \tag{3.42}$$

with $C^A_{5(D_{13})}(0)$ from the corresponding off diagonal GT relation (see Appendix B.2 and Table 3.1), and set $M^*_A = 1.0$ GeV as for the other N^*. The other axial form factors $C^A_{3,4(D_{13})}$ are less important because their contribution to the amplitude squared is proportional to q^2. We neglect them together with the unknown strange vector and axial form factors.

3.3 Neutral current photon emission in nuclei

In this section we outline the framework followed to describe NC photon emission off nuclei. Both incoherent and coherent reaction channels are considered.

3.3.1 Incoherent photon emission

To study the incoherent reactions

$$\begin{aligned}\nu_l(k) + A_Z &\rightarrow \nu_l(k') + \gamma(k_\gamma) + X,\\ \bar{\nu}_l(k) + A_Z &\rightarrow \bar{\nu}_l(k') + \gamma(k_\gamma) + X,\end{aligned} \tag{3.43}$$

we pursue the many body scheme derived in Refs. [24, 34, 115] for the neutrino propagation in nuclear matter and adapted to (semi)inclusive reactions on finite nuclei by means of the local density approximation (LDA). With this formalism, the photon emission cross section is

$$\sigma_{(\nu,\bar{\nu})}\big|_{\rm incoh} = \frac{1}{|\vec{k}\,|}\frac{G^2}{16\pi^2}\int\frac{d^3k'}{|\vec{k'}|}L^{(\nu,\bar{\nu})}_{\mu\sigma}\,W^{\mu\sigma}_{{\rm NC}\gamma}\big|_{\rm incoh} \tag{3.44}$$

in terms of the leptonic tensor of Eq. (3.3) and the hadronic tensor $W^{\mu\sigma}_{{\rm NC}\gamma}|_{\rm incoh} = W^{(s)\mu\sigma}_{{\rm NC}\gamma}|_{\rm incoh} + iW^{(a)\mu\sigma}_{{\rm NC}\gamma}|_{\rm incoh}$, which is determined by the contributions to the Z^0 self-energy with a photon in the intermediate

state $\Pi^{\mu\sigma}_{Z\gamma}(q)$. Within the LDA, the computation of the hadronic tensor for finite nuclei involves an integral over the whole nuclear volume,

$$W^{(s)\mu\sigma}_{NC\gamma}\Big|_{\rm incoh} = -\Theta(q^0)\left(\frac{4\cos\theta_W}{g}\right)^2 \int \frac{d^3r}{2\pi}\ {\rm Im}\left[\Pi^{\mu\sigma}_{Z\gamma} + \Pi^{\sigma\mu}_{Z\gamma}\right](q,r) \tag{3.45}$$

$$W^{(a)\mu\sigma}_{NC\gamma}\Big|_{\rm incoh} = -\Theta(q^0)\left(\frac{4\cos\theta_W}{g}\right)^2 \int \frac{d^3r}{2\pi}\ {\rm Re}\left[\Pi^{\mu\sigma}_{Z\gamma} - \Pi^{\sigma\mu}_{Z\gamma}\right](q,r). \tag{3.46}$$

In the density expansion proposed in Ref. [24], the lowest order contribution to $\Pi^{\mu\sigma}_{Z\gamma}$ is depicted in Fig. 3.4. The black dots stand for any of the eleven terms (NP, CNP, πEx, RP, CRP with $R = \Delta(1232)$, $N(1440)$, $N(1520)$, $N(1535)$) of the elementary $Z^0N \to \gamma N$ amplitude derived in Sec. 3.2. The solid upwards and downwards oriented lines represent nucleon particle and hole states in the Fermi sea. This Z^0

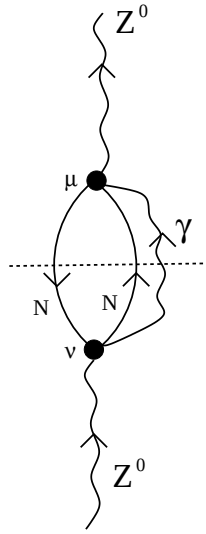

Figure 3.4: Diagrammatic representation of the one-particle-one-hole-photon (1p1hγ) contributions to the Z^0 self-energy in nuclear matter. The black dots represent $Z^0N \to \gamma N$ amplitudes.

self-energy diagram (actually 121 diagrams) is readily evaluated as [8]

$$
\begin{aligned}
-i\Pi^{\mu\nu}_{Z\gamma;1p1h\gamma}(q,r) &= i\left(\frac{g}{4\cos\theta_W}\right)^2 \sum_{N=p,n}\int\frac{d^4k_\gamma}{(2\pi)^4}\int\frac{d^4p}{(2\pi)^4}\frac{1}{k_\gamma^2+i\epsilon} \\
&\quad\times\mathrm{Tr}\left[S(p,\rho_N)\gamma^0\left(\Gamma_N^{\mu\rho}\right)^\dagger\gamma^0 S(p',\rho_N)(\Gamma_N)^\nu_{\ .\rho}\right] ,
\end{aligned}
\tag{3.47}
$$

where $p' = p + q - k_\gamma$ and $\Gamma_N^{\mu\rho}$ is the amputated amplitude for the $Z^0N \to N\gamma$ process

$$
\begin{aligned}
\Gamma_N^{\mu\rho} &= \sum_a \Gamma^{\mu\rho}_{a;N}, \quad a = NP,\, CNP,\, \pi Ex,\, RP,\, CRP \\
&\quad [R = \Delta(1232), N(1440), N(1520), N(1535)] \,.
\end{aligned}
\tag{3.48}
$$

The nucleon propagator in the medium reads

$$
S(p,\rho_N) = (\not{p} + M)G(p,\rho_N)\,, \tag{3.49}
$$

with

$$
\begin{aligned}
G(p\,;\rho_N) &= \frac{1}{p^2 - M^2 + i\epsilon} + \mathrm{i}\frac{\pi}{E(\vec{p})}n_N(\vec{p})\delta\left[p^0 - E(\vec{p})\right] \\
&= \frac{1}{p^0 + E(\vec{p}) + i\epsilon}\left[\frac{n_N(\vec{p})}{p^0 - E(\vec{p}) - i\epsilon} + \frac{1 - n_N(\vec{p})}{p^0 - E(\vec{p}) + i\epsilon}\right] .
\end{aligned}
\tag{3.50}
$$

The occupation number in the local Fermi gas $n_N(\vec{p}) = \Theta(k_F^N - |\vec{p}|)$ depends on the local density of nucleons (protons or neutrons) in the nucleus via $k_F^N(r) = (3\pi^2\rho_N(r))^{1/3}$. The nucleon energy $E(\vec{p})$ is approximated by the free one $\sqrt{\vec{p}^{\,2} + M^2}$. Substituting the explicit ex-

[8] In Eq. (3.47), it is necessary to subtract the free space contribution, i.e., the one that survives for vanishing nuclear densities and renormalizes free space couplings and masses. Actually, to obtain Eq. (3.51), we have neglected the contribution of the antiparticle pole $[p^0 = -E(\vec{p}) - \mathrm{i}\epsilon]$ in the p^0 integration. This automatically removes the unwanted vacuum part.

pressions of $S(p,\rho_N)$ and $S(p',\rho_N)$ in Eq. (3.47) one obtains

$$\begin{aligned}
&-i\Pi^{\mu\nu}_{Z\gamma;1\mathrm{p1h}\gamma}(q,r)\\
= &-\left(\frac{g}{4\cos\theta_W}\right)^2\sum_{N=p,n}\int\frac{d^4k_\gamma}{(2\pi)^4}\int\frac{d^3p}{(2\pi)^3}\frac{1}{2E(\vec{p})}\\
&\times\frac{1}{2E(\vec{p}+\vec{q}-\vec{k}_\gamma)}\frac{n_N(\vec{p})[1-n_N(\vec{p}+\vec{q}-\vec{k}_\gamma)]}{q^0-k^0_\gamma+E(\vec{p})-E(\vec{p}\,')+i\epsilon}\\
&\times\frac{1}{k^2_\gamma+i\epsilon}\mathrm{Tr}\left[(\not{p}+M)\gamma^0\left(\Gamma^{\mu\rho}_N\right)^\dagger\gamma^0(\not{p}'+M)\left(\Gamma_N\right)^\nu_{\cdot\,\rho}\right]\\
&+\left[(q-k_\gamma)\leftrightarrow-(q-k_\gamma)\right]\,. \qquad (3.51)
\end{aligned}$$

A convenient simplification can be made by evaluating the $\Gamma^{\mu\rho}_N$ amplitudes at an average nucleon hole four momentum $\langle p^\mu\rangle$. This allows us to take the spin trace in Eq. (3.51) out of the d^3p integration, which gives, up to constants, the Lindhard function, $\overline{U}_R(q-k_\gamma,k^N_F,k^N_F)$ (see Appendix B of Ref. [24] or appendix C.3 of this thesis for definition and explicit expressions). Therefore,

$$\begin{aligned}
-i\Pi^{\mu\nu}_{Z\gamma;1\mathrm{p1h}\gamma}(q,r) &= -\left(\frac{g}{4\cos\theta_W}\right)^2\frac{1}{4M^2}\sum_{N=p,n}\int\frac{d^4k_\gamma}{(2\pi)^4}\frac{1}{k^2_\gamma+i\epsilon}\\
&\quad\times\overline{U}_R(q-k_\gamma,k^N_F,k^N_F)A^{\mu\nu}_N\left(\langle p\rangle,q,k_\gamma\right)\,, \qquad (3.52)\\
A^{\mu\nu}_N &= \frac{1}{2}\mathrm{Tr}\left[\left(\langle\not{p}\rangle+M\right)\gamma^0\left(\langle\Gamma_N\rangle^{\mu\rho}\right)^\dagger\gamma^0\right.\\
&\quad\left.\times\left(\langle\not{p}\rangle+\not{q}-\not{k}_\gamma+M\right)\langle\Gamma_N\rangle^\nu_{\cdot\,\rho}\right]\,, \qquad (3.53)
\end{aligned}$$

where $\langle\Gamma_N\rangle^{\nu\rho}$ stands for $\Gamma^{\nu\rho}_N$ calculated at the average hole four momentum $\langle p^\mu\rangle$.

To derive the 1p1hγ contribution to the hadron tensor $W^{\mu\sigma}$, we remind that by construction

$$A^{\mu\nu}_N = A^{(s)\mu\nu}_N + iA^{(a)\mu\nu}_N\,, \qquad (3.54)$$

where $A^{(s)\mu\sigma}_N$ ($A^{(a)\mu\sigma}_N$) is a real symmetric (anti-symmetric) tensor. Furthermore, it is easy to see that the combinations of the Z^0 self-energy present in Eqs. (3.45) and (3.46) fulfill

$$\begin{aligned}
\mathrm{Im}\left[\Pi^{\mu\nu}_{Z\gamma;1\mathrm{p1h}\gamma}+\Pi^{\nu\mu}_{Z\gamma;1\mathrm{p1h}\gamma}\right] &= 2\mathrm{Im}\Pi^{(s)\mu\nu}_{Z\gamma;1\mathrm{p1h}\gamma},\\
\mathrm{Re}\left[\Pi^{\mu\nu}_{Z\gamma;1\mathrm{p1h}\gamma}-\Pi^{\nu\mu}_{Z\gamma;1\mathrm{p1h}\gamma}\right] &= -2\mathrm{Im}\Pi^{(a)\mu\nu}_{Z\gamma;1\mathrm{p1h}\gamma}, \qquad (3.55)
\end{aligned}$$

where $\Pi^{(s,a)\mu\nu}_{Z\gamma;1p1h\gamma}$ are obtained by replacing $A^{\mu\nu}_N$ in Eq. (3.52) by the corresponding $A^{(s,a)\mu\nu}_N$ parts.

The imaginary part of $\Pi^{\mu\nu}_{ZW;1p1h\gamma}\Big|_{s(a)}$ can be obtained following the Cutkosky rules. In this case we cut the self-energy diagram of Fig. 3.4 with a straight horizontal line. The states intercepted by the line are placed on shell by taking the imaginary part of their propagators. Technically, the rules to obtain $\mathrm{Im}\Pi^{\mu\nu}_{Z;1p1h\gamma}$ consist of the following substitutions:

$$\begin{aligned}
\Pi^{\mu\nu}_{Z\gamma}(q) &\rightarrow 2i\mathrm{Im}\Pi^{\mu\nu}_{Z\gamma}(q)\Theta(q^0), && (3.56)\\
\frac{1}{k^2_\gamma + i\epsilon} &\rightarrow 2i\mathrm{Im}\frac{1}{k^2_\gamma + i\epsilon}\Theta(k^0_\gamma)\\
&= -2\pi i\delta(k^2_\gamma)\Theta(k^0_\gamma), && (3.57)\\
\overline{U}_R(q-k_\gamma, k^N_F, k^N_F) &\rightarrow 2i\mathrm{Im}\overline{U}_R(q-k_\gamma, k^N_F, k^N_F)\Theta(q^0-k^0_\gamma). && (3.58)
\end{aligned}$$

Thus, taking into account that $A^{(s,a)\mu\nu}_N$ are real, we readily obtain

$$\begin{aligned}
W^{\mu\nu}_{1p1h\gamma}(q) &= \Theta(q^0)\frac{1}{2M^2}\int\frac{d^3r}{2\pi}\sum_{N=p,n}\frac{d^3k_\gamma}{(2\pi)^3}\frac{\Theta(q^0-E_\gamma)}{2E_\gamma}\\
&\quad\times\mathrm{Im}\overline{U}_R(q-k_\gamma, k^N_F, k^N_F)A^{\nu\mu}_N\,, && (3.59)
\end{aligned}$$

with E_γ the photon on-shell energy.

The average nucleon hole momentum $\langle p^\mu\rangle$ is chosen as follows (see the discussion after Eq. (9) of Ref. [43])

$$\langle p^0\rangle = \frac{E^N_F + E_{\min}}{2}\,, \qquad \langle|\vec{p}\,|\rangle = \sqrt{\langle p^0\rangle^2 - M^2} \tag{3.60}$$

defined by the central value of the allowed energy region, with

$$E_{\min} = \max\left(M, E^N_F - q'^0, \frac{-q'^0 + |\vec{q}\,'|\sqrt{1-4M^2/q'^2}}{2}\right), \tag{3.61}$$

where $q' = q - k_\gamma$ and $E^N_F = \sqrt{M^2 + (k^N_F)^2}$. The corresponding nucleon hole angle, in the LAB frame and with respect to $\vec{q}\,'$, is completely fixed

by the kinematics to

$$\cos\theta_N = \frac{q'^2 + 2\langle p^0\rangle q'^0}{2\langle|\vec{p}|\rangle|\vec{q}'|}\,, \tag{3.62}$$

while the azimuthal angle ϕ_N is fixed arbitrarily in the plane perpendicular to $\vec{q}'$. Similar approximations were performed, and shown to be sufficiently accurate, in studies of total inclusive and pion production in photo and electro-nuclear reactions [99–101, 116]. They were also used in Ref. [34] to compute the total inclusive neutrino induced cross section. We have checked that the approximation of Eqs. (3.60)–(3.62) induces uncertainties of at most 5%, independently of ϕ_N values. Furthermore, different choices of ϕ_N produce small variations of the order of 1-2% in the results. This approximation saves a considerable amount of computational time because there are analytical expressions for $\mathrm{Im}\overline{U}_R(q-k_\gamma, k_F^N, k_F^N)$ (see for instance Ref. [24]).

In the small density limit,

$$\mathrm{Im}\overline{U}_R(q', k_F^N, k_F^N) \simeq -\pi\rho_N M\delta\left(q'^0 + M - \sqrt{M^2+\vec{q}'^2}\right)/\sqrt{M^2+\vec{q}'^2}. \tag{3.63}$$

Substituting this expression in Eq. (3.59) one obtains

$$\lim_{\rho\to 0} W^{\mu\nu}_{1\mathrm{p1h}\gamma} \sim \int d\Omega(\hat{k}_\gamma) dE_\gamma E_\gamma \left(Z W^{\mu\nu}_{Z^0 p\to p\gamma} + N W^{\mu\nu}_{Z^0 n\to n\gamma}\right)\,, \tag{3.64}$$

where Z and N are the number of protons and neutrons in the nucleus, and $W^{\mu\nu}_{Z^0 N\to N\gamma}$ is the hadronic tensor for NC photon production on the nucleon. In this way, the strict impulse approximation is recovered. By performing the integral in Eq. (3.59), Pauli blocking and Fermi motion are taken into account.

Further nuclear medium corrections

Given the dominant role played by the ΔP contribution and since Δ properties are strongly modified in the nuclear medium [97, 117–122] a proper treatment of the Δ contribution is needed. Here, we follow Ref. [49] and modify the Δ propagator in the ΔP term as

$$\frac{1}{p_\Delta^2 - M_\Delta^2 + iM_\Delta\Gamma_\Delta} \to \frac{1}{\sqrt{p_\Delta^2}+M_\Delta}\frac{1}{\sqrt{p_\Delta^2}-M_\Delta + i(\Gamma_\Delta^{\mathrm{Pauli}}/2 - \mathrm{Im}\Sigma_\Delta)}\,; \tag{3.65}$$

$\Gamma_\Delta^{\rm Pauli}$, for which we take the expression in Eq. (15) of Ref. [98] (see also appendix C.2), is the free Δ width corrected by the Pauli blocking of the final nucleon. The imaginary part of the Δ self-energy in the medium $\mathrm{Im}\Sigma_\Delta$, is parametrized as [119] (see appendix C.1)

$$-\,\mathrm{Im}\Sigma_\Delta(\rho) = C_Q \left(\frac{\rho}{\rho_0}\right)^\alpha + C_{A2}\left(\frac{\rho}{\rho_0}\right)^\beta + C_{A3}\left(\frac{\rho}{\rho_0}\right)^\gamma , \qquad (3.66)$$

where the term proportional to C_Q accounts for the QE part while those with coefficients C_{A2} and C_{A3} correspond to the two-body ($\Delta N \to NN$) and three-body ($\Delta NN \to NNN$) absorption contributions, respectively. The parameters in Eq. (3.66) can be found in Eq. (4.5) and Table 2 of Ref. [119], given as functions of the kinetic energy in the laboratory system of a pion that would excite a Δ with the corresponding invariant mass. These parametrizations are valid in the range 85 MeV $< T_\pi <$315 MeV. Below 85 MeV, the contributions from C_Q and C_{A3} are rather small and are taken from Ref [98], where the model was extended to low energies. The term with C_{A2} shows a very mild energy dependence and we still use the parametrization from Ref. [119] even at low energies. For T_π above 315 MeV we have kept these self-energy terms constant and equal to their values at the bound. The uncertainties in these pieces are not very relevant there because the $\Delta \to N\pi$ decay becomes very large and absolutely dominant.

For the Δ mass we shall keep its free value. While there are some corrections arising from both the real part of the self-energy and random phase approximation (RPA) sums, the net effect is smaller than the precision achievable in current neutrino experiments, and also smaller than the uncertainties due to our limited knowledge of the nucleon to Δ transition form factor $C_5^A(q^2)$ (see the related discussion in Sec. II.E of Ref. [34]).

3.3.2 Coherent photon emission

The coherent reactions

$$\begin{aligned} \nu_l(k) + A_Z|_{gs}(p_A) &\to \nu_l(k') + A_Z|_{gs}(p'_A) + \gamma(k_\gamma), \\ \bar\nu_l(k) + A_Z|_{gs}(p_A) &\to \bar\nu_l(k') + A_Z|_{gs}(p'_A) + \gamma(k_\gamma)\,, \end{aligned} \qquad (3.67)$$

consist of a weak photon production where the nucleus is left in its ground state, in contrast with the incoherent production that we studied in the previous subsection, where the nucleus is either broken or left in an excited state. Here, we adopt the framework derived in Ref. [50] for neutrino-induced coherent CC and NC pion production reactions.[9] This work is, in turn, based on previous studies of coherent pion production in electromagnetic [(γ, π^0) [102], $(e, e'\pi^0)$ [103]] and hadronic reactions [(^{3}He,^{3}H π^+) [124], $p(^4\text{He},^4\text{He})X$ [125]] in the $\Delta(1232)$ region. More recently, the same scheme has been employed to study charged kaon production by coherent scattering of neutrinos and antineutrinos on nuclei [126]. The model for the coherent process is built up from the coherent scattering with each of the nucleons of the nucleus, producing an outgoing γ. The nucleon state (wave function) remains unchanged so that after summing over all nucleons, one obtains the nuclear densities. In the elementary $Z^0 N \to N\gamma$ process, energy conservation is accomplished by imposing $q^0 = E_\gamma$, which is justified by the large nucleus mass, while the transferred momentum $\vec{q} - \vec{k}_\gamma$ has to be accommodated by the nucleon wave functions. Therefore, the coherent production process is sensitive to the Fourier transform of the nuclear density.

Following Ref. [50], it is straightforward to find that

$$\left.\frac{d^3\sigma_{(\nu,\bar{\nu})}}{dE_\gamma d\Omega(\hat{k}_\gamma)}\right|_{\text{coh}} = \frac{E_\gamma}{|\vec{k}\,|}\frac{G^2}{16\pi^2}\int \frac{d^3k'}{|\vec{k}'|} L^{(\nu,\bar{\nu})}_{\mu\sigma}\, W^{\mu\sigma}_{\text{NC}\gamma}\big|_{\text{coh}}\,, \tag{3.68}$$

$$W^{\mu\sigma}_{\text{NC}\gamma}\big|_{\text{coh}} = -\frac{\delta(E_\gamma - q^0)}{64\pi^3 M^2}\mathcal{A}^{\mu\rho}(q,k_\gamma)\left(\mathcal{A}^{\sigma}_{\cdot\rho}\right)^*(q,k_\gamma)\,, \tag{3.69}$$

$$\mathcal{A}^{\mu\rho}(q,k_\gamma) = \int d^3r\; e^{i(\vec{q}-\vec{k}_\gamma)\cdot\vec{r}}\left\{\rho_p(r\,)\hat{\Gamma}^{\mu\rho}_p(r;q,k_\gamma) + \rho_n(r\,)\hat{\Gamma}^{\mu\rho}_n(r;q,k_\gamma)\right\}. \tag{3.70}$$

To evaluate the hadronic tensor, we use the model for the NC photon

[9] The predictions of Ref. [50] were updated in [123] after the reanalysis of the $\nu_\mu p \to \mu^- p\pi^+$ old bubble chamber data carried out in Ref. [40].

production off the nucleon derived in Sec. 3.2 and thus we have

$$\hat{\Gamma}^{\mu\rho}_{N}(r;q,k_\gamma) = \sum_i \hat{\Gamma}^{\mu\rho}_{i;N}(r;q,k_\gamma),\ i = NP,\ CNP,\ \pi Ex,\ RP,\ CRP$$
$$[R = \Delta, N(1440), N(1535), N(1520)] \tag{3.71}$$

$$\hat{\Gamma}^{\mu\rho}_{i;N}(r;q,k_\gamma) = \frac{1}{2}\mathrm{Tr}\left[(\not{p}+M)\gamma^0\,\Gamma^{\mu\rho}_{i;N}\right]\left.\frac{M}{p^0}\right|_{p^\mu=\left(\sqrt{M^2+\frac{(\vec{k}_\gamma-\vec{q})^2}{4}},\frac{1}{2}(\vec{k}_\gamma-\vec{q})\right)} \tag{3.72}$$

where the four-vector matrices $\Gamma^{\mu\rho}_{i;N\gamma}$ stand for the amputated photon production amplitudes off nucleons derived in Subsec. 3.2.2. We have also taken into account the modification of the $\Delta(1232)$ in the medium for the ΔP mechanism, as explained in Subsec. 3.3.1.

Now we pay attention to the approximated treatment of nucleon momentum distributions that has been adopted to obtain Eqs. (3.69)–(3.72). The initial ($\vec{p}$) and final ($\vec{p}\,'$) nucleon three momenta are not well defined. We take

$$\begin{aligned} p^\mu &= \left(\sqrt{M^2+\frac{1}{4}\left(\vec{k}_\gamma-\vec{q}\right)^2},\frac{\vec{k}_\gamma-\vec{q}}{2}\right), \\ p'^\mu &= q-k_\gamma+p=\left(\sqrt{M^2+\frac{1}{4}\left(\vec{k}_\gamma-\vec{q}\right)^2},-\frac{\vec{k}_\gamma-\vec{q}}{2}\right), \end{aligned} \tag{3.73}$$

with both nucleons being on-shell. In this way, the momentum transfer is equally shared between the initial and final nucleons. This prescription, employed in Refs. [49, 50, 52, 96], for (anti)neutrino induced coherent pion production, was earlier applied to $^{16}\mathrm{O}(\gamma,\pi^+)^{16}\mathrm{N}_{\mathrm{bound}}$ [127] and to coherent π^0 photo- and electroproduction [102, 103, 128]. The approximation is based on the fact that, for Gaussian nuclear wave functions, it leads to an exact treatment of the terms in the elementary amplitude that are linear in momentum. In Ref. [102] it was shown that in the case of π^0 photo-production, this prescription provided similar results as the explicit sum over the nucleon momenta performed in Ref. [129]. Thanks to the choice of Eq. (3.73), the sum over all nucleons is greatly simplified and cast in terms of the neutron and proton densities [see Eq. (3.70)]. Furthermore, the sum over nucleon helicities gives rise to the trace in Eq. (3.72); more details can be

found in the discussion after Eq. (6) of Ref. [50]. On the other hand, this approximation eliminates some non-local contributions to the amplitudes. In particular, the Δ momentum turns out to be well defined once the the nucleon momenta are fixed. In Ref. [130] this constraint was relaxed for weak coherent pion production via $\Delta(1232)$ excitation, while neglecting the modification of the Δ properties in the nucleus and pion distortion. It was found that non-localities in the Δ propagation cause a large reduction of the cross section at low energies. In the more realistic description of Nakamura et al. [51], the non-locality is preserved for the Δ kinetic term in a linearized version of the Δ propagator but, at the same time, a prescription similar to Eq. (3.73) for the $WN\Delta$ and $\Delta N\pi$ vertices, and a local ansatz for the in-medium Δ selfenergy have been taken. Nevertheless, the mismatch between the non-local recoil effects and the local approximations for vertices and selfenergy are likely to be minimized by the fact that the parameters in the Δ selfenergy are adjusted to describe pion-nucleus scattering data with the same model. Our point of view is that the local approach adopted here and in Refs. [49, 50, 52, 96], together with the choice of the effective nucleon-nucleon interaction in the medium [119], is internally consistent. The good agreement obtained for pion-nucleus scattering [98, 131] and coherent pion photo-production [52, 132] for medium and heavy nuclei seems to support this conjecture, although more detailed investigations are necessary. In any case, for the present study, where the coherent contribution is a small and not disentangled part of the total NCγ cross section, and in view of the uncertainty in the determination of the $N\Delta$ axial coupling $C_5^A(0)$, it is safe to disregard possible non-local corrections.

3.4 Results

Before discussing our results an important remark is due. The intermediate nucleon propagators in both the NP and CNP terms of Eq. (3.10) can be put on the mass shell for $E_\gamma \to 0$ photons, leading to an infrared divergence. This divergence should be cancelled by others present in the electromagnetic radiative corrections to the elastic process $\nu N \to \nu N$ (without photon emission). However, when the

emitted photon is too soft, its energy becomes smaller than the photon energy resolution of the detector. Such an event would be recorded as an elastic one if at all. For this reason, we have implemented a cut in the available photon phase space, demanding $E_\gamma \geq 140$ MeV, which corresponds to the MiniBooNE detection threshold [60]. This value is also approximately valid for T2K, since a visible energy ($\sim E_\gamma$) cut of 100 MeV at Super-K is employed (see for example Table XIV of Ref. [62]).

3.4.1 Neutral current photon emission off nucleons

In Fig. 3.5, we show our results for the total NC photon emission (anti)neutrino cross sections as a function of the (anti)neutrino energy. As in other weak interaction processes, the different helicities of ν and $\bar{\nu}$ are responsible for different interference patterns, resulting in smaller $\bar{\nu}$ cross sections with a more linear energy dependence. The error bands on the full model results are determined by the uncertainty in the axial $N\Delta$ coupling $C_5^A(0) = 1.00 \pm 0.11$ [40]. This is the predominant source of uncertainty in the (anti)neutrino energy range under consideration (see also the discussion of Fig. 3.8 below). We also display the contributions from the different mechanisms considered in our model (Figs. 3.2 and 3.3). The Δ mechanism is dominant and gives the same contribution for protons and neutrons, as expected from the isovector nature of the electroweak $N - \Delta$ transition. At $E_{\nu(\bar{\nu})} \sim 1.5$ GeV, the cross section from nucleon-pole terms is only about 2.5 smaller than the Δ one. Above $\sim$ 1.5 GeV, the $N(1520)$ contribution is sizable and comparable to that of the sum of the NP and CNP mechanisms, specially for $\bar{\nu}p$. However, the rest of N^* contributions considered in the model (with $N(1440)$ and $N(1535)$ intermediate states), together with the πEx contribution of Fig. 3.2(e) can be safely neglected in the whole range of (anti)neutrino energies considered in this work. The fact that the $N(1520)$ resonance is the only one, besides the $\Delta(1232)$, playing a significant role for $E_\nu < 2$ GeV has also been observed in pion production [43] and for the inclusive cross section [41].

Photon angular and energy distributions on single nucleons, for incoming (anti)neutrino energies of 1 and 2 GeV are shown in Figs. 3.6

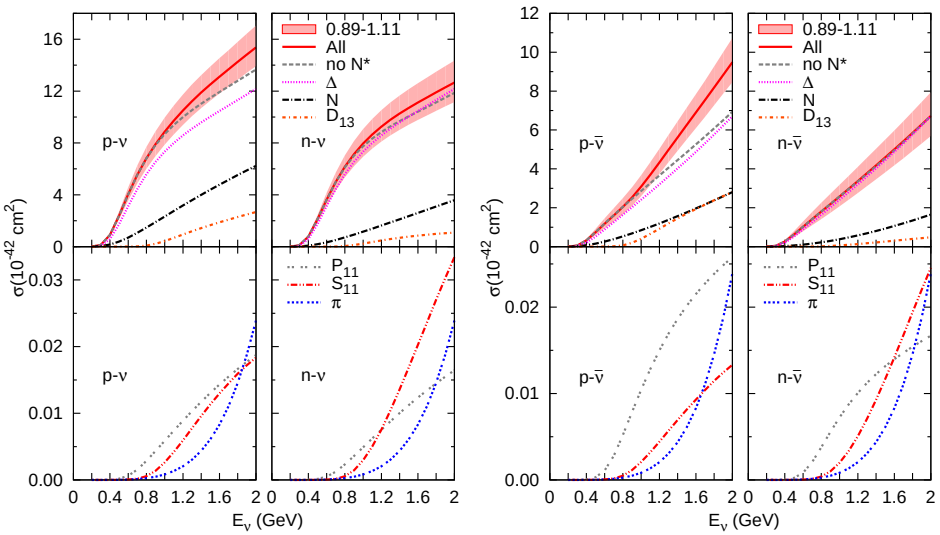

Figure 3.5: $\nu N \to \nu N\gamma$ (left) and $\bar{\nu}N \to \bar{\nu}N\gamma$ (right) cross sections on protons and neutrons as a function of the (anti)neutrino energy. A cut of $E_\gamma \geq 140$ MeV in the phase space integrals has been applied. Solid curves correspond to the results from the full model, with error bands determined by the uncertainty in the axial $N\Delta$ coupling $C_5^A(0) = 1.00 \pm 0.11$ according to the determination of Ref. [40]. The curves labeled as Δ, N and π stand for the partial contributions of the $(\Delta P + C\Delta P)$, $(NP + CNP)$ and πEx mechanisms, respectively. The D_{13}, P_{11} and S_{11} curves show the contribution of the different $(RP + CRP)$ terms driven by the N^* resonances. Finally, the lines labeled as "no N^*" display the predicted cross section without the N^* contributions.

and 3.7. Solid curves stand for the results from the full model. We also display the largest contributions among the different mechanisms considered in our model. As expected, the Δ mechanisms are also dominant in the differential cross sections, specially for reactions on neutrons and even more so for the $\bar{\nu}n \to \bar{\nu}n\gamma$ process. Nucleon and D_{13} direct and crossed pole-term contributions, though small, are not negligible, particularly for protons. The $N(1520)$ terms become more important for the largest (anti)neutrino energy. At the lower energy the

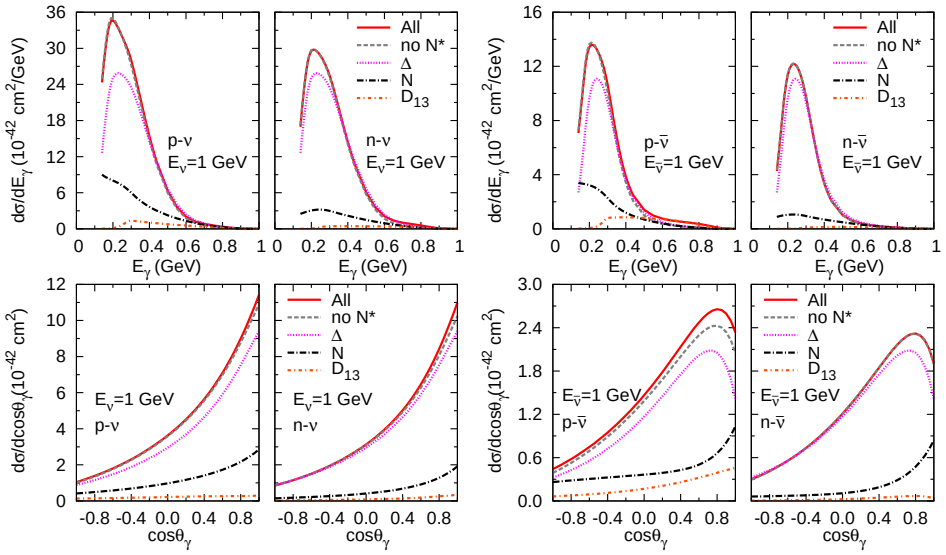

Figure 3.6: $\nu N \to \nu N\gamma$ (left) and $\bar{\nu}N \to \bar{\nu}N\gamma$ (right) photon energy (top) and photon angular (bottom) differential cross sections at $E_{\nu,\bar{\nu}} = 1$ GeV on both protons and neutrons. The angle θ_γ is referred to the direction of the incoming (anti)neutrino beam. A cut of $E_\gamma \geq 140$ MeV has been applied. Solid curves are for the full model. The curves labeled as Δ, N and D_{13} stand for the partial contributions of the $(\Delta P + C\Delta P)$, $(NP + CNP)$ and the $(N(1520)P + CN(1520)P)$ terms, respectively. The lines labeled as "no N^*" display the predictions neglecting the N^* contributions.

reaction is more forward-peaked for neutrinos than for antineutrinos. In the later case, the maximum of the distribution moves forward as the energy increases. The photon energy differential cross sections always exhibit a peak slightly above $E_\gamma = 0.2$ GeV, mainly produced by the interplay between the $\Delta-$pole and the three-body phase space photon energy distribution. The Δ propagator suppresses not only the low photon energy contributions, but also the high photon energy tail that would appear because of the boost to the LAB frame.

Next, we compare our predictions for the nucleon cross sections with those obtained in Refs. [86, 88]. These two models include the

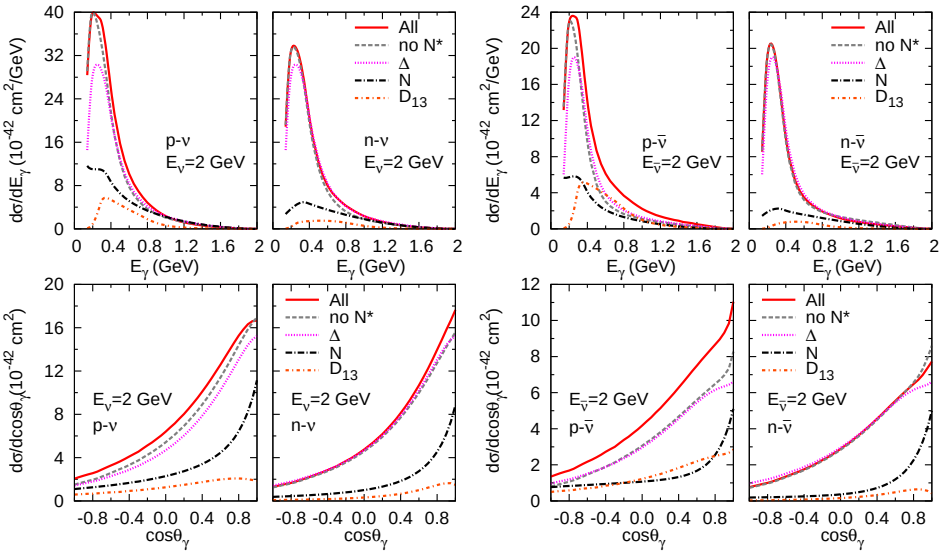

Figure 3.7: Same as Fig. 3.6, but for an (anti)neutrino energy of 2 GeV.

$NP+CNP$ and $\Delta P+C\Delta P$ mechanisms, with dominance of ΔP like in our case. The Compton-like contributions ($NP+CNP$) are determined by the electromagnetic and axial nucleon form factors, which are reasonably well constrained. The predictions of Ref. [88] for these mechanisms are similar to ours. Instead, those in Ref. [86] exhibit a steeper energy dependence, because of the higher nucleon axial mass, $M_A = 1.2$ GeV in F_A [Eq. (3.20)], used there. This choice was motivated by the first phenomenological analysis of the MiniBooNE CCQE scattering data on carbon using the relativistic Fermi gas model [133][10]. Later theoretical studies [26, 34, 134, 135] have shown that such high values of M_A encoded multi-nucleon contributions that were not taken into account in the experimental analyses. We use a lower value for $M_A = 1$ GeV, which is consistent with two independent experimental sources: bubble chamber neutrino/antineutrino induced QE reactions on hydrogen and deuterium and pion electroproduction [106]. In ad-

[10]In the final MiniBooNE analysis [6], an even larger value of $M_A \sim 1.35$ GeV was obtained.

dition to the $NP + CNP$ and $\Delta P + C\Delta P$ mechanisms, R. Hill [86] also considers $t-$channel π, ρ and ω exchanges. Only the latter one provides a non-negligible cross section that, for antineutrinos, could become comparable to the nucleon Compton-like contribution for incident energies above 1.5 GeV. However, the size of the ω contribution strongly depends on the mostly undetermined off-shell form factor and is then affected by large uncertainties.

In the model of X. Zhang and B. Serot [88], additional contact terms allowed by symmetry were considered. As pointed out in the Introduction, they notably increase the cross section above ~ 1 GeV (see Fig. 3 of that reference). In Ref. [42], it is argued that these contact terms are the low-energy manifestation of anomalous ρ and ω interactions; their contributions below 550 MeV are very small, as expected on the basis of the power counting established there. To extend these findings to higher energies, phenomenological form factors are employed [88], which are, however, not well understood. Therefore, their cross section above $E_\nu \sim 1$ GeV should be taken cautiously since contact terms are a source of uncontrolled systematics.

We now focus on the comparison for the dominant Δ contribution, which is presented in Fig. 3.8. Different values of the axial $N\Delta$ coupling $C_5^A(0)$ and photon energy cuts have been implemented in Refs. [86, 88], as specified in the caption of Fig. 3.8. We have used these inputs and compared our predictions with those found in these references, finding a good agreement particularly with Ref. [88]. In the case of Ref. [86] the agreement is better for antineutrinos than for neutrinos. However, in the actual calculations, a major difference arises from the fact that we are using a substantially lower value of $C_5^A(0) = 1.00$. Thus, our final predictions for the dominant Δ contribution are about 30% or 45% smaller than those of Refs. [88] and Ref. [86], respectively. The error bands in our results of Fig. 3.5, which are determined by the uncertainty in $C_5^A(0)$, partially englobe these discrepancies. In this context, it is worth reminding that the value of $C_5^A(0) = 1.00 \pm 0.11$ used here was determined in a combined analysis of the neutrino induced pion production ANL [136, 137] and BNL [138, 139] bubble chamber data. This was done with a model closely resembling the present one i.e. including nonresonant mechanisms, with the correct threshold behavior dictated by chiral symmetry, the dominant $\Delta(1232)$

excitation and also deuteron effects [40]. Such a consistency with pion production data on the nucleon was not attempted in Refs. [86, 88]. Actually, the ANL $\nu_\mu p \to \mu^- p \pi^+$ data are notably overestimated in Ref. [88] as can be seen in Fig. 2 of that article.

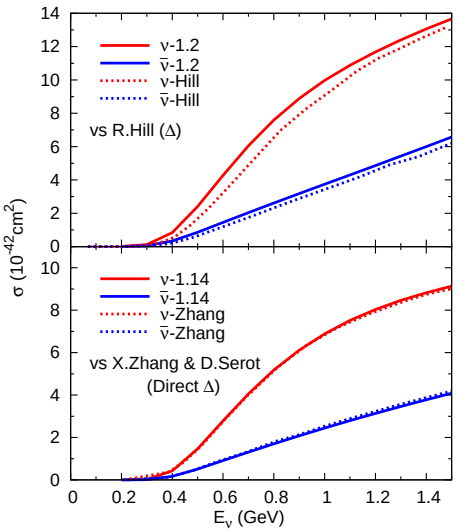

Figure 3.8: Top panel: $\Delta P + C\Delta P$ cross sections obtained by us (solid lines) and from Ref. [86] (dashed lines), for $\nu N \to \nu N\gamma$ (red upper curves) and for $\bar{\nu} N \to \bar{\nu} N\gamma$ (blue lower curves). For this comparison we have taken $C_5^A(0) = 1.2$ and no cut in E_γ as in Ref. [86] (note the $\Delta P + C\Delta P$ are finite in the $E_\gamma \to 0$ limit). Bottom panel: ΔP cross section obtained by us (solid lines) and from Ref. [88] (dashed lines), for $\nu N \to \nu N\gamma$ (red upper curves) and for $\bar{\nu} N \to \bar{\nu} N\gamma$ (blue lower curves). For this comparison we have adopted $C_5^A(0) = 1.14$ and an $E_\gamma \geq 0.2$ GeV cut, as in Ref. [88].

3.4.2 Neutral current photon emission in nuclei

For the present computations we take nuclear charge density distributions, normalized to the number of protons in the nucleus, extracted from electron scattering data [140]. The neutron matter density profiles

are parametrized in the same way as the charge densities (but normalized to the number of neutrons) with small changes from Hartree-Fock calculations [141] and supported by pionic atom data [142]. The corresponding parameters are compiled in Table I of Ref. [120]. Furthermore, these density distributions have been deconvoluted to get center-point densities following the procedure described in Ref. [143].

Incoherent reaction: $1p1h\gamma$ contribution

In the left panels of Fig. 3.9, we show our predictions for the (anti)neutrino incoherent photon emission cross sections on ^{12}C as a function of the (anti)neutrino energy up to 2 GeV. We observe that the neglect of nuclear medium corrections, as it was done in the study of the NCγ excess of events at MiniBooNE of Ref. [90], is a quite poor approximation. By taking into account Fermi motion and Pauli blocking, the cross section already goes down by more than 10%. With the full model that also includes the Δ resonance in-medium modification, the reduction is of the order of 30%. Furthermore, we corroborate the findings on nucleon targets (Fig. 3.5) about the N^* contributions [mostly the $N(1520)$] being sizable above $\sim$ 1.5 GeV, specially for antineutrino cross sections.

In the right-hand plots of Fig. 3.9, we compare our results with the predictions of Ref. [88]. As in the nucleon case (Fig. 3.8), we focus on the dominant ΔP contribution and use the same $C_5^A(0) = 1.14$ value and photon energy cut (200 MeV) as in Ref. [88]. When all the nuclear corrections are neglected, we certainly obtain the same curves as in Fig. 3.8, but multiplied by the number of nucleons (12). As can be observed in the figure, we find an excellent agreement both for neutrino and antineutrino cross sections. However, nuclear medium effects turn out to be much more important, leading to a much larger suppression ($\sim$ 50%), in the calculation of Ref. [88] for neutrinos. This seems surprising, first, because at this moderately high neutrino energies, similar nuclear corrections should be obtained with both models. In particular, one would not expect significant differences in the Δ resonance broadening in the medium when calculated with Eq. (3.66) or with the spreading potential of Ref. [52]. [11] Because of the larger nuclear

[11] We should mention that we agree better with the ΔP cross section of Ref. [88]

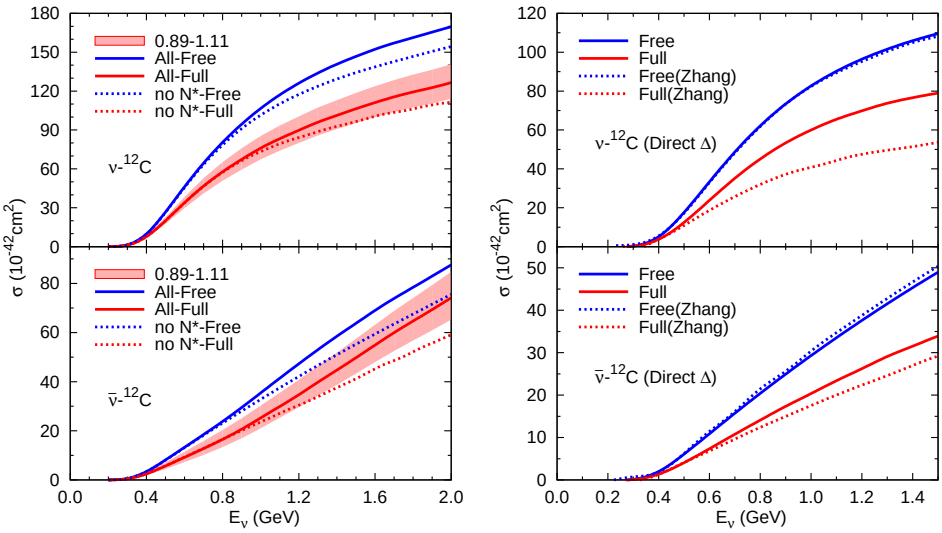

Figure 3.9: Left panel: Neutrino (top) and antineutrino (bottom) incoherent photon emission cross sections on ^{12}C. All curves in this panel have been obtained with an $E_\gamma \geq 140$ MeV cut in the phase space. Solid lines stand for results from the complete model at the nucleon level, while the dotted lines display the predicted cross sections without the N^* contributions. Curves denoted as "Free" (upper blue curves) do not include any nuclear correction: the nuclear target is treated as a mere ensemble of nucleons ($\sigma_A = Z\sigma_p + N\sigma_n$). Curves labeled as "Full" (lower red curves) take into account Pauli blocking, Fermi motion and the in medium Δ resonance broadening. The error bands show the uncertainty on the full model that arises from the determination of the axial $N\Delta$ coupling from data ($C_5^A(0) = 1.00 \pm 0.11$) [40]. Right panel: ΔP contribution to the neutrino (top) and antineutrino (bottom) photon emission cross sections on ^{12}C from Ref. [88] compared to our predictions for the same mechanism, adopting the same infrared photon energy cut $E_\gamma \geq 0.2$ GeV and $C_5^A(0) = 1.14$. The meaning of "Free" and "Full" labels is the same as in the left plots.

for neutrinos if we take an imaginary part of the Δ selfenergy twice bigger than the one in Eq. (3.66).

suppression, the ΔP cross section found in Ref. [88] is smaller than the one obtained here in spite of the 14% larger $C_5^A(0)$. In the antineutrino cross sections, the difference is not so large, and the medium effects shown in Ref. [88] are only slightly greater than those found in the present work. As a consequence of the large reduction of the ΔP contribution on ^{12}C, the contact terms become relatively important from $E_\nu = 1$ GeV on, rapidly increasing and turning dominant above 1.5 GeV (see Fig. 3 of Ref. [88]). Indeed, contact terms compensate the suppression of the ΔP mechanism, so that the incoherent cross sections predicted in Ref. [88] are comparable to ours in the 1 GeV region, but become about 40% (70%) larger than our results for 2 GeV neutrinos (antineutrinos) even though the contributions from resonances heavier that the Δ were not taken into account.

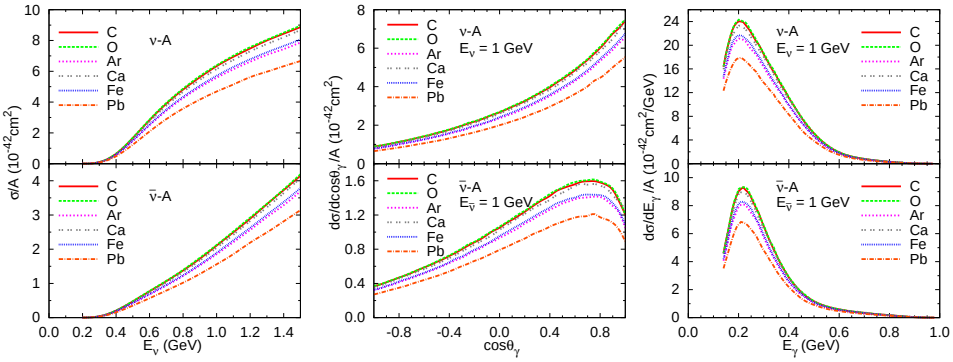

Figure 3.10: Neutrino (top) and antineutrino (bottom) incoherent NCγ total cross sections as a function of the (anti)neutrino energy (left panels), photon angular (middle panels) and photon energy (right panels) differential distributions at $E_{\nu,\bar{\nu}}$ =1 GeV. The angle θ_γ is referred to the direction of the incoming (anti)neutrino beam. Results for different nuclei (^{12}C,^{16}O,^{40}Ar, ^{40}Ca,^{56}Fe and ^{208}Pb) divided by the number of nucleons are shown. All results are obtained with the full model, including nuclear effects and implementing an $E_\gamma \geq 140$ MeV cut.

In Fig. 3.10, we show total NCγ incoherent cross sections for different nuclei (carbon, oxygen, argon, calcium, iron and lead) as a function of the (anti)neutrino energy. We also display photon angular and en-

ergy distributions for an incoming (anti)neutrino energy of 1 GeV. We notice the approximated $A-$scaling present in the results, which implies a mild A dependence of nuclear effects. Nevertheless, the cross section is smaller for heavier nuclei, particularly ^{208}Pb. We should stress that the observed deviation from scaling cannot be explained only by neutron cross sections being smaller than proton ones (around 15-20% at $E_\nu \sim 1.5$ GeV)[12].

Concerning the kinematics of the emitted photons, the main features are similar to those in Figs. 3.6 and 3.7 for scattering on single nucleons. As in that case, the reaction is more forward for neutrinos than for antineutrinos at $E_\nu = 1$ GeV. In the outgoing photon energy distributions (right panels), the peak just above $E_\gamma = 0.2$ GeV observed for nucleons is reproduced here without any shift in the peak position but with slightly larger width as the target mass increases.

Coherent reaction

Total NCγ coherent cross sections on carbon as a function of the (anti)neutrino energy are presented in Fig. 3.11. We display our results from the full calculation, from $(\Delta P + C\Delta P)$ alone, and without the mechanisms from second N^* resonance region. The N^* contributions are quite small in the coherent channel, while the Δ is absolutely dominant in both the neutrino and the antineutrino modes. Nucleon-pole contributions are negligible because the coherent kinematics favors a strong cancellation between the direct and crossed terms of the amplitude. A similar effect has been observed in weak coherent pion production [96].

For comparison, the predictions from the $(\Delta P + C\Delta P + NP + CNP)$ part of the model of Ref. [88] are also plotted. They are slightly above our corresponding results (without N^*), and within the uncertainty band of our full-model curve, up to (anti)neutrino energies of 1.4–1.5 GeV. Above these energies, there is a change of slope and a pronounced enhancement [88]. Moreover, in the model of this reference, the cross section above $E_{\nu,\bar{\nu}} = 0.65$ GeV is not dominated by the $(N + \Delta)$ mechanism, but by contact terms from higher order effective Lagrangians

[12]Note that the ΔP contribution is the same on protons and neutrons. Thus, this dominant mechanism does not contribute to such differences.

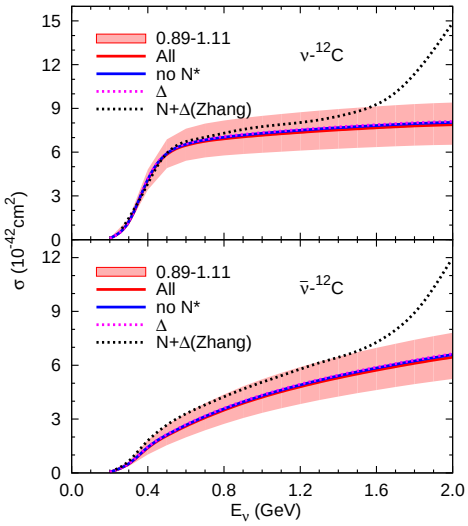

Figure 3.11: Neutrino (top) and antineutrino (bottom) total NCγ coherent cross sections on ^{12}C, as a function of the (anti)neutrino energy. A photon energy cut of $E_\gamma \geq 140$ MeV has been implemented. Red solid lines stand for results from the complete model derived in this work, including Δ resonance broadening, with error bands determined by the uncertainty of ± 0.11 in $C_5^A(0)$ [40]. The solid blue lines below, labeled as "no N^*", display the predicted cross sections without the N^* amplitudes, while the magenta dotted ones are the contributions from the $(\Delta P + C\Delta P)$ mechanisms. We also show the predictions of Ref. [88] for nucleon and Δ mechanisms (red solid lines in Fig.4 of this reference).

whose extrapolation to higher energies is uncertain. Indeed, for some choices of parameters, coherent cross sections as large as 25×10^{-42} cm^2 were obtained for $E_{\nu,\bar{\nu}} = 1.5$ GeV [88]. This amounts to a factor 3-4 larger than our predictions. We should remind here that below 500 MeV, the contact terms in the nucleon amplitudes are very small as expected based on the power counting established in Ref. [42]. Because of the substantial reduction of the Δ mechanisms, the contact terms in Ref. [88] acquire further relevance when the processes take place in

nuclei, specially for the coherent reaction.

Our results for coherent NCγ total and differential cross sections on different nuclei are shown in Fig. 3.12. Neutrino (antineutrino) coher-

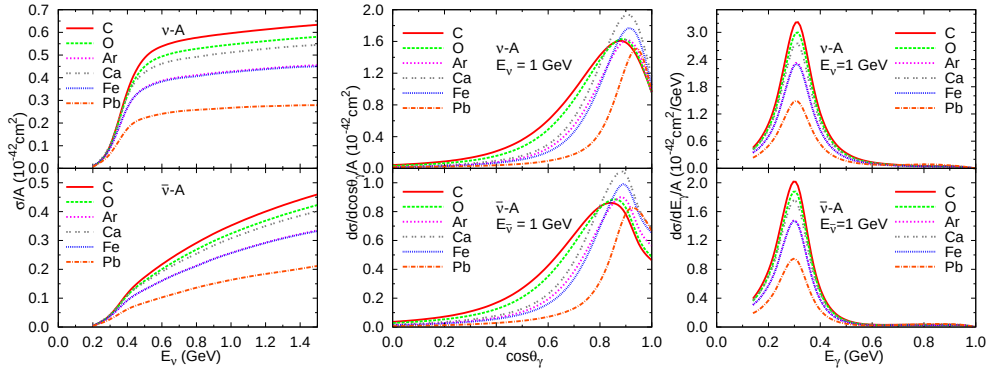

Figure 3.12: Neutrino (top) and antineutrino (bottom) total cross sections (left panels) photon angular (middle panels) and photon energy (right panels) differential distributions for the coherent NCγ reaction, obtained with our full model. The angle θ_γ is referred to the direction of the incoming (anti)neutrino beam. The kinematic region of $E_\gamma < 140$ MeV has been cut out. Results for different nuclei (^{12}C,^{16}O,^{40}Ar, ^{40}Ca,^{56}Fe and ^{208}Pb) divided by the number of nucleons are shown.

ent cross sections are about a factor 15 (10) smaller than the incoherent ones given in Fig. 3.10. Thus, the relative relevance of the coherent channel with respect to the incoherent channel is comparable, if not greater than in the pion production reactions induced by neutrinos and antineutrinos, where it is of the order of few per cent [43, 123]. Notice that in these latter reactions the coherent cross section is further reduced (by around a factor of two) because of the strong distortion of the outgoing pion, which is not present in photon production. It is also true that the incoherent cross section is reduced ($\sim 20-30\%$) by final state interactions, again absent for photons.

The coherent cross sections neither scale with A, like the incoherent one approximately does, nor with A^2 as one would expect from the coherence of the dominant isoscalar ΔP mechanism (sum of neutron

and proton amplitudes). This is due to the presence of the nuclear form factor (Fourier transform of the nuclear density for momentum $\vec{q}-\vec{k}_\gamma$), see the first paragraph of Sec. 3.3.2 and Eq. (3.70). The nuclear form factor gets its maximum values when $\vec{q}=\vec{k}_\gamma$, which corresponds to $q^2=0$. In this forward kinematics, the lepton tensor $L_{\mu\sigma}^{(\nu,\bar{\nu})} \sim q_\mu q_\sigma$, and the vector part of the amplitude squared is zero due to CVC. Furthermore, the axial contribution, which is purely transverse $\sim (\vec{k}_\gamma \times \vec{q})$ also vanishes. Therefore, the largest differential cross sections arise in kinematics that optimize the product of the amplitude squared of the elementary process times the nuclear form factor. Such a balance also appears in the (^{3}He,^{3}H π^+) reaction on nuclear targets [124] or in electron and photon induced reactions, making the electromagnetic coherent pion production cross section a rather small fraction of the total inclusive nuclear absorption one [102, 103].

The described pattern strongly influences the photon angular dependence of this reaction shown in the middle panels of Fig. 3.12 although in a non-trivial way because the θ_γ angle is given with respect to the direction of the incoming (anti)neutrino beam; it is not the angle formed by $\vec{q}$ and $\vec{k}_\gamma$, which is not observable. Actually, for each value of θ_γ, and integration over all possible $\vec{q}$ is carried out. The details of the angular distributions are determined by interferences between the dominant ΔP mechanism and the $C\Delta P$ and $N(1520)$ ones, enhanced by the kinematic constraints imposed by the nuclear form factor. The impact of the latter is apparent in the width of the angular distributions which are narrower for heavier nuclei.

Finally, in Fig. 3.12 we display the outgoing photon energy distributions (right panels). In the coherent NCγ reaction, there are two massless particles in the final state, and a third one (the nucleus) which is very massive and has a small (negligible) kinetic energy but can carry large momenta. The prominent peak observed for all nuclei is due to the dominant Δ resonance [13] shifted to slightly lower invariant masses mostly by the energy dependence of the Δ width and the interference

[13] The energy of the resonant photons in LAB can be estimated from $M_R^2 \approx (k_\gamma + p')^2$. Taking p' from Eq. (3.73) and for the situation $\vec{k}_\gamma \approx \vec{q}$ favored by the nuclear form factor, one finds that $k^0_{\gamma(R)} \approx (M_R^2 - M^2)/(2M)$. This gives 340 MeV for the $\Delta(1232)$ and 760 MeV for the $N(1520)$.

with the $C\Delta P$ mechanism. The peak position does not change appreciably from nucleus to nucleus, but it gets broader as A increases. The second, smaller and broader peak that can be discerned for neutrinos but not for antineutrinos corresponds to the excitation of the $D_{13}(1520)$ resonance.

3.5 Conclusions

Neutral current photon emission on nucleons and nuclei at intermediate energies has been theoretically investigated. We have developed a microscopic model for these reactions, in line with previous work on weak pion production [39, 43, 50, 96]. We have critically reviewed previous models for the NCγ reaction on single nucleons [42, 86, 88] and nuclei [52, 88, 91] and compared our results with those found in these references. From such a comparison, we have identified some aspects of the above studies that either needed to be improved or that were sources of uncontrolled systematic corrections.

NCγ processes are important backgrounds for $\nu_\mu \to \nu_e$ and $\bar{\nu}_\mu \to \bar{\nu}_e$ appearance oscillation experiments when photons are misidentified as $e^\pm$ from CCQE scattering of $\nu_e(\bar{\nu}_e)$. At the relevant energies for MiniBooNE and T2K experiments, the reaction is dominated by the weak excitation of the $\Delta(1232)$ resonance and its subsequent decay into $N\gamma$. Besides, we have also considered non-resonant amplitudes that, close to threshold, are fully determined by chiral symmetry, and those driven by nucleon excited states from the second resonance region. Among the latter ones, we have found a sizable contribution of the $D_{13}(1520)$ state for (anti)neutrino energies above 1.5 GeV.

The model on the nucleon is extended to nuclear targets taking into account Fermi motion, Pauli blocking and the in-medium modifications of the Δ properties in a local Fermi gas, with Fermi momenta determined from proton and neutron density distributions. We have predicted different observables for several nuclei, including some of the common ones in current and future neutrino detectors (carbon, oxygen, argon, iron). The importance of nuclear corrections in both the coherent and incoherent channels has been stressed. The A dependence of the cross section, which is different for the coherent and incoherent

reactions, has also been discussed.

In the light of our results, a new analysis of the NC induced photon production at MiniBooNE with the present model, aiming at the clarification of the role played by NCγ events in the low-energy excess observed in this experiment, looks timely and important. It will be presented in the next chapter.

Chapter 4

Single photon events from neutral current interactions at MiniBooNE

4.1 Introduction

The paradigm of three mixing flavors of neutrinos emerges from oscillation experiments with solar, atmospheric, reactor and accelerator neutrinos in which the square-mass differences and mixing angles have been determined with ever growing precision (see Ref. [144] for a recent global analysis). Nevertheless, a number of anomalies that challenge this picture has been observed. One of them has been reported by MiniBooNE [145]. The MiniBooNE experiment was designed to explore the short-baseline $\bar{\nu}_\mu \to \bar{\nu}_e$ oscillations observed at the Liquid Scintillator Neutrino Detector (LSND) [146]. It has found an excess of electron-like events over the predicted background in both ν and $\bar{\nu}$ modes [59, 61]. The excess is concentrated at $200 < E_\nu^{\rm QE} < 475$ MeV, where $E_\nu^{\rm QE}$ is the neutrino energy reconstructed assuming a charged-current quasielastic (CCQE) nature of the events (see Fig. 4.1). Recent analyses have shown that this anomaly cannot be explained by the existence of one, two [147, 148] or event three [147] families of sterile neutrinos, pointing at an explanation that does not invoke oscillations. Although there are exotic explanations based on Lorentz violation [149] or radiative decay of heavy neutrinos [150], it could have its origin in

poorly understood backgrounds or unknown systematics. Therefore, it is important to scrutinize the background prediction using our present knowledge of electroweak interactions on nucleons and nuclei.

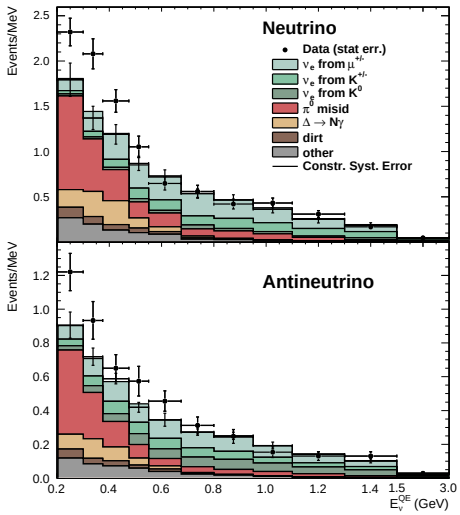

Figure 4.1: Electron-like event distributions observed at MiniBooNE in both neutrino and antineutrino modes, as a function of E_ν^{QE}. The different components of the background estimate are also shown [59].

Al low E_ν^{QE} the background is dominated by photon emission because Cherenkov detectors like MiniBooNE cannot distinguish electrons from single photons. The largest source of single photons is neutral current (NC) π^0 production where one of the photons from the $\pi^0 \rightarrow \gamma\gamma$ decay is not identified. This background has been constrained by the MiniBooNE's NCπ^0 measurement [12]. The second most important process is single photon emission in NC interactions (NCγ). The MiniBooNE analysis estimated this background using the NCπ^0 measurement, assuming that NCγ events come from the radiative decay of weakly produced resonances, mainly $\Delta \rightarrow N\gamma$ [59, 61]. This procedure neither takes into account the existence of non-resonant terms in the NCγ amplitude, nor the coherent part of the NCγ cross section in nuclei. If the NCγ emission estimate were not sufficiently accurate, this

would be relevant to track the origin of the observed excess.

The first effort to put the description of NC photon emission on solid theoretical grounds was reported in Ref. [86]. The reaction on nucleons was studied with a microscopic model developed in terms of hadronic degrees of freedom: nucleon, $\Delta(1232)$ resonance and mesons. Coherent photon emission off nuclear targets was also evaluated. With this model, the NCγ event rate at the MiniBooNE detector was calculated to be twice larger than expected from the MiniBooNE in situ estimate. The conclusion was that NCγ events give a significant contribution to the low-energy excess [90]. However, in Ref. [90], the detector material CH_2 was treated as an ensemble of nucleons, neglecting nuclear-medium effects. In addition, a rather high and constant efficiency of e-like event reconstruction ($30.6 \pm 1.4\%$) was assumed. A contrasting result, much closer to the MiniBooNE estimate, was obtained in Ref. [88], based on the chiral effective field theory of nuclei [42, 52, 91], phenomenologically extended to the intermediate energies ($E_\nu \sim 1$ GeV) of the $\nu/\bar{\nu}$ beams at MiniBooNE. In this model, a rather strong in-medium suppression of the $\Delta(1232)$ excitation is compensated by rapidly growing contact terms which are not well understood at $E_\nu \gtrsim 1$ GeV, being a source of uncontrolled systematics.

In the Chapter 3 (based on Ref. [104]), we have studied the NCγ reaction on nucleons and nuclei at intermediate energies with a realistic model that extends and improves relevant aspects of the previous work. For free nucleons, the model respects chiral symmetry at low momenta and accounts for the dominant $\Delta(1232)$ excitation using $N - \Delta(1232)$ transition form factors extracted from phenomenology. Mechanisms involving the excitation of baryon states from the second resonance region [$N^*(1440)$, $N^*(1520)$ and $N^*(1535)$] have also been incorporated in order to extend the validity of the approach towards higher energies. Both incoherent and coherent reaction channels on nuclear targets have been calculated applying standard nuclear corrections, in particular, the broadening of the $\Delta(1232)$ resonance in nuclear matter.

With this model, using the available information about the MiniBooNE (anti)neutrino flux [59, 151], detector mass and composition [59], and detection efficiency [152], we now predict the NCγ events at MiniBooNE. We investigate the photon energy and angle, as well as the reconstructed (anti)neutrino energy distributions, estimating the un-

certainty in the theoretical model. We pay attention to the contribution of antineutrinos in neutrino mode (and vice-versa), and discuss the impact of N^* excitation mechanisms. Our predictions are compared to the the MiniBooNE in situ estimate [59, 152] and the results of Ref. [88].

The chapter is based on Ref. [153]. In Sec. 4.2 the theoretical model of the NCγ reaction on nucleons and nuclei is briefly described. We refer the reader to Chapter 3 for more details. The expressions for the single photon electron-like events in the conditions of the MiniBooNE experiment are given in Sec. 4.3. We show our results and the comparisons to former estimates in Sec. 4.4, followed by the conclusions in Sec. 4.5.

4.2 Theoretical description of NC photon emission on nucleons and nuclei

The model of Ref. [104] (Chapter 3) for NC photon emission off nucleons,

$$\nu(\bar{\nu}) + N \to \nu(\bar{\nu}) + N + \gamma\,, \tag{4.1}$$

is defined by the set of Feynman diagrams for the hadronic current shown in Fig. 4.2.

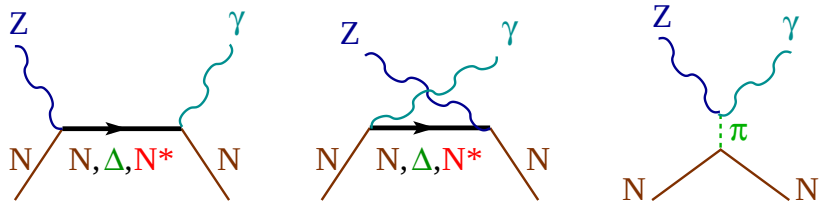

Figure 4.2: Feynman diagrams for the hadronic current for NC photon emission considered in Ref. [104] (Chapter 3). The first two diagrams stand for direct and crossed baryon pole terms with nucleons and resonances in the intermediate state: BP and CBP with $B = N$, $\Delta(1232)$, $N^*(1440)$, $N^*(1520)$, $N^*(1535)$. The third diagram represents the t-channel pion exchange: πEx.

As discussed in the previous chapter, the structure of nucleon pole terms, NP and CNP, at threshold is fully constrained by gauge and chiral symmetries, and the PCAC. They are infrared divergent when the photon energy $E_\gamma \to 0$ but this becomes irrelevant when the experimental detection threshold ($E_\gamma > 140$ MeV in the case of MiniBooNE [60]) is taken into account. The extension towards higher energy transfers required to make predictions at $E_\nu \sim 1$ GeV is performed using phenomenological parametrizations of the weak and electromagnetic form factors. Strange form factors, whose present values are consistent with zero [154] have been neglected.

The most prominent contribution to the cross section arises from the weak excitation of the $\Delta(1232)$ resonance followed by its radiative decay. The ΔP and $C\Delta P$ terms can be written in terms of vector and axial $N-\Delta$ transition form factors. The vector form factors are related to the helicity amplitudes extracted in the analysis of pion photo- and electro-production data. We have adopted the parametrizations of the helicity amplitudes obtained with the unitary isobar model MAID [111]. After adopting the Adler model [113, 114], the axial transition is expressed in terms of a single form factor, C_5^A in the notation of Ref. [155], for which we assume a standard dipole dependence on the square of the four-momentum transferred to the nucleon by the neutrino (q^2)

$$C_5^A(q^2) = C_5^A(0)\left(1 - \frac{q^2}{M_A^2}\right)^{-2}, \tag{4.2}$$

with $C_5^A(0) = 1.00 \pm 0.11$ and $M_A = 0.93$ GeV determined in a fit to $\nu_\mu d \to \mu^- \Delta^{++} n$ BNL and ANL data [40].

A similar strategy has been followed for the N^*P and CN^*P amplitudes: the electroweak $N - N^*$ transition currents, whose general structure depends on the spin and parity of the excited resonance, are parametrized in terms of vector and axial transition form factors. The vector form factors are expressed in terms of the empirical helicity amplitudes extracted in the MAID analysis. There is no experimental information that could be used to constrain the axial form factors. Following Ref. [41], we have kept only the leading axial terms and used PCAC to derive off-diagonal Goldberger-Treiman relations between the corresponding axial couplings and the $N^* \to N\pi$ partial decay widths.

For the q^2 dependence we have assumed a dipole ansatz like in Eq. (4.2) with a natural value of $M_A^* = 1.0$ GeV.

Finally, the πEx mechanism originates from the $Z\gamma\pi^0$ vertex fixed by the axial anomaly of QCD. It is nominally of higher order [42] and gives a negligible contribution to the NCγ cross section. We have assumed that other higher order terms can be also neglected.

The integrated NCγ cross sections and other observables have been computed with this model in Sec. IV A of Ref. [104] (Chapter 3.4.1). Although the $\Delta(1232)$ is dominant, the nucleon-pole terms and the contribution of the $N^*(1520)$ become important at $E_\nu > 1$ GeV.

The model has been then extended to nuclear targets for both the incoherent

$$\nu(\bar{\nu}) + A_Z|_{gs} \to \nu(\bar{\nu}) + X + \gamma \tag{4.3}$$

and coherent

$$\nu(\bar{\nu}) + A_Z|_{gs} \to \nu(\bar{\nu}) + A_Z|_{gs} + \gamma \tag{4.4}$$

reactions. For the incoherent process we have taken into account Fermi motion and Pauli blocking in a local Fermi gas, with Fermi momenta determined from proton and neutron density distributions. For the coherent one we have followed the framework derived in Ref. [50] for weak coherent pion production reactions. The nuclear current is obtained by summing the contributions of all nucleons. In this sum, the nucleon wave functions remain unchanged and one obtains nuclear density distributions. In both types of reactions, the broadening of the $\Delta(1232)$ in the nuclear medium is considered. The resonance decay width is reduced because the final nucleon in $\Delta \to \pi N$ can be Pauli blocked but, on the other hand, it increases because of the presence of many body processes such as $\Delta N \to NN$, $\Delta N \to NN\pi$ and $\Delta NN \to NNN$ (collisional broadening). These new decay channels have been parametrized as a function of the local density in Ref. [119]. The resulting cross sections and photon distributions for different target nuclei can be found in Sec. IV B of Ref. [104] (Chapter 3.4.2).

4.3 Single photon events at MiniBooNE

The number of NCγ events at the MiniBooNE detector with a given photon energy (E_γ) in the Laboratory frame and polar angle with

respect to the incoming neutrino beam direction (θ_γ) can be cast as

$$\frac{dN}{dE_\gamma d\cos\theta_\gamma} = \varepsilon(E_\gamma) \sum_{l=\nu_\mu,\bar{\nu}_\mu} N_{\rm POT}^{(l)} \sum_{t=p,\,^{12}{\rm C}} N_t \int dE_\nu \phi_l(E_\nu) \frac{d\sigma_{l\,t}(E_\nu)}{dE_\gamma d\cos\theta_\gamma} \,. \tag{4.5}$$

Here $\varepsilon(E_\gamma)$ stands for the energy dependent detection efficiency for e-like events provided by the MiniBooNE Collaboration [152] and displayed in the left panel of Fig. 4.3. The integral over the Laboratory neutrino energy covers most of the neutrino fluxes ϕ_l. We take into account intrinsic (before oscillations) ν_μ and $\bar{\nu}_\mu$ components in both neutrino and antineutrino modes (right panel of Fig. 4.3)[1] but not the intrinsic ν_e and $\bar{\nu}_e$ ones, as we have checked that their contribution to the number of events is negligible. Fluxes with $E_\nu > 3$ GeV are also neglected. The total number of protons on target (POT) $N_{\rm POT}^{(\nu)} = 6.46 \times 10^{20}$ in ν mode [61] and $N_{\rm POT}^{(\bar{\nu})} = 11.27 \times 10^{20}$ in $\bar{\nu}$ mode [59]. The sum over t takes into account that, according to the target composition (mineral oil, CH_2), the interactions can take place on single protons or on ^{12}C nuclei,

$$N_p = \frac{2}{14} M N_A = \frac{1}{7} M N_A \,, \qquad N_{^{12}{\rm C}} = \frac{12}{14} M \frac{N_A}{12} = \frac{1}{14} M N_A \,, \tag{4.6}$$

where $M = 806$ tons is the detector mass [59] and N_A, the Avogadro number.

Using Eq. (4.5) and the cross section model of Chapter 3 (Ref. [104]) outlined in the previous section, it is straightforward to obtain event distributions for the observable photon energy and angle. These will be presented and discussed in the next section. On the other hand, as a source of irreducible background to the electron CCQE events from $\nu_\mu \to \nu_e$ ($\bar{\nu}_\mu \to \bar{\nu}_e$) oscillations, it is important to predict the event distribution as a function of $E_\nu^{\rm QE}$. In the MiniBooNE study, the latter is determined from the energy and angle of the outgoing electron, assuming that it originated in a $\nu\, n \to e^-\, p$ ($\bar{\nu}\, p \to e^+\, n$) interaction

[1] The flux predictions at MiniBooNE have been refined in Ref. [156] with two different methods. The analysis shows that while the spectral shape is well modeled, the ν flux component in $\bar{\nu}$ mode has been overestimated. Therefore this component should be rescaled by 0.76±0.11 or 0.65±0.23 depending on the method. We adopt the more precise and less model dependent [156] value of 0.76.

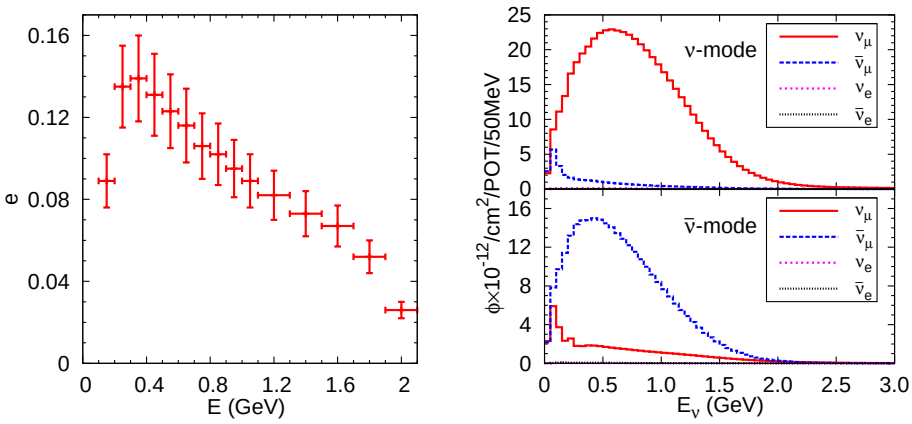

Figure 4.3: Left panel: Detection efficiency of electron-like events at the MiniBooNE detector as a function of the energy deposit [152] (E_γ in our case). Right panel: The predicted flux at MiniBooNE in ν and $\bar{\nu}$ modes [151].

on a bound neutron (proton) at rest

$$E_\nu^{\rm QE} = \frac{2(m_N - E_B)E' - E_B^2 + 2m_N E_B}{2\left[(m_N - E_B) - E'(1 - \cos\theta')\right]}\,, \tag{4.7}$$

with m_N the nucleon mass. The difference between the proton and neutron masses, and the electron mass have been neglected for simplicity; $E_B = 34$ MeV is the constant binding energy assumed by MiniBooNE for Carbon nuclei [7]. When photons from NCγ events are misidentified as electrons, $E_\nu^{\rm QE}$ is misreconstructed according to the above equation, with E_γ and θ_γ replacing the energy and angle of the outgoing electron E' and θ'. Then, one has that

$$\begin{aligned}\frac{dN}{dE_\nu^{\rm QE}} &= \int dE_\gamma d\cos\theta_\gamma \frac{dN}{dE_\gamma d\cos\theta_\gamma} \\ &\quad \times\delta\left(E_\nu^{\rm QE} - \frac{2(m_N - E_B)E_\gamma - E_B^2 + 2m_N E_B}{2\left[(m_N - E_B) - E_\gamma(1 - \cos\theta_\gamma)\right]}\right)\,. \end{aligned}\tag{4.8}$$

4.4 Results

In this section, we present our predictions for NCγ e-like events as functions of $E_\nu^{\rm QE}$, E_γ and $\cos\theta_\gamma$. We compare to the MiniBooNE in situ estimate [152] and the results of Ref. [88].

4.4.1 $E_\nu^{\rm QE}$ distribution of the NC photon events

Our results for the $E_\nu^{\rm QE}$ distributions are shown in Fig. 4.4 using the same bin sizes as MiniBooNE [152]. The partial contributions from the reaction on protons and on ^{12}C targets (both incoherent and coherent) are displayed. The yields from the incoherent channel are the largest ones. Those from the coherent channel and the reaction on protons, which are comparable, are smaller but not negligible. In ν mode (left panel of Fig. 4.4) the contributions of the $\bar{\nu}_\mu$ flux are small and could be safely neglected. However, in $\bar{\nu}$ mode (right panel of Fig. 4.4), there is a considerable amount of events from ν_μ interactions. This is because the cross section for neutrinos is about 2.5 times larger than that for antineutrinos [104] and, in addition, the ν_μ flux component in the $\bar{\nu}$ mode is considerable, much more than the $\bar{\nu}_\mu$ one in the ν mode (see the right panel of Fig. 4.3).

Next, we display the $E_\nu^{\rm QE}$ distributions for the total number of events in Fig. 4.6. The error bands correspond to the uncertainty in the axial $N\Delta$ coupling $C_5^A(0) = 1.00 \pm 0.11$ [40]. The comparison with the MiniBooNE in situ estimate [59, 152] shows a good agreement; the shapes are similar and the peak positions coincide. The largest discrepancy is observed in the lowest energy bin. In the two bins with the largest number of events, the two calculations are consistent within our errorbars. For higher $E_\nu^{\rm QE}$ values, our results are systematically above the MiniBooNE estimate although the differences are small. The error in the detection efficiency ($\sim 15\%$) [152], not considered in this comparison, will partially account for the discrepancies. The fair agreement between our predictions and the MiniBooNE estimates can be also appreciated by comparing Figs. 4.1 and 4.5. Both figures differ only in the NCγ component of the background that in the latter one has been calculated with our full model.

We have also plotted our results without the contributions from

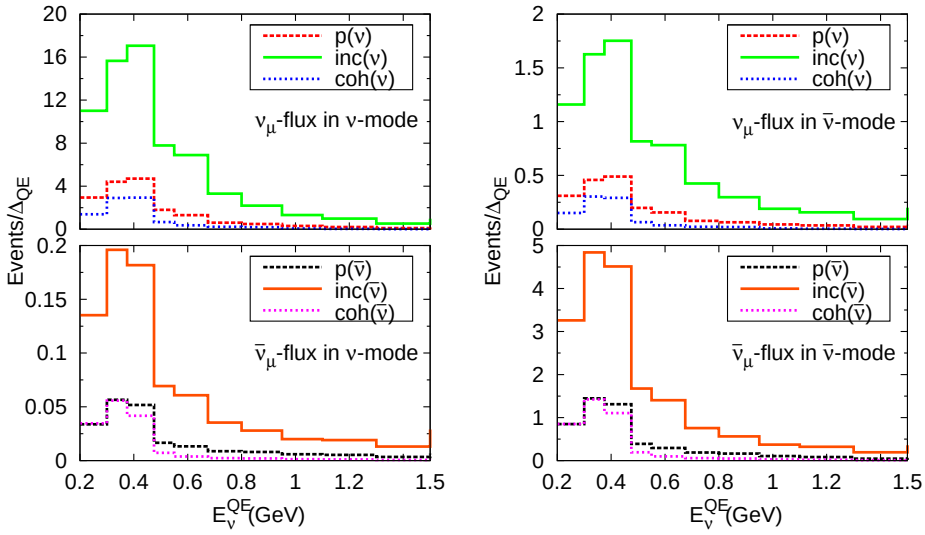

Figure 4.4: Distribution of NCγ e-like events at MiniBooNE as a function of the reconstructed (anti)neutrino energy ($E_\nu^{\rm QE}$) for the ν_μ (top) and $\bar{\nu}_\mu$ (bottom) MiniBooNE fluxes in the ν (left) and $\bar{\nu}$ (right) modes. The curves labeled as "p", "inc" and "coh" stand for the contributions of the $\nu(\bar{\nu}) - p$, $\nu(\bar{\nu}) - ^{12}$C incoherent and coherent reactions, respectively. The model parameters are given in Ref. [104]. $\Delta_{\rm QE}$ denotes the size of the $E_\nu^{\rm QE}$ bin in the experimental set up.

the N^* states populating the second resonance peak. The differences with the full calculation are small and only sizable at higher $E_\nu^{\rm QE}$ (compared with the number of events in these bins). The small impact of these heavier resonances is expected in view of the rather low energies present in the MiniBooNE flux. It is interesting that the inclusion of the N^* increases the differences with the MiniBooNE estimate above the maximum ($E_\nu^{\rm QE} > 0.475$ GeV). This might reflect the fact that resonance excitation at MiniBooNE is calculated with the phenomenologically outdated model of Rein and Sehgal [157] (see for instance the discussion in Ref. [158]).

Before finishing this subsection, in Tables 4.1 and 4.2, we compile the NCγ events in three bins of $E_\nu^{\rm QE}$ in order to compare to Ref. [88]. Our results without N^* can be confronted with the lower bound in

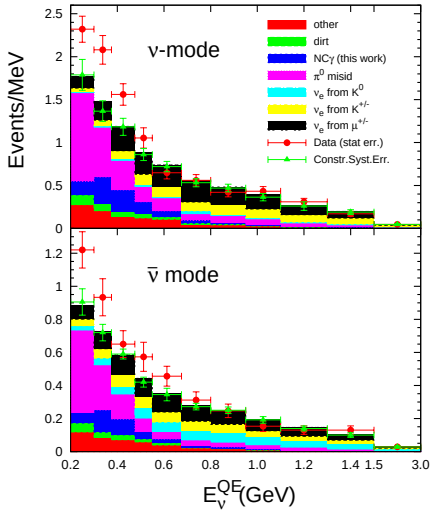

Figure 4.5: Same as Fig. 4.1, but replacing the MiniBooNE $\Delta \to N\gamma$ background estimate by our prediction for the NCγ event distribution.

Ref. [88] obtained with Δ and nucleon-pole terms alone. Except for the first bin, Ref. [88] predicts less events than we do. This difference, which is considerable in the third bin, could be partially attributed to the much stronger reduction of the incoherent cross section found in Ref. [88] (see Fig. 9 and the related discussion in Ref. [104]). Instead, the upper bound in the prediction of Ref. [88], calculated including contact terms, is larger than our results and than the MiniBooNE estimate, particularly in the third bin. As mentioned in Ref. [88], this large difference should be taken with caution. Indeed, the higher order contact terms extrapolated away from threshold are a source of systematic errors.

4.4.2 E_γ distribution of the NC photon events

The partial contributions of the different reaction channels to the E_γ distributions are shown in Fig. 4.7. The same features discussed above are present. All distributions have a maximum at $E_\gamma = 0.2 - 0.3$ GeV

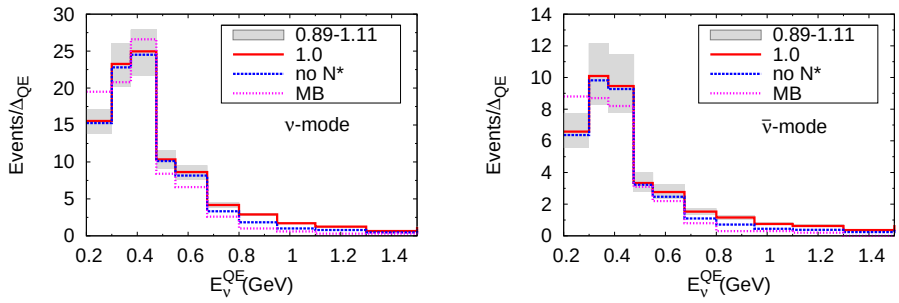

Figure 4.6: $E_\nu^{\rm QE}$ distributions of total NCγ events for the ν (left) and $\bar{\nu}$ (right) modes. The error bands correspond to the uncertainty in $C_5^A(0) = 1.00 \pm 0.11$ [40], while curves denoted as "1.0" display the results obtained with the central value of $C_5^A(0)$. The curves labeled as "no N^*" show results from our model without the $N^*(1440)$, $N^*(1520)$ and $N^*(1535)$ contributions. The "MB" histograms display the MiniBooNE estimates [152].

except for the coherent reaction induced by antineutrinos, which shows a broader peak. The agreement of the full model with the MiniBooNE estimate is very good for this observable, even at the lowest photon-energy bin, as can be seen in Fig. 4.8. Our results overlap with the range estimated in Ref. [88] except at the lowest energies, where both our predictions and MiniBooNE's are smaller. Nevertheless, it should be recalled that considering the lowest limit of the range estimated in Ref. [88], where the model content of the two approaches is very similar, we predict more NCγ events than Zhang and Serot [88] for $E_\gamma > 0.2$ GeV.

4.4.3 cosθ_γ distribution of the NC photon events

The partial contributions to the cosθ_γ distributions of NCγ events, presented in Fig. 4.9, show some interesting features. The distributions from incoherent scattering on ^{12}C are more forward peaked for neutrinos than for antineutrinos; the latter have a maximum around cos$\theta_\gamma \sim 0.7$. As expected, the coherent events are the most forward

Table 4.1: $E_\nu^{\rm QE}$ distributions of the NCγ events at MiniBooNE (ν mode). Our predictions for the different partial contributions, their sum with the error band from the uncertainty in the determination of the $N\Delta$ axial coupling, $C_5^A(0)$, and the results without N^* are displayed. In addition, the lower ($\Delta + N$) and upper (Full) limits in the calculation of Ref. [88] and the MiniBooNE estimate are shown. The asterisk (*) stands for figures obtained with $E_\nu^{\rm QE} < 1.25$ GeV rather than 1.3 GeV.

	ν mode		
$E_\nu^{\rm QE}$(GeV)	[0.2,0.3]	[0.3,0.475]	[0.475,1.3]
p(ν_μ)	2.94	9.11	4.69
inc(ν_μ)	11.01	32.70	22.47
coh(ν_μ)	1.38	5.83	1.52
p($\bar{\nu}_\mu$)	0.03	0.11	0.06
inc($\bar{\nu}_\mu$)	0.14	0.38	0.23
coh($\bar{\nu}_\mu$)	0.03	0.10	0.02
Total	15.54	48.23	29.98
Band [from $C_5^A(0)$]	[13.79,17.11]	[41.83,53.91]	[25.92,31.87]
no N^*	15.27	47.31	26.60
Zhang($\Delta + N$)	17.6	43.1	19.3*
Zhang (Full)	21.4	51.9	37.5*
MiniBooNE	19.5	47.4	19.9

peaked. For antineutrinos, and in the forward direction, we predict larger yields from coherent photon emission than from the proton channels. The comparison with the MiniBooNE in situ estimate, displayed in Fig. 4.10, reveals that we predict more forward peaked distributions than MiniBooNE does. This is not surprising as we have sizable coherent contributions, not considered in the MiniBooNE estimate.

Table 4.2: Same as Table 4.2, but for the $\bar{\nu}$ mode case.

	$\bar{\nu}$ mode		
$E_\nu^{\rm QE}$(GeV)	[0.2,0.3]	[0.3,0.475]	[0.475,1.3]
p(ν_μ)	0.31	0.95	0.58
inc(ν_μ)	1.16	3.38	2.67
coh(ν_μ)	0.15	0.59	0.16
p($\bar{\nu}_\mu$)	0.85	2.76	1.23
inc($\bar{\nu}_\mu$)	3.26	9.35	5.09
coh($\bar{\nu}_\mu$)	0.85	2.53	0.47
Total	6.58	19.55	10.16
Band [from $C_5^A(0)$]	[5.53,7.74]	[16.01,23.63]	[8.76,11.86]
no N^*	6.36	19.09	9.03
Zhang($\Delta + N$)	6.8	16.7	6.0*
Zhang (Full)	9.1	22.0	18.0*
MiniBooNE	8.8	16.9	6.9

4.5 Conclusions

With our microscopic model of Chapter 3 (Ref. [104]) for (anti)neutrino-induced NC photon emission on nucleons and nuclei, we have calculated the contribution from these processes to the electron-like irreducible background at the MiniBooNE experiment. To this aim we have taken into account the detector mass and composition, detection efficiency and the relevant components of the (anti)neutrino flux. Event distributions for photon energy and polar angle, relative to the direction of the incoming neutrino, have been obtained. We have also considered the distributions in the neutrino energy, misreconstructed assuming a CCQE nature for the events; this variable is used in the oscillation analysis as an estimator for the true neutrino energy. The largest contribution to the NCγ events in the mineral oil (CH_2) target of MiniBooNE arises from the incoherent reaction on ^{12}C although the interactions on the two protons and coherent scattering on ^{12}C produce sizable, and similar in magnitude, yields. The contribution from muon neutrinos in antineutrino mode is found to be important, unlike the insignificant

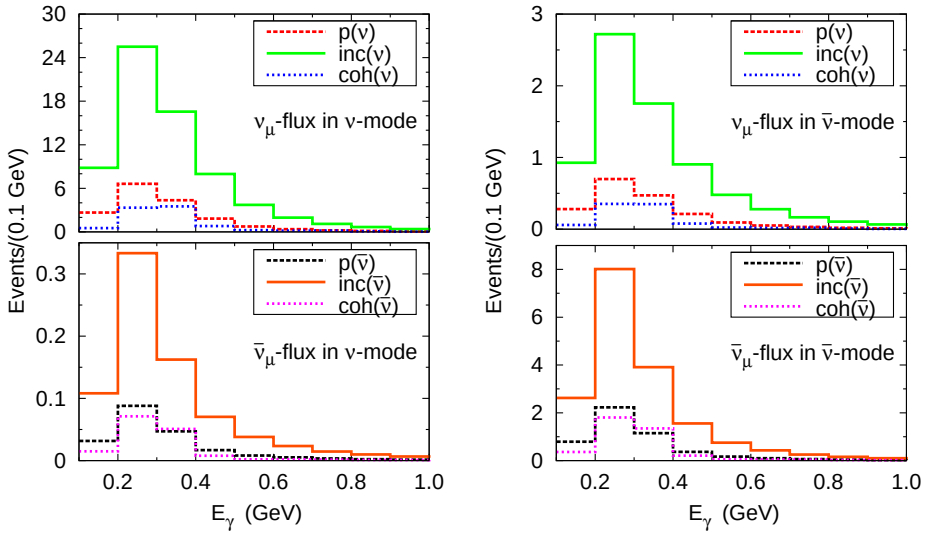

Figure 4.7: Distribution of NCγ e-like events at MiniBooNE as a function of the photon energy for the ν_μ (top) and $\bar{\nu}_\mu$ (bottom) MiniBooNE fluxes in the ν (left) and $\bar{\nu}$ (right) modes. The curves have the same meanings as in Fig. 4.4.

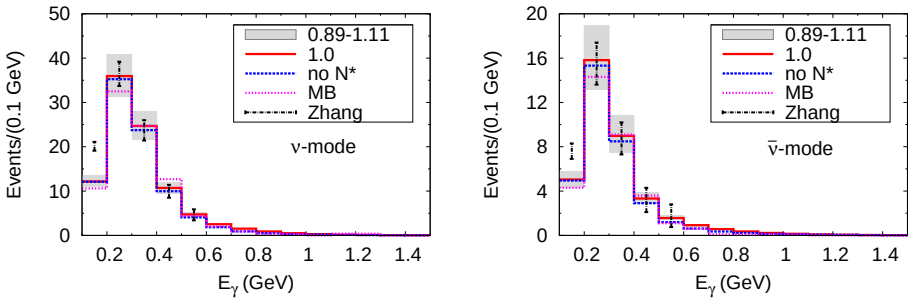

Figure 4.8: Photon energy distributions of total NCγ events for the ν (left) and $\bar{\nu}$ (right) modes. The segments, labeled as "Zhang", go from the lower to the upper estimates in Tables IV and V of Ref. [88]. All the other curves and bands denote the same as in Fig. 4.6.

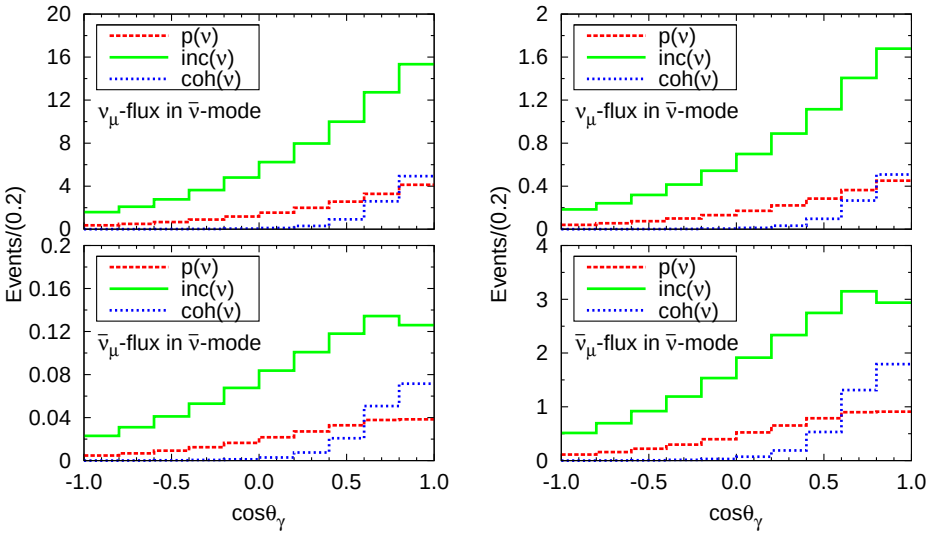

Figure 4.9: Photon angular distribution of NCγ e-like events at MiniBooNE for ν_μ (top) and $\bar{\nu}_\mu$ (bottom) MiniBooNE fluxes in the ν (left) and $\bar{\nu}$ (right) modes. The description of the curves is the same as in Fig. 4.4.

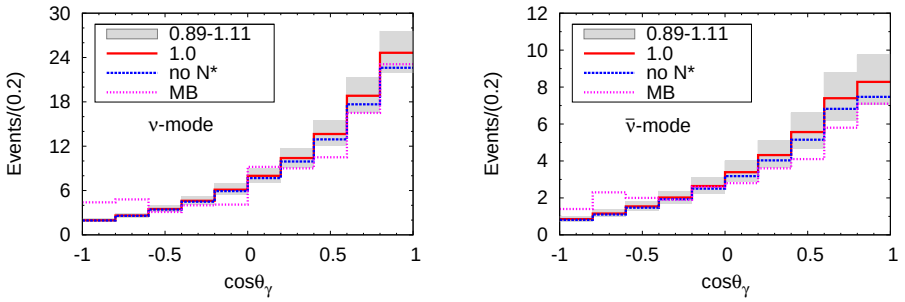

Figure 4.10: Photon angular distributions of total NCγ events for the ν (left) and $\bar{\nu}$ (right) modes. Curves and bands denote the same as in Fig. 4.6.

one of muon antineutrinos in neutrino mode.

These results have been confronted with the MiniBooNE in situ esti-

mate, obtained by tuning the resonance production model to the NCπ^0 measurement without taking into account non-resonant mechanisms or the coherent part of the cross section. They have also been compared to the estimates of the model of Zhang and Serot [88] based on an effective theory extended to higher energies using phenomenological form factors. The overall agreement is good in spite of the differences in the approaches, in contrast to the findings of Hill [90], obtained with a rather high and energy independent detection efficiency and neglecting nuclear effects. Therefore, we conclude that photon emission processes from single-nucleon currents cannot explain the excess of the signal-like events observed at MiniBooNE. Multinucleon mechanisms, which provide a significant amount of the CCQE-like cross section [26, 34], await to be investigated for this channel. Although these processes are bound to have some repercussion, they are unlikely to alter the picture dramatically. The forthcoming MicroBooNE experiment [159], capable of distinguishing photons from electrons, should be able to shed light on this puzzle.

Chapter 5

Photon emission of neutrino neutral current interactions in T2K

5.1 Introduction

More than 15 years of dedicated experimental studies have established the oscillations of three flavors of massive neutrinos. Recently, the circle has been rounded by the determination of the so called reactor neutrino mixing angle θ_{13}. The first indication at a 2.5σ significance of a nonzero value of θ_{13} was provided by the T2K experiment in a study of ν_e appearance in a ν_μ beam [160]. Afterwards it has been precisely measured from $\bar{\nu}_e$ disappearance in nuclear reactor neutrino experiments [161–163]. The significance of the T2K ν_e appearance result has now reached 7.3σ [164]. The increasing precision in these experiments opens the door to a determination of the CP violating phase in the lepton sector. Indeed, the tension between reactor data and T2K favors a $\delta_{CP} = -\pi/2$ [164] although the picture is still far from clear because the MINOS combined ν_μ disappearance and ν_e appearance prefers a $\delta_{CP} = \pi/2$ [165].

Further progress in this direction requires a better control over systematic errors and, in particular, of irreducible backgrounds. For this purpose, a better understanding of neutrino interactions with matter is mandatory. The ongoing effort in this direction englobes more precise

measurements of different (anti)neutrino cross sections on nuclear targets, theoretical work aimed at a better description of weak reactions on both nucleons and nuclei, and improvement of the Monte Carlo simulation codes; see the reviews of Refs. [22, 85, 158] for different aspects of these problems.

Super-Kamiokande (SK), the far detector of the T2K experiment, is a water Cherenkov detector (see Fig 5.1 for an illustration). As such, it is incapable of discriminating the diffuse rings of $e^{\pm}$ originated in charged current interactions by electron neutrinos from those created by photons. The largest part of such a background originates in π^0 production in neutral current (NC) interactions (NCπ^0) when the two photons from $\pi^0 \to \gamma\gamma$ produce overlapping rings or when one of them is not detected. Another relevant source is the NC single photon emission (NCγ) reaction. Although NCπ^0 has a larger cross section than NCγ, the π^0 background can be reduced with dedicated reconstruction algorithms, while the NCγ one remains irreducible. Indeed, in the latest T2K analysis [164], the NCπ^0 background was reduced by 69 % with respect to the previous appearance selection [62]. In this context, the relative relevance of the NCγ channel is significantly enhanced.

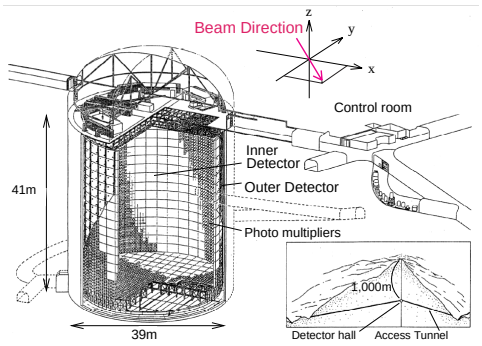

Figure 5.1: A schematic view of the SK detector [62]

The interest in a detailed theoretical study of the NCγ reaction [42, 52, 86, 91, 104] followed the observation of an excess of electron-like events at low reconstructed energies in the MiniBooNE detector, in both neutrino and antineutrino modes [59, 61]. It was suggested that an anomalous contribution to NC photon emission could be responsible

for this [166]. However, in spite of the fact that first studies indicated that NCγ indeed accounted for the excess [90], more recent analyses considering nuclear effects and realistic acceptance corrections [88, 153] obtain a number of photon-induced electron-like events which is consistent with the estimate made by MiniBooNE using a poor resonance production model tuned to the experiment's own NCπ^0 measurement. It has also been proposed that additional photons from electromagnetic heavy neutrino decays could be at the heart of the MiniBooNE anomaly [150, 167], which would have implications for other experiments such as T2K and MicroBooNE.

Here, we apply our microscopic model for the NCγ reaction [104] to predict the number of NCγ events at the SK detector, as well as their energy and angular distributions, for the flux and beam exposure of the latest T2K ν_e appearance study [164]. The event number and distributions are compared to the T2K estimates (before efficiency corrections) [168] obtained with the NEUT event generator [169]. A detailed account of the theoretical model with comparisons to previous results is given in Chapter 3 while a brief description can be found in Sec. 4.2 of Chapter 4.

5.2 Photon events at SK

Once the differential cross sections for the components of the detector (H_2O) are established, it is straightforward to obtain the number of NCγ events for a given photon energy and direction with respect to the neutrino beam,

$$\frac{dN}{dE_\gamma d\cos\theta_\gamma} = N_{\rm POT} \sum_{l=\nu,\bar\nu} \sum_{t=p,\,^{16}{\rm O}} N_t \int dE_\nu \phi_l(E_\nu) \frac{d\sigma_{l\,t}(E_\nu)}{dE_\gamma d\cos\theta_\gamma} \,. \quad (5.1)$$

Here, the total number of protons and ^{16}O nuclei in the SK inner detector is

$$N_p = \frac{2}{18} M N_A = \frac{1}{9} M N_A \,, \qquad N_{^{18}0} = \frac{16}{18} M \frac{N_A}{16} = \frac{1}{18} M N_A \,, \quad (5.2)$$

where $M = 2.25 \times 10^{10}$ grams is the fiducial mass, and N_A, the Avogadro number. Our estimate is for the recent T2K ν_e appearance

analysis, corresponding to a total number of protons on target (POT) $N_{\rm POT} = 6.57 \times 10^{20}$ in ν mode [164]. The flux of the off-axis neutrino beam from Tokai has a narrow peak with median energy 630 MeV at SK [170] (see Fig. 5.2). We neglect its contribution above $E_\nu = 3$ GeV. In spite of the rather long tail, a sizable contribution of the $E_\nu > 3$ GeV region would require a considerably large cross section at high energies, which we do not expect (see the discussion in Ref. [158]). The negative result in the single photon search performed by the NOMAD experiment [171], with an average energy of the neutrino flux of $E_\nu \sim 25$ GeV, is in line with our assumption. As the NC interaction is flavor independent, the composition of the beam after oscillations can be ignored.

The SK energy dependent detection efficiencies for e-like events are not publically available, and hence they could not be considered in Eq. (5.1), in contrast to the case of the MiniBooNE experiment (see Eq. (4.5)). Thus, in what follows, any comparison with real NCγ events at SK will be only indicative due to the lack of efficiency correction in our estimate. On the other hand, we have implemented a cut in the available photon phase space, demanding $E_\gamma \geq 100$ MeV, which corresponds to the visible energy ($\sim E_\gamma$) cut employed at SK [62].

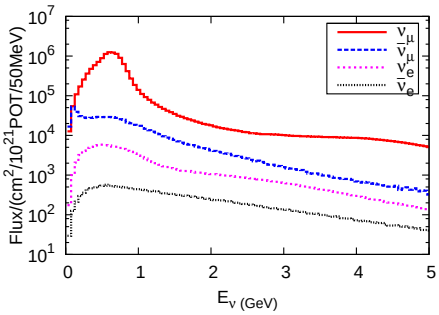

Figure 5.2: The T2K flux prediction at the SK detector [170] (without oscillations). Shown only below 5 GeV although it is simulated up to 30 GeV.

It will be instructive to show also the (non observable) neutrino-energy event distribution, which can be easily related to the integrated

cross section

$$\frac{dN}{dE_\nu} = N_{\rm POT} \sum_{l=\nu,\bar{\nu}} \sum_{t=p,\,^{16}{\rm O}} N_t \phi_l(E_\nu) \sigma_{l\,t}(E_\nu)\,. \tag{5.3}$$

5.3 Results

The photon energy and angular distributions of the NCγ events at SK are shown in Fig. 5.3 for the different channels, i.e. NCγ on protons and on ^{16}O (coherent and incoherent). The contributions of the ν_μ and $\bar{\nu}_\mu$ components of the flux are displayed. The incoherent reaction is the largest and peaks at $E_\gamma \sim 200 - 300$ MeV, reflecting the importance of the $\Delta(1232)$. The yield of nucleons and the coherent channel, both similar in size, is smaller but still important. The $\bar{\nu}_\mu$ contribution is quite small, representing around 2-3% of the total. Other flux components are totally negligible. The angular distributions are forward peaked, particularly for the coherent reaction. The latter has larger incidence than the nucleon channel in the forward direction. On the other hand, the angular dependence for the incoherent reaction induced by antineutrinos is softer than the neutrino one and peaks around $\cos\theta_\gamma = 0.7$. Similar features in the energy and angular distributions were obtained in the case of MiniBooNE [153].

Summing over all bins in the histograms above, one finds that the total number of NCγ events is

$$\mathcal{N} = 0.421 \pm 0.051\,. \tag{5.4}$$

The error corresponds to the uncertainty in the determination of the axial $N\Delta$ coupling from data ($C_5^A(0) = 1.00 \pm 0.11$). This is a small quantity compared to the 28 e-like events detected at SK [164] . Nevertheless, it shall be relevant in future attempts to measure δ_{CP}. This result becomes even more significant when compared to the NEUT equivalent figure of

$$\mathcal{N}_{\rm NEUT} = 0.165 \pm 0.019\,. \tag{5.5}$$

Indeed, using the NCγ cross section model of Ref. [104] we predict 2-3 times more events than the T2K estimate does.

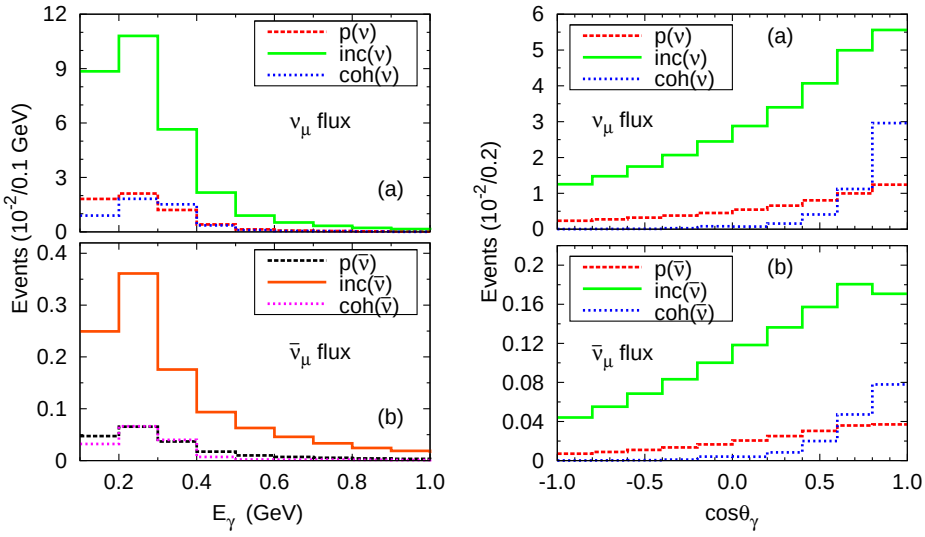

Figure 5.3: Photon energy (left) and angular (right) distributions of NCγ events at SK from the T2K flux. The curves labeled as "p", "inc" and "coh" stand for the contributions of the $\nu(\bar{\nu}) - p$, $\nu(\bar{\nu}) - {}^{16}\mathrm{O}$ incoherent and coherent reactions, respectively. Upper (lower) plots are for the ν_μ ($\bar{\nu}_\mu$) components of the flux.

In view of this discrepancy, we have performed more detailed comparisons with the NEUT NCγ prediction and confronted the photon energy and angular distributions. Figure 5.4 does not reveal any significant shape difference between the two models although one can notice that the E_γ distribution is somewhat broader in NEUT. The neutrino energy dependence of the events, displayed in Fig. 5.5 also shows a good agreement in the shape even if the distribution predicted by NEUT is slightly broader than the one obtaned with the model of Ref. [104].

The comparisons in Figs. 5.4 and 5.5 indicate that the disagreement is due to a discrepancy in the size (normalization) of the integrated cross sections in the two models. This is consistent with the comparison of the NCγ integrated cross sections on ^{12}C from different models, as a function of E_ν displayed in Fig. 9 of Ref. [145], where the NEUT result is clearly below the rest.

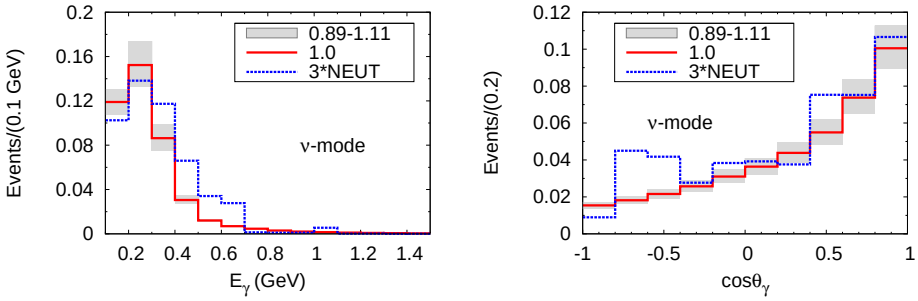

Figure 5.4: E_γ and $\cos\theta_\gamma$ distribution of NCγ events at SK obtained from the model of Ref. [104] (solid line) and from NEUT [168, 169] (dashed line). The error band is the theoretical error of the model of Ref. [104], corresponding to the uncertainty of $C_5^A(0) = 1.00 \pm 0.11$. The NEUT results have been multiplied by a factor of 3.

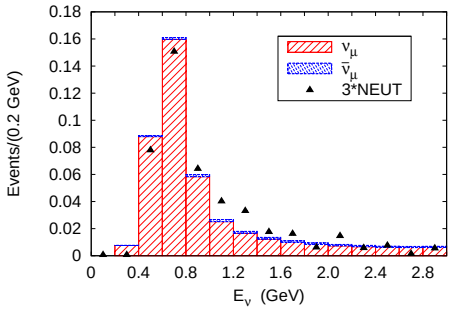

Figure 5.5: E_ν distribution of NCγ events at SK for the T2K experiment. The red histogram stands for the ν_μ flux contribution in the neutrino mode, while the small correction depicted in blue accounts for the contribution due to the $\bar{\nu}_\mu$ contamination present in the neutrino mode. The results from the NEUT generator, denoted by triangles, have been multiplied by a factor of 3.

5.4 Conclusions

The microscopic model of Ref. [104] for single photon emission in (anti)neutrino NC interactions has been applied to predict the number of such events at the inner SK water Cherenkov detector, as well as their energy and angular distributions. With this model one can take into account not only the radiative decay of weakly excited $\Delta(1232)$ resonance on both nucleons and nuclei, but also smaller, although relevant, contributions from nucleon pole terms and the coherent channel (details can be found in Ref. [104]). For a $N_{\rm POT} = 6.57 \times 10^{20}$ we predict 0.421 ± 0.051 events without efficiency corrections. Only 2-3% of it arises from the $\bar{\nu}_\mu$ contamination of the ν_μ beam. This small but irreducible background has to be realistically estimated in order to increase the precision in the determination of oscillation parameters, particularly in δ_{CP} measurements.

Remarkably, our prediction is 2.6 times larger than the one obtained from the main T2K Monte Carlo generator NEUT [169]. In a detailed inspection, we have found no significant differences in the shapes of the photon energy, photon angular and neutrino energy distributions in the two models. The large difference in normalization cannot be solely attributed to the lack of non-Δ production amplitudes or coherent photon emission in NEUT. It points at a mismodeling of the NCγ production by $\Delta(1232)$ excitation. It is also important to recall that, as shown in Ref. [104], the number of NCγ events at the MiniBooNE detector predicted by the same microscopic model used here is consistent with the MiniBooNE *in situ* estimate obtained with the NUANCE generator [172] tuned to the NCπ^0 measurement [12].

The T2K near detector ND280 may be able to constrain the NEUT prediction in the future by selecting γ candidate events, as done for example in Refs. [173, 174].

Chapter 6

Low-lying even parity meson resonances and spin-flavor symmetry revisited

6.1 Introduction

The study of the lowest–lying hadron resonances dynamics has received a lot of attention in the last decades, in particular since it was realized that some of them cannot be easily accommodated as radial or angular excitations of the Constituent Quark Model (CQM) ground states. Some examples are the low-lying scalar $f_0(500)$, $f_0(980)$, $a_0(980)$ and $K_0^*(800)$, or axial vector $a_1(1260)$, $b_1(1235)$, $h_1(1170)$, $f_1(1285)$, $K_1(1270)$ mesons. The field has experimented a considerable boost in the last decade, because several clear candidates for exotic states can be found among the recently discovered hidden bottom and charm XYZ resonances reported by the Belle, BABAR, $D0$ and CDF collaborations[1]. There has been a steady activity in the context of CQM's aiming to supplement these models with exotic components due to existence of tetraquark degrees of freedom inside of the hadrons (see for instance the discussion in Ref. [177]). Such components might lead to

[1]For instance, the isovector $J^{PC} = 1^{+-}$ $Z_b(10610)$ and $Z_b(10650)$ resonances (which are located just a few MeV above the $B\bar{B}^*$ and $B^*\bar{B}^*$ thresholds, respectively [175]) or the 1^{++} isoscalar hidden charm state $X(3872)$ placed close to the $D^0\bar{D}^{0*}$ threshold [176].

extended CQM schemes where the known exotic resonances could be generated and their main features be described. Here, however, we will pay attention to a different approach, in which the hadron resonances appear as bound or resonant states of an interacting pair of ground state hadrons (mesons of the π octet and the ρ nonet and baryons of the N octet and $\Delta(1232)$ decuplet, when the study is limited to the three lightest quark flavors). In this molecular picture, hadron resonances show up as poles in the First or Second Riemann Sheets (FRS/SRS) of certain hadron–hadron amplitudes. The positions of the poles determine masses and widths of the resonances, while the residues for the different channels define the corresponding coupling or branching fractions[2]. The interaction among the ground state hadrons is thus the first ingredient to build this molecular scheme. These are usually obtained from Effective Field Theories (EFT's) that incorporate constrains deduced from some relevant exact or approximate symmetries of Quantum Chromodynamics (QCD). In this context, it is clear that Chiral Perturbation Theory (ChPT) [63, 179, 180] and Heavy Quark Spin Symmetry (HQSS) [66, 67, 181] should play relevant roles, when designing interactions involving Goldstone bosons or charm/bottom hadrons, respectively. In this work, we will focus in the light SU(3) flavor sector and we will leave the extension of this discussion to heavy molecules for future research.

ChPT is a systematic implementation of chiral symmetry and of its pattern of spontaneous and explicit breaking, and it provides a model independent scheme where a large number of low-energy non-perturbative strong-interaction phenomena can be understood. It has been successfully applied to study different processes involving light (u and d) or strange (s) quarks. Because ChPT provides the scattering amplitudes as a perturbative series, it cannot describe non-analytical features as poles. Thus, ChPT cannot directly describe the nature of hadron resonances. In recent years, it has been shown that by unitarizing the ChPT amplitudes in coupled channels, the region of application of ChPT can be greatly extended. This approach, commonly referred as Unitary Chiral Perturbation Theory (UChPT), has received

[2]Some studies have also adopted an hybrid approach performing coupled channels calculations including quark model and molecular configurations (see for instance the discussion in Ref. [178]).

much attention and provided many interesting results, in particular in the meson-meson sector where we will concentrate our attention in this work, [64, 65, 68, 182–200]. It turns out that many meson-meson resonances and bound states appear naturally within UChPT. These states are then interpreted as having "dynamical nature." In other words, they are not genuine $q\bar{q}$ states, but are mainly built out of their meson-meson components[3]. To distinguish among these two pictures, it has been suggested to follow the dependence on a variable number of colors $N_C(> 3)$ of the resonance properties by assuming that hadronic properties scale similarly as if N_C was large. Some interesting results are being obtained from this perspective [202–208], and at present there exists some controversy on the nature of the $f_0(500)$ resonance [203, 207, 208] for which accurate models are available.

The present work is an update of Ref. [68], where was derived a spin-flavor extension of chiral symmetry to study the S-wave meson-meson interaction involving members not only of the π-octet, but also of the ρ-nonet. The similar approach for baryon-meson dynamics was initiated in [209, 210]. Elastic unitarity in coupled channels is restored in [68] by solving a renormalized coupled-channel Bethe–Salpeter Equation (BSE) with an interaction kernel deduced from spin-flavor extensions of the ChPT amplitudes. In the scheme of Ref. [68], the spin-flavor symmetry was explicitly broken to account for physical masses and decay constants of the involved mesons, and also when the amplitudes were renormalized. Nevertheless, the underlying SU(6) symmetry was still present and served to organize the set of even parity meson resonances found in that work. Indeed, it was shown that most of the low-lying even parity PDG (Particle Data Group Collaboration [70]) meson resonances, specially in the $J^P = 0^+$ and 1^+ sectors, could be classified according to multiplets of the SU(6) spin-flavor symmetry group. However, some resonances, like the isoscalar $f_0(1500)$ or $f_1(1420)$ states, could not be accommodated within this scheme and it was claimed that these states could be clear candidates to be glueballs or hybrids [68].

Chiral symmetry (CS), and its breaking pattern, is encoded in the approach of Ref. [68] at leading order (LO) by means of the Weinberg-

[3]The situation is similar in the meson-baryon sector, for recent works there see Refs. [74, 201].

Tomozawa (WT) soft pion theorem [211, 212]. This CS input strongly constraints the pseudoscalar–pseudoscalar (PP) and pseudoscalar–vector (PV) channels, since the mesons of the pion octet were identified with the set of Nambu-Goldstone bosons that appear for three flavors (due to the spontaneous breaking of CS). Thus, the main features (masses, widths, branching fractions and couplings) of the lowest nonet of S-wave scalar resonances [$f_0(500)$, $f_0(980)$, $a_0(980)$ and $K_0^*(800)$] found in Ref. [68] do not significantly differ from those obtained in previous SU(3) UChPT approaches [187, 189, 193]. This is because these resonances are generated from the interaction of Nambu-Goldstone bosons, and the influence of the vector–vector (VV) components in these states is small.

The PV and VV sectors have been also systematically studied in Refs. [195, 198, 199], respectively. These works adopt the formalism of the hidden gauge interaction for vector mesons [213, 214].[4] In the $PV \to PV$ sector, as mentioned above, CS constrains the interactions, and the interactions derived in Ref. [68] and those used in Ref. [195] totally agree at LO in the chiral expansion, despite their different apparent structure and origin. As a consequence, the results of Ref. [68] are in general in good agreement with those previously obtained in Ref. [195], which among others include the prediction of a two pole structure for the $K_1(1270)$ resonance [196]. However, the simultaneous consideration of PV and VV channels made the approach of Ref. [68] different from that followed in Ref. [195] in few cases. One of the most remarkable cases was that of the $h_1(1595)$ resonance, which was dynamically generated for the first time in the work of Ref. [68]. The interference $PV \to VV$ amplitudes turned out to play a crucial role in producing this state in [68], and that is presumably the reason why the $h_1(1595)$ resonance was generated neither in the $PV \to PV$ study of [195], nor in the $VV \to VV$ scheme of Ref. [199]. Possibly, the situation is similar for the $K_1(1650)$ state. These two resonances helped to

[4]Strictly speaking, the study of axial-vector resonances carried out in Ref. [195] does not use the hidden gauge formalism. There, a contact WT type Lagrangian is employed. However, the tree level amplitudes so obtained coincide with those deduced within the hidden gauge formalism, neglecting q^2/m_V^2 in the t-exchange contributions [215] and considering only the propagation of the time component of the virtual vector mesons.

envisage a clearer SU(6) pattern in [68], which is also followed to some extent in nature, and that is missed in the separate works of Refs. [195] and [199].

In general terms, the model of Ref. [68] provides a fairly good description of the $J^P = 0^+$ and $J^P = 1^+$ sectors. However, from a phenomenological point of view, the model of Ref. [68] led to a much poorer description of the $J^P = 2^+$ sector, which for S-wave is constructed out of VV interactions. Indeed, the well established $f_2(1270)$ and $K_2^*(1430)$ resonances are difficult to accommodate in the scheme, which needs to be somehow pushed to its limits of validity. The hidden gauge interaction for vector mesons model used in [199] seems to be more successful in describing the properties of the $f_2(1270)$ and $K_2^*(1430)$ resonances. This latter model and that of Ref. [68] are related for $PV \to PV$ scattering, thanks to CS, but they are completely unrelated in the VV sector.

The SU(6) spin-flavor symmetry is severely broken in nature. Certainly it is mandatory to take into account mass breaking effects by using different pseudoscalar and vector mesons masses. However, this cannot be done by just using these masses in the kinematics of the amplitudes derived in a straight SU(6) extension of the WT Lagrangian, since this would lead to flagrant violations of the soft pion theorems in the $PV \to PV$ sector due to the large vector meson masses. Instead in [68], a proper mass term was added to the extended WT Lagrangian that produced different pseudoscalar and vector meson masses, *while preserving, or softly breaking, chiral symmetry.* Such term, besides providing masses to the vector mesons, gives rise to further contact interaction terms (local). However, some other local interaction SU(6) symmetry breaking terms respecting (softly breaking) CS can be designed, as we show in this work. The nature of the contact terms can only be fully unraveled by requiring consistency with the QCD asymptotic behaviour at high energies [216], which is far from being trivial. As an alternative, we will present here a phenomenological analysis of the effects on the resonance spectrum due to the inclusion of new VV interactions consistent with CS. Thus, in first place, we will find in this work the most general four meson-field local (involving no derivatives) terms consistent with the chiral symmetry breaking pattern of QCD, and constructed by using a single trace, in the spirit of the large

N_C expansion. Next, we will show that the inclusion of these pieces leads to a considerable improvement of the description of $J^P = 2^+$ sector, without spoiling the main features of the predictions obtained in Ref. [68] for the $J^P = 0^+$ and $J^P = 1^+$ sectors.

The chapter is based on Ref. [217] and it is organized as follows. First, we briefly review in Sec. 6.2 the model derived in Ref. [68], including a brief discussion (Subsec. 6.2.2) on the BSE in coupled channels, and the renormalization scheme used to obtain finite amplitudes. Next in Sec. 6.3, we study the interplay between the SU(6) symmetry breaking local terms and CS, and design two new interaction terms. Their phenomenological implications are studied in Sec. 6.4. There, we present results in terms of the unitarized amplitudes and search for poles on the complex plane. We discuss the results sector by sector trying to identify the obtained resonances or bound states with their experimental counterparts [70], and compare our results with earlier studies, in particular that of Ref. [68]. A brief summary and some conclusions follow in Sec. 6.5. In Appendix D.1, we show that there are just three chiral invariant four meson contact interactions, if only a single trace is allowed to construct them. In Appendix D.2 the various potential matrices derived in this work are compiled for the different hypercharge, isospin and spin sectors.

6.2 SU(6) extension of the SU(3)-flavor Weinberg-Tomozawa Lagrangian

In this section, we briefly review the model derived in Ref. [68] to describe the S-wave interaction of four mesons of the π-octet and/or ρ-nonet.

6.2.1 The interaction

In Ref. [68], the BSE was solved by using as a kernel the amplitude $\mathcal{H}$ given by Eq. (40) of Ref. [68] (Eq. (6.20) in this chapter). This amplitude consists of three different contributions. Two of them ($\mathcal{D}_{\rm kin}$ and $\mathcal{D}_a$) come from the straight extension to SU(6) of the kinetic part of the LO WT SU(3)–flavor interaction, while the third one, $\mathcal{D}_m$, is orig-

inated by the mechanism implemented in [68] to give different masses to pseudoscalar and vector mesons. To give mass to the vector mesons certainly requires breaking SU(6) in the Lagrangian, not only through mass terms but also by interaction terms, due to chiral symmetry.

The lowest-order chiral Lagrangian describing the interaction of pseudoscalar Nambu-Goldstone bosons is [180]

$$\mathcal{L} = \frac{f^2}{4}\mathrm{Tr}\left(\partial_\mu U^\dagger \partial^\mu U + \mathcal{M}(U + U^\dagger - 2)\right), \tag{6.1}$$

where $f \sim 90\,\mathrm{MeV}$ is the chiral-limit pion decay constant, $U = e^{\mathrm{i}\sqrt{2}\Phi/f}$ is a unitary 3×3 matrix that transforms under the linear realization of $\mathrm{SU(3)_L}\otimes\mathrm{SU(3)_R}$, with

$$\Phi = \begin{pmatrix} \frac{1}{\sqrt{6}}\eta + \frac{1}{\sqrt{2}}\pi^0 & \pi^+ & K^+ \\ \pi^- & \frac{1}{\sqrt{6}}\eta - \frac{1}{\sqrt{2}}\pi^0 & K^0 \\ K^- & \bar{K}^0 & -\sqrt{\frac{2}{3}}\eta \end{pmatrix}, \tag{6.2}$$

and the mass matrix $\mathcal{M} = \mathrm{diag}(m_\pi^2, m_\pi^2, 2m_K^2 - m_\pi^2)$ is determined by the pion and kaon meson masses.

The straight SU(6) extension of Eq. (6.1) from SU(3) to SU(6) is [68]

$$\mathcal{L}_{\mathrm{SU(6)}} = \frac{f_6^2}{4}\mathrm{Tr}\Big(\partial_\mu U_6^\dagger \partial^\mu U_6 + \mathcal{M}_6(U_6 + U_6^\dagger - 2)\Big), \qquad U_6 = e^{\mathrm{i}\sqrt{2}\Phi_6/f_6} \tag{6.3}$$

where U_6 is now a unitary 6×6 matrix that transforms under the linear realization of $\mathrm{SU(6)_L}\otimes\mathrm{SU(6)_R}$. The Hermitian matrix Φ_6 is the meson field in the **35** irreducible representation of SU(6), and $f_6 = f/\sqrt{2}$ [210]. SU(6) spin-flavor symmetry allows to assign the vector mesons of the ρ nonet and the pseudoscalar mesons of the π octet in the same (**35**)

SU(6) multiplet. A suitable choice for the Φ_6 field is[5]

$$\Phi_6 = \underbrace{P_a \frac{\lambda_a}{\sqrt{2}} \otimes \frac{I_{2\times 2}}{\sqrt{2}}}_{\Phi_P} + \underbrace{R_{ak} \frac{\lambda_a}{\sqrt{2}} \otimes \frac{\sigma_k}{\sqrt{2}} + W_k \frac{\lambda_0}{\sqrt{2}} \otimes \frac{\sigma_k}{\sqrt{2}}}_{\Phi_V}, \quad a = 1, \ldots, 8, \quad k = 1, 2, 3 \tag{6.4}$$

with λ_a the Gell-Mann and $\boldsymbol{\sigma}$ the Pauli spin matrices, respectively, and $\lambda_0 = \sqrt{2/3}\, I_{3\times 3}$ ($I_{n\times n}$ denotes the identity matrix in the n dimensional space). P_a are the π, K, η fields, while R_{ak} and W_k stand for the ρ-vector nonet fields, considering explicitly the spin degrees of freedom.

The first term[6] in $\mathcal{L}_{\mathrm{SU(6)}}$ preserves both chiral and spin-flavor symmetries. The second term breaks explicitly chiral symmetry, and taking for instance $\mathcal{M}_6 = m_6 I_{6\times 6}$, provides a common mass, m_6, for all mesons belonging to the SU(6) **35** irreducible representation. However, the SU(6) spin-flavor symmetry is severely broken in nature and it is indeed necessary to take into account mass breaking effects by using different pseudoscalar and vector mesons masses.

To this end in Ref. [68], the following mass term, which replaces that in Eq. (6.3), was considered

$$\begin{aligned} \mathcal{L}^{(m)}_{\mathrm{SU(6)}} &= \frac{f_6^2}{4} \mathrm{Tr}\Big(\mathcal{M}(U_6 + U_6^\dagger - 2) \Big) \\ &\quad + \frac{f_6^2}{32} \mathrm{Tr}\Big(\mathcal{M}'(\boldsymbol{\sigma}\, U_6\, \boldsymbol{\sigma}\, U_6^\dagger + \boldsymbol{\sigma}\, U_6^\dagger\, \boldsymbol{\sigma}\, U_6 - 6) \Big) . \end{aligned} \tag{6.5}$$

Here the matrix $\mathcal{M}$ acts only in flavor space and it is to be understood as $\mathcal{M} \otimes I_{2\times 2}$, and similarly for $\mathcal{M}'$, so that $\mathrm{SU(2)_{spin}}$ invariance is preserved by these mass matrices. Besides, these matrices should be diagonal in the isospin basis of Eq. (6.2) so that charge is conserved. Also, $\boldsymbol{\sigma}$ stands for $I_{3\times 3} \otimes \boldsymbol{\sigma}$.

The first term in $\mathcal{L}^{(m)}_{\mathrm{SU(6)}}$ is fairly standard. It preserves spin-flavor symmetry when $\mathcal{M}$ is proportional to the identity matrix and introduces a soft breaking of chiral symmetry when $\mathcal{M}$ is small. This term

[5] Matrices, A^i_j, in the dimension 6 space are constructed as a direct product of flavor and spin matrices. Thus, an SU(6) index i, should be understood as $i \equiv (\alpha, \sigma)$, with $\alpha = 1, 2, 3$ and $\sigma = 1, 2$ running over the (fundamental) flavor and spin quark degrees of freedom, respectively.

[6] In what follows, we will refer to it as the kinetic term.

gives the same mass to pseudoscalar and vector mesons multiplets. Note that terms of this type are sufficient to give different mass to pseudoscalars (e.g. π and K) when SU(N_F) is embedded into SU(N'_F) (a larger number of flavors). They are not sufficient however to provide different P and V masses when SU(N_F) is embedded into SU($2N_F$) (spin-flavor).

The second term in $\mathcal{L}^{(m)}_{\rm SU(6)}$ only gives mass to the vector mesons: indeed, if one would retain in U_6 only the pseudoscalar mesons, U_6 would cancel with $U_6^\dagger$ (since these matrices would commute with $\boldsymbol{\sigma}$) resulting in a cancellation of the whole term. This implies that this term does not contain contributions of the form PP (pseudoscalar mass terms) nor $PPPP$ (purely pseudoscalar interaction). In addition, when $\mathcal{M}'$ is proportional to the identity matrix (i.e., exact flavor symmetry) chiral symmetry is also exactly maintained, because the chiral rotations of U_6 commute with $\boldsymbol{\sigma}$. This guarantees that this term will produce the correct $PV \to PV$ contributions to ensure the fulfillment of soft pion WT theorem [211, 212] even when the vector mesons masses are not themselves small.

At order Φ_6^2, the Lagrangian of Eq. (6.5) provides proper mass terms for P and V mesons, while at order Φ_6^4 it gives rise to four meson interaction terms. In the exploratory study of Ref. [68], the chiral breaking mass term ($\mathcal{M}$) was neglected, and a common mass, m_V, for all vector mesons ($\mathcal{M}' = m_V^2 I_{3\times3}\, I_{2\times2}$) was used.[7] With these simplifications, the interaction piece deduced from $\mathcal{L}^{(m)}_{\rm SU(6)}$ reads [68]

$$\mathcal{L}^{(m;\,\rm int)}_{\rm SU(6)} \;=\; \frac{m_V^2}{8f^2}{\rm Tr}\left(\Phi_6^4 + \boldsymbol{\sigma}\,\Phi_6^2\,\boldsymbol{\sigma}\Phi_6^2 - \frac{4}{3}\boldsymbol{\sigma}\,\Phi_6\,\boldsymbol{\sigma}\,\Phi_6^3\right). \qquad (6.6)$$

This term gives rise to the local $\mathcal{D}_m$ contribution to the four meson amplitude $\mathcal{H}$ in Eq. (40) of Ref. [68]. The other two contributions, $\mathcal{D}_{\rm kin}$ and $\mathcal{D}_a$, to $\mathcal{H}$ come from the first term (kinetic) of $\mathcal{L}_{\rm SU(6)}$ in Eq. (6.3). In addition, in Ref. [68] were also considered spin-flavor

[7] A vector meson nonet averaged mass value $m_V = 856\,$MeV was employed in [68]. Note, however, that the simplifying choice $\mathcal{M} = 0$, $\mathcal{M}' = m_V^2$, refers only to the interaction terms derived from the Lagrangian $\mathcal{L}^{(m)}_{\rm SU(6)}$. For the evaluation of the kinematical thresholds of different channels, real physical meson masses were used in [68].

symmetry-breaking effects due to the difference between pseudoscalar- and vector-meson decay constants, and an ideal mixing between the ω and ϕ mesons (see Subsec. IID of Ref. [68] for some more details, and Table II for the values of the meson and decay constants used in the numerical calculations).

6.2.2 Scattering Matrix and coupled-channel unitarity

The four meson amplitude $\mathcal{H}$ of Eq. (40) of Ref. [68] is used as kernel of the BSE, which is solved and renormalized for each YIJ (hypercharge, isospin and spin) sector[8] in the so called *on-shell* scheme [191], T^{YIJ} is given by

$$T^{YIJ}(s) = \frac{1}{1 - V^{YIJ}(s)\, G^{YIJ}(s)} V^{YIJ}(s). \tag{6.7}$$

where $V^{YIJ}(s)$ (a matrix in the coupled-channel space) stands for the projection of the scattering amplitude, $\mathcal{H}$, in the YIJ sector. The corresponding quantity in the present work is defined below by Eqs. (6.19), (6.20) and (6.21). $\sqrt{s}$ is the center or mass energy of the initial or final meson pair. $G^{YIJ}(s)$ is the loop function and it is diagonal in the coupled-channel space. Suppressing the indices, it is written for each channel as

$$G(s) = \bar{G}(s) + G((m_1 + m_2)^2). \tag{6.8}$$

The finite function $\bar{G}(s)$ can be found in Eq. (A9) of Ref. [218], and it displays the unitarity right-hand cut of the amplitude. On the other hand, the constant $G((m_1+m_2)^2)$ contains the logarithmic divergence. After renormalizing using the dimensional regularization scheme, one finds

$$\begin{aligned} & G(s = (m_1 + m_2)^2) \\ = \; & \frac{1}{16\pi^2} \left[a(\mu) + \frac{2}{m_1 + m_2} \left(m_1 \ln \frac{m_1}{\mu} + m_2 \ln \frac{m_2}{\mu} \right) \right], \end{aligned} \tag{6.9}$$

[8] Note that for the $Y = 0$ channels, G-parity is conserved. Thus in the $Y = 0$ sectors, the kernel amplitude becomes block-diagonal, with each block corresponding to odd and even G-parities.

where μ is the scale of the dimensional regularization. Changes in the scale are reabsorbed in the subtraction constant $a(\mu)$, so that the results remain scale independent. Any reasonable value for μ can be used. In Ref. [68] $\mu = 1\,\mathrm{GeV}$ was adopted and we take the same choice in the present work.

Poles, s_R, in the SRS of the corresponding BSE scattering amplitudes ($T^{YIJ}(s)$) determine the masses and widths of the dynamically generated resonances in each YIJ sector (namely $s_R = M_R^2 - \mathrm{i}\, M_R \Gamma_R$). In some cases, there appear real poles in the FRS of the amplitudes which correspond to bound states. Finally, the coupling constants of each resonance to the various meson-meson states (i, j indices) are obtained from the residues at the pole, by matching the BSE amplitudes to the expression

$$T_{ij}^{YIJ}(s) = \frac{g_i g_j}{s - s_R}\,, \tag{6.10}$$

for energy values $\sqrt{s}$ close to the pole. The couplings, g_i, are complex in general.

6.3 SU(6) symmetry breaking terms and chiral invariance

Regarding the spin symmetry breaking term of $\mathcal{L}_{\mathrm{SU(6)}}^{(m)}$ (the term with $\mathcal{M}'$ in Eq. (6.5)), it should be noted that there is a large ambiguity in choosing it. Being a contact term, it cannot contain $PPPP$ contributions, due to chiral symmetry, and for the same reason the terms $PPVV$ are also fixed, as already noted. However, $VVVV$ terms are not so constrained. One can easily propose alternative forms for $\mathcal{L}_{\mathrm{SU(6)}}^{(m)}$ which would still be acceptable from general requirements but would yield different $VVVV$ interactions. The choice in Eq. (6.5) is just the simplest or minimal one.

Let us consider the contact or ultra-local terms, i.e., involving no derivatives, that can be written down with the desired properties. These properties include hermiticity, C, P and T, invariance under rotations and chiral symmetry. Of course, spin-flavor cannot be maintained, as we want to give different masses to pseudoscalar and vector mesons.

In the absence of derivatives, the parity transformation is equivalent to $U_6 \to U_6^\dagger$, likewise, C implies $U_6 \to U_6^T$ (transposed), and time-reversal is $U_6 \to U_6$ but acting antilinearly. As it turns out, C and T invariances are automatically implied by the other symmetries if the coupling constants are real (o purely imaginary if ϵ_{ijk} is involved).[9]

Rotational invariance is ensured if the only tensors involved are Pauli matrices, as well as δ_{ij} and ϵ_{ijk}.

Under chiral transformations $U_6 \to \Omega_L^\dagger U_6 \Omega_R$, where $\Omega_{L,R}$ are matrices of SU(N_F), (so actually, they denote $2N_F \times 2N_F$ matrices of the form $\Omega_{L,R} \times I_{2\times 2}$). Vector invariance ($\Omega_L = \Omega_R$), the diagonal part of the chiral group, is automatic if the operators are constructed as traced products of U_6, $U_6^\dagger$ and $\boldsymbol{\sigma}$ that commutes with the flavor matrices $\Omega_{L,R}$. Note that the matrix $\mathcal{M}'$ in Eq. (6.5) must be a multiple of the identity if vector invariance is exactly enforced, as we do in this discussion. Finally, full chiral invariance requires that U_6 and $U_6^\dagger$ blocks should occupy alternate positions in the trace (cyclically), with Pauli matrices inserted in between.

A closer look shows that there should be at least one $\boldsymbol{\sigma}$ between consecutive U_6 and $U_6^\dagger$ (cyclically), and also no more than one $\boldsymbol{\sigma}$ is required due to the relation $\sigma_i\sigma_j = \delta_{ij} + \mathrm{i}\epsilon_{ijk}\sigma_k$. Therefore the total number of $\boldsymbol{\sigma}$ operators is even and so the number of ϵ_{ijk} is also even. This implies that no Levi-Civita tensor ϵ_{ijk} is needed, due to the identity

$$\begin{aligned}\epsilon_{ijk}\epsilon_{abc} &= \delta_{ia}\delta_{jb}\delta_{kc} + \delta_{ib}\delta_{jc}\delta_{ka} + \delta_{ic}\delta_{ja}\delta_{kb} \\ &\quad -\delta_{ia}\delta_{jc}\delta_{kb} - \delta_{ic}\delta_{jb}\delta_{ka} - \delta_{ib}\delta_{ja}\delta_{kc}. \end{aligned} \tag{6.11}$$

This leads us to the conclusion that the most general contact interaction with the required symmetries are traced products of blocks

$$\mathcal{U}_{ij} = \sigma_i U_6 \sigma_j U_6^\dagger, \tag{6.12}$$

that is, products of blocks $\mathrm{Tr}(\mathcal{U}_{ij}\mathcal{U}_{kl}\cdots)$, with the indices contracted in any order.

[9]Strictly speaking, we cannot invoke the CPT theorem, since our interaction is unitary and local but does not have full Lorentz invariance. Nevertheless, T turns out to be an automatic consequence of C and P, and the other assumptions (locality, unitarity and rotational invariance).

In principle, there is an infinite number of such interactions (although relations among them do appear if a concrete number of flavors, say $N_F = 3$, is assumed). Nevertheless, the interaction is not needed to all orders in the meson field Φ_6, rather only quadratic and quartic terms need to be retained.[10] Clearly, there is just a finite number of such $O(\Phi_6^2) + O(\Phi_6^4)$ chiral invariant terms, for the simple reason that only a finite number of quadratic plus quartic structures can be written down. Without assuming chiral symmetry there are 21 such generic structures (and only 18 if $N_F = 3$ is specifically assumed). Chiral symmetry imposes relations and reduces the number from 21 to 10 (9 if $N_F = 3$ is assumed). This is a rather large number of parameters. In order to reduce the problem to a more manageable size, we will consider here only terms with just a single trace (rather than products of them). We only mention that such restriction can be justified from large N_C arguments [219, 220]. The restriction to a single trace puts conditions on the possible mass terms for the vector mesons, specifically $\mathrm{Tr}(\Phi_6^2)$ and $\mathrm{Tr}((\sigma_i\Phi_6)^2)$ are allowed but $(\mathrm{Tr}(\sigma_i\Phi_6))^2$ is discarded. This implies that the ρ and ω mesons cannot be given different masses. Such degeneracy is very well satisfied experimentally and this gives some basis to our simplifying assumption.

If only terms with a single trace are retained, the number of possible quadratic plus quartic operators is 8, and just 3 combinations of them are chirally invariant. We show this in detail in Appendix D.1.

The three chiral invariant combinations can be obtained by expanding three independent operators of the type $\mathrm{Tr}(\mathcal{U}_{ij}\mathcal{U}_{kl}\cdots)$ to order Φ_4^4. Up to two $\mathcal{U}_{ij}$ blocks and a single trace, only three different operators can be written down, and they are sufficient for our purposes:

$$\begin{aligned} \mathcal{O}_1 &= \mathrm{Tr}(\mathcal{U}_{ii} - 3)\,, \\ \mathcal{O}_2 &= \mathrm{Tr}(\mathcal{U}_{ii}\mathcal{U}_{jj} - 9) + \mathrm{h.c.}, \\ \mathcal{O}_3 &= \mathrm{Tr}(\mathcal{U}_{ij}\mathcal{U}_{ij} + 3)\,. \end{aligned} \tag{6.13}$$

[10] Parity invariance, $\Phi_6 \to -\Phi_6$ implies that the interaction contains only terms with an even number of meson fields. Of course, this is would no longer be true if derivatives were allowed, since this would allow anomalous terms involving $\epsilon_{\mu\nu\alpha\beta}$ [108, 109].

Expanding in the fields, we find

$$\begin{aligned}
\mathcal{O}_1 &= \frac{3}{f^2}\mathrm{Tr}\bigg(-4\Phi_6^2+\frac{4}{3}\sigma_i\Phi_6\sigma_i\Phi_6\bigg) \\
&\quad +\frac{4}{f^4}\mathrm{Tr}\bigg(\Phi_6^4+\sigma_i\,\Phi_6^2\,\sigma_i\Phi_6^2-\frac{4}{3}\sigma_i\,\Phi_6\,\sigma_i\,\Phi_6^3\bigg) \\
&\quad +\mathcal{O}(\Phi_6^6)\,, \qquad (6.14)\\
\frac{\mathcal{O}_2-20\mathcal{O}_1}{12} &= \frac{16}{f^4}\mathrm{Tr}\bigg(\Phi_6^4+\frac{5}{6}\sigma_i\,\Phi_6^2\,\sigma_i\Phi_6^2-\frac{4}{3}\sigma_i\,\Phi_6\,\sigma_i\,\Phi_6^3 \\
&\quad +\frac{1}{6}\Phi_6\,\sigma_i\,\Phi_6\,\sigma_i\,\Phi_6\,\sigma_j\Phi_6\,\sigma_j \\
&\quad +\frac{1}{6}\mathrm{i}\epsilon_{ijk}\Phi_6^2\,\sigma_i\,\Phi_6\,\sigma_j\,\Phi_6\,\sigma_k\bigg)+\mathcal{O}(\Phi_6^6), \qquad (6.15)\\
\frac{\mathcal{O}_3}{3} &= \frac{16}{f^4}\mathrm{Tr}\bigg(\Phi_6^4-\frac{4}{3}\sigma_i\,\Phi_6\,\sigma_i\,\Phi_6^3+\frac{1}{3}\Phi_6\,\sigma_i\,\Phi_6\,\sigma_j\,\Phi_6\,\sigma_i\Phi_6\,\sigma_j \\
&\quad -\frac{2}{3}\mathrm{i}\epsilon_{ijk}\Phi_6^2\,\sigma_i\,\Phi_6\,\sigma_j\,\Phi_6\,\sigma_k\bigg)+\mathcal{O}(\Phi_6^6). \qquad (6.16)
\end{aligned}$$

These three operators are linearly independent. Moreover, we show in the Appendix D.1 that, up to order $\mathcal{O}(\Phi_6^4)$, any other operator arising from the set of chiral invariant Lagrangians $\mathrm{Tr}(\mathcal{U}_{ij}\mathcal{U}_{kl}\cdots)$ can be expressed as a linear combination of $\mathcal{O}_{1,2,3}$. This is one of the most important results of this work.

The coupling of the operator $\mathcal{O}_1$ has to be $f^2m_V^2/32$, to generate a proper mass term for the vector mesons. This implies

$$\mathcal{L}_1=\frac{f^2m_V^2}{32}\mathcal{O}_1=-\frac{1}{2}m_V^2\mathrm{Tr}\big(\Phi_V^2\big)+\mathcal{L}_{\mathrm{SU(6)}}^{(m;\,\mathrm{int})}+\mathcal{O}(\Phi_6^6)\,, \qquad (6.17)$$

with $\mathcal{L}_{\mathrm{SU(6)}}^{(m;\,\mathrm{int})}$ given in Eq. (6.6). However, a priori we cannot fix the couplings g_2 and g_3 of the operators $\mathcal{O}_2$ and $\mathcal{O}_3$, which were set arbitrarily to zero in Ref. [68]. Here, we aim to explore the physical consequences of keeping these two interaction terms finite. Thus, we will consider here an additional contact four meson interaction Lagrangian

$$\delta\mathcal{L}_{\mathrm{SU(6)}}^{(m;\,\mathrm{int})}=\frac{f^2m_V^2}{64}\left(\frac{g_2}{4\pi}\frac{\mathcal{O}_2-20\mathcal{O}_1}{12}+\frac{g_3}{4\pi}\frac{\mathcal{O}_3}{3}\right)\,. \qquad (6.18)$$

When the terms above are taken into account, the final S-wave four meson amplitude, $\mathcal{H}$ reads

$$\mathcal{H} = \mathcal{H}_0 + \delta\mathcal{H}\,, \tag{6.19}$$

$$\mathcal{H}_0 = \frac{1}{6f^2}\left(3s - \sum_{i=1}^{4} q_i^2\right)\mathcal{D}_{\rm kin} + \frac{m_V^2}{8f^2}\mathcal{D}_m + \frac{1}{2f^2}\frac{m_V^4}{s}\mathcal{D}_a\,, \tag{6.20}$$

$$\delta\mathcal{H} = \frac{m_V^2}{16\pi f^2}\left(g_2\mathcal{D}_2 + g_3\mathcal{D}_3\right)\,, \tag{6.21}$$

where $s = (q_1 + q_2)^2$ is the usual Mandesltam variable, with q_1 and q_2 (q_3 and q_4) the four-momenta of the initial (final) mesons. The first term, $\mathcal{H}_0$, coincides with the four meson amplitude used in Ref. [68] (see Eq. (40) of this reference) as kernel of the BSE.[11] The second term, $\delta\mathcal{H}$, is the new dynamical input. The physical consequences of this term will be studied in this work. The coupled-channel matrices $\mathcal{D}_{2,3}$ are obtained from the Lagrangian $\delta\mathcal{L}^{(m;\,\rm int)}_{\rm SU(6)}$ in Eq. (6.18), with the convention $-\mathrm{i}\,\delta\mathcal{H} = \mathrm{i}\delta\mathcal{L}^{(m;\,\rm int)}_{\rm SU(6)}$. These matrices are compiled in Appendix D.2. We have verified that the sets of matrices $\mathcal{D}_m$, $\mathcal{D}_2$ and $\mathcal{D}_3$ (computed for $N_F = 3$) are globally linearly independent. By inspection of these matrices, it can be checked that in the $J = 1$ sector, the new contribution $\delta\mathcal{H}$ vanishes provided $7g_2 + 12g_3 = 0$.

6.4 Results and Discussion

In this section, we will address the consequences of adding the amplitude $\delta\mathcal{H}$ to the kernel of the BSE, from a phenomenological point of view. To that end in each $YIGJ$ sector, we will compare the spectrum of resonances obtained from the pole structure of the renormalized BSE T-matrix in the FRS and SRS with the main properties of the meson states listed in the PDG [70]. To better isolate the effects of $\delta\mathcal{H}$, we will frequently refer also to the previous results obtained in Ref. [68].

The main obstacle to carry out the above program is the enormous freedom that a priori exists for fixing the subtraction constants. This

[11] The matrices $\mathcal{D}_{\rm kin}$, $\mathcal{D}_{\rm a}$ and $\mathcal{D}_{\rm m}$ are compiled in the Appendix A of [68].

is not only true for the present model, all schemes that restore unitarity suffer from the same problem [64, 65, 68, 182–200]. The origin of this freedom should be traced back to the renormalization procedure needed to render finite the unitarized amplitudes, that always involve a non-perturbative re-summation. Since all meson-meson theories are effective, their renormalization inescapably requires the introduction of new and undetermined low energy constants (rLECs). For the interaction of Goldstone bosons, these rLECs can be related to the low energy constants that appear in the higher order Lagrangian terms of the systematic chiral expansion [64, 65, 182–186, 189, 191–194], and in some cases, they might be constrained with other physical observables. However, no such systematic expansion exists when the involved bosons are vectors, and consequently, their related rLECs remain to a large extent unconstrained. Often, the unknown rLECs are tuned to best reproduce the physical properties of the resonances generated by the non-perturbative unitary re-summation.

In the renormalization scheme followed in [68], the rLECs are encoded by the subtraction constants $a(\mu)$ that appear in the expression of the renormalized loop function in Eq. (6.9). There is one such constant for each $YIGJ$ sector and for each channel of the associated coupled channels space. The $a(\mu)$ are free parameters prior to supplementing more detailed information from QCD. As said, the situation is similar in the rest of the approaches applied to the study of vector mesons. A practical solution to the impasse is found in the literature [68, 195–199], namely, for $\mu = 1\,\mathrm{GeV}$, the various $a(\mu)$ are fixed to values around -2. The $a(\mu)$'s are let to vary around the value -2 to best describe the known phenomenology in each $YIGJ$ sector. This default value of -2 is suggested from analysis where an ultraviolet (UV) hard cutoff Λ is used to renormalize the loop function, instead of dimensional regularization. The relation between the subtraction constant $a(\mu)$ at the scale μ and Λ is

$$\begin{aligned} a(\mu) &= -\frac{2}{m_1+m_2}\left\{ m_1 \ln\left[\frac{\Lambda+\sqrt{\Lambda^2+m_1^2}}{\mu}\right]\right. \\ &\left. +m_2 \ln\left[\frac{\Lambda+\sqrt{\Lambda^2+m_2^2}}{\mu}\right]\right\}. \end{aligned} \tag{6.22}$$

For $\mu \sim 1\,\mathrm{GeV}$, and assuming a cutoff of the same order of magnitude, -2 turns out to be a natural choice for the subtraction constant $a(\mu)$.

The idea behind the above choice for the range of variation of the rLECs is to focus on the resonances whose dynamics is mostly determined by the unitarity loops. A clear example of one such resonance is the $f_0(500)$, that is dynamically generated from $\pi\pi$ re-scattering with a cutoff value of the order of 700 MeV [187]. This translates to $a(\mu = 1\,\mathrm{GeV}) \sim -0.7$. However, to similarly describe the ρ-meson, purely from $\pi\pi$ re-scattering, requires $a(\mu = 1\,\mathrm{GeV}) \sim -12$ [65, 191]. This would lead to unnatural values for the UV cutoff, of the order of 200 GeV (note the logarithmic dependence). Actually, the ρ-meson is rather insensitive to the chiral loops and its dynamics is mostly determined by the low energy constants that appear in the $\mathcal{O}(p^4)$ chiral Lagrangian [205].

In our scheme, the mesons of the ρ-nonet, used to build the coupled channels space, are *preexisting states* (to adopt the terminology of [190]), rather than dynamically generated from the re-scattering of Goldstone bosons. In this view, it looks appropriated to restrict the rLECs to values that could be related to reasonable values of the UV cutoff. Specifically, Λ will be allowed to lie in the interval $[0.5, 5]\,\mathrm{GeV}$. Even after this constraint, there is still a large freedom in varying all different rLECs.

Another ambiguity in the model needs to be fixed, namely, the values of the two new couplings g_2 and g_3 in Eq. (6.21), which are totally undetermined yet. To be practical, we introduce here a further simplification by imposing the relation

$$g_2 = -\frac{12}{7} g_3. \tag{6.23}$$

This relation between g_2 and g_3 guarantees the $J = 1$ sectors are not affected by the new amplitude $\delta\mathcal{H}$. Note that in the $J = 1$ sector, the $PV \to PV$ terms are constrained by chiral symmetry and that in the previous analysis of Ref. [68], where $\delta\mathcal{H}$ was neglected, this sector was quite successfully described. Among other, the $\left[I^G(J^{PC})\right]$ $0^-(1^{+-})$ $h_1(1170)$, $h_1(1380)$ and $h_1(1595)$, the $1^+(1^{+-})$ $b_1(1235)$, the $1^-(1^{+-})$ $a_1(1260)$ and $a_1(1640)$ resonances were dynamically generated. Furthermore, the double pole structure of the $I(J^P) = \frac{1}{2}(1^+)$ $K_1(1270)$

resonance, firstly uncovered in [195, 196], was strongly confirmed in Ref. [68], as well.

Assuming natural values for g_3, we have let this coupling vary in the interval $[-25, 25]$. For each value of g_3, we have looked at the different YIG sectors for $J = 0$ and $J = 2$, and have examined the pattern of generated resonances, when the rLECs $a(\mu)$'s are left to vary in each particle–channel in the numerical range associated to UV cutoffs comprised in the interval $[0.5, 5]$ GeV. We find that, in general, the $J = 0$ sectors are not much affected by the new couplings. Simultaneously, values of $|g_3| \leq 0.25$ yield a definitely better description of the main features of the PDG $J^P = 2^+$ low-lying resonances than that achieved in Ref. [68]. Specifically, in the results to be presented below we have taken

$$\frac{g_3 m_V^2}{16\pi f^2} = 0.1 \ . \tag{6.24}$$

For this value of g_3, a quite good overall description of the different $J = 0, 2$ sectors is obtained. Small variations around this value, keeping $|g_3| \leq 0.25$, can be compensated by the rLECs leading to descriptions of similar quality.

The value of the new coupling is relatively small. A tentative argument can be advanced to explain why such small value was to be expected. In the heavy quark limit, QCD shows an approximate spin-symmetry [66, 67, 181] that requires the spin symmetry breaking terms to be suppressed by at least one power of the heavy quark mass. Since the operators to which g_3 couples ought to be suppressed in a hypothetical large m_V limit, the natural combination $g_3 m_V^2/(16\pi f^2)$ that appears in the Lagrangian should be of order $\Lambda_{\rm QCD}/m_V$, or $g_3 \sim \mathcal{O}((\Lambda_{\rm QCD}/m_V)^3)$, with $\Lambda_{\rm QCD} \sim 250\,{\rm MeV}$ standing for some energy scale relevant in the problem, in addition to the averaged vector mass.

In what follows, we will present and discuss the results that we have found in the various $YIGJ$ sectors.

6.4.1 Hypercharge 0, isospin 0 and spin 0

In this sector we find four poles. Their positions and couplings are compiled in Table 6.1, where we have also collected the pole positions found in our previous work of Ref. [68]. Masses and widths listed in

Table 6.1: Pole positions (in MeV) and moduli of the couplings $|g|$ (in GeV) in the $(Y, I, J) = (0, 0, 0)$ sector that corresponds to the $I^G(J^{PC}) = 0^+(0^{++})$ quantum numbers. The subtraction constant has been set to the default values $a = -2.0$ in all channels. We also compile the results obtained in Ref. [68], where $\delta\mathcal{H}$ was set to zero, and the available information in the PDG on masses and widths (in MeV) of the possible counterparts. The channels open for decay have been highlighted in boldface.

(M_R, Γ_R)	$(631, 406)$	$(969, 0)$	$(1365, 124)$	$(1729, 104)$
$\pi\pi$	**3.54**	**0.03**	**0.53**	**0.04**
$\bar{K}K$	0.38	2.49	**3.26**	**0.83**
$\eta\eta$	0.38	2.06	**0.82**	**3.16**
$\rho\rho$	8.17	2.96	1.27	**0.32**
$\omega\omega$	8.29	2.12	2.74	**0.39**
$\omega\phi$	0.11	1.42	7.12	3.27
$\bar{K}^*K^*$	7.72	3.34	10.54	2.38
$\phi\phi$	1.94	3.01	10.33	13.66
(M_R, Γ_R) [68]	$(602, 426)$	$(969, 0)$	$(1349, 124)$	$(1722, 104)$
PDG (M_R, Γ_R) [70]	$f_0(500)$ $(400 \sim 550,$ $400 \sim 700)$	$f_0(980)$ $(990 \pm 20,$ $40 \sim 100)$	$f_0(1370)$ $(1200 \sim 1500,$ $200 \sim 500)$	$f_0(1710)$ $(1720 \pm 6,$ $135 \pm 8)$

the PDG [70] of the possible resonances that could be identified with these states are also given in the table. As anticipated, the inclusion of $\delta\mathcal{H}$ in the present work has very little effect and the present results are qualitatively similar to those already obtained in [68]. We refer to that work for further details and grounds on the identification proposed in Table 6.1. Very briefly, the lowest two poles can be easily identified with the $f_0(600)$ and $f_0(980)$ resonances. There are some differences with other works [189, 193] mainly because we have neglected the pseudoscalar meson mass terms and have included vector meson-vector meson channels. The identification of the other two poles is less direct, though it is quite reasonable to associate them to the $f_0(1370)$, and $f_0(1710)$ resonances, as it is argumented in [68]. On the other hand, the $I^G = 0^+(J^{PC} = 0^{++})$ $f_0(1500)$ resonance cannot be accom-

modated within this scheme and thus it would be a clear candidate to be a glueball or a hybrid.

A final remark concerns the $f_0(500)$, in the most recent update of the PDG [70], the traditionally large range of values for the $f_0(500)$ mass (previously called $f_0(600)$ or σ) has been considerably shrunk, thanks to the consideration of recent determinations of the position of this pole obtained in dispersive approaches [221, 222]. As can be seen in Table 6.1, now the mass of the σ lies in the interval $400 - 550\,\text{MeV}$. The scheme presented here easily accommodates masses for the σ of the order of 500 MeV, just by slightly modifying the subtraction constants (rLECs). Note that for a better comparison with our previous work of Ref. [68], in Table 6.1, all subtraction constants have been set to the default values $a = -2.0$, as in this latter reference. However, using instead -2.3 for the PP channels and -1.1 for the VV ones, we find that M_R is about 500 MeV and 992 MeV for the $f_0(500)$ and $f_0(980)$ poles, respectively, in much better agreement with the masses listed for these resonances in the last edition of the PDG. The positions of the other two poles placed at higher energies are not significantly changed, thus our qualitative discussion of this sector remains unchanged.

6.4.2 Hypercharge 0, isospin 0 and spin 2

In this sector, we find two poles in the SRS/FRS of our amplitudes (see Table 6.2). We fine-tune a common value of the rLECs to obtain a mass for the first state (bound) in the vicinity of that quoted in the PDG for the $f_2(1270)$. Having fixed the rLECs, we find a second pole located at $(1658, 74)\,\text{MeV}$, with mass and width close to those of the $f_2(1640)$ resonance. Moreover, this second pole has large couplings to the $\rho\rho$, $\bar{K}^*K^*$ and $\omega\omega$ channels, which will naturally account for the seen decay modes of the $f_2(1640)$ resonance into $\omega\omega$ and also into $\bar{K}K$ and $\pi\pi\pi\pi$ through loop mechanisms, like those depicted in Fig. 6.1.

These loops mechanisms might also provide a sizable width to the first pole that we have identified with the $f_2(1270)$ resonance. Indeed, this resonance is quite broad ($\Gamma \sim 185\,\text{MeV}$) while in our case, it appears as a bound state (pole in the FRS) of zero width. Besides, there exist other mechanisms like d-wave $\pi\pi$ decays, which could also be important in this case because the large available phase space. Note

Table 6.2: Same as in Table 6.1, but for the $(Y, I, J) = (0, 0, 2)$ sector that corresponds to the $I^G(J^{PC}) = 0^+(2^{++})$ quantum numbers. The subtraction constant has been set to $a = -3.88$ in all channels.

(M_R, Γ_R)	$(1279, 0)$	$(1658, 74)$
$\rho\rho$	4.40	**3.56**
$\omega\omega$	4.08	**1.74**
$\omega\phi$	1.74	2.24
$\bar{K}^*K^*$	4.08	5.58
$\phi\phi$	10.20	4.21
(M_R, Γ_R) [68]	$(1289, 0)$	$(1783, 38)$
PDG	$f_2(1270)$	$f_2(1640)$
(M_R, Γ_R) [70]	$(1275.1 \pm 1.2, 185.1^{+2.9}_{-2.4})$	$(1639 \pm 6, 99^{+60}_{-40})$

that the $\bar{K}K$ decay mode ($\sim$4.5%) quoted in the PDG for the $f_2(1270)$ resonance can be easily accommodated in our scheme thanks to the large couplings of our state to the $\bar{K}^*K^*$ and $\phi\phi$ channels.

In the hidden gauge model of Ref. [199] two states were also generated in this sector, whose masses agree remarkably well with those of the $f_2(1270)$ and $f_2'(1525)$ resonances.[12] There, these two resonances appear mostly as $\rho\rho$ and $\bar{K}^*K^*$ bound states, respectively. In our case these channels are still dominant but with a substantial contribution from the sub-dominant channels. (An exception comes from $\phi\phi$, with a sizable coupling but a relatively high threshold.) The presence of relatively important subdominant channels prevents us from identifying the second pole obtained in our approach with the $f_2'(1525)$ resonance. This is because this resonance has the distinctive feature of having a very small branching fraction into the $\pi\pi$ channel ($\sim$ 0.8%) what seems hard to accommodate with the sizable $\rho\rho$ coupling of our state. On the other hand, the $\bar{K}K$ mode, that we expect to be dominant for our second state, has not been seen in the decays of $f_2(1565)$ and $f_2(1810)$ resonances. This finally brings us to identify our second pole in Table 6.2 with the $f_2(1640)$ resonance.

[12] Thanks to a suitable fine-tuning of the subtraction constants.

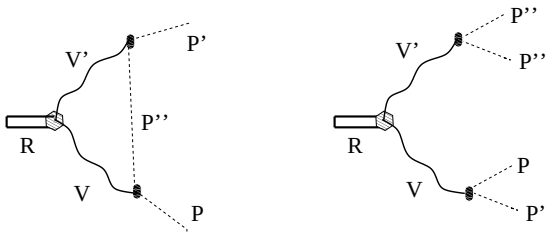

Figure 6.1: Resonance (R) decay to two (left) or four (right) pseudoscalar mesons (P, P', P'', P''') through its s-wave (filled pattern hexagon) coupling to two vector mesons (V,V') and the p-wave coupling (black ovals) of these latter mesons to two pseudoscalar mesons.

A final remark is in order here. In our previous analysis carried out in Ref. [68], we also found two poles and made the same identifications as here. However in that work, we could not fine tune the subtraction constants to obtain masses for the second state below 1.75 GeV. Thanks to the consideration of $\delta\mathcal{H}$ in the present analysis we have been able to predict two resonances with the appropriate masses to be identified with the $f_2(1270)$ and $f_2(1640)$ states. Nevertheless to achieve this, we have needed to use values of the subtraction constant of around -3.9. This in turn implies large UV cutoff values of around 3.5 GeV, somehow in the limit of what one would expect for resonances dynamically generated by the unitarity loops driven by the LO potential. These large UV cutoffs might signal some resemblance between the nature of these states and that of the so called *preexisting states*, like the ρ meson, for which higher order corrections (not driven by unitarity) in the potential play an important role in their dynamics [205].

6.4.3 Hypercharge 0, isospin 1 and spin 0

There are five coupled channels in this sector: $\pi\eta$, $\bar{K}K$, $\rho\omega$, $\rho\phi$ and $\bar{K}^*K^*$ and we now find two poles in the SRS of the amplitudes. Our results are compiled in Table 6.3. The lowest pole should be identified with the $a_0(980)$, which has been obtained in all previous studies considering only pseudoscalar-pseudoscalar coupled channels. In our

Table 6.3: Same as in Table 6.1, but for the $(Y, I, J) = (0, 1, 0)$ sector that corresponds to the $I^G(J^{PC}) = 1^-(0^{++})$ quantum numbers. The subtraction constants have been fixed to $a = -3.5$ in the PP channels and to $a = -2.16$ in the VV channels.

(M_R, Γ_R)	$(970, 90)$	$(1493, 86)$	
$\eta\pi$	**2.67**	**1.68**	
$\bar{K}K$	2.82	**2.26**	
$\omega\rho$	7.33	2.04	
$\phi\rho$	2.62	8.24	
$\bar{K}^*K^*$	0.09	8.08	
(M_R, Γ_R) [68]	$(990, 92)$	$(1442, 10)$	$(1760, 24)$
PDG (M_R, Γ_R) [70]	$a_0(980)$ $(980 \pm 20,$ $50 \sim 100)$	$a_0(1450)$ $(1474 \pm 19,$ $265 \pm 13)$	

scheme, its couplings to the $\pi\eta$ and $K\bar{K}$ are large, in agreement with the results of earlier studies and with the data, but it also presents large couplings to the heaviest vector channels, $\omega\rho$ and $\phi\rho$. When comparing to the results of Ref. [68], we see that the couplings of this resonance to vector channels have drastically changed, though these heavier channels have little influence on the position of this lowest pole and on its allowed decay modes.

The pole at $(M_R, \Gamma_R) = (1493, 86)\,\text{MeV}$ can be naturally associated to the $a_0(1450)$ and its main features are similar to those found in [68]. It decays to $\pi\eta$ and $K\bar{K}$, which is in agreement with the data. Its large couplings to the vector channels, whose thresholds are now closer, will give rise to new significant $\omega\pi\pi$ and $\bar{K}K\pi\pi$ decay modes, and to an important enhancement of its width thanks to the broad spectral functions of the ρ and K^* resonances.

Finally, as can be seen in the table, in our previous analysis of Ref. [68], we found a third pole, located at $(M_R, \Gamma_R) = (1760, 24)\,\text{MeV}$, and whose dynamics was mostly dominated by the vector channels. This further state could not be associated to any known state, since the PDG only reports two a_0 resonances below 2 GeV. Nevertheless, in

Ref. [68] we suggested with some cautions that this third pole, though placed quite below, might be identified with the very broad $a_0(2020)$ resonance ($\Gamma = 330 \pm 75\,\text{MeV}$). This latter resonance is not firmly established at all, and needs further confirmation. (Indeed, it appears in the section of *Further states* of the PDG.) In the present re-analysis, where the new spin symmetry breaking terms contained in $\delta\mathcal{H}$ have been included, this state is no longer dynamically generated.

6.4.4 Hypercharge 0, isospin 1 and spin 2

Table 6.4: Same as in Table 6.1, but for the $(Y, I, J) = (0, 1, 2)$ sector that corresponds to the $I^G(J^{PC}) = 1^-(2^{++})$ quantum numbers. The subtraction constant has been set to $a = -3.88$ in all channels.

(M_R, Γ_R)	$(1319, 0)$	$(1747, 12)$
$\omega\rho$	8.41	**1.55**
$\phi\rho$	1.92	3.48
$\bar{K}^*K^*$	5.32	4.82
(M_R, Γ_R) [68]	$(1228, 0)$	$(1775, 12)$
PDG	$a_2(1320)$	$a_2(1700)$
(M_R, Γ_R) [70]	$(1318.3^{+0.5}_{-0.6}, 107 \pm 5)$	$(1732 \pm 16, 194 \pm 40)$

There are three coupled channels in this sector: $\bar{K}^*K^*$, $\omega\rho$, and $\phi\rho$, and we find two poles, one in the FRS and the other one in the SRS of the amplitudes (see Table 6.4), which might be associated to the $a_2(1320)$ and $a_2(1700)$ resonances. The first state, bound in our model, couples strongly to the $\omega\rho$ channel, and its couplings would give rise to the observed $\pi\pi\pi$ and $\omega\pi\pi$ decay modes of the $a_2(1320)$ thanks to the width of the virtual ρ meson. In our previous analysis [68], we could not place the mass of this state above 1230 MeV, despite we tried some fine-tuning of the subtraction constants. Thus here, as it was also the case in the $(Y, I, J) = (0, 0, 2)$ sector, we find a better overall description of the sector thanks to the inclusion of the $\delta\mathcal{H}$ terms.

The $a_2(1320)$ resonance is not dynamically generated in the hidden gauge model of Ref. [199], though there it is reported one state whose

features are similar to those of the second (heaviest) pole found here. This second pole might be associated to the $a_2(1700)$, since its mass and expected decays into $\omega\rho$, $\omega\pi^-\pi^0$ and $K\bar{K}$ (from the decays into virtual $\phi\rho$ or $K^*\bar{K}^*$ pairs) are in good agreement with the information listed in the PDG for the $a_2(1700)$ resonance. However, the state predicted here, as it was the case in Refs. [68, 199] turns out to be much narrower than this resonance. This is probably an indication that other mechanisms, such as coupled-channel d-wave dynamics, might play an important role in this case. Nevertheless, there exists a large uncertainty in the experimental status of the $a_2(1700)$.

Finally, we should point out here that in this sector, we have also needed to make use of large UV cutoffs ($\sim 3.5\,\mathrm{GeV}$), somehow in the limit of what one would expect for resonances dynamically generated by the unitarity loops driven by the LO potential.

6.4.5 Hypercharge 1, isospin 1/2 and spin 0

In this sector we find three poles, with positions and couplings compiled in Table 6.5. There we have also collected the pole positions found in our previous work of Ref. [68]. Masses and widths listed in the PDG [70] of the possible resonances that could be identified with these states are also given in the table. As in the $(Y, I, J) = (0, 0, 0)$ sector, the inclusion of $\delta\mathcal{H}$ in the present work has very little effect, and the present results are quite similar to those already obtained in [68]. Again, we refer to that work for further details and grounds on the identification proposed in Table 6.5. Very briefly, it looks quite natural to identify the first two poles with the PDG $K_0^*(800)$ and $K_0^*(1430)$ states, in spite of being the latter one much wider than the pole found in our scheme. The $K\pi$ branching fraction for this resonance is $93\% \pm 10\%$. For our pole at $1425\,\mathrm{MeV}$, the direct coupling to $K\pi$ is not so dominant over the other open channel, ηK. However, the couplings to the closed channels $K^*\rho$, $K^*\omega$, $K^*\phi$ channels are much larger. As a consequence, the resonance can decay into a virtual $K^*\rho$ pair and significantly enhance the $K\pi$ decay probability, through the loop mechanism depicted in the left panel of Fig. 6.1, thanks to the broad ρ and K^* spectral functions.

The identification of the third pole with the broad $K_0^*(1950)$ resonance is less straightforward. Nevertheless, it should be pointed out

that the $K_0^*(1950)$ resonance is not firmly established yet and needs further confirmation [70].

A final comment is related with the employed UV cutoffs in this sector. Those turn out to be of the order of 1 GeV in this case, as it was also the case in the $(Y, I, J) = (0, 0, 0)$ sector, indicating that the dynamics of the resonances in both sectors are mostly governed by the logs that appear in the unitarity loops. This naturally explains why, for instance, the $K_0^*(800)$ is so wide, since it is placed well above the relevant threshold $K\pi$. Indeed, this resonance is very similar to the $f_0(500)$, and it cannot be interpreted as a Breit-Wigner narrow resonance.

Table 6.5: Same as in Table 6.1, but for the $(Y, I, J) = (1, 1/2, 0)$ sector that corresponds to the $I(J^P) = \frac{1}{2}(0^+)$ quantum numbers. The subtraction constant has been set to $a = -1.52$ in all channels. The assignment of the third pole to the $K_0^*(1950)$ resonance is uncertain.

(M_R, Γ_R)	$(816, 434)$	$(1425, 54)$	$(1782, 90)$
$K\pi$	**4.83**	**1.91**	**0.06**
ηK	2.20	**1.02**	**2.92**
$K^*\rho$	6.29	8.11	**0.68**
$K^*\omega$	2.29	10.69	**1.07**
$K^*\phi$	2.15	5.70	12.21
(M_R, Γ_R) [68]	$(812, 347)$	$(1428, 48)$	$(1787, 74)$
PDG (M_R, Γ_R) [70]	$K_0^*(800)$ $(682 \pm 29,$ $547 \pm 24)$	$K_0^*(1430)$ $(1425 \pm 50,$ $270 \pm 80)$	$K_0^*(1950)$ $(1945 \pm 22,$ $201 \pm 90)$

6.4.6 Hypercharge 1, isospin 1/2 and spin 2

In this sector (Table 6.6), we find two poles in the FRS/SRS of the amplitudes. In the PDG, two K_2^* resonances [$K_2^*(1430)$ and $K_2^*(1980)$] are reported below 2 GeV [70], though only the lightest one is firmly established. In the analysis of Ref. [68] just one state was found, and moreover, the subtraction constants could not be fine-tuned to bring its

Table 6.6: Same as in Table 6.1, but for the $(Y, I, J) = (1, 1/2, 2)$ sector that corresponds to the $I(J^P) = \frac{1}{2}(2^+)$ quantum numbers. The subtraction constant has been set to $a = -4.32$ in all channels. The assignment of the second pole to the $K_2^*(1980)$ resonance is uncertain.

(M_R, Γ_R)	$(1430, 0)$	$(1624, 0)$
$K^*\rho$	6.30	6.21
$K^*\omega$	4.23	0.39
$K^*\phi$	6.81	2.88
(M_R, Γ_R) [68]	$(1701, 313)$	
PDG	$K_2^*(1430)$	$K_2^*(1980)$
(M_R, Γ_R) [70]	$(1429 \pm 4, 104 \pm 6)$	$(1973 \pm 26, 373 \pm 70)$

mass below 1.7 GeV. The consideration of $\delta\mathcal{H}$ in the current approach overcomes this problem, and it allows to generate a pole in the region of 1430 MeV. According to the PDG, the $K_2^*(1430)$ has a width of 104 ± 6 MeV, in our approach we find a bound state, located below all the thresholds. The PDG branching fractions are around 50%, 25%, 9% and 3% for the D-wave modes $K\pi$, $K^*\pi$, $K\rho$ and $K\omega$, respectively. In addition, the branching fraction of the $K^*\pi\pi$ channel is only about 13%. Certainly, these modes can be also originated from the decay of the resonance to $K^*\rho$, $K^*\omega$ and $K^*\phi$ virtual pairs. In particular, we expect the $K^*\rho$ channel to play an important role, because of the broad spectral functions of both the K^* and ρ mesons and its proximity to the mass of the resonance, since it can trigger a significant part of the observed $K_2^*(1430)$ decays into $K\pi$ and $K^*\pi\pi$ (see Fig. 6.1). Note that the large $K^*\phi$ coupling also provides a contribution to the dominant $K\pi$ mode.

We should note, however, that we need to use values of the subtraction constants that amount to UV cutoffs above 4 GeV, which put some doubts on the real nature of this state, as we discussed in (Y, I, J) =(0,0,2) and (0,1,2) sectors. It might be the case that large UV cutoffs are needed to compensate the genuine (non resonant driven) D-wave channels ignored in the present coupled channels approach. In particular, in Ref. [68] it was already pointed out the possible influ-

ence of the D-wave pseudoscalar-vector meson $K^*\pi$ channel, which lies closer to the resonance mass than the pseudoscalar-pseudoscalar channels.

The hidden gauge approach of Ref. [199] for $VV \to VV$ scattering produces a resonance in this sector, with mass fine-tuned to 1430 MeV, and properties quite similar to those found here. There, all D-wave type interactions were also ignored.

On the other hand, little is known about the $K_2^*(1980)$, and the assignment of our second pole to this resonance is clearly uncertain. (Note that in Ref. [68], a second pole was not generated in this sector.) The large width of this state ($\Gamma \sim 400$) makes less meaningful the difference between its mass and that of our pole, which might be then associated to this resonance. Still, it should be noted again that the $K_2^*(1980)$ resonance is not yet firmly established and needs further confirmation. It might well happen that the pole obtained here corresponds to a different state not yet detected.

6.4.7 Exotics

Table 6.7: Same as in Table 6.1, but for the $(Y, I, J) = (0, 2, 0)$ sector that corresponds to the exotic $I^G(J^{PC}) = 2^+(0^{++})$ quantum numbers. The subtraction constant has been set to $a = -1.51$ in all channels.

(M_R, Γ_R)	$(1420, 110)$
$\pi\pi$	**2.74**
$\rho\rho$	9.99
(M_R, Γ_R) [68]	$(1418, 108)$
PDG	$X(1420)$
(M_R, Γ_R) [70]	$(1420 \pm 20, 160 \pm 10)$

Exotics refers here to meson states with quantum numbers that cannot be formed by a $q\bar{q}$ pair. Quantum numbers with $I > 1$ or $|Y| > 1$ are exotic.

Besides the exotic poles with $J = 1$ in the sectors $(Y = 1, I = 3/2)$ and $(Y = 2, I = 0)$ already reported in Ref. [68], we find another

three exotic states with $J = 0$ in region $1.4 - 1.6\,\text{GeV}$. Their positions and couplings are compiled in Tables 6.7, 6.8 and 6.9. In these tables, we have also collected the pole positions found in Ref. [68]. These scalar exotic states appear in the sectors $(Y = 0, I = 2)$, $(Y = 1, I = 3/2)$ and $(Y = 2, I = 1)$. As already pointed out in Ref. [68], the matrices $\mathcal{D}_{\text{kin}}$ and $\mathcal{D}_m$ in Eq. (6.20) are identical in the three sectors. The analogous statement holds for the new interactions $\mathcal{D}_2$ and $\mathcal{D}_3$ (Eq. (6.21)). Thus, clearly the three spin zero exotic states are just related by flavor rotations.

Table 6.8: Same as in Table 6.1, but for the $(Y, I, J) = (1, 3/2, 0)$ sector that corresponds to the exotic $I(J^P) = \frac{3}{2}(0^+)$ quantum numbers. The subtraction constant has been set to $a = -2.0$ in all channels.

(M_R, Γ_R)	$(1438, 140)$
$K\pi$	**3.26**
$K^*\rho$	10.86
(M_R, Γ_R) [68]	$(1431, 140)$

As in the $(Y, I, J) = (0, 0, 0)$ and $(Y, I, J) = (1, 1/2, 0)$ sectors, the inclusion of $\delta\mathcal{H}$ in the present work has very little effect and the present results are quite similar (practically identical) to those already obtained in [68]. We refer to that work for further details as well as for an overall picture of the poles with exotic quantum numbers predicted for this SU(6) extension of the WT Lagrangian. In short, there is only state listed in the PDG that can be associated with the exotic resonances predicted by our model. This is the $X(1420)$ resonance, but it needs further confirmation and its current evidence comes from a statistical indication [223] for a $\pi^+\pi^+$ resonant state in the $\bar{n}p \to \pi^+\pi^+\pi^-$ annihilation reaction with data collected by the OBELIX experiment. In our model, the pole is mainly a $\rho\rho$ bound state with a small coupling to the $\pi\pi$ channel that moves the pole to the SRS. Within our scheme, the $\rho\rho \to \rho\rho$ amplitude is totally symmetric under $I \leftrightarrow J$ exchange. As a consequence our $\rho\rho$ potential in this sector $(I = 2, J = 0)$ is the same as that in the $I = 0, J = 2$ one. BSE amplitudes in both sectors will become different because of coupled-channel and renormalization

effects. Nevertheless, we expect the $X(1420)$ to be the counterpart of the $f_2(1270)$, which appeared with a large $\rho\rho$ spin two isoscalar component. As mentioned, the other two spin zero exotic states in the $(Y = 1, I = 3/2)$ and $(Y = 2, I = 1)$ sectors should be related to $X(1420)$ by a flavor rotation. However, there is no experimental evidence of their existence yet.

Table 6.9: Same as in Table 6.1, but for the $(Y, I, J) = (2, 1, 0)$ sector that corresponds to the exotic $I(J^P) = 1(0^+)$ quantum numbers. The subtraction constant has been set to $a = -2.0$ in all channels.

(M_R, Γ_R)	$(1568, 132)$
$\bar{K}K$	**3.50**
$\bar{K^*}K^*$	11.49
(M_R, Γ_R) [68]	$(1563, 132)$

Finally, we just mention that the $\mathcal{D}_{\rm kin}$, $\mathcal{D}_m$, $\mathcal{D}_2$ and $\mathcal{D}_3$ matrices are identical in the three sectors $(Y, I, J) = (0, 2, 2), (1, 3/2, 2)$ and $(2, 1, 2)$. They provide a repulsive interaction and hence no resonance is predicted in those exotic sectors by our model.

6.5 Summary

We have reviewed the model presented in Ref. [68] to address the dynamics of the low-lying even parity meson resonances. It is based on a spin-flavor extension of the chiral WT Lagrangian, which is then used to study the S-wave meson-meson interaction involving members not only of the π-octet, but also of the ρ-nonet. Elastic unitarity in coupled channels is restored by solving a renormalized coupled channels BSE, and a certain pattern of SU(6) spin–flavor symmetry breaking is implemented. The model probed to be phenomenologically successful in the $J^P = 0^+$ and 1^+ sectors. Actually in [68], it was shown that most of the low-lying even parity PDG meson resonances in these two spin sectors could be classified according to multiplets of SU(6). However the scheme of Ref. [68] is not so successful for the sectors with

spin 2. It fails to appropriately describe some well established $J^P = 2^+$ resonances, like the $K_2^*(1430)$, that in the hidden gauge formalism for vector mesons used in Ref. [199] are dynamically generated in a natural manner. In this work, we have improved on that by supplementing the model of Ref. [68] with new local VV interactions consistent with CS.

To provide different pseudoscalar and vector mesons masses, a simple spin-symmetry breaking local term that preserved CS was designed in [68]. Here, we have studied in detail the structure of the SU(6) symmetry breaking local terms that respect (or softly break) CS. Thus, in this work, we have derived the most general contact terms consistent with the chiral symmetry breaking pattern of QCD as expressed in terms of the field U. We have also shown that there is a finite number of chirally invariant contact four meson-field interactions, restricted also by the other symmetries of the problem. To reduce the number of parameters to a manageable size, and in the spirit of large N_C, we have restricted our analysis to interactions involving just one trace.

Further, we have carried out a phenomenological discussion of the effects of these new terms. We find that their inclusion leads to a considerable improvement of the description of the $J^P = 2^+$ sector, without spoiling the main features of the predictions obtained in Ref. [68] for the $J^P = 0^+$ and $J^P = 1^+$ sectors. In particular, we have found a significantly better description of the $I^G(J^{PC}) = 0^+(2^{++})$, $1^-(2^{++})$ and the $I(J^P) = \frac{1}{2}(2^+)$ sectors, that correspond to the $f_2(1270)$, $a_2(1320)$ and $K_2^*(1430)$ quantum numbers, respectively. Besides the position of the resonances, we also estimate the couplings of those resonances to the different channels, which is relevant to describe the state structure and its favored decay modes. Our analysis shows that 2^+ states systematically require cutoff values which lie in the boundary of their natural hadronic domain. This could be an indication that D-wave mechanisms play some role in the formation of such states. The fact that, in many cases, the thresholds of the main channels are not too close to the resonance position, also suggests that pure S-wave interactions would not necessarily saturate the formation mechanisms of those resonances. Of course, for some particular mesonic resonances, it could also be the case that they are mostly genuine rather than dynamically generated. With this possible caveat in mind, we can say that the model produces a rather robust and successful scheme to study the low-lying even par-

ity resonances that are dynamically generated by the logs that appear in the unitarity loops.

Chapter 7

Theoretical study of the $\gamma N \to K\Lambda(1520)$ reaction

7.1 Introduction

Nucleon excited states below 2.0 GeV have been extensively studied, from both the experimental and the theoretical points of view [70]. However, the current knowledge on the properties of states around or above 2.0 GeV is still in its infancy [70]. On the other hand, in this region of energies, many theoretical predicted *missing* N^* *states*, within the constituent quark [71] or chiral unitary [72–76] approaches, have so far not been observed. The associated strangeness production reaction $\gamma p \to K^+\Lambda(1520)$ might be adequate to study the N^* resonances around 2.0 GeV, as long as they have significant couplings to the $K\Lambda(1520)$ pair, and could shed light on the complicated dynamics that governs the highly excited nucleon (or in general baryon) spectrum. In addition, a thorough and dedicated study of the strangeness production mechanism in this reaction has the potential to achieve a deeper understanding of the interaction among strange hadrons and, also, of the nature of the baryon resonances.

There were pioneering measurements at Cornell [224] and CEA [225], and in the 1970s, the first $\gamma p \to K^+\Lambda(1520)$ cross sections in the high-energy region $E_\gamma = 11$ GeV (SLAC [226]), and in the range 2.8-4.8 GeV (LAMP2 Collaboration [227]) were reported. In 2001, the CLAS Collaboration investigated this process in electroproduction [228], at

electron beam energies of 4.05, 4.25, and 4.46 GeV, in the kinematic region spanning the squared momentum transfer Q^2 from 0.9 to 2.4 GeV^2, and for invariant masses from 1.95 to 2.65 GeV. Later, in 2010, this reaction was examined at photon energies below 2.4 GeV in the SPring-8 LEPS experiment using a forward-angle spectrometer and polarized photons [78, 79], and from threshold to 2.65 GeV with the SAPHIR detector at the electron stretcher facility ELSA in Bonn [229]. Very recently, the exclusive $\Lambda(1520)$ ($\equiv \Lambda^*$) photoproduction cross section has been measured by using the CLAS detector for energies from threshold up to an invariant γp mass $W = 2.85$ GeV [80].

The theoretical activity has run in parallel. There exist several effective hadron Lagrangian studies [230–238] for laboratory photon energies ranging from threshold up to about 5 GeV. These theoretical studies have traditionally been limited by the lack of knowledge on the $\bar{K}^* N \Lambda^*$ coupling strength. This fact, in conjunction with the use of largely different form factors to account for the compositeness of the hadrons, has led to contradicting predictions of the dominant reaction mechanism in the process. Some light was shed on this issue in [236]. There, the SU(6) Weinberg-Tomozawa chiral unitary model proposed in [209] was used to predict a relatively small $\bar{K}^* N \Lambda^*$ coupling and, hence, to conclude that the $\bar{K}$ exchange and contact mechanisms dominated the $\gamma p \to K^+ \Lambda(1520)$ reaction. Besides, in the higher energy region, the quark-gluon string mechanism with the $\bar{K}$ Regge trajectory was shown [236] to reproduce both the LAMP2 energy and the angular distribution data [227].

The theory groups have also paid attention to another distinctive feature of the data. The LEPS energy dependence of the forward-angle cross section rises from threshold to a maximum near $W = 2.15$ GeV, followed by a decline [79]. It was suggested that this could be an effect of the odd parity D_{13} (L_{2T2J}) N^* intermediate resonance at around 2.1 GeV [234, 237–239]. In the scheme of Refs. [234] and [239], the contribution of the spin-parity $J^P = 3/2^-$ $N^*(2080)$ ($\equiv N^*$) resonance[1]

[1]Before the 2012 Particle Date Group (PDG) review, all the evidence for a $J^P = 3/2^-$ state with a mass above 1.8 GeV was filed under a two-star $N^*(2080)$. There is now evidence [240] of two states in this region, and the PDG has split the older data (according to mass) between a three-star $N^*(1875)$ and a two-star $N(2120)$ [70].

turned out to be very small. Hence in these works, such a contribution was not expected to explain the bump structure at forward angles reported by LEPS. This was primarily owing to the unnecessarily small $N^*\Lambda^*K$ coupling and probably the excessively large width of the resonance used in these references. However in Ref. [237], within the effective Lagrangian approach of Ref. [236], the role played by the $N(2120)$ resonance in the $\gamma p \to K^+\Lambda(1520)$ reaction was revisited, and found that the experimental LEPS Collaboration data could be fairly well described assuming a large $N^*\Lambda^*K$ coupling, which would be supported by some constituent quark models [241]. Yet, the recent analysis carried out in [242] taking the hadron resonance couplings from [241], shows that the D_{13} $N(2120)$ resonance also plays an important role in reproducing the $\Lambda(1520)$ electroproduction CLAS data [228] properly. A large $N^*\Lambda^*K$ coupling scenario has also been investigated in the $pp \to pK^+\Lambda^*$ and $\pi^- p \to K^0\Lambda^*$ hadronic $\Lambda(1520)$ production reactions [243]. Note that a resonance with these quantum numbers in the 2.1 GeV energy region, albeit with some uncertainty in the precise position, is unavoidable owing to the attractive character and strength of the vector-baryon interaction within the schemes of Refs. [73] and [74]. Furthermore, a recent analysis [244] of the $\gamma p \to K^0\Sigma^+$ CBELSA/TAPS data [245], which exhibits a peak in the cross section around $\sqrt{s} = 1.9$ GeV followed by a fast downfall around $\sqrt{s} = 2.0$ GeV, also provides support for the existence of a $J^P = 3/2^-$ nucleon excited state around 2 GeV.

On the other hand, the comparison of the recent CLAS measurements [80] with different effective Lagrangian model predictions [231, 238], obtained by using the parameters fitted to the LEPS [78, 79] and LAMP2 [227] data, indicates that the current model calculations can not describe the CLAS differential cross sections well over the entire energy and angular ranges available in the experiment.

In the present work, we aim to achieve an improved description of the recent CLAS data, which would provide further support for the existence of the $N(2120)$ resonance, and additional constraints on its properties. Within the scheme of Ref. [237], and in addition to the contact, t-channel $\bar{K}$ exchange, and s-channel nucleon and $N(2120)$ resonance pole contributions, we also study the u-channel $\Lambda(1115)$ ($\equiv \Lambda$) hyperon pole term. The latter mechanism has been ignored

in all previous calculations [231, 236–238] because information on the $\Lambda^*\Lambda\gamma$ coupling is scarce [235], and because it is expected to provide small contributions for forward K^+ angles, where the LEPS data lie. However, u-channel mechanisms might make important contributions at the backward K^+ angles that have become accessible in the recent CLAS experiment. As a consequence, it is not surprising, that previous theoretical calculations that reasonably described the LEPS data, were not as successful in describing the recent CLAS differential cross sections, which span a much wider range of K^+ angles.

Taking these considerations into account, and using the combination of the effective Lagrangian approach and the isobar model, we present in this chapter a combined theoretical analysis of the recent $\gamma p \to K^+\Lambda(1520)$ CLAS [80] and LEPS [79] data that includes the contribution from the u-channel Λ hyperon pole term.

The chapter is based on Ref. [246] and it is organized as follows. In Sec. 7.2, we discuss the formalism and the main ingredients of the model, while our numerical results and discussion are presented in Sec. 7.3. Finally, a short summary and conclusions are given in Sec. 7.4.

7.2 Formalism and ingredients

7.2.1 Feynman Amplitudes

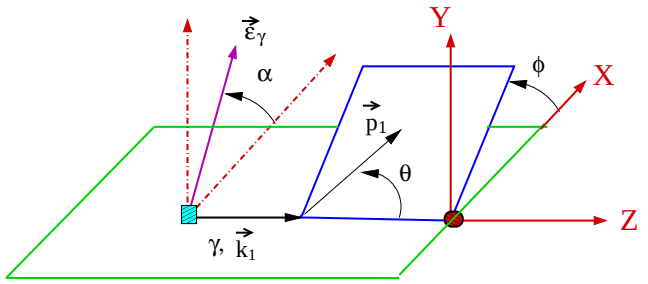

Figure 7.1: Definition of the different angles used in this work.

The invariant scattering amplitudes that enter our model for calcu-

lation of the total and differential cross sections for the reaction,

$$\gamma(k_1,\lambda)p(k_2,s_p)\to K^+(p_1)\Lambda^*(p_2,s_{\Lambda^*}) \tag{7.1}$$

are defined as

$$-iT_i=\bar{u}_\mu(p_2,s_{\Lambda^*})A_i^{\mu\nu}u(k_2,s_p)\epsilon_\nu(k_1,\lambda) \tag{7.2}$$

where u_μ and u are dimensionless Rarita-Schwinger and Dirac spinors, respectively, while $\epsilon_\nu(k_1,\lambda)$ is the photon polarization vector. In addition, s_p and s_{Λ^*} are the baryon polarization variables. The sub-index i stands for the contact, t-channel antikaon exchange, s-channel nucleon and N^* pole terms and novel u-channel Λ pole mechanism, which are depicted in Fig. 7.2. In our final results, and for simplicity, we do not consider the u-channel $\Sigma^0(1193)$ pole term, as we expect its contribution to be much smaller than that from the $\Lambda(1115)$ hyperon. We come back to this point below. Moreover, higher-excited hyperons would be farther off-shell in the u-channel, and have not been taken into account either.

To compute the contributions of these terms, we use the interaction Lagrangian densities of Refs. [234, 236, 237, 246],

$$\mathcal{L}_{\gamma KK}=-ie(K^-\partial^\mu K^+-K^+\partial^\mu K^-)A_\mu, \tag{7.3}$$

$$\mathcal{L}_{Kp\Lambda^*}=\frac{g_{KN\Lambda^*}}{m_K}\bar{\Lambda}^{*\mu}(\partial_\mu K^-)\gamma_5 p\ +\text{h.c.}, \tag{7.4}$$

$$\mathcal{L}_{\gamma pp}=-e\bar{p}\left(\not{A}-\frac{\kappa_p}{2M_N}\sigma_{\mu\nu}(\partial^\nu A^\mu)\right)p+\text{h.c.}, \tag{7.5}$$

$$\mathcal{L}_{\gamma Kp\Lambda^*}=-ie\frac{g_{KN\Lambda^*}}{m_K}\bar{\Lambda}^{*\mu}A_\mu K^-\gamma_5 p\ +\text{h.c.}, \tag{7.6}$$

$$\mathcal{L}_{\gamma NN^*}=\frac{ief_1}{2m_N}\bar{N}^*_\mu\gamma_\nu F^{\mu\nu}N\ -\frac{ef_2}{(2m_N)^2}\bar{N}^*_\mu F^{\mu\nu}\partial_\nu N\ +\text{h.c.}, \tag{7.7}$$

$$\mathcal{L}_{K\Lambda^*N^*}=\frac{g_1}{m_K}\bar{\Lambda}^*_\mu\gamma_5\gamma_\alpha(\partial^\alpha K)N^{*\mu}\ +\frac{ig_2}{m_K^2}\bar{\Lambda}^*_\mu\gamma_5\left(\partial^\mu\partial_\nu K\right)N^{*\nu}\ +\text{h.c.}, \tag{7.8}$$

$$\mathcal{L}_{\gamma\Lambda\Lambda^*}=-\frac{ih_1}{2m_\Lambda}\bar{\Lambda}^*_\mu\gamma_\nu F^{\mu\nu}\Lambda+\frac{h_2}{(2m_\Lambda)^2}\bar{\Lambda}^*_\mu F^{\mu\nu}\partial_\nu\Lambda\ +\text{h.c.} \tag{7.9}$$

$$\mathcal{L}_{KN\Lambda}=-ig_{KN\Lambda}\bar{\Lambda}\gamma_5 K^- p\ +\text{h.c.}, \tag{7.10}$$

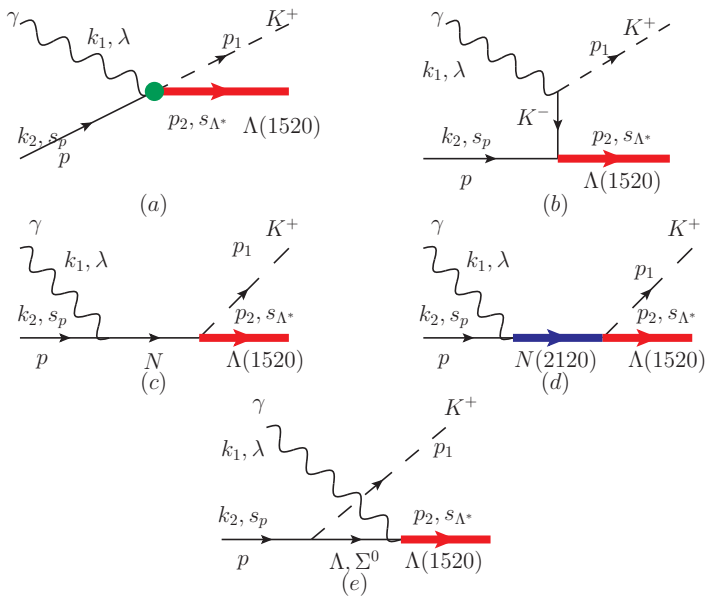

Figure 7.2: The model for $\gamma p \to K\Lambda(1520)$. It consists of the contact (a), t-channel antikaon exchange (b), s-channel nucleon (c) and N^* pole terms (d) and novel u-channel Λ (Σ^0) pole mechanism (e). In the diagram, we also show the definition of the kinematical (k_1, k_2, p_1, p_2) and polarization $(\lambda, s_p, s_{\Lambda^*})$ variables that we use in the present calculation. In addition, we use $q_u = k_2 - p_1 = p_2 - k_1$, with $u = q_u^2$.

where $e = \sqrt{4\pi\alpha} > 0$ ($\alpha = 1/137.036$ is the fine-structure constant), $\kappa_p = 1.79$, A_μ and $F_{\mu\nu} = \partial_\mu A_\nu - \partial_\nu A_\mu$ are the proton charge and magnetic moment, and the photon field and electromagnetic field tensor, respectively. We use the Rarita-Schwinger formalism (Appendix A.2) to describe the spin $J = 3/2$ Λ^* and N^* resonances, while the $N(2120)$ electromagnetic $f_{1,2}$ and hadronic $g_{1,2}$ couplings will be fitted to the experimental data. Note that the $\gamma\Lambda\Lambda^*$ vertex is gauge invariant by itself. h_1 and h_2 are magnetic coupling constants, while $g_{KN\Lambda}$ is a strong one.

With the above Lagrangians, one readily finds

$$A_t^{\mu\nu} = -e\frac{g_{KN\Lambda^*}}{m_K}\frac{1}{t - m_K^2} q_t^\mu (q_t^\nu - p_1^\nu)\gamma_5 \, f_c, \qquad (7.11)$$

$$
\begin{aligned}
A_s^{\mu\nu} &= -e\frac{g_{KN\Lambda^*}}{m_K}\frac{1}{s-m_N^2}\, p_1^\mu\gamma_5\,[\not k_1\gamma^\nu\, f_{\rm s} + (\not k_2 + m_N)\gamma^\nu\, f_{\rm c} \\
&\quad +(\not k_1 + \not k_2 + m_N) i\,\frac{\kappa_p}{2m_N}\sigma_{\nu\rho}k_1^\rho\, f_{\rm s}\Big], \qquad (7.12)\\
A_c^{\mu\nu} &= e\frac{g_{KN\Lambda^*}}{m_K} g^{\mu\nu}\gamma_5\, f_{\rm c}, \qquad (7.13)\\
A_R^{\mu\nu} &= \gamma_5(\frac{g_1}{m_K}\not p_1 g^{\mu\rho} - \frac{g_2}{m_K^2}p_1^\mu p_1^\rho)\frac{\not k_1 + \not k_2 + M_{N^*}}{s - M_{N^*}^2 + iM_{N^*}\Gamma_{N^*}} \\
&\quad \times P_{\rho\sigma}\Big[\frac{ef_1}{2m_N}(k_1^\sigma\gamma^\nu - g^{\sigma\nu}\not k_1) \\
&\quad +\frac{ef_2}{(2m_N)^2}(k_1^\sigma k_2^\nu - g^{\sigma\nu}k_1\cdot k_2)\Big] f_R, \qquad (7.14)\\
A_u^{\mu\nu} &= \Big[\frac{h_1}{2m_\Lambda}(k_1^\mu\gamma^\nu - g^{\mu\nu}\not k_1) + \frac{h_2}{(2m_\Lambda)^2}(k_1^\mu q_u^\nu - g^{\mu\nu}k_1\cdot q_u)\Big] \\
&\quad \times\frac{\not q_u + m_\Lambda}{u - m_\Lambda^2} g_{KN\Lambda}\gamma_5 f_u\,. \qquad (7.15)
\end{aligned}
$$

The sub-indices c, t, s, R and u stand for the contact term, t-channel kaon exchange, s-channel nucleon and N^* pole terms, u-channel Λ pole mechanism. In the above equations, m_Λ and q_u are the mass and the four-momentum of the $\Lambda(1115)$, respectively, while M_{N^*} and Γ_{N^*} are the mass and the total decay width of the N^* resonance, which will be fitted to the experimental data. Besides, t, s and u are the Mandelstam variables which are: $t = q_t^2 = (k_1 - p_1)^2$, $s = (k_1 + k_2)^2$ and $u = q_u^2 = (p_2 - k_1)^2$. The projector of spin 3/2 is

$$
\begin{aligned}
P_{\rho\sigma} &= -g_{\rho\sigma} + \frac{1}{3}\gamma_\rho\gamma_\sigma + \frac{2}{3M_{N^*}^2}(k_1+k_2)_\rho(k_1+k_2)_\sigma \\
&\quad +\frac{1}{3M_{N^*}}(\gamma_\rho(k_1+k_2)_\sigma - \gamma_\sigma(k_1+k_2)_\rho). \qquad (7.16)
\end{aligned}
$$

In addition, in the above expressions of the different contributions, we have already included the form factors which are necessary to be introduced since the hadrons are not pointlike particles. We take the following parameterization for those form factors:

$$
f_i = \frac{\Lambda_i^4}{\Lambda_i^4 + (q_i^2 - M_i^2)^2}, \quad i = s,\ t,\ R,\ u \qquad (7.17)
$$

$$f_c = f_s + f_t - f_s f_t, \quad \text{and} \begin{cases} q_s^2 = q_R^2 = s, \\ M_s = m_N, \\ M_t = m_K, \\ M_R = M_{N^*}, \\ M_u = m_\Lambda, \end{cases} \tag{7.18}$$

where the form factor of f_c is chosen such that the on-shell of the coupling constants are reproduced and the gauge invariance is kept. We will consider different cut-off values for the background and resonant terms, i.e. $\Lambda_s = \Lambda_t = \Lambda_u = \Lambda_B \neq \Lambda_R$, which will be fitted to the experimental data of $\gamma p \to K^+\Lambda(1520)$ differential cross section.

7.2.2 Coupling constants

We use $g_{KN\Lambda^*} = 10.5$, as determined from the $\Lambda^* \to pK^-$ decay width (we use for the full decay width $\Gamma_{\Lambda^*} = 15.6$ MeV and a value of 0.45 for the $\Lambda^* \to \bar{K}N$ branching ratio [70]), while the $N^*N\gamma$ coupling constants f_1 and f_2 could be fixed, in principle, from the N^* helicity amplitudes $A_{1/2}$ and $A_{3/2}$ [247],

$$A_{1/2}^{p^*} = \frac{e\sqrt{6}}{12}\sqrt{\frac{k_\gamma}{m_N M_{N^*}}}\left[f_1 + \frac{f_2}{4m_N^2}M_{N^*}(M_{N^*} + m_N)\right], \tag{7.19}$$

$$A_{3/2}^{p^*} = \frac{e\sqrt{2}}{4m_N}\sqrt{\frac{k_\gamma M_{N^*}}{m_N}}\left[f_1 + \frac{f_2}{4m_N}(M_{N^*} + m_N)\right], \tag{7.20}$$

where $k_\gamma = (M_{N^*}^2 - m_N^2)/(2M_{N^*})$, and the the superscript p^* indicates the positive-charge D_{13} resonance.

On the other hand, we take $g_{KN\Lambda} \sim -14$ as estimated from the SU(3) flavor symmetry [248] Bonn-Jülich model for the meson-exchange hyperon-nucleon interactions in free scattering [249]. Note that at lowest order in the chiral expansion [250, 251],

$$\frac{g_{\pi^0 pp}}{g_{K^+p\Lambda}} \sim -\frac{D+F}{\frac{D+3F}{\sqrt{3}}}, \qquad \frac{g_{K^+p\Sigma^0}}{g_{K^+p\Lambda}} \sim -\frac{D-F}{\frac{D+3F}{\sqrt{3}}}, \tag{7.21}$$

with $D \sim 0.8$ and $F \sim 0.5$, which justifies $|g_{KN\Lambda}/g_{\pi NN}| \sim 1$. Besides, we see that the $g_{K^+p\Sigma^0}$ is about four or five times smaller than $g_{K^+p\Lambda}$, and this is also compatible with the findings in [249]. The latter relationship between couplings gives support for neglecting the u-channel

Table 7.1: Theoretical predictions (in keV) for the radiative width $\Gamma(\Lambda(1520) \to \Sigma^0\gamma)$.

Approach	Γ [keV]
NRQM [253, 254]	55–75
MIT Bag [254]	17
RCQM [255]	293
Chiral Bag [256]	49
Algebraic [257]	180
BonnBSCQM [258]	157
χQM [259]	92
UChPT [260]	71

Σ^0 pole contribution, despite that the strength of the electromagnetic $\gamma\Sigma^0\Lambda^*$ coupling could be similar to, or even larger than, that involving the $\Lambda(1115)$ hyperon [252].

The Σ^0 radiative decay of the $\Lambda(1520)$ has not been observed yet, while $\Gamma(\Lambda(1520) \to \Lambda\gamma)$ has been measured to be of the order of 130 keV [70]. There exist various (Table 7.1) theoretical estimates [253–260] for the width of $\Gamma(\Lambda(1520) \to \Sigma^0\gamma)$, ranging from the 17 keV predicted within the MIT bag model [254] up to the 293 keV obtained in the RCQM (relativistic constituent quark model) approach followed in [255]. If the $\Lambda(1520)$ were a SU(3) singlet and assuming that the photon is a U-spin singlet, U-spin invariance guarantees that decay into the U-spin triplet linear combination $(\Sigma^0 + 3\Lambda)$ would be 0 [252]. Thus one would predict[2] $\Gamma(\Lambda(1520) \to \Sigma^0\gamma) \sim 3\times$(phase space)$\times\Gamma(\Lambda(1520) \to \Lambda\gamma) \sim 230$ keV, in the upper-band of the various predictions listed in Table 7.1.

Despite this large ambiguity, one can safely conclude that even though the electromagnetic $\gamma\Sigma^0\Lambda^*$ coupling was bigger than the $\gamma\Lambda\Lambda^*$

[2]In the original work in Ref. [252], it was assumed that the phase space scaled as the decaying photon momentum from what follows $\Gamma(\Lambda(1520) \to \Sigma^0\gamma) \sim 2.5 \times \Gamma(\Lambda(1520) \to \Lambda\gamma)$ [252]. However, as we see below (Eqs. (7.22)–(7.24)), the decay width rather scales down as the cube of the photon momentum, which leads to the lower value, about 230 keV.

one, it would not be large enough to compensate for the big reduction induced by the ratio of hadronic couplings $\left(g_{K^+p\Sigma^0}/g_{K^+p\Lambda}\right)^2 \sim 1/20$. Hence, it seems reasonable to assume that the $\Sigma^0(1193)$ contribution to the $\gamma p \to K^+\Lambda(1520)$ reaction would be much smaller than that of the $\Lambda(1115)$ hyperon. On the other hand, taking into account the u-channel $\Sigma^0(1193)$ term would require adopting some theoretical model for the electromagnetic $\Lambda^*\Sigma^0\gamma$ amplitude. However, we see that important discrepancies among the various approaches, even in predicting the radiative decay width $\Gamma(\Lambda(1520) \to \Sigma^0\gamma)$. Fitting this amplitude to data is not a realistic option either, because both the Λ and the Σ^0 u-channel poles are quite close, and the available data cannot effectively discriminate between their contributions. Thus, in the final results, and for the sake of simplicity, we do not include the u-channel $\Sigma^0(1193)$ mechanism. Nevertheless, we estimate the possible impact of this term assuming U-spin SU(3) symmetry.

The $\gamma\Lambda\Lambda^*$ coupling constants h_1 and h_2 could be fixed from the $\Lambda^* \to \Lambda\gamma$ partial decay width [70],

$$\Gamma_\gamma = \frac{m_\Lambda k_\gamma^2}{2\pi M_{\Lambda^*}} \left(|A_{1/2}|^2 + |A_{3/2}|^2\right), \tag{7.22}$$

with,

$$A_{1/2} = \frac{\sqrt{6}}{12}\sqrt{\frac{k_\gamma}{m_\Lambda M_{\Lambda^*}}}\left[h_1 + \frac{M_{\Lambda^*}h_2}{4m_\Lambda^2}(M_{\Lambda^*} + m_\Lambda)\right], \tag{7.23}$$

$$A_{3/2} = \frac{\sqrt{2}}{4m_\Lambda}\sqrt{\frac{k_\gamma M_{\Lambda^*}}{m_\Lambda}}\left[h_1 + \frac{h_2}{4m_\Lambda}(M_{\Lambda^*} + m_\Lambda)\right], \tag{7.24}$$

where $k_\gamma = (M_{\Lambda^*}^2 - m_\Lambda^2)/(2M_{\Lambda^*})$ is the photon center of mass (c.m.) frame decay momentum. With the value of $\Gamma_\gamma = 0.133$ MeV, as quoted in the PDG [70], we could get a constraint on the values of h_1 and h_2,

$$ah_1^2 + bh_2^2 + ch_1h_2 = d, \tag{7.25}$$

with

$$a = \frac{m_\Lambda^2 + 3M_{\Lambda^*}^2}{24m_\Lambda^3 M_{\Lambda^*}}k_\gamma^3, \qquad b = \frac{M_{\Lambda^*}(m_\Lambda + M_{\Lambda^*})^2}{96m_\Lambda^5}k_\gamma^3, \tag{7.26}$$

$$c = \frac{(m_\Lambda + M_{\Lambda^*})(m_\Lambda + 3M_{\Lambda^*})}{48m_\Lambda^4}k_\gamma^3, \quad d = \frac{2\pi M_{\Lambda^*}\Gamma_\gamma}{m_\Lambda}. \tag{7.27}$$

7.2.3 Differential cross section

With the ingredients given above, the unpolarized c.m. differential cross section can be easily obtained as,

$$\frac{d\sigma}{d\cos\theta_{\rm c.m.}} = \frac{|\vec{k}_1^{\rm c.m.}||\vec{p}_1^{\rm c.m.}|}{8\pi}\frac{m_N M_{\Lambda^*}}{(W^2-m_N^2)^2}\sum_{s_p,s_{\Lambda^*},\lambda}|T|^2\,, \quad (7.28)$$

with W the invariant mass of the γp pair. Further, $\vec{k}_1^{\rm c.m.}$ and $\vec{p}_1^{\rm c.m.}$ are the photon and K^+ meson c.m. three-momenta, and $\theta_{\rm c.m.}$ is the K^+ polar scattering angle (Fig. 7.1). The differential cross section $d\sigma/d(\cos\theta_{\rm c.m.})$ depends on W and also on $\cos\theta_{\rm c.m.}$. As mentioned above, the model accounts for a total of five mechanisms: contact, t-channel antikaon exchange, s-channel nucleon and N^* pole terms, evaluated in [237], and the u-channel Λ pole contribution discussed here. In principle, the free parameters of the model are: (i) the mass and width (M_{N^*} and Γ_{N^*}) of the $N(2120)$ resonance, (ii) the cut off parameters $\Lambda_s = \Lambda_t = \Lambda_u \equiv \Lambda_B$ and Λ_R, and (iii) the $N(2120)$ resonance electromagnetic $\gamma N N^*$ (ef_1, ef_2) and strong $N^*\Lambda^* K$ (g_1, g_2) couplings and the $\Lambda(1520)$ magnetic $\gamma\Lambda\Lambda^*$ (h_1) one. Note that the second coupling h_2 in Eq. (7.7) is given in terms of h_1 and the Λ^* radiative decay width (see Eq. (7.25)).

In the next section, we fit the parameters of the model to the differential cross-section data from the CLAS and LEPS Collaborations.

7.3 Numerical results and discussion

First, we have performed[3] a nine-parameter (ef_1, ef_2, g_1, g_2, $\Lambda_s = \Lambda_t = \Lambda_u \equiv \Lambda_B$, Λ_R, M_{N^*}, Γ_{N^*} and h_1) χ^2-fit to the $d\sigma/d(\cos\theta_{\rm c.m.})$ data from the CLAS Collaboration [80] (fit I). There is a total of 157 available data points displayed in Fig. 7.3. The $d\sigma/d(\cos\theta_{\rm c.m.})$ data, as a function of $\cos\theta_{\rm c.m.}$, are given for nine intervals of the invariant γp mass W from the reaction threshold 2.02 GeV up to 2.85 GeV. To compute the cross sections in each interval we always use the corresponding mean value of W. (We have checked that variations with respect to

[3]We take $M_{\Lambda^*} = 1.5195$ GeV, m_K= 0.4937 GeV and $m_\Lambda = 1.1157$ GeV.

calculation of the average value of the differential cross sections for each W range turn out to be very small.) We have also carried out a combined fit to the CLAS [80] and LEPS [79], $d\sigma/d(\cos\theta_{\rm c.m.})$ data (fit II). In this second fit, we have a total of 216 data points (in addition to the former CLAS differential cross sections, we have also fitted to the LEPS data depicted in Fig. 7.4).

Table 7.2: Values of some parameters determined in this work and in Ref. [237]. Fit I (II) parameters have been adjusted to the CLAS (combined CLAS [80] and LEPS [79]) $\gamma p \to K^+\Lambda(1520)$ $d\sigma/d(\cos\theta_{\rm c.m.})$ data, while fit C in Ref. [237] was obtained by considering only the LEPS differential cross sections.

	Fitted Parameters		
	This work		Ref. [237]
	Fit I	Fit II	Fit C
g_1	1.7 ± 0.4	1.6 ± 0.2	1.4 ± 0.3
g_2	4.6 ± 1.2	2.2 ± 0.5	5.5 ± 1.8
Λ_B [MeV]	630 ± 2	620 ± 2	604 ± 2
Λ_R [MeV]	933 ± 52	1154 ± 47	909 ± 55
ef_1	0.123 ± 0.015	0.126 ± 0.012	0.177 ± 0.023
ef_2	-0.094 ± 0.014	-0.097 ± 0.010	-0.082 ± 0.023
M_{N^*}[MeV]	2172 ± 10	2135 ± 4	2115 ± 8
Γ_{N^*}[MeV]	287 ± 54	184 ± 11	254 ± 24
h_1	0.68 ± 0.05	0.64 ± 0.05	–
χ^2/dof	2.5	2.5	1.2
χ^2/dof (No N^*)	5.6	9.9	24
χ^2/dof (No Λ)	3.0	3.0	–
χ^2/dof (No N^*,Λ)	6.3	9.9	–
	Derived Observables		
$A^{p^*}_{1/2}[10^{-3}\text{GeV}^{-1/2}]$	-7.6 ± 3.9	-7.3 ± 3.0	3.6 ± 8.6
$A^{p^*}_{3/2}[10^{-2}\text{GeV}^{-1/2}]$	2.5 ± 1.0	2.5 ± 0.8	5.8 ± 2.1
$\Gamma_{N^*\to\Lambda^* K}$ [MeV]	56 ± 27	30 ± 8	19 ± 7
$\frac{\Gamma_{N^*\to\Lambda^* K}}{\Gamma_{N^*}}$[%]	19.0 ± 10.3	16.2 ± 4.2	7.5 ± 2.8
h_2	-0.43 ± 0.08	-0.38 ± 0.07	–

The fitted parameters from the above two fits are listed in Table 7.2, where we also report our previous results from a best fit (fit C of Ref. [237]) only to the LEPS data of Ref. [79]. We also give for each

fit, the predicted nucleon D_{13} resonance width $\Gamma_{N^*\to\Lambda^* K}$ (Eq. (18) in Ref. [237]), helicity amplitudes (Eqs. (15) and (16) in Ref. [237]) for the positive-charge state and the h_2 magnetic $\gamma\Lambda\Lambda^*$ coupling [Eq. (7.25)].[4]

As commented before, LEPS data lie in the K^+ forward angle region and were taken below $E_\gamma = 2.4$ GeV, while the recent CLAS measurements span a much larger K^+ angular and photon energy regions. The χ^2/dof for both fit I and fit II are acceptable, of the order of 2.5. The new CLAS measurements are quite accurate (excluding some data close to threshold) with statistical errors ranging from about 10%, at high scattering angles, down to 5% or less for forward angles. The systematical errors of the experimental data (11.6% [80] and 5.92% [79], for CLAS and LEPS, respectively) have been added in quadratures to the statistical ones and taken into account in the present new fits. We see that the N^* resonance parameters from the new fits I and II turn out to be in reasonable agreement with those obtained in Ref. [237]. Thus, the first conclusion is that the CLAS data provide further support for the existence of an odd parity 3/2 wide nucleon resonance with a mass in the region of 2.1 GeV and a width of around 200 MeV. This is compatible with the Breit-Wigner parameters, $M_{BW} = 2.15 \pm 0.06$ GeV and $\Gamma_{BW} = 330 \pm 45$ MeV, reported in [240]. The latter reference also provides experimental values for its helicity amplitudes

$$A^{p^*}_{1/2}[10^{-3}\mathrm{GeV}^{-1/2}] = 125 \pm 45\,, \tag{7.29}$$

$$A^{p^*}_{3/2}[10^{-2}\mathrm{GeV}^{-1/2}] = 15 \pm 6\,, \tag{7.30}$$

which however do not seem entirely consistent with previous measurements [261],

$$A^{p^*}_{1/2}[10^{-3}\mathrm{GeV}^{-1/2}] = -20 \pm 8\,, \tag{7.31}$$

$$A^{p^*}_{3/2}[10^{-2}\mathrm{GeV}^{-1/2}] = 1.7 \pm 1.1\,, \tag{7.32}$$

quoted in the 2008 PDG edition [262], which in turn are in better agreement with our predictions in Table 7.2. Note that the latter

[4] This is a second rank equation and it has two possible solutions. One of them turns out to be strongly disfavored by the χ^2-fit. To be more quantitative, in our final results (fit II), χ^2/dof would pass from 2.5 to 3.1 if the other solution were considered.

helicity amplitudes are used in [242], where the $ep \to eK^+\Lambda(1520)$ CLAS data in Ref. [228] were successfully described. Nevertheless, given the two-star status (evidence of existence is only fair) granted to the $N(2120)$ resonance in the multichannel partial wave analysis of pion and photo-induced reactions off protons carried out in [240], the discrepancy with our predicted helicity amplitudes should not be used to rule out our fits, but rather one could use them to further constrain these elusive observables. On the other hand, within this scheme, the $N(2120)$ resonance would have a large partial decay width into $\Lambda^* K$, which is compatible with the findings of the constituent quark model approach in Ref. [241]. Indeed, in that reference, $\Gamma_{N^* \to \Lambda^* K}$ is predicted to be 7^{+24}_{-6} MeV for a resonance mass of 2080 MeV. This value for the width is compatible within errors with the value of 30 ± 8 MeV found in this work. Moreover, because the $\Lambda(1520)K^+$ threshold is located so close to $M_{N^*} = 2080$ MeV, the width would increase by at least a factor of two if the resonance mass was instead taken as 2120 MeV. Hence, the constituent quark model of Ref. [241] would predict central values for $\Gamma_{N^* \to \Lambda^* K}$ in the vicinity of 15 MeV for the current PDG value of M_{N^*}. On the other hand, the width quoted in [241] leads to[5] $|g_1| = 1.25$, in good agreement with our fitted value. The analysis carried out in [242] for the $\Lambda(1520)$ electroproduction reaction off the proton uses this value for g_1, fixes g_2 to 0 and, as mentioned above, uses the helicity amplitudes given in Ref. [261]. Thus, the set of N^* couplings used in Ref. [242], where the important role played by the D_{13} $N(2120)$ resonance is also highlighted, turns out to be similar to that found in this work.

The differential $d\sigma/d(\cos\theta_{\rm c.m.})$ distributions from the combined fit (fit II) to the CLAS [80] and LEPS [79] data are shown in Figs. 7.3 and 7.4, and compared with the experimental data. Only statistical errors are displayed in these two figures. The contributions from different mechanisms of the model are shown separately.

In the first of these two figures, the differential cross sections as a function of $\cos\theta_{\rm c.m.}$, for different γp invariant mass intervals, are displayed and contrasted with the recent CLAS measurements. Dashed (blue) and dotted (green) lines show the contributions from background

[5]The width is rather insensitive to g_2 because its contribution is suppressed by the K^+ meson c.m. three-momentum.

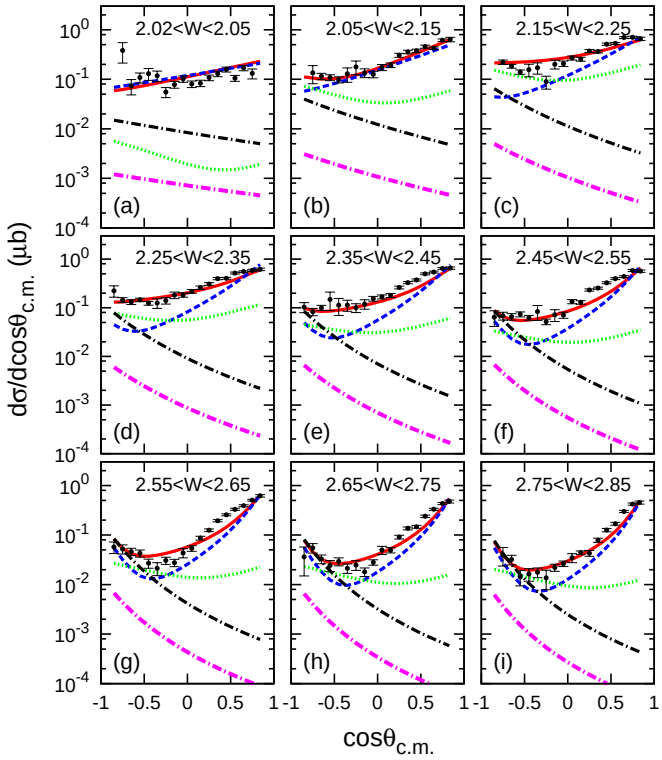

Figure 7.3: Fit II $\gamma p \to K^+\Lambda(1520)$ differential cross sections as a function of $\cos\theta_{\rm c.m.}$ compared with the CLAS data [80] for different γp-invariant mass intervals (in GeV). Only statistical errors are displayed.

(contact, t-channel $\bar{K}$ exchange and s-channel nucleon and u-channel Λ pole mechanisms) and $N(2120)$ resonance terms, respectively. Dash-dotted (black) curves represent for the u-channel $\Lambda(1115)$ contribution separately, while the solid (red) lines display the results obtained from the full model (background+N^*). Finally, the dash-dotted (magenta) curves represent the u-channel $\Sigma^0(1193)$ contribution, not included in the final results [solid (red) lines], as determined from electromagnetic U-spin ($h^{\Sigma}_{1,2} = -\sqrt{3}h_{1,2}$) and leading order chiral [Eq. (7.21)] symmetries. Near threshold the CLAS cross section is fairly flat. In the highest energy bin the cross section is quite forward peaked, with a hint of plateauing toward the most forward angles. Also evident is

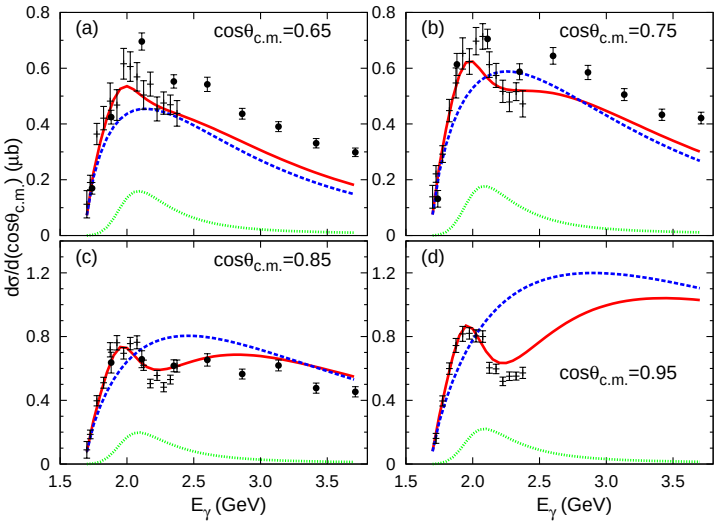

Figure 7.4: Fit II $\gamma p \to K^+\Lambda(1520)$ differential cross section as a function of the LAB frame photon energy for different c.m. K^+ polar angles. We also show the experimental LEPS [79] (crosses) and CLAS [80] (filled circles) data. Only statistical errors are displayed.

that the cross section flattens or even rises slightly toward large angles. We find an overall good description of the data, both at forward and at backward K^+ angles and for the whole range of measured γp invariant masses, W. We see that as W increases, the contribution of the u-channel $\Lambda(1115)$ pole term produces an enhancement at backward angles, and it becomes more and more relevant. Indeed, it turns out to be essential above $W \geq 2.35$ GeV and $\cos\theta_{\rm c.m.} \leq -0.5$. The present model provides a better description of the recent CLAS data than that obtained within the schemes of Refs. [239] and [238], whose predictions are reported in [80]. The major improvement can be appreciated at backward angles, as it is mostly attributable to the u-channel $\Lambda(1115)$ pole mechanism.

For comparison, we also display in Fig. 7.3 the contribution from the u-channel $\Sigma^0(1193)$ term, which is not included in fit II. The $\Sigma^0(1193)$ amplitude takes the same form as that of the $\Lambda(1115)$ mechanism (Eq. (7.15)), with the obvious replacements of coupling constants

and hyperon masses. For the electromagnetic ones, we have assumed U-spin invariance ($h^{\Sigma}_{1,2} = -\sqrt{3}h_{1,2}$), while we have taken $g_{K^+p\Sigma^0} = 3.2$, as deduced from leading order vector chiral symmetry (Eq. (7.21)). As anticipated, the u-channel Σ^0 contribution turns out to be a small fraction of the Λ one, and can be safely neglected.

In Fig. 7.4, the differential cross section deduced from the results of the nine-parameter fit II, as a function of the LAB frame photon energy and for different forward c.m. K^+ angles, is shown and compared both to CLAS [80] and to LEPS [79] data. In this figure, dashed (blue) and dotted (green) lines show the contributions from the background[6] and N^* resonance terms, respectively, while the solid (red) lines display the full result. We see that the bump structure in the differential cross section at forward K^+ angles is fairly well described thanks to the significant contribution from the N^* resonance in the s-channel. Indeed, these results are similar to those already reported and discussed in Ref. [237], and the description of these forward LEPS data achieved here is also comparable to that exhibited in Ref. [237]. The CLAS data points shown in Fig. 7.4 were obtained from the appropriate CLAS cross sections displayed in Fig. 7.3, relating W to the LAB photon energy. Returning to the latter figure, we see that our model underestimates the CLAS data for values of $\cos\theta_{\rm c.m.}$ in the 0.5-0.75 interval, and in particular at high energies, $W \geq 2.3$ GeV. We will study this region in the next section by taking into account Regge effects.

We have also performed several best fits, where either one or both of the s-channel $N(2120)$ resonance and the u-channel $\Lambda(1115)$ pole terms have been switched off. The corresponding χ^2/dof are also compiled in Table 7.2, which turn out to be larger, and in most cases, unacceptable on statistical grounds.[7]

[6]The contribution of the u-channel $\Lambda(1115)$ pole mechanism for these forward angles is negligible.

[7]Note that the quantitative effect on χ^2/dof of disconnecting the u-channel $\Lambda(1115)$ contribution is not big. This is because the forward angle LEPS data are rather insensitive to this mechanism, as well as the low energy CLAS cross section. As commented in the discussion of Fig. 7.3, only the backward high energy CLAS cross sections are being effected by this term, but there the qualitative effect is important. Despite the limited number of data points, which in addition suffer from large statistical fluctuations, the improvement on the total χ^2/dof is still

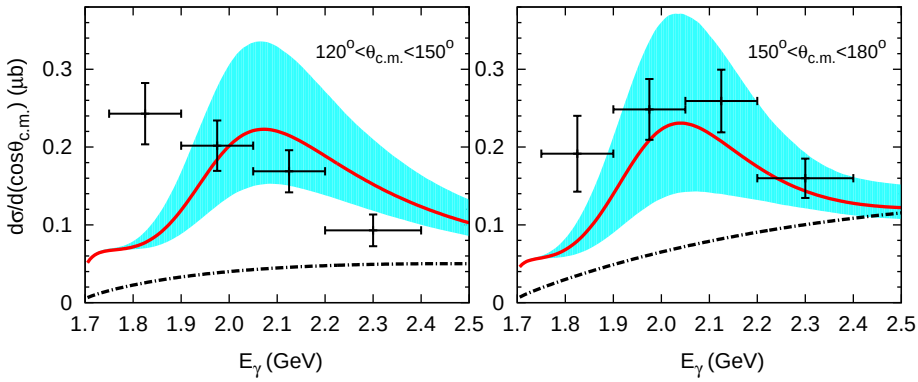

Figure 7.5: Fit II $\gamma p \to K^+\Lambda(1520)$ differential cross section as a function of the LAB frame photon energy for backward K^+ angles [solid (red) lines].

In Fig. 7.5, we display the average $\langle d\sigma/d(\cos\theta_{\rm c.m.})\rangle$ distribution (Eq. (7.33)) from the full model and compare it with LEPS data from Ref. [78]. The 68% CL bands inherited from the Gaussian correlated statistical errors of the fit II parameters. Finally, the dash-dotted (black) curves show the u-channel $\Lambda(1115)$ contribution. There, events were accumulated for two angular intervals $\theta_{\rm c.m.}$ $=(120-150)^0$ and $\theta_{\rm c.m.}$ $=(150-180)^0$, with the photon energy varying in the region $1.9 \leq E_\gamma \leq$ 2.4 GeV. Since the angular intervals are quite wide, we have partially integrated the differential cross section, and evaluated

$$\left\langle \frac{d\sigma}{d(\cos\theta_{\rm c.m.})} \right\rangle = \frac{\int_{\cos\theta^{\rm up}_{\rm c.m.}}^{\cos\theta^{\rm dw}_{\rm c.m.}} \frac{d\sigma}{d(\cos\theta_{\rm c.m.})} d(\cos\theta_{\rm c.m.})}{\int_{\cos\theta^{\rm up}_{\rm c.m.}}^{\cos\theta^{\rm dw}_{\rm c.m.}} d(\cos\theta_{\rm c.m.})}, \tag{7.33}$$

taking $(\theta^{\rm dw}_{\rm c.m.}, \theta^{\rm up}_{\rm c.m.})$ to be $(120^0, 150^0)$ or $(150^0, 180^0)$, respectively. In Fig. 7.5, the shaded regions account for the uncertainties inherited from those affecting the parameters compiled in Table 7.2. They represent 68% confidence-level (CL) bands and were obtained using a Monte Carlo simulation. As shown in Figs. 7.5(a) and 7.5(b), the present model provides a fair description of these backward K^+ angular data.

significant (3.0 vs 2.5).

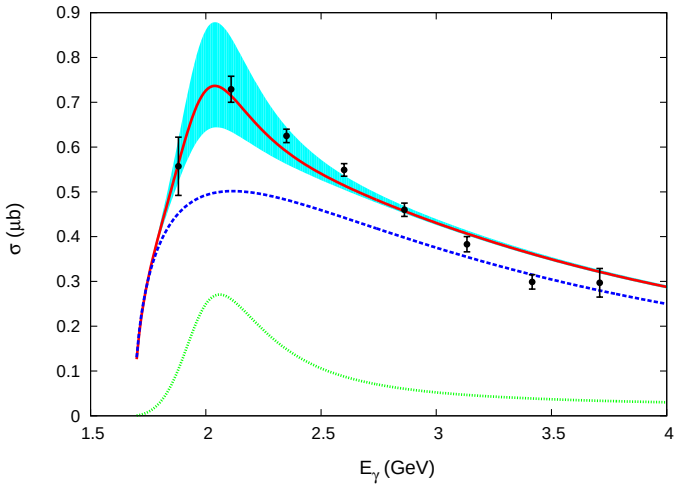

Figure 7.6: Total $\gamma p \to K^+\Lambda^*$ cross section deduced from the results of fit II. We display it as a function of the LAB photon energy and compare with the CLAS data from Ref. [80].

This is in sharp contrast to the results of our previous work [237] (see Fig. 4 in Ref. [237]), where the u-channel $\Lambda(1115)$ mechanism was not considered. Indeed, the latter contribution is also depicted in Fig. 7.5. We see that it increases with the photon energy and that becomes quite relevant for the most backward angles [Fig. 7.5(b)].

Finally, we have also calculated the total cross section of the $\gamma p \to K^+\Lambda(1520)$ reaction as a function of the photon energy. The results are shown in Fig. 7.6 and compared to the experimental data from CLAS. Dashed (blue) and dotted (green) lines show the contributions from the background and N^* resonance terms, respectively, while the solid (red) line displays the results from the full model. The shaded region accounts for the 68% CL band inherited from the Gaussian correlated statistical errors of the fit II parameters. We see that the model provides an excellent description of the integrated CLAS cross sections thanks to an important contribution from the photo-excitation of the $N(2120)$ resonance and its subsequent decay into a $\Lambda(1520)K^+$ pair. This mechanism seemed also to be responsible for the bump structure

in the LEPS differential cross section at forward K^+ angles discussed in Fig. 7.4. Thus, one can definitely take advantage of the apparently important role played by this resonant mechanism in the LEPS and CLAS data to better constrain some of the $N(2120)$ properties (Table 7.2), starting from its mere existence.

It is noteworthy that the contribution from the u-channel $\Lambda(1115)$ mechanism is very small in the integrated cross section, as it is only significant for backward K^+ angles.

7.4 Summary and Conclusions

We have carried out a new analysis of the $\gamma p \to \Lambda(1520)K^+$ reaction at low energies within an effective Lagrangian approach and the isobar model. We have presented results from a combined fit to the recent CLAS [80] and LEPS [79], $d\sigma/d(\cos\theta_{\rm c.m.})$ data. Within the scheme of Ref. [237], and in addition to the contact, t-channel $\bar{K}$ exchange, and s-channel nucleon and $N(2120)$ resonance pole contributions, we have also studied the u-channel $\Lambda(1115)$ hyperon pole term. The latter mechanism has been ignored in all previous calculations [231, 236–238] that relied on the very forward K^+ angular LEPS data [78, 79], where its contribution was expected to be small.

We have shown that when the contributions from the $N(2120)$ resonance and the $\Lambda(1115)$ are taken into account, both the new CLAS and the previous LEPS data can be simultaneously described. Actually, we find an overall good description of the data, both at forward and at backward K^+ angles, and for the whole range of measured γp invariant masses. The contribution of the u-channel $\Lambda(1115)$ pole term produces an enhancement at backward angles, and it becomes more and more relevant as the photon energy increases, becoming essential above $W \geq 2.35$ GeV and $\cos\theta_{\rm c.m.} \leq -0.5$. On the other hand, the CLAS data (see for instance Fig. 7.6), clearly support the existence of an odd parity 3/2 wide nucleon resonance with a mass in the region of 2.1 GeV, a width of around 200 MeV and a large partial decay width into $\Lambda^* K$. The recent analysis carried out in [242] of $\Lambda(1520)$ electroproduction off the proton also concludes that the D_{13} $N(2120)$ resonance plays an important role. It is re-assuring that the N^* couplings used in [242]

turn out to be quite similar to those determined in this work. These characteristics could be easily accommodated within the constituent quark model results of Capstick and Roberts in Ref. [241]. Such resonance might be identified with the two stars PDG $N(2120)$ state. This would confirm previous claims [237, 238] from the analysis of the bump structure in the LEPS differential cross section at forward K^+ angles discussed in Fig. 7.4, and contradict previous negative claims made in [234] and [239] regarding this point.

Following [241], besides the $N(2120)$ D_{13} resonance, both of the weakly established states $N(2090)$ S_{11} and $N(2200)$ D_{15} [in the 2012 PDG review [70], these excited nucleons appear in the listings as the two-star $N(1895)$ and $N(2060)$, respectively], were also visible in $\Lambda(1520)K$ production reactions [see Fig. 6 of Ref. [241]]. If these resonances were take into account, one might wonder whether their contributions could affect the $N(2120)$ parameters in a significant way. Fortunately, the work of S. Nam on electroproduction of $\Lambda(1520)$ off the nucleon [242] sheds some light into this issue. There, the $D_{13}(2120)$, $S_{11}(2090)$ and $D_{15}(2200)$ resonances were considered, and it was found that the contributions of the two latter ones are negligible and much smaller than that of the $D_{13}(2120)$ state [see Figs. 6(a) and 11(a) in Ref. [242]].

On the other hand, the N^* resonance parameters from the new fits carried out in this work turn out to be in reasonable agreement with those obtained in Ref. [237], and the bulk of the conclusions of that reference still hold. In particular, the sign discrepancy (see Fig. 6 in [237]) of the predictions of the model for the polar-angle average photon-beam asymmetry, as a function of E_γ, with the SPring-8 LEPS data of Ref. [79] still persists.

In addition, our model underestimates the CLAS data for values of $\cos\theta_{\rm c.m.}$ in the 0.5-0.75 interval, and in particular at high energies, $W \geq 2.3$ GeV, where the Reggeon mechanism plays an important role. We will study this reaction within a Regge-plus-resonance model in the next chapter.

In summary, we conclude that the associated strangeness production reaction $\gamma p \to K^+\Lambda(1520)$ is an adequate tool to study the properties of the $N(2120)$ resonance, and provides strong hints of its existence. This would corroborate the theoretical expectations of the chiral

inspired unitary [73, 74] and constituent quark [241] models, and would make more plausible the analysis of the $\gamma p \to K^0\Sigma^+$ CBELSA/TAPS data carried out in [244], where the existence of a $J^P = 3/2^-$ nucleon excited state around 2 GeV has also been claimed. In addition, the study of the $\gamma p \to K^+\Lambda(1520)$ reaction also sheds light on the structure of $\Lambda(1520)$ [74, 263], and its properties such as the $\bar{K}^* N \Lambda^*$ [236] and $K\Lambda^* N^*$ vertices (this work and Ref. [237]) and its radiative $\Lambda^* \to \Lambda\gamma$ decay [h_1 and h_2 magnetic couplings, Eq. (7.7), determined in this work].

Chapter 8

Regge signatures from forward CLAS $\Lambda(1520)$ photoproduction data

8.1 Introduction

In Chapter 7, we have carried out a combined analysis of CLAS and LEPS data for $\gamma p \to K^+\Lambda(1520)$ reaction within an effective Lagrangian approach and the isobar model. Indeed, the model leads to an overall good description of both sets of data, both at forward and backward K^+ angles, and for the whole range of measured γp invariant masses in the CLAS and LEPS experiments. However, for invariant masses $W > 2.35$ GeV and forward angles, some small discrepancies (though systematic) between the CLAS data and the theoretical predictions appear (see lower panels of Fig. 7.3 of Chapter 7, collected here in the Fig. 8.2), which led to a moderate value of the best-fit $\chi^2/dof \sim 2.5$.

This should not be entirely surprising, since the model of Chapter 7 is not suited at high energies and forward angles, where quark-gluon string mechanisms could become important [235, 236, 264]. Actually, it is obvious from the analysis of the experimental hadron cross section data that the Reggeon and the Pomeron exchange mechanisms play a crucial role at high energies and small transferred momenta [265, 266]. The underlying philosophy of the Regge formalism is as follows. In

modelling the reaction amplitude for the $\gamma p \to KY$ process at high energies and small $|t|$ or $|u|$, instead of considering the exchange of a finite selection of individual particles, the exchange of entire Regge trajectories is taken into account. This exchange can take place in the t channel (kaonic trajectories) or u channel (hyperonic trajectories). As such, Regge theory offers an elegant way to circumvent the controversial issue of modelling high-spin, high-mass particle exchange.

Different dominant mechanisms have been proposed to describe the LAMP2 (Daresbury laboratory [227]) high energy differential cross sections. Thus, in Refs. [235, 264] it was claimed a large contribution from a t-channel $\bar{K}^*$ Regge exchange. However, in Ref. [236], it was argued that the $\bar{K}^*$ contribution should be quite small, almost negligible, since the $K^*N\Lambda^*$ coupling is expected to be much smaller than the value implicitly assumed in the previous works[1]. Nevertheless, a Reggeon exchange model, but with a $\bar{K}$- (instead of a $\bar{K}^*$) trajectory was also used in Ref. [236]. It was also discussed there that the $\bar{K}$ Reggeon mechanism is more favored by the LAMP2 data than the $\bar{K}^*$ Reggeon one, and that it is able to reproduce the available experimental data in the region from $E_\gamma^{\rm LAB} \sim 2.8$ GeV up to 5 GeV. Reggeized propagators for the $\bar{K}$ and $\bar{K}^*$ exchanges in the t-channel implemented in a gauge-invariant manner were employed in Ref. [239] and compared to Daresbury data. Note, however, that the $\bar{K}^*$ exchange contribution was also neglected in Ref. [239].

In this chapter, we aim to correlate the systematic (small) visible discrepancies, at high γp invariant masses and small angles, among the theoretical predictions of last chapter and the CLAS data with Regge effects. To this end, we improve on the model of last chapter by including the contribution of a $\bar{K}-$Regge trajectory exchange at high energies and low momentum transfers. We use a hybrid model which interpolates from the hadron effective Lagrangian approach, for energies close to threshold, to the quark-gluon string reaction mechanism

[1]This is because the $\Lambda(1520)$ resonance is located very close to the threshold energy of the $\pi\Sigma^*$ channel, which dominates the $\Lambda(1520)$ dynamics. Indeed, it could be considered as bound state of these two hadrons, with some corrections from coupled channel dynamics. For very small binding energies, all the couplings of the resonance tend to zero as the mass of the bound state approaches the $\pi\Sigma^*$ threshold [267].

approach, respecting gauge invariance.

Recently, it has appeared a work [268] with similar objectives and ideas. There, the crucial role played by the u-channel $\Lambda(1115)$ hyperon pole term at backward angles is confirmed, as well as the importance of the $N^*(2120)$ resonance to describe the LEPS data. Moreover, Regge effects are also discussed and taken into account, within a hybrid model that has indeed many formal resemblances[2] with the one that will be presented in this work. However, in sharp contrast with the model derived here, $\bar{K}^*$ Regge trajectory effects are considered in Ref. [268] and claimed to provide a considerable contribution at high energies. It is also claimed in this reference that the contribution from $\bar{K}$ and $\bar{K}^*$ exchange play a similar role in the reproduction of the CLAS data. Furthermore, the couplings of the $N^*(2120)$ state are fixed to those deduced in the constituent quark model of Refs. [241, 269], and a large width of 330 MeV is also set for this resonance. In this way, a great opportunity to take advantage of the accurate LEPS and CLAS data, not only for claiming the existence of the two-star $N^*(2120)$ state, but also for constraining/determining some of its poorly known properties is somehow missed in the analysis carried out in Ref. [268].

The present chapter is based on Ref. [270] and it is organized as follows. In Sec. 8.2, we shall discuss the formalism and the main ingredients of the model. In Sec. 8.3, we will present our main results and finally, a short summary and conclusions will be given in Sec. 8.4.

8.2 Formalism and ingredients

8.2.1 Feynman amplitudes

Within the effective Lagrangian approach for the $\Lambda(1520)$ photoproduction reaction,

$$\gamma(k_1,\lambda)p(k_2,s_p) \to K^+(p_1)\Lambda^*(p_2,s_{\Lambda^*}), \tag{8.1}$$

[2]Nevertheless, as we will explain below, some of the parameters found in Ref. [268] make difficult/doubtful the theoretical interpretation of the scheme of this reference, since t-channel Regge effects would have also been considered for large scattering angles.

the invariant scattering amplitudes are defined as

$$-iT_i = \bar{u}_\mu(p_2, s_{\Lambda^*}) A_i^{\mu\nu} u(k_2, s_p) \epsilon_\nu(k_1, \lambda), \tag{8.2}$$

where the kinematical variables (k_1, k_2, p_1, p_2) are defined as in Chapter 7, with t, s and u, the Mandelstam variables: $t = q_t^2 = (k_1 - p_1)^2$, $s = (k_1 + k_2)^2$ and $u = q_u^2 = (p_2 - k_1)^2$. On the other hand, u_μ and u are dimensionless Rarita-Schwinger and Dirac spinors, respectively, while $\epsilon_\nu(k_1, \lambda)$ is the photon polarization vector. In addition, s_p and s_{Λ^*} are the proton and $\Lambda(1520)$ polarization variables, respectively. The sub-index i stands for the contact, t-channel antikaon exchange, s-channel nucleon and $N^*(2120)$ ($\equiv N^*$) resonance pole terms and the u-channel Λ pole mechanism (depicted in Fig. 7.2 of Chapter 7). In Eq. (8.2), $A_i^{\mu\nu}$ are the reduced tree level amplitudes which can be obtained from the effective Lagrangian densities given in last chapter. For the sake of completeness, we also present here these amplitudes (see Refs. [237, 246] or the previous chapter for some more details):

$$A_t^{\mu\nu} = -e\frac{g_{KN\Lambda^*}}{m_K}\frac{1}{t - m_K^2} q_t^\mu (q_t^\nu - p_1^\nu)\gamma_5 \, f_{\rm c}, \tag{8.3}$$

$$\begin{aligned} A_s^{\mu\nu} = & -e\frac{g_{KN\Lambda^*}}{m_K}\frac{1}{s - m_N^2} \, p_1^\mu \gamma_5 \, [\not{k}_1 \gamma^\nu \, f_{\rm s} + (\not{k}_2 + m_N)\gamma^\nu \, f_{\rm c} \\ & + (\not{k}_1 + \not{k}_2 + m_N) i \, \frac{\kappa_p}{2m_N} \sigma_{\nu\rho} k_1^\rho \, f_{\rm s}\Big], \end{aligned} \tag{8.4}$$

$$A_c^{\mu\nu} = e\frac{g_{KN\Lambda^*}}{m_K} g^{\mu\nu}\gamma_5 \, f_{\rm c}, \tag{8.5}$$

$$\begin{aligned} A_R^{\mu\nu} = & \gamma_5 \left(\frac{g_1}{m_K}\not{p}_1 g^{\mu\rho} - \frac{g_2}{m_K^2} p_1^\mu p_1^\rho\right) \frac{\not{k}_1 + \not{k}_2 + M_{N^*}}{s - M_{N^*}^2 + i M_{N^*}\Gamma_{N^*}} \\ & \times P_{\rho\sigma}\left[\frac{e f_1}{2m_N}(k_1^\sigma \gamma^\nu - g^{\sigma\nu}\not{k}_1) \right. \\ & \left. + \frac{e f_2}{(2m_N)^2}(k_1^\sigma k_2^\nu - g^{\sigma\nu} k_1 \cdot k_2)\right] f_R, \end{aligned} \tag{8.6}$$

$$\begin{aligned} A_u^{\mu\nu} = & \left[\frac{h_1}{2m_\Lambda}(k_1^\mu \gamma^\nu - g^{\mu\nu}\not{k}_1) + \frac{h_2}{(2m_\Lambda)^2}(k_1^\mu q_u^\nu - g^{\mu\nu} k_1 \cdot q_u)\right] \\ & \times \frac{\not{q}_u + m_\Lambda}{u - m_\Lambda^2} g_{KN\Lambda}\gamma_5 f_u. \end{aligned} \tag{8.7}$$

Form factors, needed because the hadrons are not point-like particles, have been also included in the above expressions. We use the following parametrization [271, 272]:

$$f_i = \frac{\Lambda_i^4}{\Lambda_i^4 + (q_i^2 - M_i^2)^2}, \quad i = s,\ t,\ R,\ u \tag{8.8}$$

$$f_c = f_s + f_t - f_s f_t, \quad \text{and} \begin{cases} q_s^2 = q_R^2 = s, \\ M_s = m_N, \\ M_t = m_K, \\ M_R = M_{N^*}, \\ M_u = m_\Lambda, \end{cases} \tag{8.9}$$

where the form of f_c is chosen such that the on-shell values of the coupling constants are reproduced and gauge invariance is preserved.

8.2.2 Regge contributions

We base our model on the exchange of a dominant $\bar{K}$ Regge trajectory in the t-channel, as suggested in Ref. [236]. The kaon trajectory represents the exchange of a family of particles with kaon-type internal quantum numbers. We will discuss two different models to include the Regge contribution in the present calculation [3]:

- model A: In this case, the kaon Regge trajectory contribution is obtained from the Feynman amplitude $A_t^{\mu\nu}$ of Eq. (8.3) by replacing the usual kaon pole-like Feynman propagator by a so-called Regge propagator, while keeping the rest of the vertex structure, i.e.,

$$\frac{1}{t - m_K^2} \to \left(\frac{s}{s_0}\right)^{\alpha_K} \frac{\pi \alpha'_K}{\Gamma(1 + \alpha_K)\sin(\pi \alpha_K)}, \tag{8.10}$$

  with $\alpha_K(t) = \alpha'_K(t - m_K^2) = 0.8\ \text{GeV}^{-2} \times (t - m_K^2)$, the linear Reggeon trajectory associated to the kaon quantum numbers. The constant s_0 is taken as the Mandelstam variable s at threshold [$s_0 = (m_K + M_{\Lambda^*})^2$], and it is introduced to fix the dimensions

[3] We remind that when Reggeized propagators are employed the gauge invariance is broken, and that t-channel Regge effects should only be relevant for forward angles and high energies. These two points will be addressed below.

and to normalize the coupling constants. This approach is similar to that followed in Ref. [239], which was also adopted in Ref. [268]. The scattering amplitude for the Reggeon exchange will finally read

$$(A_t^{\mu\nu})^{\rm Regg} = -e\frac{\bar{g}_{KN\Lambda^*}}{m_K}\frac{1}{t-m_K^2}q_t^\mu(q_t^\nu - p_1^\nu)\gamma_5\mathcal{F}_A^{\rm Regg}, \quad (8.11)$$

$$\mathcal{F}_A^{\rm Regg}(t) = \left(\frac{s}{s_0}\right)^{\alpha_K}\frac{\pi\alpha'_K(t-m_K^2)}{\Gamma(1+\alpha_K)\sin(\pi\alpha_K)}, \quad (8.12)$$

where $\bar{g}_{KN\Lambda^*} = g_{KN\Lambda^*}\times\hat{f}$, with $\hat{f}$ a overall normalization factor of the Reggeon exchange contribution. Actually, Reggeon couplings to mesons and baryons might be, in general, different by up to a factor of 2 [266]. This undetermined scale will be fitted to the available data.

Note that the Regge propagator of Eq. (8.10) has the property that it reduces to the Feynman propagator $1/(t-m_K^2)$ if one approaches the first pole on the trajectory (i.e. $t\to m_K^2$, and thus $\mathcal{F}_A^{\rm Regg}\to 1$). This means that the farther we go from the pole, the more the result of the Regge model will differ from conventional Feynman diagram based models.

- model B: In the region of negative t, the Reggeized propagator in Eq. (8.12) exhibits a factorial growth[4], which is in principle not acceptable [273]. Accordingly, the authors of Refs. [236, 266] proposed the use of a form factor that decreased with t and a simplified expression for the Regge contribution[5]

$$T_{\rm Regg}\sim\frac{e\bar{g}_{KN\Lambda^*}}{m_K}\left(\frac{s}{s_0}\right)^{\alpha_K(t)}F(t), \quad (8.13)$$

[4]Note, $[\Gamma(1+\alpha_K)\sin(\pi\alpha_K)]^{-1} = \Gamma(1-\alpha_K)/\pi\alpha_K$.

[5]In Refs. [236, 266], trajectories with a rotating ($e^{-i\pi\alpha_K(t)}$) phase, instead of a constant phase (see for instance the discussion in Ref. [274]) were assumed. The difference is an additional factor $(-1)^{\alpha_K(t)}$ in Eq. (8.13), which only affects to the interference between the Regge and hadronic contributions. Such interference occurs only in a limited window of γp invariant masses and t values, that is not well theoretically defined. Nevertheless, the CLAS data favor a constant phase as used in Eq. (8.13).

with $F(t)$ a Gaussian form factor that accounts for the compositeness of the external (incoming and outgoing) hadrons,

$$F(t) = e^{t/a^2}, \tag{8.14}$$

with a typical value of the cutoff parameter $a \sim 2$ GeV. By analogy with model A, we include in this context the Regge effects by replacing the form factor f_c in Eq. (8.3) by,

$$f_c \;\; \rightarrow \;\; \hat{f} \times \mathcal{F}_B^{\rm Regg} = \hat{f} \times \left(\frac{s}{s_0}\right)^{\alpha_K(t)} e^{t/a^2} \, . \tag{8.15}$$

Considerations on gauge invariance

The inclusion of Regge effects, in either of the two models , breaks gauge invariance. The amplitudes of the s-channel $N^*(2120)$ and the u-channel $\Lambda(1115)$ pole mechanisms are gauge invariant by themselves, while some cancellations among the t-channel $\bar{K}$ exchange, the s-channel nucleon pole and contact-term contributions are needed to fulfill gauge invariance. In the s-channel nucleon pole amplitude, the terms modulated by the form factor f_s are already gauge invariant. Thus, the cancellations mentioned refer only to the part of the T_s amplitude affected by the form factor f_c. We will denote this partial amplitude as T_s^*. Thus, any modification of the t-channel $\bar{K}$ exchange mechanism should have an appropriate counterpart in the nucleon pole and contact term contributions. To restore gauge invariance we follow the procedure discussed in Refs. [275, 276] and also adopted in [239], and replace $(T_t^{\rm Regg} + T_s^* + T_c)$ by

$$T_t^{\rm Regg} + (T_s^* + T_c) \times \hat{f} \times \mathcal{F}_{A,B}^{\rm Regg} \, . \tag{8.16}$$

Hybrid hadron and Reggeon exchange model

We propose a hybrid mechanism to study the $\gamma p \to K^+\Lambda(1520)$ reaction in the range of laboratory photon energies explored by the CLAS Collaboration data. At the lowest invariant masses, near threshold, we consider the effective Lagrangian model of last chapter, which amplitudes were collected in Subsec. 8.2.1. However, for the higher photon energies ($W > W_0$) and at low momentum transfers ($|t| < t_0$), or

equivalently very forward K^+ angles, we assume that the string quark–gluon mechanism, discussed in Subsec. 8.2.2, is dominant. Here, W_0 is a certain value of the γp invariant mass above which the Regge contribution starts becoming relevant. Similar considerations apply to the Mandelstam variable t, and its distinctive value t_0, which limits the kaon scattering angles where the Regge behaviour is visible. We will implement a smooth transition/interpolation between both reaction mechanisms [236], following the procedure adopted in Ref. [239]. Actually, we define/parametrize this hybrid model by using the invariant amplitudes of Eqs. (8.3)–(8.7), but replacing the form factor f_c by $\bar{f}_c$

$$f_c \to \bar{f}_c \equiv \mathcal{F}_{A,B}^{\rm Regg} \times \hat{f} \times \mathcal{R} + f_c(1-\mathcal{R}) \tag{8.17}$$

with

$$\mathcal{R} = \mathcal{R}_W \times \mathcal{R}_t, \tag{8.18}$$

$$\mathcal{R}_W = \frac{1}{1+e^{-(W-W_0)/\Delta W}}, \tag{8.19}$$

$$\mathcal{R}_t = \frac{1}{1+e^{(|t|-t_0)/\Delta t}}, \tag{8.20}$$

where we fix $W_0 = 2.35$ GeV and $\Delta W = 0.08$ GeV from the qualitative comparison of the predictions of last chapter with the CLAS data and from the findings of Ref. [239]. In addition, we consider t_0 and Δt as free parameters that will be fitted to data.

It is easy to understand that $\mathcal{R}_W$ goes to one or to zero when $W \gg W_0$ or $W \ll W_0$, respectively, while $\mathcal{R}_t$ will tend to zero if $|t| \gg t_0$ and to one when $|t| \ll t_0$, as long as t_0 is sufficiently bigger than Δt. In this way, the amplitude of the reaction smoothly shifts from that determined from Eqs. (8.3)–(8.7) for $W \ll W_0$ to another one for $W \gg W_0$ that it is calculated using $T_t^{\rm Regg}$, instead of T_t, with the replacement of Eq. (8.16) implemented to preserve gauge invariance. Thus, Regge effects are incorporated with the variation of $\mathcal{R}_W$ from zero to one. Similar considerations apply to the variation of the Mandelstam variable t. The transition from the Regge model to the the effective Lagrangian one is controlled by the skin parameters ΔW and Δt.

Finally, we note that gauge invariance is accomplished at any value of $\mathcal{R}$.

8.2.3 Differential cross section

The unpolarized differential cross section in the center of mass (c.m.) frame for the $\gamma p \to K^+\Lambda(1520)$ reaction reads

$$\frac{d\sigma}{d\cos\theta_{\rm c.m.}} = \frac{m_N M_{\Lambda^*}|\vec{k}_1^{\rm c.m.}||\vec{p}_1^{\rm c.m.}|}{8\pi\left(W^2-m_N^2\right)^2}\sum_{\lambda,s_p,s_{\Lambda^*}}|T|^2, \qquad (8.21)$$

where $\vec{k}_1^{\rm c.m.}$ and $\vec{p}_1^{\rm c.m.}$ are the photon and K^+ meson c.m. three-momenta, and $\theta_{\rm c.m.}$ is the K^+ polar scattering angle. The differential cross section $d\sigma/d(\cos\theta_{\rm c.m.})$ depends on W and also on $\cos\theta_{\rm c.m.}$.

In addition to the three new free parameters (t_0, Δt and $\hat{f}$) introduced to account for Regge effects, the model of last chapter already had nine free parameters: i) the mass and width (M_{N^*} and Γ_{N^*}) of the $N^*(2120)$ resonance, ii) the cut off parameters $\Lambda_s = \Lambda_t = \Lambda_u \equiv \Lambda_B$ and Λ_R, and iii) the $N^*(2120)$ resonance electromagnetic $\gamma N N^*$ (ef_1, ef_2) and strong $N^*\Lambda^* K$ (g_1, g_2) couplings and the $\Lambda(1520)$ magnetic $\gamma\Lambda\Lambda^*$ (h_1) one. To reduce the number of best-fit parameters, we have kept unchanged the contribution of the u-channel Λ pole contribution, and thus we have set the $\gamma\Lambda\Lambda^*$ coupling to the value obtained in the Fit II of last chapter ($h_1 = 0.64$). This is justified since the contribution of the u-channel Λ pole term is only important for backward K^+ angles, and the Regge mechanism should only play certain role at forward angles, In addition, we have also fixed Λ_B to the value of 620 MeV quoted in last chapter. This cutoff parameter also appears in T_u, and in the definition of the form-factor f_c, which following Eq. (8.17) is replaced by $\bar{f}_c$ to account for Regge effects at high energies and low momentum transfers [6].

Thus, finally, we have ten free parameters which will be fitted to the recent differential cross section data from the CLAS [80] and LEPS [79] experiments.

[6] Λ_B also appears in the definition of the f_s form-factor that affects to some pieces of the s-channel nucleon pole term. These contributions are however quite small since they are greatly suppressed by f_s, and do affect very little the best fit.

8.3 Numerical results and discussion

We have performed a ten-parameter (g_1, g_2, Λ_R, ef_1, ef_2, M_{N^*}, Γ_{N^*}, t_0, Δt and $\hat{f}$) χ^2-fit to the LEPS [79] and CLAS [80] measurements of $d\sigma/d(\cos\theta_{\rm c.m.})$. There is a total of 216 available data (157 points from CLAS and another 59 ones from LEPS, depicted in Figs. 8.1 and 8.3, respectively). The systematical errors of the experimental data (11.6% [80] and 5.92% [79], for CLAS and LEPS, respectively) have been added in quadratures to the statistical ones and taken into account in the fits, as it was done in last chapter. LEPS data lie in the K^+ forward angle region and were taken below $E_\gamma = 2.4$ GeV, while the recent CLAS measurements span a much larger K^+ angular and photon energy regions (nine intervals of the γp invariant mass from the reaction threshold, 2.02 GeV, up to 2.85 GeV) [7].

We have considered two different schemes to include Regge effects (models A and B), as discussed in Subsec. 8.2.2. Best fit results are listed in Table 8.1, where we also compile the obtained parameters in our previous work (Fit II of last chapter). For each fit, we also give the predicted $N^*(2120)$ partial decay width $\Gamma_{N^*\to\Lambda^*K}$ (Eq. (18) of Ref. [237]) and the resonance helicity amplitudes (Eqs. (15) and (16) of Ref. [237]) for the positive-charge state.

A χ^2/dof around 1.3 is obtained for both model A and B fits. This is significantly better than the best fit value obtained (2.5) in our previous work of last chapter, where Regge effects were not considered. We also see that the effective Lagrangian approach parameters (g_1, g_2, Λ_R, ef_1, ef_2, M_{N^*}, Γ_{N^*}), determined in the new fits carried out in this work, turn out to be in good agreement with those obtained in last chapter. Thus, the conclusions of last chapter still hold, in particular this new study gives further support to the existence of the two-star $N^*(2120)$ resonance, and its relevance in the CLAS & LEPS $\gamma p \to K^+\Lambda(1520)$ data. On the other hand, the hybrid model parameters (t_0, Δt and $\hat{f}$) turn out to be reasonable from what one would expect by a direct inspection of the CLAS data (t_0, Δt) and previous estimates [236, 266].

The fits obtained here are of similar quality to the best ones re-

[7] To compute the cross sections in each interval, we always use the corresponding mean value of W, as in last chapter.

Table 8.1: Values of some parameters determined in this work and in last chapter. Model A(B) parameters have been adjusted to the combined LEPS [79] and CLAS [80] $\gamma p \to K^+\Lambda(1520)$ $d\sigma/d(\cos\theta_{\rm c.m.})$ data including Regge effects as discussed in Eq. (8.12) (Eq. (8.15)). In the last column, we compile some results from Fit II of last chapter, where the mechanism of Reggeon exchange was not considered. Finally, we also give for each fit, the predicted $N^*(2120)$ partial decay width $\Gamma_{N^*\to\Lambda^*K}$, and the helicity amplitudes for the positive-charge N^* state.

	This work		Chapter 7
	model A	model B	Fit II
g_1	1.3 ± 0.2	1.4 ± 0.2	1.6 ± 0.2
g_2	0.9 ± 0.5	1.1 ± 0.5	2.2 ± 0.5
Λ_R [MeV]	1252 ± 78	1259 ± 76	1154 ± 47
ef_1	0.134 ± 0.016	0.123 ± 0.015	0.126 ± 0.012
ef_2	-0.110 ± 0.014	-0.100 ± 0.013	-0.097 ± 0.010
M_{N^*}[MeV]	2146 ± 5	2145 ± 5	2135 ± 4
Γ_{N^*}[MeV]	174 ± 14	171 ± 13	184 ± 11
t_0[GeV^2]	0.73 ± 0.04	0.94 ± 0.05	–
Δt[GeV^2]	0.28 ± 0.02	0.30 ± 0.04	–
$\hat{f}$	0.38 ± 0.01	0.37 ± 0.01	–
χ^2/dof	1.3	1.3	2.5
	Derived Observables		
$A^{p^*}_{1/2}[10^{-3}\text{GeV}^{-1/2}]$	-9.7 ± 4.1	-8.8 ± 3.8	-7.3 ± 3.0
$A^{p^*}_{3/2}[10^{-2}\text{GeV}^{-1/2}]$	2.3 ± 1.1	2.1 ± 1.0	2.5 ± 0.8
$\Gamma_{N^*\to\Lambda^*K}$ [MeV]	22 ± 7	25 ± 7	30 ± 8
$\frac{\Gamma_{N^*\to\Lambda^*K}}{\Gamma_{N^*}}$[%]	12.9 ± 3.9	14.8 ± 4.5	16.2 ± 4.2

ported in Ref. [268], where in addition to the Regge effects driven by kaon exchange in the $t-$channel, some sizable Regge contributions induced by $\bar{K}^*$ exchanges are included as well. However, as mentioned in the introduction, theoretically it is difficult to accommodate a $\bar{K}^*$ mechanism contribution as large as that claimed in Ref. [268] (see Secs. 3.1 and 3.2 of this latter reference). On the other hand, a bunch of N^* resonances are included in the approach followed in Ref. [268]. Their couplings and masses are in most cases fixed to the constituent quark model predictions of Refs. [241, 269] and a common width of 330 MeV is assumed for all of them. Among all of them, it turns out to be

the $N^*(2120)$, the state that provides the most important contribution, which confirms previous claims [237, 238] . We have adopted a different point of view and have used the accurate CLAS & LEPS $\gamma p \to K^+\Lambda(1520)$ data not only to claim the existence of the $N^*(2120)$ resonance, but also to establish some of its properties. Thus, we find a much narrower state ($\Gamma_{N^*} \sim 170 - 175$ MeV) and complete different helicity amplitudes. Moreover, the values used in Ref. [268] ($A^{p^*}_{1/2} = 36$ and $A^{p^*}_{3/2} = -43$ in $[10^{-3}\text{GeV}^{-1/2}]$ units) are incompatible both with

$$A^{p^*}_{1/2}[10^{-3}\text{GeV}^{-1/2}] = 125 \pm 45 \tag{8.22}$$

$$A^{p^*}_{3/2}[10^{-2}\text{GeV}^{-1/2}] = 15 \pm 6\,, \tag{8.23}$$

given in Ref. [240] and with previous measurements [261]

$$A^{p^*}_{1/2}[10^{-3}\text{GeV}^{-1/2}] = -20 \pm 8 \tag{8.24}$$

$$A^{p^*}_{3/2}[10^{-2}\text{GeV}^{-1/2}] = 1.7 \pm 1.1 \tag{8.25}$$

quoted in the 2008 PDG edition [262], that in turn are in quite good agreement with our predictions in Table 8.1. Having improved the quality of our fit, achieving now an accurate description of the CLAS data for all angles and invariant mass windows (see below), our results give an important support to the measurements of Ref. [261], which do not seem entirely consistent with those reported in Ref. [240]. Given the two stars status (evidence of existence is only fair) granted to the $N^*(2120)$ resonance in the multichannel partial wave analysis of pion and photo-induced reactions off protons carried out in Ref. [240], the discrepancy with our predicted helicity amplitudes should not be used to rule out our fits, but rather one should interpret our results as further constrains on these elusive observables. Note that the helicity amplitudes given in Eqs. (8.24) and (8.25) were also used in Ref. [242], where the $ep \to eK^+\Lambda(1520)$ CLAS data of Ref. [228] was successfully described.

In addition, there is a disturbing feature in the fits presented in [268]. There, it is found $t_0 \sim 3$ GeV^2, though with a large error, while we obtain values in the range 0.7–0.9 GeV^2. A value of t_0 as high as 3 GeV^2 necessarily changes the meaning of the interpolating function $\mathcal{R}_t$ in Eq. (8.20), since it will not effectively filter now forward angles. This

is easily understood if one realizes that for $W = 2.4$ GeV, $|t|$ remains below 2.5 GeV^2 for all possible K^+ c.m. angles, and for the highest invariant mass $W = 2.8$ GeV, the bound $t = -3$ GeV^2 is reached for $\cos\theta_{\rm c.m.} = -0.3$. Thus in the scheme employed in [268], the transition function $\mathcal{R}_t$ effectively modifies the predictions of the effective Lagrangian approach allowing for some Regge effects for large scattering angles, which seems quite doubtful. Probably, this dis-function of the physical meaning of $\mathcal{R}_t$ could be a consequence of the unnecessary complexity of the scheme used in Ref. [268] with various N^* contributions and the inclusion of $\bar{K}^*$ driven effects, with parameters in some cases fixed to values with little theoretical/experimental support. Nevertheless, it should be acknowledged that the work of Ref. [268] is pioneer in exploring the possible existence of Regge effects in the CLAS data.

The differential $d\sigma/d(\cos\theta_{\rm c.m.})$ distributions calculated with the model B best-fit parameters are shown in Figs. 8.1 and 8.3 as a function of $\cos\theta_{\rm c.m.}$ and for various γp invariant mass intervals. Model A results are totally similar and for brevity, they will not be discussed any further. Only statistical errors are displayed in these two figures and the contributions from different mechanisms are shown separately. Thus, we split the full result into three main contributions: effective Lagrangian approach background, Reggeon exchange and resonance $N^*(2120)$. The first one corresponds to the t-channel $\bar{K}$ exchange, nucleon pole, contact and u-channel $\Lambda(1115)$ hyperon pole terms of Eqs. (8.3)–(8.5) and (8.7), but evaluated with the modified form-factor $f_c(1-\mathcal{R})$ instead of f_c, as discussed in Eq. (8.17). (Note that f_c appears neither in the $\Lambda(1115)$ nor in the resonance $N^*(2120)$ mechanisms because both of them are gauge invariant by themselves). The Reggeon contribution is calculated from the f_c terms of the $\bar{K}$ exchange, nucleon pole and contact terms of Eqs. (8.3)–(8.5) and (8.7), but now evaluated with the generalized Regge form-factor $\mathcal{F}_B^{\rm Regg}\hat{f}\mathcal{R}$.

In Fig. 8.1, we show our predictions and the data of the CLAS collaboration [80]. The blue-dashed and black-dash-dotted curves stand for the contributions from the effective Lagrangian approach background and Reggeon exchange mechanism, respectively. The green-dotted lines show the contribution of the $N^*(2120)$ resonance term, while the red-solid lines display the results obtained from the full model. In Fig. 8.2 and for comparison purposes, we display the final results

from our previous Fit II carried out in last chapter, where Regge effects were not considered. We find an overall good description of the data for the whole range of measured γp invariant masses and it is significantly better than that exhibited in the right panels. We see that the Regge improved model provides now an excellent description of the CLAS data for values of $\cos\theta_{\rm c.m.}$ above 0.5, and high energies, $W \geq 2.3$ GeV, as expected. On the other hand, by construction Regge contributions effectively disappear at low invariant masses $W < 2.3$ GeV and backward K^+ angles. Thus, we recover for this latter kinematics the effective Lagrangian approach, including resonance $N^*(2120)$ and hyperon $\Lambda(1115)$ contributions, which successfully described the data in this region [246].

In the left panels of Fig. 8.3, the differential cross section deduced from the results of the model B fit, as a function of the LAB frame photon energy and for different forward c.m. K^+ angles, is shown and compared both to LEPS [79] and CLAS [80] datasets. The blue-dashed and black-dash-dotted curves stand for the contributions from the effective Lagrangian approach background and Reggeon exchange mechanism, respectively. The green-dotted lines show the contribution of the $N^*(2120)$ resonance term, while the red-solid lines display the results obtained from the full model. In the right panels and for the sake of clarity, we display the final results from our previous Fit II carried out in last chapter, where Regge effects were not considered. We see the description of LEPS data is almost not affected by the Regge contributions, and the bump structure in the differential cross section at forward K^+ angles is fairly well described thanks to the significant contribution from the N^* resonance in the $s-$channel, as pointed out in last chapter. However, the inclusion of Regge effects significantly improves the description of the CLAS data [8], as one would expect from the discussion of the results of Fig. 8.1. Moreover, the hybrid model presented in this work provides a better energy behavior for the forward cross section at energies higher than those explored by the CLAS data (see the two (d) panels in Fig. 8.3).

Fig. 8.4 shows the $\Lambda(1520)$ total photoproduction cross section as

[8] The CLAS cross sections shown in the figure were obtained from the appropriate CLAS measurements displayed in Fig. 8.1, relating W to the LAB photon energy.

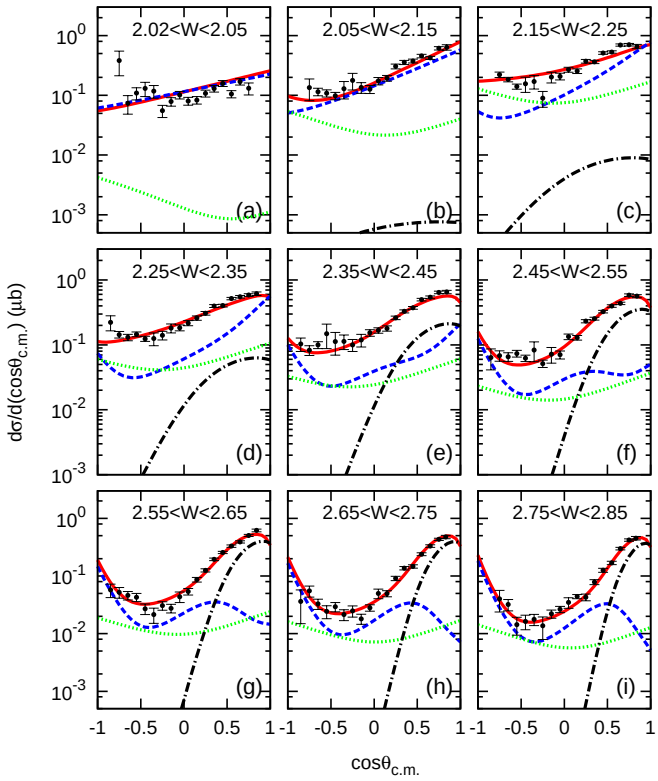

Figure 8.1: Model B $\gamma p \to K^+\Lambda(1520)$ differential cross sections as a function of $\cos\theta_{\rm c.m.}$ compared with the CLAS data [80] for different γp invariant mass intervals (indicated in the different panels in GeV units). Only statistical errors are displayed.

a function of the photon energy. The blue-dashed and black-dash-dotted curves stand for the contributions from the effective Lagrangian approach background and Reggeon exchange mechanism, respectively. The green-dotted lines show the contribution of the $N^*(2120)$ resonance term, while the red-solid lines display the results obtained from the full model. The shaded region accounts for the 68% CL band inherited from the Gaussian correlated statistical errors of the parameters. Despite the overall normalization of the CLAS [9] measurements [80] is in rather strong disagreement with the data from LAMP2 [227], the

[9]We display extrapolated total cross sections, from data summed over the useful

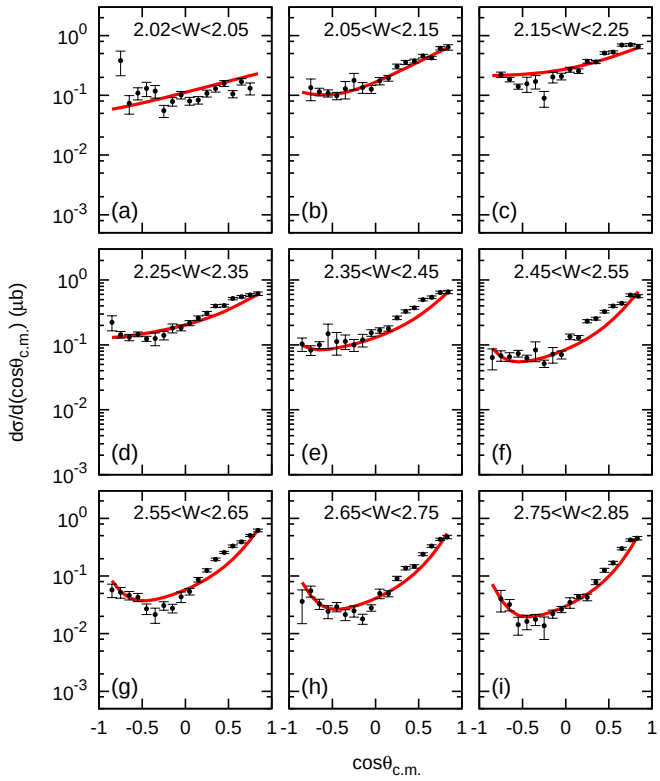

Figure 8.2: Total results from our previous Fit II carried out in Chapter 7, where Regge effects were not considered.

photon energy dependence of both data sets seems compatible above 2.3 or 2.4 GeV. This can be appreciated in Fig. 8.4, where the LAMP2 cross sections have been scaled down by a factor 0.6. This agreement might give some support to the idea of finding Regge signatures in the CLAS data. Results from model B are also shown, which turn out to provide a good description of both sets of data. We should, however, prevent the reader about the *ad hoc* modification of the normalization of the old LAMP2 cross sections [10]. Nevertheless, it is reassuring that

acceptance of the detector, to 4π (red points in Fig. 11 of Ref. [80]).

[10]The low energy SAPHIR data [229] is in even in a stronger disagreement with the data from LAMP2, with the CLAS results lying almost exactly between these two measurements [80].

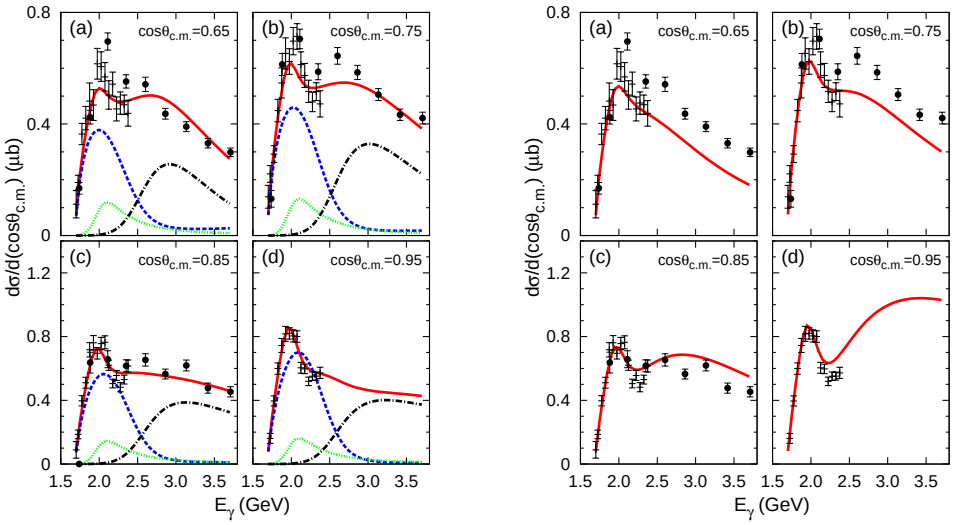

Figure 8.3: Left: Model B $\gamma p \to K^+\Lambda(1520)$ differential cross section as a function of the LAB frame photon energy for different c.m. K^+ polar angles. We also show the experimental LEPS [79] (crosses) and CLAS [80] (black dots) data. Only statistical errors are displayed. Right: Total results from our previous Fit II carried out in Chapter 7), where Regge effects were not considered.

the hybrid model presented in this work, including Regge effects, is able to predict the photon energy dependence of the LAMP2 data at energies well above than those explored by the CLAS data.

8.4 Conclusions

We have presented some evidences of Regge signatures in the CLAS data at forward angles, despite the energies involved in that experiment are only moderately high. This is not entirely surprising, because above $E_\gamma > 2.3 - 2.4$ GeV, and up to an overall normalization, the CLAS $\Lambda(1520)$ total cross section dependence on the photon energy matches that inferred from the LAMP2 data, which extends up to 5 GeV, in a region where the Regge behavior is expected to be visible (see Fig. 8.4). Indeed, we find a significant improvement on the descrip-

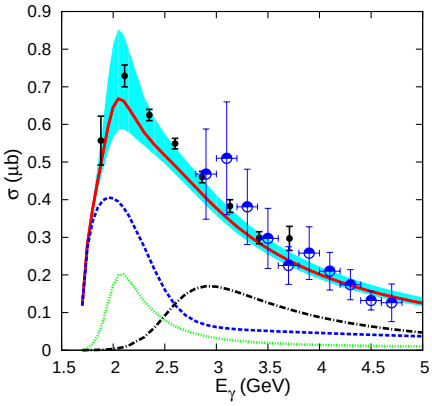

Figure 8.4: Total $\gamma p \to K^+\Lambda^*$ cross section as a function of the photon energy. Black filled circles and blue open circles stand for CLAS [80] and LAMP2 [227] data, respectively. LAMP2 cross sections have been scaled down by a factor 0.6. Results from model B are also shown.

tion of the CLAS high energy forward cross sections, when the effective Lagrangian approach of last chapter is supplemented with some string quark–gluon mechanism contributions determined by a kaon trajectory. Now, there are no visible systematic discrepancies between the hybrid approach predictions and the data. Thus, we confirm the findings of the recent work of Ref. [268] on the importance of the Regge effects in achieving an accurate description of the CLAS forward angular distributions.

We do not need to include any contribution from a $\bar{K}^*$ trajectory, in accordance to the analysis of the LAMP2 data carried out in Refs. [236, 239]. This is re-assuring since the $t-$channel $\bar{K}^*$ contribution should be quite small, almost negligible, in sharp contrast with previous works [231, 235, 264, 268], where a large $g_{K^*N\Lambda^*}$ coupling was assumed. Such big values for this coupling are ruled out by unitarized chiral models [74, 236, 277], that predict values for $g_{K^*N\Lambda^*}$ around a factor 10 (20) smaller than for instance those used in Refs. [231, 235, 268], and by measurements of the photon-beam asymmetry, as discussed in Ref. [239].

We have designed a gauge invariant hybrid model which smoothly interpolates from the hadron effective Lagrangian approach [246], at

energies close to threshold, to a model that incorporates quark-gluon string reaction mechanism contributions at high energies and forward K^+ scattering angles. We find an accurate description of both CLAS and LEPS data. The latter set of low energy cross sections is not affected by the inclusion of Regge effects. The bump structure observed at forward K^+ angles in these data is well described thanks to the significant contribution from the two-star $J^P = 3/2^-$ $N^*(2120)$ resonance in the s-channel, which existence gets a strong support from this improved analysis that is now fully consistent with the accurate CLAS data. Thus, this associated strangeness production reaction becomes an excellent tool to determine the properties of this resonance (helicity amplitudes determined by the couplings ef_1 and ef_2 or the strength of the $K\Lambda^* N^*$ vertex). In what respects to the CLAS data, Regge effects play a crucial role at forward angles for energies above 2.35 GeV, as commented before, while the backward angle data highlight the importance of the u-channel $\Lambda(1115)$ hyperon pole term. This latter fact can be used to constrain the radiative $\Lambda^* \to \Lambda\gamma$ decay, as it was firstly emphasized in last chapter.

The t-range explored by the CLAS data is not large enough to fully restrict the Regge form-factor, which is the major difference among the two models (A and B) introduced in this work. Though, in the region of negative t, the Reggeized propagator in Eq. (8.12) exhibits a factorial growth, which is in principle not acceptable, the limited range of momentum transfers accessible in the data does not see this unwanted behaviour. This is the same reason why the Gaussian cutoff parameter a in Eq. (8.14) is not further constrained. Unfortunately, the existing large discrepancies among CLAS and LAMP2 data sets prevents the inclusion of this latter experiment in the analysis carried out in this work. This constitutes an open problem, that might require new dedicated experiments.

Chapter 9

Conclusions

In this thesis we have discussed the following topics: NC photon emission reactions on nucleons and nuclei at intermediate energies, even parity meson resonance properties within an SU(6) spin-flavor symmetry scheme, $\Lambda(1520)$ photo-production reaction on protons.

In the first part (Chapters 3 - 5), we have investigated the NCγ emission reactions on nucleons and nuclei at intermediate energies. These processes are an important background for $\nu_\mu \to \nu_e$ and $\bar{\nu}_\mu \to \bar{\nu}_e$ oscillation experiments when photons are misidentified as $e^\pm$ from CCQE scattering of $\nu_e(\bar{\nu}_e)$.

In Chapter 3, we have developed a microscopic model for NC photon emission, based on previous work on weak pion production [39, 43, 50, 96]. At intermediate energies, the reaction on nucleons is dominated by the weak excitation of the $\Delta(1232)$ resonance and its subsequent decay into $N\gamma$. We have also calculated contributions from non-resonant mechanisms that, close to threshold, are fully determined by chiral symmetry. To extend the validity of the model to higher energies, contributions from the nucleon excited states [$N(1440)$, $N(1520)$ and $N(1535)$] of the second resonance region have been considered as well. Among them, we have found that the D_{13} $N(1520)$ resonance terms give a sizable contribution for (anti)neutrino energies above 1.5 GeV. The nucleon pole contributions are also relatively important, while the rest of N^* contributions, together with that of the πEx mechanism, can be safely neglected in the whole energy region studied in this work. The major source of uncertainties in the model comes from the lack

of a precise knowledge of the axial $N\Delta$ coupling $C_5^A(0)$, for which we have used a value of 1.00 ± 0.11, obtained in a reanalysis [40] of the $\nu p \to \mu^- p \pi^+$ ANL and BNL old bubble chamber data.

Next, we have extended the model to study the reaction on nuclear targets, taking into account Fermi motion, Pauli Blocking and the in-medium modifications of the Δ properties. We have predicted differential and total cross sections for several nuclei, including some of the common ones in current and future neutrino detectors (carbon, oxygen, argon, iron). The importance of nuclear corrections, in both the coherent and incoherent channels, has been stressed. The cross section dependence on the mass number and on the neutrino energy, different for the coherent and incoherent reactions, has been also discussed. Nuclear effects produce reductions of the order of 30% on the magnitude of the distributions of events and drastic changes in the shapes, becoming thus essential to achieve an accurate understanding of the response of the detectors in oscillation experiments.

In light of these results, a new analysis of the NC-induced photon production at MiniBooNE and T2K experiments with the present model, aiming at the clarification of the role played by NCγ events in these experiments, looked timely and important. This has been the goal of the next two chapters.

First, in Chapter 4, we have used our microscopic model to study the contribution from the NC photon emission processes to the electron-like irreducible background of the MiniBooNE experiment. Taking into account the detector mass, composition and efficiency, and the relevant components of the (anti)neutrino flux, we have calculated photon energy and polar angle (relative to the direction of the incoming neutrino) and reconstructed neutrino energy event distributions. This latter variable is relevant in the oscillation analysis, since it is used as the true neutrino energy. The largest contribution to the NCγ events in the mineral oil (CH_2) target of MiniBooNE arises from the incoherent reaction on ^{12}C, although the interactions on the two protons and coherent scattering on ^{12}C produce sizable, and similar in magnitude, yields. The contribution from muon neutrinos in antineutrino mode is found to be important, unlike the insignificant one of muon antineutrinos in neutrino mode.

We have compared our predictions with the results of Zhang and

Serot [88], based on an effective theory extended to higher energies using phenomenological form factors. The overall agreement is good in spite of the differences in the approaches. Moreover, the predictions of our model are in good agreement with the MiniBooNE in situ estimate, though there are some minor deviations, which could be partially accounted by the error on the detection efficiency ($\sim 15\%$). The conclusion of our work is that the NCγ processes cannot explain the excess of the signal-like events observed at MiniBooNE. This is in sharp contrast to the findings of Hill [90], obtained with a rather high and energy independent detection efficiency and neglecting nuclear effects. The forthcoming MicroBooNE experiment [159], capable of distinguishing photons from electrons, should be able to shed light on this puzzle.

In Chapter 5, we have applied our NCγ model to predict the single photon event rate at the SK water detector for the flux of the T2K experiment in neutrino mode. For a beam exposure of $N_{\rm POT} = 6.57\times10^{20}$, we obtain 0.421 ± 0.051 events without efficiency corrections. This prediction is 2.6 times larger than the one obtained from the NEUT Monte Carlo generator. The discrepancy is mostly in normalization, as we find similar shapes in photon energy, photon angular and neutrino energy distributions with both models. It can be only partially attributed to the lack of non-Δ production amplitudes or coherent photon emission in NEUT. The largest differences are likely to be related to the fact that NEUT, as many other neutrino event generators, use the outdated resonance model of Rein and Sehgal [157], which fails to reproduce electroproduction data. We conclude that further effort is needed to realistically estimate this small but irreducible background and increase the precision in the determination of oscillation parameters, particularly in δ_{CP} measurements.

Finally, it should be stressed that multinucleon mechanisms, which provide a significant amount of the CCQE-like cross section [26, 34], await to be investigated for the NCγ channel. Although these processes are bound to have some repercussion, they are unlikely to alter the picture dramatically.

In the second part of the thesis (Chapters 6 to 8), we have studied the lowest lying even parity meson resonances within a model

that starts from SU(6) flavor-spin symmetry, and the $\Lambda(1520)$ photoproduction reaction $\gamma p \to K\Lambda(1520)$.

Chapter 6 is devoted to the study of the low-lying even parity meson resonances dynamics. First, we have reviewed the model of Ref. [68], which provides a spin–flavor extension of the chiral SU(3) WT Lagrangian. The model predicts S-wave four meson interactions involving members not only of the π-octet, but also of the ρ-nonet. When Goldstone bosons are involved, the model is consistent with chiral symmetry and its breaking pattern as inferred from QCD. In addition, its extension to heavy flavors would be in principle also consistent with heavy quark spin symmetry, which is a proper QCD symmetry in the $m_Q \to \infty$ limit. Such a model leads to a fairly good description of the $J^P = 0^+$ and $J^P = 1^+$ sectors[1]. However, it is not so successful in the $J^P = 2^+$ sector, where it fails to appropriately describe some well established resonances, like the $f_2(1270)$ and $K_2^*(1430)$ states. We have improved on that by supplementing the model of Ref. [68] with new local VV interactions consistent with chiral symmetry.

To provide different pseudoscalar and vector mesons masses, a simple spin-symmetry breaking local term that preserved chiral symmetry was designed in [68]. In Chapter 6, we have studied in detail the structure of the SU(6) symmetry breaking local terms that respect (or softly break) chiral symmetry. We have derived the most general contact terms consistent with the chiral symmetry breaking pattern of QCD as expressed in terms of the auxiliary field $U = \exp i\sqrt{2}\phi/f$. We have also shown that there is a finite number of chirally invariant contact four meson-field interactions, restricted also by the other symmetries of the problem. To reduce the number of parameters to a manageable size, and in the spirit of large N_C, we have restricted our analysis to interactions involving just one trace.

Furthermore, we have carried out a phenomenological discussion of the effects of these new terms, and have found that their inclusion leads to a considerable improvement of the description of the $J^P = 2^+$

[1]Elastic unitarity in coupled channels is restored by solving an ultraviolet renormalized BSE. Resonances show up as poles in the first or second Riemann sheets of the unitarized meson–meson amplitudes. The positions of the poles determine masses and widths of the resonances, while the residues for the different channels define the corresponding coupling or branching fractions.

resonances, without spoiling the main features of the predictions obtained in Ref. [68] for the $J^P = 0^+$ and $J^P = 1^+$ spin–parity channels. In particular, we have found a significantly better description of the $I^G(J^{PC}) = 0^+(2^{++})$, $1^-(2^{++})$ and the $I(J^P) = \frac{1}{2}(2^+)$ sectors, that correspond to the $f_2(1270)$, $a_2(1320)$ and $K_2^*(1430)$ quantum numbers, respectively. Besides the position of the resonances, we also estimated the couplings of these states to the different particle channels, This information is relevant to describe the structure of the resonance and its favored decay modes. Our analysis shows that 2^+ states systematically require cutoff values which lie in the boundary of their natural hadronic domain. This could be an indication that D-wave mechanisms play some role in the formation of such states, or that some of these resonances are mostly genuine states. With this possible caveat in mind, we can say that the model provides a rather robust and successful scheme to study the low-lying even parity meson resonances that are dynamically generated by the logs that appear in the unitarity loops.

In Chapters 7 and 8, we have carried out a new analysis of the $\gamma p \to \Lambda(1520)K^+$ reaction at low energies within an effective Lagrangian approach and the isobar model. Possible Regge effects have been also investigated. We have presented results from combined fits to the recent CLAS [80] and LEPS [79], $d\sigma/d(\cos\theta_{\rm c.m.})$ data.

In the first of the these two chapters, we adopted the scheme of Ref. [237], and in addition to the contact, t-channel $\bar{K}$ exchange, and s-channel nucleon and $N(2120)$ resonance pole contributions, we have also studied the u-channel $\Lambda(1115)$ hyperon pole term. The latter mechanism had been ignored in all previous calculations [231, 236–238] that relied on the very forward K^+ angular LEPS data [78, 79], where its contribution was expected to be small.

Our model can simultaneously describe the new CLAS and the previous LEPS data. The contribution of the u-channel $\Lambda(1115)$ pole term plays an important role at backward angles, and it becomes more and more relevant as the photon energy increases, becoming essential above $W \geq 2.35$ GeV and $\cos\theta_{\rm c.m.} \leq -0.5$. The CLAS data also clearly support the existence of an odd parity $J = 3/2$ wide nucleon resonance with a mass in the region of 2.1 GeV, a width of around 200 MeV and a large partial decay width into $\Lambda^* K$. These features could be easily

accommodated within the constituent quark model results of Capstick and Roberts in Ref. [241] for the two stars PDG $N(2120)$ state. This would confirm previous claims [237, 238] from the analysis of the bump structure in the LEPS differential cross section at forward K^+ angles discussed in Fig. 7.4, and contradict previous negative claims made in [234] and [239] regarding this point. The recent analysis carried out in [242] of $\Lambda(1520)$ electroproduction off the proton also supports the existence of D_{13} $N(2120)$ resonance and its important role in these processes. All these findings would corroborate the theoretical expectations on the $N(2120)$ obtained in the chiral inspired unitary [73, 74] and constituent quark [241] models, and would make more plausible the analysis of the $\gamma p \to K^0\Sigma^+$ CBELSA/TAPS data carried out in [244], where the existence of a $J^P = 3/2^-$ nucleon excited state around 2 GeV was also claimed.

In Chapter 8, we have presented some evidences of Regge signatures in the CLAS data at forward angles, despite the energies involved in that experiment are only moderately high. This is not entirely surprising, because above $E_\gamma > 2.3 - 2.4$ GeV, and up to an overall normalization, the CLAS $\Lambda(1520)$ total cross section dependence on the photon energy matches that inferred from the LAMP2 data, which extends up to 5 GeV, in a region where the Regge behavior is expected to be visible (see Fig. 7.6). Indeed, we find a significant improvement on the description of the CLAS high energy forward cross sections, when the effective Lagrangian approach of Chapter 7 is supplemented with some string quark–gluon mechanism contributions determined by a kaon trajectory. Now, there are no visible systematic discrepancies between the hybrid approach predictions and the data.

We designed a gauge invariant hybrid model which smoothly interpolates from the hadron effective Lagrangian approach [246], at energies close to threshold, to a model that incorporates quark-gluon string reaction mechanism contributions at high energies and forward K^+ scattering angles. We have found an accurate description of both CLAS and LEPS data. The latter set of low energy cross sections is not affected by the inclusion of Regge effects. The bump structure observed at forward K^+ angles in these data is well described thanks to the significant contribution from the two-star $J^P = 3/2^-$ $N^*(2120)$ resonance in the s-channel, which existence gets a stronger support from

this improved analysis that is now fully consistent with the accurate CLAS data.

In summary, we have shown that the associated strangeness production reaction $\gamma p \to K^+\Lambda(1520)$ reaction is an excellent tool to determine the existence and properties of the $N(2120)$ resonance (helicity amplitudes or the strength of the $K\Lambda^* N^*$ vertex). We have seen that this reaction also sheds light on the structure of the $\Lambda(1520)$ resonance [74, 263], and its properties such as the $\bar{K}^* N\Lambda^*$ and $K\Lambda^* N^*$ vertices (this work and Ref. [237]) and its radiative $\Lambda^* \to \Lambda\gamma$ decay [h_1 and h_2 magnetic couplings, Eq. (7.7), determined in this work]. Finally, we have also presented some evidences of Regge signatures in the recent CLAS data at forward angles for this reaction.

Chapter 10

Resumen de la tesis

Las oscilaciones de neutrinos atmosféricos se observaron por vez primera en Super-Kamiokande (SK) [278] y K2K [279], detectando en SK los neutrinos producidos en el acelerador de protones KEK, situado a 250 Km. A partir de entonces y gracias a la intensa actividad experimental y teórica en el campo en los últimos años, se ha conseguido delimitar con más o menos precisión los parámetros de oscilación [70]. Tanto los experimentos futuros, como los que se están realizando en la actualidad, aspiran a una más precisa determinación de las masas, los ángulos de mezcla de las diferentes especies de neutrinos y la posible fase de violación de simetría CP. Para ello es crucial el conocimiento exacto de la sección eficaz neutrino-núcleo con un error inferior al 10% en núcleos como ^{12}C ó ^{16}O.

Para las energías de los neutrinos atmosféricos o de los experimentos de MiniBooNE y T2K, los tratamientos en núcleos finitos suelen ser insuficientes puesto que no contienen ingredientes dinámicos fundamentales: excitaciones tipo Δ-hueco, contribuciones de dos cuerpos, producción de piones etc. En la región de la resonancia $\Delta(1232)$ existen en la literatura modelos fiables para la descripción de reacciones nucleares inclusivas, y de producción coherente e incoherente de piones, mediados tanto por CC como por NC, a partir de modelos microscópicos en nucleones. En concreto, resulta de especial interés para este trabajo el modelo desarrollado en las Refs. [34, 39, 43, 50], donde además de la excitación de la resonancia $\Delta(1232)$, se incluyen mecanismos no resonantes que se deducen del patrón de rotura espontánea de

simetría quiral de QCD. En esta memoria, en primer lugar, se ha extendido el modelo de las Refs. [34, 39, 43, 50] al estudio de procesos de emisión de fotones en reacciones de neutrinos con núcleos y nucleones mediadas por corrientes neutras (NCγ) a energías intermedias. Estos procesos son un fondo importante en los experimentos de oscilaciones de neutrinos y se requiere de un conocimiento preciso de los mismos, incluyendo sus importantes correcciones nucleares, para poder determinar, y estimar/controlar los errores sistemáticos, de los parámetros que gobiernan el fenómeno de las oscilaciones de neutrinos.

Por otra parte, hemos también prestado atención en esta memoria a la naturaleza y a algunas propiedades de ciertas resonancias hadrónicas. La comprensión de determinados aspectos de la interacción entre hadrones a energías bajas e intermedias ha experimentado un gran avance en los últimos años gracias al concepto y uso de teorías efectivas. El planteamiento general consiste en estudiar procesos de QCD a bajas energías, en lugar de en términos de grados de libertad de quarks y gluones, en términos de mesones y bariones directamente. Al mismo tiempo, se imponen en la teoría resultante tantas propiedades satisfechas por QCD como sea posible. De esta forma se consigue una importante reducción de parámetros libres y por tanto un mayor poder predictivo de la teoría efectiva. De especial relevancia a bajas energías, son las EFT's Teoría Quiral de Perturbaciones (TQP) y la Teoría Efectiva de Quarks Pesados (HQET). TQP (HQET) explota la simetría bajo rotaciones quirales (de espín-sabor) que QCD presenta en el límite de masa nula (infinita) de los quarks.

Es comúnmente aceptado que los estados fundamentales de mesones y bariones están compuestos por parejas $q\bar{q}$ o por tres quarks respectivamente. Sin embargo el espectro de estados excitados hadrónicos es, en principio, mucho más rico. Así, la simple hipótesis de que las resonancias hadrónicas corresponden a excitaciones de los quarks, como se supone en los modelos de quarks constituyentes, es incapaz de describir la estructura y propiedades de multitud de estados tanto en el sector mesónico como en el bariónico. Por ejemplo, los primeros estados excitados con números cuánticos de nucleón son las resonancias $N^*(1440)$ $(1/2^+)$ y $N^*(1535)$ $(1/2^-)$. En modelos de quarks, para estudiar estos estados se requiere energías de excitación de alrededor de 500 ó 600 MeV. Desde el punto de vista energético es más favorable

la excitación de un pión, y por tanto es plausible que estos estados puedan contener una importante componente resonante pión-nucleón. Esta es básicamente la idea subyacente en la llamada Teoría Unitaria Quiral (TUQ) [64, 65], que utiliza en primer lugar TQP para describir las interacciones entre los mesones y bariones fundamentales (octetes del pión y del nucleón) en el régimen de bajas energías, por debajo de la aparición de las primeras resonancias. La dinámica de resonancias no puede ser descrita utilizando una expansión perturbativa, ya que estos estados están asociados a polos en el plano complejo de las amplitudes y por tanto su dinámica es genuinamente no perturbativa. Así, el otro ingrediente fundamental de la TUQ consiste en unitarizar las amplitudes resultantes, con objeto de describir resonancias y estados ligados (polos en diferentes hojas de Riemann de las amplitudes).

Las interacciones de bosones de Goldstone (piones, kaones, etc..) entre sí o con otros hadrones queda determinada por la simetría quiral. No es este el caso de los mesones vectoriales, como el ρ o el mesón extraño K^*. Es importante extender el formalismo de la TUQ para incluir estos mesones, puesto que parecen ser también estados genuinos $q\bar{q}$, como se desprende de diversos resultados en limite N_c grande [202, 207]. Con objeto de tener en cuenta los grados de libertad asociados a los vectores, diversos modelos han sido utilizados en la literatura, como por ejemplo el formalismo del *hidden gauge* empleado en la Ref. [199]. En la tesis, utilizaremos la propuesta de la Ref. [68], donde se parte del Lagrangiano quiral de Weinberg-Tomozawa y se extiende a un grupo de simetría SU(6) de espín–sabor, que posteriormente es explícitamente rota. Este modelo es sugerente, porque satisface simetría quiral, y si eventualmente es extendido a sabores pesados (c, b,..), acomodaría la simetría aproximada de espín (HQSS) que se deduce de QCD en ese sector. Utilizando este modelo de simetría SU(6), hemos estudiado en la segunda parte de la tesis, las propiedades de las resonancias mesónicas de paridad positiva y más baja energía.

Por último también hemos estudiado, utilizando Lagrangianos efectivos, la reacción de foto-producción de la resonancia bariónica $\Lambda(1520)$ con blancos de protones. Las predicciones que se han obtenido para la reacción $\gamma p \to K\Lambda(1520)$ han sido comparadas con las recientes medidas de los experimentos LEPS [79] y CLAS [80]. Esta resonancia bariónica está bien establecida, su señal es clara desde el punto de

vista experimental y se acomoda de forma natural en un modelo SU(6) para el sector bariónico [74], análogo al descrito anteriormente para mesones. Además, la reacción anterior filtra de forma natural estados intermedios con isospín 1/2, muchos de ellos estudiados en [74], y cuyas propiedades pueden ser determinadas/estudiadas gracias a las precisas medidas de LEPS y CLAS. El análisis realizado en esta tesis confirma la relación directa existente entre el máximo local que aparece cerca del umbral para ángulos pequeños en los datos de LEPS y CLAS y la resonancia $J^P = 3/2^-$ $N^*(2120)$. Además se discute como estas medidas se pueden utilizar para determinar propiedades tanto de esta resonancia, como de la $\Lambda(1520)$.

- **Estudio de procesos NCγ**

  La primera parte de la tesis (Capítulos 2–5) está dedicada a las reacciones de emisión NCγ en nucleones y núcleos para energías intermedias del neutrino incidente. Estos procesos son un fondo importante en los experimentos de oscilaciones de neutrinos del tipo $\nu_\mu \to \nu_e$ y $\bar{\nu}_\mu \to \bar{\nu}_e$, cuando los fotones son identificados de forma errónea con $e^\pm$ originados en la difusión CCQE de un $\nu_e(\bar{\nu}_e)$.

  En primer lugar en el Capítulo 2, se repasan de forma breve algunos conceptos básicos relacionados con las corrientes electrodébiles de leptones y quarks. A partir del Lagrangiano de la interacción electro-débil, basado en la simetría gauge local $SU(2) \times U(1)$ y su rotura espontánea a través del mecanismo de Higgs, se introducen las corrientes electromagnética y neutra que se utilizan en el capítulo siguiente. En el Capítulo 3, se deriva un modelo microscópico para describir la emisión de fotones en reacciones de (anti)neutrinos con núcleos y nucleones mediadas por NC. Como se mencionó, este modelo está basado en trabajos anteriores similares desarrollados para estudiar la producción débil de piones [39, 43, 50, 96]. En la reacción sobre nucleones, además de términos no resonantes que, en la región de bajas energías, quedan completamente determinados por la simetría quiral, hemos también considerado la excitación de la resonancia $\Delta(1232)$ y su posterior desintegración en el canal $N\gamma$. Este mecanismo es dominante en el régimen de energías intermedias

consideradas en esta memoria. Además, también se han tenido en cuenta contribuciones de excitaciones nucleónicas ($N(1440)$, $N(1520)$ y $N(1535)$) de la segunda región de resonancias. De entre estas últimas, hemos encontrado que el término de la resonancia D_{13} $N(1520)$ da lugar a las contribuciones mayores y que resultan ser relevantes para energías del (anti)neutrino de alrededor de 1.5 GeV o superiores.

A continuación se ha extendido el modelo para estudiar procesos en núcleos, teniendo en cuenta efectos debidos al movimiento de Fermi, al bloqueo de Pauli y a la modificación de las propiedades de la resonancia Δ en el seno de un medio nuclear. Se han realizado predicciones de diversas secciones eficaces diferenciales y totales para varios núcleos, incluyendo los más comunes que se usan en los detectores de neutrinos actuales o que se utilizarán en futuros experimentos (carbono, oxígeno, argón, hierro). Se han estudiado procesos incoherentes y coherentes, donde el núcleo blanco queda en su estado inicial, de emisión de fotones. En ambos tipos de reacciones, los importantes efectos nucleares han sido puestos de manifiesto, y se ha discutido con detalle la dependencia de las secciones eficaces encontradas del número másico A y de la energía del neutrino incidente.

Los resultados obtenidos apuntan la conveniencia de un nuevo análisis, utilizando nuestro modelo microscópico, de la producción de fotones en procesos mediados por corrientes neutras para las condiciones específicas del experimento de MiniBooNE. Este experimento encuentra un exceso a bajas energías de sucesos NCγ respecto a las predicciones del Monte Carlo utilizado por la colaboración. Este estudio es abordado en el capítulo siguiente.

Utilizando el modelo desarrollado en el Capítulo 3 para estudiar las reacciones NCγ, hemos calculado en el Capítulo 4 la contribución de estos procesos al fondo irreducible para las medidas (aparición) $\nu_\mu \to \nu_e$ y $\bar{\nu}_\mu \to \bar{\nu}_e$ del experimento MiniBooNE [59, 61]. Estos procesos son origen de un fondo no deseado porque en el gran tanque Cherenkov utilizado como detector lejano en este experimento, los fotones son frecuentemente identificados de forma errónea con $e^\pm$ que provendrían eventual-

mente de la difusión CCQE de un $\nu_e(\bar{\nu}_e)$. Se han considerado los detalles del detector (masa, composición y eficiencia) y las diversas componentes de los flujos de neutrinos y antineutrinos utilizados en el experimento MiniBooNE, y se han obtenido distribuciones de sucesos en función de la energía y el ángulo polar del fotón, relativo a la dirección del neutrino incidente. También se han calculado las distribuciones de sucesos en términos de la energía del neutrino, reconstruida incorrectamente suponiendo que los sucesos se originan tras procesos de difusión CCQE. Esta última variable es importante, pues en los experimentos de oscilaciones de neutrinos es utilizada como si fuera la energía real del neutrino que ha inducido el suceso. La contribución de sucesos NCγ más importante en el aceite mineral (CH_2), que se utiliza como blanco en el experimento de MiniBooNE, se debe al canal de colisión incoherente con el núcleo de ^{12}C. Las interacciones con los dos protones de la molécula CH_2 y el proceso coherente con ^{12}C dan lugar también a un número de sucesos similar en magnitud y que resulta necesario tener en cuenta. La contribución originada por la contaminación de neutrinos muónicos en el modo antineutrino es también importante. Sin embargo, la contribución análoga debida a los antineutrinos presentes en el flujo de neutrinos resulta ser mucho más pequeña, y despreciable en muy buena aproximación.

Hemos comparado nuestros resultados con las estimaciones utilizadas por la colaboración MiniBooNE en su análisis. El Monte Carlo (NUANCE [172]) utilizado por MiniBooNE en la obtención de estos resultados incluye únicamente la contribución de resonancias. Así mecanismos no resonantes, o el canal coherente no son conside-rados. Sin embargo y para mejorar las predicciones, el Monte Carlo se compara con las medidas experimentales de producción de π^0 en procesos mediados por corrientes neutras, y las diferencias observadas son utilizadas para reajustar el modelo de producción resonante, que posteriormente se utiliza para predecir las distribuciones NCγ. También hemos comparado nuestras predicciones con las estimaciones del modelo desarrollado por los Drs. Zhang y Serot [88]. En este modelo se parte de una teoría efectiva a bajas energías, que incorpora simetría quiral, y que en

principio cuenta con un contaje bien determinado. El modelo se extiende a energías más altas, para poder comparar con MiniBooNE, utilizando factores de forma fenomenológicos. En líneas generales encontramos, a pesar de las importantes diferencias de los modelos, un buen acuerdo con ambas predicciones. Sin embargo, nuestros resultados discrepan de forma significativa con los obtenidos por el Dr. Hill en la referencia [90], donde se utiliza una eficiencia independiente de la energía y muy alta, además de no considerar efectos nucleares. Por tanto concluimos que procesos de emisión de fotones inducidos por corriente nucleares de un cuerpo no pueden explicar el exceso de sucesos observados por MiniBooNE.

En estudios teóricos recientes de la sección eficaz CCQE, también medida por MiniBooNE, mecanismos que involucran dos o más nucleones han resultado jugar un papel bastante importante [26, 34]. En principio, se podría pensar en contribuciones análogas (2p2hγ) en este canal, y que planteamos estudiar en el futuro inmediato. Sin embargo aunque la detección de estos nuevos modos de interacción será relevante, no esperamos que cambien la situación de forma dramática. A este respecto, el futuro experimento MicroBooNE [159] si que será mucho mas importante, y previsiblemente arrojará luz a este puzle, puesto que MicroBooNE utilizará un detector de argón líquido donde sí que será posible distinguir electrones de fotones.

En la siguiente sección de la memoria, Capítulo 5, se ha utilizado el modelo microscópico del Capítulo 3 para predecir el número de sucesos NCγ en el interior del gran tanque Cherenkov SK, utilizado en el experimento T2K como detector lejano. También se han calculado distribuciones angulares y energéticas, tal y como se hizo en el capítulo anterior para el caso de MiniBooNE.

Utilizando $N_{\mathrm{POT}} = 6.57 \times 10^{20}$, encontramos 0.421 ± 0.051 sucesos sin incluir correcciones de eficiencia del detector. En esta ocasión, la contribución originada por la contaminación de neutrinos muónicos en el modo antineutrino no es significativa, y solo es del orden del 2-3%.

Este fondo irreducible, aunque pequeño, afecta a la determi-

nación de los parámetros de oscilaciones, en particular a la medida de la fase de violación de CP δ_{CP}, y por tanto debe de ser estimado de forma precisa/realista. Así los resultados obtenidos en este capítulo son relevantes, ya que nuestra predicción es alrededor de 2.6 veces mayor que la que se obtiene utilizando el Monte Carlo NEUT [169], que es principal generador de sucesos empleado en el análisis de datos dentro del experimento T2K. Es una discrepancia en la normalización global, puesto que la forma de las distribuciones energéticas de fotones y neutrinos, y angulares de los fotones predichas por ambos modelos son muy parecidas, y no se aprecian entre ellas diferencias significativas. En principio, se podría atribuir la diferencia de normalización a que NEUT no incorpora el canal de emisión coherente de fotones o que en este Monte Carlo, mecanismos no resonantes de producción de fotones no están tampoco incluidos. Sin embargo, hemos discutido que parte de esta diferencia se origina también en la propia contribución (dominante) de la resonancia $\Delta(1232)$ a procesos NCγ, como también se infiere de comparaciones entre las predicciones de NEUT para el canal NCγ y las obtenidas con otros modelos similares, en el contexto del experimento MiniBooNE [145].

Así, la situación en T2K es a priori diferente que en MiniBooNE, donde vimos en el Capitulo 3, que nuestras predicciones si que eran consistentes con las estimaciones elaboradas por la colaboración experimental.

- **Resonancias hadrónicas**

  En la segunda parte de la tesis hemos estudiado el espectro mesónico de resonancias de baja energía y paridad positiva, utilizando un modelo que parte de simetría SU(6) de espín–sabor, y la reacción de foto-producción $\gamma p \to K\Lambda(1520)$ de la resonancia bariónica $\Lambda(1520)$.

  - **Espectro de resonancias mesónicas de paridad positiva**

    En el Capítulo 6, en primer lugar hemos revisado el modelo desarrollado en la Ref. [68] para generar dinámicamente las

excitaciones mesónicas de paridad positiva de más baja energía. Este modelo parte del Lagrangiano quiral de Weinberg-Tomozawa que es extendido a un grupo de simetría SU(6) de espín–sabor. De esta forma se obtiene la interacción en onda S entre mesones, no solo del octete del pión, sino también del octete de mesones vectoriales que incluye el $\rho(770)$. La simetría SU(6) presenta sustanciales correcciones en la naturaleza, así que el modelo incorpora un cierto patrón de su rotura. Con esta interacción se soluciona la BSE en canales acoplados, estudiando con detalle su renormalización, que permite restaurar unitariedad elástica. Para los distintos sectores de espín, isospín y extrañeza se buscan polos en la primera y segunda hoja de Riemann de las amplitudes. La posición de las singularidades en el plano complejo determinan masas, y en su caso anchuras de desintegración, de las resonancias mesónicas asociadas a las mismas, gracias al principio de máxima analiticidad de Mandelstam. Las predicciones del modelo son, desde el punto de vista fenomenológico, muy buenas para los sectores 0^+ y 1^+. De hecho, como se comprueba en [68], la mayor parte del espectro mesónico de paridad positiva de más baja energía en estos sectores se puede clasificar de acuerdo con multipletes del grupo de simetría SU(6). Sin embargo, este esquema no es tan exitoso en el sector de espín 2, y no es capaz de describir apropiadamente algunas resonancias con $J^P = 2^+$, como el estado $K_2^*(1430)$, que están bien establecidas desde el punto de vista experimental. Este sector por su parte parece estar bien descrito y de forma natural por el modelo de la Ref. [199], que está basado el formalismo del *hidden gauge*.

En este contexto, en el Capítulo 6 se ha mejorado el modelo de la Ref. [68], considerando nuevas interacciones entre mesones vectoriales consistentes con simetría quiral. En el modelo original se generan masas diferentes para los mesones pseudo-escalares y vectoriales utilizando un único término local que rompe la simetría de espín-sabor, de forma consistente con simetría quiral. En este capítulo, hemos estu-

diado con detalle la estructura de los términos locales que rompen la simetría SU(6), y que respetan (o que rompen *suavemente*) simetría quiral. Se ha encontrado la forma general de todas las interacciones locales, expresadas en términos del campo $U = \exp i\sqrt{2}\phi/f$, que son consistentes con el patrón de rotura espontánea de la simetría quiral que se infiere de QCD. Hemos también comprobado que involucrando solo cuatro campos de mesones, solo existe un número finito de interacciones locales invariantes quirales, e invariantes bajo transformaciones discretas de paridad, inversión temporal y conjugación de carga. En línea con el contaje para gran número de colores, N_c, hemos restringido el análisis solo para operadores que involucren una sola traza. De esta forma, hemos reducido el número de nuevas interacciones, al orden más bajo en el número de campos de mesones, a solo tres. A continuación, se ha realizado una discusión fenomenológica detallada del efecto de estos nuevos términos. Hemos encontrado que la inclusión de los mismos posibilita una descripción más satisfactoria del sector $J^P = 2^+$, sin modificar de forma sustancial la predicciones del modelo de la Ref. [68] en los sectores $J^P = 0^+$ y $J^P = 1^+$. En particular, la mejora es notoria en los canales $I^G(J^{PC}) = 0^+(2^{++})$, $1^-(2^{++})$ y $I(J^P) = \frac{1}{2}(2^+)$, que se corresponden con los números cuánticos de las resonancias $f_2(1270)$, $a_2(1320)$ y $K_2^*(1430)$. Además de la posición de estos estados, también hemos calculado los acoplamientos de estas resonancias a los diversos pares de mesones que se incorporan en la resolución de la BSE en el espacio de canales acoplados. Estos acoplamientos son relevantes a la hora de describir los diferentes modos de desintegración y la estructura de las resonancias que han sido generadas. El análisis que hemos realizado, sin embargo, sistemáticamente necesita de valores muy altos de la masa de corte, utilizada para la renormalizar la BSE, en el límite aceptable de lo que uno esperaría para estados dinámicamente generados (estados para los cuales los logaritmos de unitariedad juegan un papel importante/esencial). Esta circunstancia podría in-

dicar que interacciones de onda D, no consideradas, serían importantes en la formación de estas resonancias. De hecho, en muchos casos, los umbrales de los canales más relevantes no están muy próximos a la posición de la resonancia, por lo cual no es extraño pensar que la consideración de únicamente interacciones en onda S sea insuficiente para la generación dinámica de algunas de estas excitaciones mesónicas. Además, también habría que considerar que algunos de estos estados podrían ser genuinos en lugar de dinámicamente generados. En cualquier caso, y con esta posible salvedad, podemos concluir que el modelo derivado en este capítulo proporciona un marco adecuado para el estudio de las resonancias mesónicas de paridad positiva de más baja energía, que son dinámicamente generadas por los logaritmos que aparecen en las correcciones necesarias para restaurar unitariedad elástica en canales acoplados.

– **Foto-producción de la resonancia** $\Lambda(1520)$

En los capítulos 7 y 8, hemos realizado un estudio detallado de la reacción $\gamma p \to \Lambda(1520)K^+$ cerca del umbral utilizando un modelo de Lagrangianos efectivos. En el análisis también hemos considerado la existencia de efectos debidos a difusión tipo Regge. Los parámetros libres del modelo han sido ajustados a las medidas experimentales de las secciones eficaces diferenciales $d\sigma/d(\cos\theta_{\rm c.m.})$ publicadas recientemente por las colaboraciones LEPS [79] y CLAS [80].

En el primer de estos dos capítulos y utilizando el modelo de la Ref. [237] para la reacción[1] $\gamma p \to \Lambda(1520)K^+$, se ha calculado por primera vez la contribución en el canal u del hiperón $\Lambda(1115)$. Este mecanismo no había sido considerado previamente [231, 236–238], puesto que está muy suprimido para los ángulos de difusión pequeños del K^+ saliente medidos en LEPS. Sin embargo, las secciones eficaces de la colaboración CLAS cubren también ángulos grandes, para los cuales uno espera que esta nueva contribución sea re-

[1]Se incluyen los mecanismos de contacto, de intercambio de un kaón, y de un nucleón y de la resonancia $N(2120)$, en los canales t y s, respectivamente.

levante. La no inclusión hasta ahora del mecanismo de la $\Lambda(1115)$ explica también por qué los modelos anteriores no describen apropiadamente los nuevos datos de CLAS. Como se discute en el Capítulo 7, gracias a la inclusión de las contribuciones de la resonancia $N(2120)$ y el término del barión $\Lambda(1115)$ se consigue una descripción simultánea bastante buena de los dos conjuntos (LEPS y CLAS) de secciones eficaces angulares, tanto para ángulos pequeños como para grandes, y para todo el rango de masas invariantes (W) del par γp exploradas en estos dos experimentos. La contribución en el canal u del hiperón $\Lambda(1115)$ incrementa de forma significativa la sección eficaz para grandes ángulos, siendo más y más relevante a medida que la energía del fotón aumenta, convirtiéndose en esencial por encima de $W \geq 2.35$ GeV y $\cos\theta_{\rm c.m.} \leq -0.5$. Por otra parte, los datos de CLAS (véase por ejemplo la Fig. 7.6) claramente favorecen la existencia de una resonancia ancha ($\Gamma \sim 200$ MeV) en la región de 2.1 GeV. Este estado tendría paridad negativa, espín 3/2, isospín 1/2 y una anchura parcial de desintegración en el canal $\Lambda(1520)K$ apreciable. Estos resultados corroboran conclusiones similares obtenidas en el estudio reciente de la Ref [242] sobre la electro-producción de la resonancia $\Lambda(1520)$ en protones. Esta resonancia se correspondería con la D_{13} $N(2120)$, que cuenta con la calificación de dos estrellas en la clasificación del PDG. Además, las características de la resonancia $N^*(2120)$ determinadas en [242] son muy similares a las obtenidas en esta tesis, y están en un buen acuerdo cualitativo con las predicciones del modelo quark de Capstick y Roberts [241]. Confirmamos, de esta forma, las conclusiones de los trabajos de las referencias [237, 238] obtenidas para esta resonancia a partir del análisis del máximo local que aparece en la sección eficaz medida por LEPS en la región de ángulos pequeños y en la proximidad del umbral (véase Fig. 7.4), y por otra parte claramente estamos en desacuerdo con los resultados negativos de las Refs. [234] y [239] sobre el papel jugado por la resonancia $N^*(2120)$ en la descripción de los datos de LEPS.

Los parámetros de la resonancia N^* obtenidos en nuestro ajuste combinado a los datos de LEPS y CLAS comparan cualitativamente bien con los publicados en la Ref. [237]. Por tanto, como ocurre en este trabajo previo, nuestras predicciones para la asimetría de espín, promediada respecto al ángulo polar del fotón saliente, difieren en un signo de la medida experimental de la misma realizada por la colaboración LEPS [79] en el laboratorio SPring-8 (Japón).

En resumen, en este capítulo concluimos que la reacción $\gamma p \to K^+\Lambda(1520)$ resulta ser un instrumento adecuado para estudiar las propiedades de la resonancia $N(2120)$, y que de hecho proporciona pruebas firmes sobre su existencia. Esto corrobora diversas predicciones teóricas al respecto que se deducen de modelos de quarks constituyentes [241] y de esquemas basados en TUQ [73, 74]. Un análisis reciente [244] de las medidas de la colaboración CBELSA/TAPS de la reacción $\gamma p \to K^0\Sigma^+$, también apunta la existencia de una excitación nucleónica con espín-paridad $J^P = 3/2^-$ y masa de alrededor de 2 GeV.

Finalmente es interesante mencionar que este estudio de la reacción $\gamma p \to K^+\Lambda(1520)$ también proporciona detalles sobre la resonancia $\Lambda(1520)$ [74, 263], y de algunas de sus propiedades tales como la naturaleza de los vértices $\bar{K}^*N\Lambda^*$ y $K\Lambda^*N^*$ (este trabajo y la Refs. [236, 237]) y su desintegración radiativa $\Lambda^* \to \Lambda\gamma$ [acoplamientos magnéticos h_1 y h_2, Eq. (7.7), determinados en este capítulo].

En el último capítulo de la tesis (Capítulo 8) hemos estudiado de nuevo las secciones eficaces de la reacción $\gamma p \to \Lambda(1520)K^+$ medidas por la colaboración CLAS, en especial en la dirección hacia delante. En esta región de ángulos pequeños y para $E_\gamma > 2.3 - 2.4$ GeV, existen pequeñas, aunque sistemáticas, discrepancias entre las predicciones del modelo desarrollado en el capítulo anterior y los datos experimentales. Hemos correlacionado estas desviaciones con efectos difractivos o Regge, a pesar de que las energías involucradas son solo moderadamente altas. Así en este capítulo, hemos considerado la contribución de una trayec-

toria Regge con números cuánticos de kaón para ángulos pequeños y las energías invariantes W más altas exploradas por CLAS. Gracias a la inclusión de este nuevo mecanismo, se consigue una descripción de los datos de CLAS mucho más precisa que con los Lagrangianos efectivos utilizados en el Capítulo 7. De hecho, no son visibles ahora discrepancias sistemáticas. Estos resultados confirman parcialmente las conclusiones del reciente estudio realizado en la Ref. [268].

En este último capítulo, se ha diseñado un modelo híbrido, invariante *gauge*, que interpola suavemente entre el esquema basado en Lagrangianos efectivos del Capítulo 7, para energías cercanas al umbral de producción, y un modelo de difusión Regge para altas energías y ángulos de K^+ pequeños. Los efectos Regge son prácticamente despreciables para las energías y ángulos relevantes en las medidas de LEPS, que restringen las propiedades de la resonancia $N^*(2120)$. Los efectos Regge juegan un papel importante solo para ángulos pequeños y energías del fotón por encima de 2.35 GeV. Gracias a esta descripción más precisa de los datos de CLAS y LEPS, no solo concluimos la posible existencia de difusión difractiva en las medidas de CLAS, sino que ganan más credibilidad las conclusiones del capítulo anterior referentes a la resonancia $N^*(2120)$ y a la importancia del mecanismo del hiperón $\Lambda(1115)$.

El rango de valores de la variable de Mandelstam t explorado en las medidas de CLAS no es, sin embargo, lo suficientemente amplio como para restringir de forma efectiva el factor de forma de Regge. Es precisamente, este factor de forma la principal diferencia entre los dos modelos estudiados en este capítulo. Así, aunque para valores de t negativos, el propagador tipo Regge de la Eq. (8.12) presenta un crecimiento factorial, en principio inaceptable, el limitado rango de momentos transferidos accesibles en los datos de CLAS no permite que este comportamiento indeseado sea visible. Esta es la misma razón por la cual no se puede determinar el parámetro de corte Gaussiano a introducido en el factor de forma de la Eq. (8.14). Finalmente, es intere-

sante mencionar que en la región donde se solapan, existen importantes discrepancias en el tamaño global, aunque no en la dependencia de t, entre los datos de CLAS y los más antiguos del experimento LAMP2 (Daresbury LAB [227]). Esto constituye un problema abierto, y requeriría una nueva medida experimental independiente. Los datos de LAMP2 se extienden hasta energías del fotón más altas (alrededor de 5 GeV), y en ellos se aprecian claramente trazas de un comportamiento tipo Regge (Fig. 8.4). Sin embargo, y debido al problema con la normalización global, no hemos incluido este conjunto de datos en nuestros ajustes.

Appendix A

Reference formulae

A.1 Metric and conventions

Matrices

The components of the Pauli spin vector $\vec{\sigma} = (\sigma^1, \sigma^2, \sigma^3)$ matrices are,

$$\sigma^1 = \begin{pmatrix} 1 & 0 \\ 0 & -1 \end{pmatrix}, \ \sigma^2 = \begin{pmatrix} 0 & -i \\ i & 0 \end{pmatrix}, \ \sigma^3 = \begin{pmatrix} 1 & 0 \\ 0 & -1 \end{pmatrix}, \tag{A.1}$$

and they fulfill,

$$(\sigma_i)^2 = 1\,, \quad \mathrm{Tr}[\sigma_i] = 0\,, \tag{A.2}$$

$$\sigma_i \sigma_j = i \sum_k \epsilon_{ijk} \sigma^k + \delta_{ij} I\,, \tag{A.3}$$

where ϵ_{ijk} is the totally anti-symmetric Levi-Civita tensor, $\epsilon_{123} = +1$, and I is the 2×2 identity matrix.

Dirac matrix

For the Dirac matrices, we use the following representation,

$$\vec{\gamma} = (\gamma^1, \gamma^2, \gamma^3) = \begin{pmatrix} 0 & \vec{\sigma} \\ -\vec{\sigma} & 0 \end{pmatrix}, \tag{A.4}$$

$$\gamma_0 = \gamma^0 = \begin{pmatrix} I & 0 \\ 0 & -I \end{pmatrix}, \tag{A.5}$$

$$\gamma_5 = \gamma^5 = \begin{pmatrix} 0 & I \\ I & 0 \end{pmatrix}, \tag{A.6}$$

$$\gamma^i = -\gamma_i\,, \quad \gamma_5 = i\gamma^0\gamma^1\gamma^2\gamma^3. \tag{A.7}$$

The matrices have the following properties:

$$\sigma^{\mu\nu} = \frac{i}{2}[\gamma^\mu, \gamma^\nu]\,, \tag{A.8}$$

$$\{\gamma^\mu, \gamma^\nu\} = 2g^{\mu\nu}\,, \tag{A.9}$$

$$\left\{\gamma^\mu, \gamma^5\right\} = 0\,, \tag{A.10}$$

where the metric tensor $g^{\mu\nu}$ is,

$$g^{\mu\nu} = g_{\mu\nu} = \begin{pmatrix} 1 & 0 & 0 & 0 \\ 0 & -1 & 0 & 0 \\ 0 & 0 & -1 & 0 \\ 0 & 0 & 0 & -1 \end{pmatrix}. \tag{A.11}$$

Traces of Dirac matrices can be evaluated as follows,

$$\begin{aligned}
\mathrm{Tr}[\mathbf{1}] &= 4\,, && \text{(A.12)}\\
\mathrm{Tr}[\text{any odd of } \gamma's] &= 0\,, && \text{(A.13)}\\
\mathrm{Tr}[\gamma^\mu\gamma^\nu] &= 4g^{\mu\nu}\,, && \text{(A.14)}\\
\mathrm{Tr}[\gamma^\mu\gamma^\nu\gamma^\rho\gamma^\sigma] &= 4\left(g^{\mu\nu}g^{\rho\sigma} - g^{\mu\rho}g^{\nu\sigma} + g^{\mu\sigma}g^{\nu\rho}\right), && \text{(A.15)}\\
\mathrm{Tr}[\gamma^5] &= \mathrm{Tr}[\gamma^\mu\gamma^\nu\gamma^5] = 0\,, && \text{(A.16)}\\
\mathrm{Tr}[\gamma^\mu\gamma^\nu\gamma^\rho\gamma^\sigma\cdots] &= \mathrm{Tr}[\cdots\gamma^\sigma\gamma^\rho\gamma^\nu\gamma^\mu]\,. && \text{(A.17)}
\end{aligned}$$

Contractions of the Dirac matrices can be computed using,

$$\begin{aligned}
\gamma_\lambda\gamma^\lambda &= 4\,, && \text{(A.18)}\\
\gamma_\lambda\gamma^\nu\gamma^\lambda &= -2\gamma^\nu\,, && \text{(A.19)}\\
\gamma_\lambda\gamma^\alpha\gamma^\beta\gamma^\lambda &= 4g^{\alpha\beta}\,, && \text{(A.20)}\\
\gamma_\lambda\gamma^\alpha\gamma^\beta\gamma^\rho\gamma^\lambda &= -2\gamma^\rho\gamma^\beta\gamma^\alpha\,. && \text{(A.21)}
\end{aligned}$$

Gell-Mann matrices

We use the standard Gell-Mann form of the $SU(3)$ matrices representing flavor (or color) degrees of freedom:

$$\lambda_1 = \begin{pmatrix} 0 & 1 & 0 \\ 1 & 0 & 0 \\ 0 & 0 & 0 \end{pmatrix}, \ \lambda_2 = \begin{pmatrix} 0 & -i & 0 \\ i & 0 & 0 \\ 0 & 0 & 0 \end{pmatrix}, \ \lambda_3 = \begin{pmatrix} 1 & 0 & 0 \\ 0 & -1 & 0 \\ 0 & 0 & 0 \end{pmatrix},$$
$$\lambda_4 = \begin{pmatrix} 0 & 0 & 1 \\ 0 & 0 & 0 \\ 1 & 0 & 0 \end{pmatrix}, \ \lambda_5 = \begin{pmatrix} 0 & 0 & -i \\ 0 & 0 & 0 \\ i & 0 & 0 \end{pmatrix}, \ \lambda_6 = \begin{pmatrix} 0 & 0 & 0 \\ 0 & 0 & 1 \\ 0 & 1 & 0 \end{pmatrix},$$
$$\lambda_7 = \begin{pmatrix} 0 & 0 & 0 \\ 0 & 0 & -i \\ 0 & i & 0 \end{pmatrix}, \ \lambda_8 = \frac{1}{\sqrt{3}} \begin{pmatrix} 1 & 0 & 0 \\ 0 & 0 & 0 \\ 0 & 0 & -2 \end{pmatrix}, \tag{A.22}$$

with,

$$\lambda_\pm = (\lambda_1 \pm i\lambda_2). \tag{A.23}$$

A.2 Spinors

J=1/2

The Dirac equation reads,

$$(i\gamma_\mu \partial^\mu - m)\psi(x) = 0\,, \tag{A.24}$$

which is Lorentz invariant. The general solutions can be written as a linear combination of plane waves,

$$\psi(x) = \sum_{s=\pm 1/2} \int \frac{d^3p}{2E(2\pi)^3} \left[b(p,s) u_s(p) e^{-ip\cdot x} + d^\dagger(p,s) v_s(p) e^{+ip\cdot x} \right], \tag{A.25}$$

where s is the spin projection, and $E = \sqrt{\vec{p}^2 + m^2}$. The operators $b^\dagger(p,s)$ and $b(p,s)$ create or annihilate a Dirac particle of spin projection s and four momentum p^μ, while the operators $d^\dagger(p,s)$ and $d(p,s)$ create or annihilate an antiparticle. The explicit form of the positive

energy spinors $u_s(p)$ reads,

$$u_s(p) = \sqrt{E+m}\begin{pmatrix} 1 \\ \frac{\vec{\sigma}\cdot\vec{p}}{E+m} \end{pmatrix}\varphi_s, \tag{A.26}$$

$$\varphi_{\frac{1}{2}} = \begin{pmatrix} 1 \\ 0 \end{pmatrix}, \quad \varphi_{-\frac{1}{2}} = \begin{pmatrix} 0 \\ 1 \end{pmatrix}, \tag{A.27}$$

the antiparticle spinor $v_s(p)$ is related to $u_s(p)$ by charge conjugation,

$$v_s(p) = i\eta_c\gamma^2 u_s^*(p) \tag{A.28}$$

where η_c is an arbitrary phase factor.

The spinors $u_s(p)$ and $v_s(p)$ satisfy,

$$(\gamma_\mu p^\mu - m)u_s(p) = 0\,, \tag{A.29}$$

$$(\gamma_\mu p^\mu + m)v_s(p) = 0\,, \tag{A.30}$$

and the relations,

$$u_s^\dagger(p)u_r(p) = v_s^\dagger(p)v_r(p) = 2E\delta_{sr}\,, \tag{A.31}$$

$$\bar{u}_s(p)u_r(p) = -\bar{v}_s(p)v_r(p) = 2M\delta_{sr}\,, \tag{A.32}$$

where $\bar{u}_s = u_s^\dagger(p)\gamma_0$ and $\bar{v}_s = v_s^\dagger(p)\gamma_0$. Thus, we arrive at the completeness relations,

$$\sum_s u_s(p)\bar{u}_s(p) = \not{p} + m, \quad \sum_s v_s(p)\bar{v}_s(p) = \not{p} - m\,, \tag{A.33}$$

with $\not{p} = \gamma_\mu p^\mu$.

J=3/2

For spin 3/2 resonances, the Rarita–Schwinger spinors can be constructed by combining Dirac spinors $u_s(p)$ with the spin 1 vector $e_\mu(p)$. The intermediate photon can have three polarizations $\epsilon^\mu_{(i)}$ defined as

$$\epsilon^\mu_\pm = \mp\frac{1}{\sqrt{2}}\big(0;1,\pm i,0\big)\,, \tag{A.34}$$

$$\epsilon^\mu_0 = \frac{1}{\sqrt{Q^2}}\big(q^z;0,0,q^0\big)\,, \tag{A.35}$$

and $Q^2 = -q^2$. The general form of the four-vector $e^\mu(p,\lambda)$ is obtained by boosting from the particle rest frame to any Lorentz frame,

$$e^\mu(p,\lambda) = \left(\frac{\vec{\epsilon}_\lambda \cdot \vec{p}}{M_\Delta}, \vec{\epsilon}_\lambda + \frac{\vec{p}(\vec{\epsilon}_\lambda \cdot \vec{p})}{M_\Delta + p_0} \right) , \tag{A.36}$$

with the polarization vectors given by

$$\vec{\epsilon}_{\pm 1} = \mp \frac{1}{\sqrt{2}} \big(1, \pm i, 0\big), \tag{A.37}$$

$$\vec{\epsilon}_0 = \big(0, 0, 1\big). \tag{A.38}$$

Through this thesis $\epsilon^\mu_{(i)}$ and $e^\mu_{(i)}$ refer to photons and to $J = 3/2$ baryon states, respectively.

The Rarita–Schwinger spinors are constructed from the polarization vector $e^\mu(p,\lambda)$ and the spinors $u_s(p)$ as,

$$u_\mu(p, s_\Delta) = \sum_{\lambda, s} \langle 1\lambda \, \frac{1}{2} s | \frac{3}{2} s_\Delta \rangle e_\mu(p,\lambda) u_s(p) \, . \tag{A.39}$$

The states with various helicities are given by,

$$\psi^{(3/2)}_\mu = e_\mu(p,+1) u_{\frac{1}{2}}(p) \, , \tag{A.40}$$

$$\psi^{(1/2)}_\mu = \sqrt{\frac{2}{3}} e_\mu(p,0) u_{\frac{1}{2}}(p) + \sqrt{\frac{1}{3}} e_\mu(p,+1) u_{-\frac{1}{2}}(p) \, , \tag{A.41}$$

$$\psi^{(-1/2)}_\mu = \sqrt{\frac{2}{3}} e_\mu(p,0) u_{-\frac{1}{2}}(p) + \sqrt{\frac{1}{3}} e_\mu(p,-1) u_{\frac{1}{2}}(p) \, , \tag{A.42}$$

$$\psi^{(-3/2)}_\mu = e_\mu(p,-1) u_{\frac{1}{2}}(p) \, , \tag{A.43}$$

with the spinors given in Eq. (A.27).

A.3 Feynman rules and cross section formulae

External particles

- Fermion

$$u_s(k) \quad \text{for an incoming particle} \tag{A.44}$$
$$\bar{u}_s(k) \quad \text{for an outgoing particle} \tag{A.45}$$
$$\bar{v}_s(k) \quad \text{for an incoming antiparticle} \tag{A.46}$$
$$v_s(k) \quad \text{for an outgoing antiparticle} \tag{A.47}$$

- Photon

$$\epsilon_\mu(k_\gamma) \quad \text{for an incoming photon} \tag{A.48}$$
$$\epsilon^*_\mu(k_\gamma) \quad \text{for an outgoing photon} \tag{A.49}$$

Propagators

- Photon:

$$-\frac{ig^{\mu\nu}}{k_\gamma^2} \tag{A.50}$$

- Massive vector boson ($W^\pm$ or Z^0):

$$\frac{i}{q^2 - M_V^2}\left(-g^{\mu\nu} + \frac{q^\mu q^\nu}{M_V^2}\right) \approx \frac{ig^{\mu\nu}}{M_V^2}\,,\ |q|^2 \ll M_V^2 \tag{A.51}$$

  where M_V is the mass of the $W^\pm$ or Z^0 bosons.

- $J = 1/2$ Fermion:

$$\frac{\not{p} + m}{p^2 - m^2 + i\epsilon} \tag{A.52}$$

- $J = 3/2$ Fermion:

$$\frac{\not{p} + M^*}{p^2 - M^{*2} + i\epsilon} P_{\rho\sigma} \tag{A.53}$$

with

$$P_{\rho\sigma} = -g_{\rho\sigma} + \frac{1}{3}\gamma_\rho\gamma_\sigma + \frac{2}{3M_{N^*}^2}(k_1+k_2)_\rho(k_1+k_2)_\sigma + \frac{1}{3M_{N^*}}(\gamma_\rho(k_1+k_2)_\sigma - \gamma_\sigma(k_1+k_2)_\rho). \quad \text{(A.54)}$$

Vertices

- Electromagnetic vertex:

$$-ie\gamma_\mu \quad \text{(A.55)}$$

- Weak vertex: $W^\pm$ exchange:

$$-i\frac{g}{2\sqrt{2}}\gamma_\mu(1-\gamma_5), \quad \text{for leptons}, \quad \text{(A.56)}$$

$$-i\frac{g}{2\sqrt{2}}\gamma_\mu\mathcal{C}(1-\gamma_5), \quad \text{for quarks}, \quad \text{(A.57)}$$

$$\text{(A.58)}$$

  where $\mathcal{C}$ is the Cabbibo mixing matrix, as shown in Eq. (2.22).

- Weak vertex: Z^0 exchange:

$$-i\frac{g}{2\cos\theta_W}\frac{1}{2}\gamma_\mu(1-\gamma_5), \quad \text{for leptons}, \quad \text{(A.59)}$$

$$-i\frac{g}{2\cos\theta_W}\left[\mathcal{C}_L(1-\gamma_5)+\mathcal{C}_R(1+\gamma_5)\right], \text{ for quarks} \quad \text{(A.60)}$$

  where $\mathcal{C}_L = t_3 - Q\times\sin^2\theta_W$ and $\mathcal{C}_R = Q\times\sin^2\theta_W$, with Q the quark charge.

Cross section

Considering a scattering process in which two particles, with four-momenta $p_i = (E_i, \vec{p}_i)$, $i = 1, 2$, collide and produce N final particles with four-momenta $p_f = (E_f, \vec{p}_f)$, $f = 1, 2, \cdots, N$, the unpolarized differential cross section can now be written,

$$d\sigma = (2\pi)^4\delta^4\left(\sum_f p_f - \sum_i p_i\right)\frac{1}{4E_1E_2v_{rel}} \times\left(\prod_f \frac{d^3p_f}{(2\pi)^3 2E_f}\right)|\mathcal{M}|^2, \quad \text{(A.61)}$$

where v_{rel} is the relative velocity of the colliding particles. $\mathcal{M}$ is the Feynman amplitude for the process. Eq. (A.61) holds in any Lorentz frame in which the colliding particles move col-linearly. In such a frame the relative velocity v_{rel} is given by the expression,

$$E_1 E_2 v_{rel} = \left[(p_1 p_2)^2 - m_1^2 m_2^2\right]^{1/2}, \tag{A.62}$$

where m_1 and m_2 are the masses of the colliding particles.

Appendix B

Form factors

B.1 Relations between electromagnetic form factors and helicity amplitudes

The $\gamma N \to R$ helicity amplitudes describe the nucleon-resonance transition depending on the polarization of the incoming virtual photon and the baryon-spin projections onto the direction of the photon momentum. We follow the definitions adopted in the MAID analysis [111, 112], from which the empirical parametrizations of the helicity amplitudes are taken. Namely[1]

$$\mathcal{A}_{1/2} = \sqrt{\frac{2\pi\alpha}{k_R}} \left\langle S_z^* = \frac{1}{2} \left| \epsilon_\mu^{(+)} J_{EM}^\mu \right| S_z = -\frac{1}{2} \right\rangle \frac{1}{\sqrt{2M}\sqrt{2M_R}}, \quad \text{(B.1)}$$

$$\mathcal{A}_{3/2} = \sqrt{\frac{2\pi\alpha}{k_R}} \left\langle S_z^* = \frac{3}{2} \left| \epsilon_\mu^{(+)} J_{EM}^\mu \right| S_z = \frac{1}{2} \right\rangle \frac{1}{\sqrt{2M}\sqrt{2M_R}}, \quad \text{(B.2)}$$

$$\mathcal{S}_{1/2} = -\sqrt{\frac{2\pi\alpha}{k_R}} \left\langle S_z^* = \frac{1}{2} \left| \frac{|\vec{k}\,|}{\sqrt{Q^2}} \epsilon_\mu^{(0)} J_{EM}^\mu \right| S_z = \frac{1}{2} \right\rangle \frac{1}{\sqrt{2M}\sqrt{2M_R}}, \quad \text{(B.3)}$$

[1]It should be pointed out that the $1/(\sqrt{2M}\sqrt{2M_R})$ factor in the definition of the helicity amplitudes comes from the normalization of Dirac spinors ($\bar{u}u = 2M$, $\bar{u}_R u_R = 2M_R$) adopted in the present work.

in the resonance rest frame (notice that $S_{1/2}$ is not Lorentz invariant) and with the z-axis parallel to the photon momentum. In other words,

$$k^\mu = (k^0, 0, 0, |\vec{k}|), \quad p^\mu = (\sqrt{M^2 + \vec{k}^2}, 0, 0, -|\vec{k}|),$$
$$p^{*\mu} = (p + k)^\mu = (M_R, 0, 0, 0) \tag{B.4}$$

are the virtual photon, nucleon and resonance four-momenta. In addition, $Q^2 = -k^2$ and

$$k_R = \frac{M_R^2 - M^2}{2M_R}\,. \tag{B.5}$$

The photon polarization vectors are given by

$$\epsilon^\mu_{(\pm)} = \mp\frac{1}{\sqrt{2}}(0, 1, \pm i, 0), \quad \epsilon^\mu_{(0)} = \frac{1}{\sqrt{Q^2}}(|\vec{k}\,|, 0, 0, k^0)\,. \tag{B.6}$$

Finally, S_z (S_z^*) denotes the nucleon (resonance) spin projection onto the z axis.

With these definitions and the currents of Section 3.2.2, it is straightforward to derive the following equations connecting helicity amplitudes and electromagnetic form factors [41].

$N(1440)$

$$A^{p,n}_{1/2} = \sqrt{\frac{\pi\alpha[(M_R - M)^2 + Q^2]}{2M(M_R^2 - M^2)}}\left[\frac{Q^2}{2M^2}F_1^{p,n} + \frac{M_R + M}{M}F_2^{p,n}\right] \tag{B.7}$$

$$\begin{aligned} S^{p,n}_{1/2} &= -\sqrt{\frac{\pi\alpha[(M_R + M)^2 + Q^2]}{M(M_R^2 - M^2)}}\frac{(M_R - M)^2 + Q^2}{4MM_R} \\ &\quad \times\left[\frac{M_R + M}{2M}F_1^{p,n} - F_2^{p,n}\right] \end{aligned} \tag{B.8}$$

$N(1535)$

$$A^{p,n}_{1/2} = \sqrt{\frac{\pi\alpha[(M_R + M)^2 + Q^2]}{2M(M_R^2 - M^2)}}\left[\frac{Q^2}{2M^2}F_1^{p,n} + \frac{M_R - M}{M}F_2^{p,n}\right] \tag{B.9}$$

$$S_{1/2}^{p,n} = \sqrt{\frac{\pi\alpha[(M_R-M)^2+Q^2]}{M(M_R^2-M^2)}}\frac{(M_R+M)^2+Q^2}{4MM_R} \times\left[\frac{M_R-M}{2M}F_1^{p,n}-F_2^{p,n}\right] \quad \text{(B.10)}$$

$\Delta(1232)$

$$A_{1/2}^{p,n} = \sqrt{\frac{\pi\alpha[(M_R-M)^2+Q^2]}{3M(M_R^2-M^2)}}\left[\frac{M^2+MM_R+Q^2}{MM_R}C_3^V -\frac{M_R^2-M^2-Q^2}{2M^2}C_4^V-\frac{M_R^2-M^2+Q^2}{2M^2}C_5^V\right] \quad \text{(B.11)}$$

$$A_{3/2}^{p,n} = \sqrt{\frac{\pi\alpha[(M_R-M)^2+Q^2]}{M(M_R^2-M^2)}}\left[\frac{M+M_R}{M}C_3^V+\frac{M_R^2-M^2-Q^2}{2M^2}C_4^V +\frac{M_R^2-M^2+Q^2}{2M^2}C_5^V\right] \quad \text{(B.12)}$$

$$S_{1/2}^{p,n} = \sqrt{\frac{\pi\alpha[(M_R+M)^2+Q^2]}{6M(M_R^2-M^2)}}\frac{(M_R-M)^2+Q^2}{M_R^2} \times\left[\frac{M_R}{M}C_3^V+\frac{M_R^2}{M^2}C_4^V+\frac{M_R^2+M^2+Q^2}{2M^2}C_5^V\right] \quad \text{(B.13)}$$

$N(1520)$

$$A_{1/2}^{p,n} = \sqrt{\frac{\pi\alpha[(M_R+M)^2+Q^2]}{3M(M_R^2-M^2)}}\left[\frac{M^2-MM_R+Q^2}{MM_R}C_3^{p,n} -\frac{M_R^2-M^2-Q^2}{2M^2}C_4^{p,n}-\frac{M_R^2-M^2+Q^2}{2M^2}C_5^{p,n}\right] \quad \text{(B.14)}$$

$$A_{3/2}^{p,n} = \sqrt{\frac{\pi\alpha[(M_R+M)^2+Q^2]}{M(M_R^2-M^2)}}\left[\frac{M-M_R}{M}C_3^{p,n} -\frac{M_R^2-M^2-Q^2}{2M^2}C_4^{p,n}-\frac{M_R^2-M^2+Q^2}{2M^2}C_5^{p,n}\right] \quad \text{(B.15)}$$

$$S_{1/2}^{p,n} = -\sqrt{\frac{\pi\alpha[(M_R-M)^2+Q^2]}{6M(M_R^2-M^2)}}\frac{(M_R+M)^2+Q^2}{M_R^2} \left[\frac{M_R}{M}C_3^{p,n}+\frac{M_R^2}{M^2}C_4^{p,n}+\frac{M_R^2+M^2+Q^2}{2M^2}C_5^{p,n}\right] \quad \text{(B.16)}$$

B.2 Off diagonal Goldberger-Treiman relations

We consider an effective Lagrangian for the $RN\pi$ vertex, which is then used to calculate the πN decay width of the resonance. Using the Particle Data Group (PDG) [70] values for the decay width and πN branching ratio, one can fix the $RN\pi$ coupling. Thanks to PCAC

$$\partial_\mu A_{NCI}^\mu(x) = 2f_\pi m_\pi^2 \pi^0\,, \quad \text{(B.17)}$$

the latter coupling can be related to the dominant axial coupling in A_{NCI}^μ, which is the isovector part of the neutral current. This is the so called off diagonal GT relation. It establishes that in the soft pion limit

$$p_{\pi^0}^\mu \left\langle R|A_\mu^{NCI}(0)|N\right\rangle = -2if_\pi \left\langle R|\mathcal{L}_{RN\pi}|N\pi^0\right\rangle. \quad \text{(B.18)}$$

As in Refs. [41, 93], we distinguish between different cases, depending on the spin, parity and isospin of the resonance. Let us start with spin 1/2 states with isospin 1/2, like the $P_{11}(1440)$ and $S_{11}(1535)$. In this case

$$\mathcal{L}_{R_{1/2}N\pi} = \frac{f}{m_\pi}\bar{\Psi}\left\{\begin{array}{c}\gamma^\mu\gamma_5\\ \gamma^\mu\end{array}\right\}(\partial_\mu\vec{\pi}\cdot\vec{\tau})\,\Psi_{R_{1/2}} + h.c.\,, \quad \text{(B.19)}$$

where Ψ, $\Psi_{R_{1/2}}$ and $\vec{\pi}$ are the nucleon, resonance and pion fields[2]; $\vec{\tau}$ are the isospin Pauli matrices. The upper (lower) Lagrangian holds for positive (negative) parity resonances. The partial $R\to\pi N$ decay width is

$$\Gamma_{R_{1/2}\to N\pi} = \frac{3}{4\pi M_R}\left(\frac{f}{m_\pi}\right)^2 (M_R\pm M)^2\,(E_N\mp M)\,|\vec{p}_N|\,, \quad \text{(B.20)}$$

[2]Our convention is such that $(\pi^1-i\pi^2)/\sqrt{2}$ creates a π^- or annihilates a π^+ while a $\pi^3=\pi^0$ field creates or annihilates a π^0.

where

$$E_N = \sqrt{M^2 + \vec{p}_N^{\,2}} = \frac{M_R^2 + M^2 - m_\pi^2}{2M_R}\,. \tag{B.21}$$

The upper (lower) signs in Eq. (B.20) stand for positive (negative) parity resonances. The off diagonal GT relation amounts to

$$F_{A(R)}(0) = -2\frac{f}{m_\pi} f_\pi\,, \tag{B.22}$$

regardless of the parity. The coupling $F_{A(R)}(0)$ defined in Eq. (3.36) is now expressed in terms of f/m_π extracted from the $R \to \pi N$ decay width given above.

For $J = 3/2$ resonances, $\Delta(1232)$ and $D_{13}(1520)$ in our case,

$$\mathcal{L}_{R_{3/2}N\pi} = \frac{f^*}{m_\pi}\bar{\Psi}\left\{\begin{array}{c} 1 \\ \gamma_5 \end{array}\right\}\left(\partial_\mu\vec{\phi}\cdot\vec{\mathbf{t}}\right)\Psi^\mu_{R_{3/2}} + h.c. \tag{B.23}$$

where $\Psi^\mu_{R_{3/2}}$ is the resonance spin 3/2 field in the Rarita-Schwinger representation; $\vec{\mathbf{t}} = \vec{\tau}$ stands for isospin 1/2 resonances and $\vec{\mathbf{t}} = \vec{\mathbf{T}}$ (3/2 to 1/2 isospin transition operator)[3] for isospin 3/2 ones. The upper (lower) Lagrangian applies for positive (negative) parity states. The partial $R \to \pi N$ decay width is then given by

$$\Gamma_{R_{3/2}\to N\pi} = \frac{c_I}{6\pi}\left(\frac{f^*}{m_\pi}\right)^2 \frac{E_N \pm M}{2M_R}|\vec{p}_N|^3, \tag{B.24}$$

where the upper (lower) sign stands for positive (negative) parity resonances while $c_I = 1(3)$ for isospin 1/2 (3/2). Then we deduce

$$C^A_{5(R)}(0) = d_I\frac{f^*}{m_\pi} f_\pi\,, \tag{B.25}$$

where the numerical value of f^*/m_π is obtained from Eq. (B.24). The coefficient $d_I = -2$ is for isospin 1/2 states like the $D_{13}(1520)$ and $d_I = \sqrt{2/3}$ for isospin 3/2 ones, like the $\Delta(1232)$. The corresponding $C^A_{5(R)}(0)$ couplings determined by this GT relation were defined in Eqs. (3.42) and (3.29). It should be reminded that for the $N-\Delta(1232)$ transition, rather than the $C^A_5(0)$ value from Eq. (B.25), we use the one fitted in Ref. [40] to the $\nu_\mu p \to \mu^- p\pi^+$ ANL and BNL bubble chamber data.

[3] Normalized in such a way that the isospin matrix element $\left\langle \frac{3}{2}\,\frac{3}{2}\right| T_1^\dagger + iT_2^\dagger \left|\,\frac{1}{2}\,\frac{1}{2}\right\rangle = -\sqrt{2}$.

B.3 Decay modes of the second region resonances

In Table B.1, we compile the most relevant $P_{11}(1440)$, $D_{13}(1520)$ and $S_{11}(1535)$ decay modes and their branching ratios, taking values within the ranges of the PDG estimates [70].

Table B.1: Main decay modes, branching fractions (Γ_i/Γ) and relative angular momenta L of the decay particles, for the N^* resonances considered in this work.

$N(1440)$			$N(1520)$			$N(1535)$		
Mode	Fr(%)	L	Mode	Fr(%)	L	Mode	Fr(%)	L
$N\pi$	65	1	$N\pi$	60	2	$N\pi$	45	0
$\Delta\pi$	20	1	$\Delta\pi$	15	0	$N\eta$	42	0
$N\sigma$	15	0	$\Delta\pi$	12.5	2	$\Delta\pi$	1	2
			$N\rho$	9	0	$N\rho$	2	0
			$N\rho$	3.5	2	$N\sigma$	2	1
						$N(1440)\pi$	8	0

To obtain the partial width of a decay mode into unstable particles we use [280]

$$\Gamma_{R\to ab}(W) = \Gamma_{R\to ab}(W = M_R)\frac{\rho_{ab}(W)}{\rho_{ab}(M_R)} \tag{B.26}$$

where W denotes the resonance invariant mass. The function ρ_{ab} is given by

$$\begin{aligned}\rho_{ab}(W) &= \int d(p_a^2)d(p_b^2)\mathcal{A}(p_a^2)\mathcal{A}(p_b^2)\frac{p_{ab}^{2L+1}(W^2,p_a^2,p_b^2)}{W} \\ &\quad \times\Theta(W-\sqrt{p_a^2}-\sqrt{p_b^2}), \\ p_{ab}^2 &= \frac{\lambda(W^2,p_a^2,p_b^2)}{4W^2}\,,\end{aligned} \tag{B.27}$$

where p_{ab} denotes the center-of-mass momentum of the final state products, and L the relative angular momentum (Table B.1). The vacuum spectral function $\mathcal{A}_a$ reads

$$\mathcal{A}(p_a^2) = -\frac{1}{\pi}\mathrm{Im}\left(\frac{1}{p_a^2 - M_a^2 + iM_a\Gamma_a(p_a^2)}\right). \tag{B.28}$$

If one of the decay products (a) is a stable particle, then $\Gamma_a = 0$ and the vacuum spectral function can be written as

$$\mathcal{A}(p_a^2) = \delta(p_a^2 - M_a^2) \tag{B.29}$$

so that ρ_{ab} becomes,

$$\begin{aligned}\rho_{ab}(W) &= \frac{M_b}{\pi W}\int d(p_b^2)\frac{\Gamma_b(p_b^2)}{(p_b^2 - M_b^2)^2 + M_b^2\Gamma_b^2(p_b^2)} \\ &\quad \times p_{ab}^{2L+1}(W^2, M_a^2, p_b^2)\,\Theta(W - M_a - \sqrt{p_b^2})\,. \end{aligned}\tag{B.30}$$

If both final particles are stable, then

$$\rho_{ab}(W) = \frac{p_{ab}^{2L+1}(W^2, M_a^2, M_b^2)}{W}\,\Theta(W - M_a - M_b)\,. \tag{B.31}$$

Appendix C

Nuclear medium Δ-properties and the Lindhard function

C.1 Δ selfenergy

We give expressions for the coefficients (C_Q, C_{A_2} and C_{A_3}) and exponents (α and $\beta = \gamma/2$) of the imaginary part of the Δ self-energy (Eq. (3.66) of Chapter 3) [119]. The coefficients and exponents could be parametrized in an approximate way in the range of $85 < T_\pi < 315$ MeV with the formula given by,

$$C(T_\pi) \;=\; ax^2 + bx + c; \quad x = \frac{\omega_\pi - m_\pi}{m_\pi}, \tag{C.1}$$

where C stands for any of the 5 coefficients and exponents (C_Q, C_{A_2}, C_{A_3}, α and $\beta = \gamma/2$). ω and m_π are the energy and mass of the pion that would excite a Δ with the corresponding invariant mass in the LAB frame. The values of a, b and c are compiled in Table C.1. In some occasions, and for simplicity, we use some averages for momentum and energy of the particles inside of the nuclear environment. Thus, in the Lab frame of pion collision experiments, the average momentum of

Table C.1: Coefficient of Eq. (C.1) for an analytical interpolation of $\mathrm{Im}\Sigma_\Delta$ [119].

	C_Q (MeV)	C_{A_2} (MeV)	C_{A_3} (MeV)	α	β
a	-5.19	1.06	-13.46	0.382	-0.038
b	15.35	-6.64	46.17	-1.322	0.204
c	2.06	22.66	-20.34	1.466	0.613

the nucleon is given by,

$$\begin{aligned} \left\langle \vec{p}_N^{\,2} \right\rangle &= \frac{\frac{1}{(2\pi)^3}\int_0^{p_F} \vec{p}_N^{\,2} n_N(\vec{p}_N) d^3\vec{p}_N}{\frac{1}{(2\pi)^3}\int_0^{p_F} n_N(\vec{p}_N) d^3\vec{p}_N} \\ &= \frac{3}{5}p_F^2, \end{aligned} \tag{C.2}$$

the average energy and momentum of the Δ resonance are,

$$\begin{aligned} E_\Delta &= \omega_\pi + E_N \\ &= \omega_\pi + \sqrt{M_N^2 + \vec{p}_N^{\,2}} \\ &\approx \omega_\pi + M_N + \frac{3}{5}p_F^2, \end{aligned} \tag{C.3}$$

$$\begin{aligned} \left\langle \vec{p}_\Delta^{\,2} \right\rangle &= \left\langle (\vec{p}_N^{\,2} + \vec{k}_\pi^{\,2}) \right\rangle \\ &= \left\langle \vec{p}_N^{\,2} \right\rangle + \left\langle \vec{k}^{\,2} 2_\pi \right\rangle + 2\left\langle (\vec{p}_N \cdot \vec{k}_\pi \right\rangle \\ &\approx \frac{3}{5}p_F^2 + \vec{k}_\pi^{\,2}. \end{aligned} \tag{C.4}$$

and the invariant mass of Δ could be approximated by,

$$s_\Delta = E_\Delta^2 - \left\langle \vec{p}_\Delta^{\,2} \right\rangle, \tag{C.5}$$

while the average energy of pion can be averaged by

$$\omega_\pi = \frac{s_\Delta - m_\pi^2 - M_N^2 - \left(\frac{3p_F^2}{10M_N}\right)^2}{\frac{3p_F^2}{10M_N} + M_N}. \tag{C.6}$$

C.2 Pauli blocking of the $\Delta \to \pi N$ decay

The Pauli blocking of the $\Delta \to \pi N$ decay reduces the $\Gamma_\Delta^{\rm free}$ free width in the nuclear environment. For the Pauli blocked width, we use the approximation derived in [98]

$$\Gamma_\Delta^{\rm Pauli} = \Gamma_\Delta^{\rm free} \frac{I_1 + I_2}{2} \,. \tag{C.7}$$

The angular integrals I_1 and I_2 read,

$$I_1 = 1 + \Theta(\tilde{q} - 1) \left(-\frac{1}{5\tilde{q}^2} \right) \Theta(1 - \tilde{q}) \left[\tilde{q} - 1 - \frac{\tilde{q}^3}{5} \right], \tag{C.8}$$

$$I_2 = 1 + \Theta(\tilde{q} - 1) \left[-\frac{3}{5\tilde{q}^2} - \frac{4}{21\tilde{q}^6} + \frac{18}{35\tilde{q}^4} \right], \tag{C.9}$$

with

$$\tilde{q} = \frac{q}{k_F}, \tag{C.10}$$

where q is the pion-nucleon c.m. momentum, and k_F is the Fermi momentum.

C.3 Lindhard function

In a non-symmetric nuclear medium, the relativistic Lindhard function is defined as

$$\begin{aligned} \overline{U}_R(q, k_F^n, k_F^p) &= 2 \int \frac{d^3p}{(2\pi)^3} \frac{M}{E(\vec{p})} \frac{M}{E(\vec{p}+\vec{q})} \frac{\Theta(k_F^n - |\vec{p}\,|)\Theta(|\vec{p}+\vec{q}\,| - k_F^p)}{q^0 + E(\vec{p}) - E(\vec{p}+\vec{q}) + \mathrm{i}\,\epsilon} \\ &\quad + (q \to -q) \end{aligned} \tag{C.11}$$

The two contributions above correspond to the direct and the crossed *ph* excitation terms, respectively. For positive transferred energy only the direct term has imaginary part, which is given by

$$\begin{aligned} \mathrm{Im}\overline{U}_R(q, k_F^n, k_F^p) &= \int d^3p \mathcal{F}_R(q, \vec{p}, k_F^n, k_F^p) \\ &= -M^2 \frac{\Theta(q^0)\Theta(-q^2)}{2\pi|\vec{q}\,|} \Theta(E_F^n - E_F^p + q^0) \\ &\quad \times \Theta(E_F^n - \mathcal{E}_R^p)(E_F^n - \mathcal{E}_R^p) \end{aligned} \tag{C.12}$$

with

$$\begin{aligned}
\mathcal{F}_R(q,\vec{p},k_F^n,k_F^p) &= -\frac{M^2}{4\pi^2}\frac{\Theta(q^0)\delta(q^0+E(\vec{p})-E(\vec{p}+\vec{q}\,))}{E(\vec{p})E(\vec{p}+\vec{q})} \\
&\quad \times\Theta(k_F^n-|\vec{p}\,|)\Theta(|\vec{p}+\vec{q}\,|-k_F^p) \qquad \text{(C.13)} \\
\mathcal{E}_R^p &= \text{Max}\left\{M, E_F^p-q^0, \frac{-q^0+|\vec{q}\,|\sqrt{1-4M^2/q^2}}{2}\right\}, \\
E_F^{n,p} &= \sqrt{M^2+(k_F^{n,p})^2}, \qquad \text{(C.14)}
\end{aligned}$$

being Max(...) the maximum of the quantities included in the bracket. In the low density approximation,

$$\text{Im}U_N(q) \approx -\pi\rho k_F(|\vec{q}\,|)\delta(q^0-\epsilon(\vec{q}). \qquad \text{(C.15)}$$

Appendix D

SU(6)

D.1 Chiral invariant four meson interaction with a single trace

In this appendix we show that, the operators $\mathcal{O}_1$, $\mathcal{O}_2$, $\mathcal{O}_3$ in Eq. (6.13), already saturate the most general chiral invariant interaction, modulo $O(\Phi_6^6)$, stemming from single trace Lagrangian terms.

Rather than doing the expansion of the most general term $\mathrm{Tr}(\mathcal{U}_{ij}\mathcal{U}_{kl}\cdots)$ in powers of the meson field, we just write down the possible operators in terms of the meson field and seek the most general combination invariant under infinitesimal chiral rotations. To alleviate the notation, we use $U_6 = e^{\phi}$, ϕ being antihermitian and dimensionless. This is related with the usual meson field by $\phi = 2i\Phi_6/f$.

The 8 possible terms, assuming other symmetries but not chiral invariance, are as follows

$$\begin{aligned}
A_1 &= \mathrm{Tr}(\phi^2),\\
A_2 &= \mathrm{Tr}(\sigma_i\phi\sigma_i\phi),\\
A_3 &= \mathrm{Tr}(\phi^4),\\
A_4 &= \mathrm{Tr}(\sigma_i\phi\sigma_i\phi^3),\\
A_5 &= \mathrm{Tr}(\sigma_i\phi^2\sigma_i\phi^2),\\
A_6 &= i\epsilon_{ijk}\mathrm{Tr}(\sigma_i\phi\sigma_j\phi\sigma_k\phi^2),\\
A_7 &= \mathrm{Tr}(\sigma_i\phi\sigma_i\phi\sigma_j\phi\sigma_j\phi),\\
A_8 &= \mathrm{Tr}(\sigma_i\phi\sigma_j\phi\sigma_i\phi\sigma_j\phi). \qquad \text{(D.1)}
\end{aligned}$$

The operators A_1 and A_2 give mass to the mesons, the other provide interaction.

Under a chiral rotation $U_6 \to \Omega_L^\dagger U_6 \Omega_R$, and this induces a non linear transformation on ϕ. Vector invariance ($\Omega_L = \Omega_R$) is a similarity transformation which produces the same transformation on ϕ and it is trivially satisfied by the 8 operators. Therefore we consider just axial transformations $\Omega_L = \Omega_R^\dagger$. Only infinitesimal transformations are needed, $\Omega_R = e^{\delta\alpha/2} = 1 + \frac{1}{2}\delta\alpha$, with $\delta\alpha$ infinitesimal, antihermitian and spinless. This induces the transformation

$$\delta\phi = \delta\alpha + \frac{1}{12}\delta\alpha\phi^2 + \frac{1}{12}\phi^2\delta\alpha - \frac{1}{6}\phi\delta\alpha\phi + O(\phi^4). \qquad \text{(D.2)}$$

(To all orders in the meson field, the infinitesimal axial variation contains only even powers of ϕ.)

The variations of A_1 and A_2 produce terms of $O(\phi)$ that can only be canceled by choosing a suitable combination of the two operators. Also they produce terms of $O(\phi^3)$. They should cancel with the corresponding variations from the quartic terms, taking suitable combinations of them. The cancellation to order $O(\phi^5)$ is of no concern to us as this involves $O(\phi^6)$ interactions. The cancellation will be automatic for the expansion of any of the terms $\mathrm{Tr}(\mathcal{U}_{ij}\mathcal{U}_{kl}\cdots)$ since chiral invariance is manifest in those terms.

For a generic operator $H = \sum_{i=1}^{8} c_i A_i$, the condition $\delta H = O(\phi^5)$ gives the following conditions

$$\begin{aligned}
0 &= 2c_1 + 6c_2, \\
0 &= 4c_3 + 3c_4, \\
0 &= -\frac{1}{3}c_2 + c_4 + 8c_7 + 4c_8, \\
0 &= \frac{1}{6}c_2 + c_4 + 2c_5 - 2c_6, \\
0 &= \frac{1}{6}c_2 + c_4 + 2c_5 - 2c_6, \\
0 &= 2c_6 - 2c_7 + 4c_8. \qquad \text{(D.3)}
\end{aligned}$$

They correspond, respectively, to the vanishing of the coefficients of $\mathrm{Tr}(\phi\delta\alpha)$, $\mathrm{Tr}(\phi^3\delta\alpha)$, $\mathrm{Tr}(\phi\sigma_i\phi\sigma_i\phi\delta\alpha)$, $\mathrm{Tr}(\sigma_i\phi\sigma_i\phi^2\delta\alpha)$, $\mathrm{Tr}(\sigma_i\phi^2\sigma_i\phi\delta\alpha)$, and $i\epsilon_{ijk}\mathrm{Tr}(\sigma_i\phi\sigma_j\phi\sigma_k\phi\delta\alpha)$.

The 5 independent relations leave 3 chiral invariant combinations. They can be taken as

$$\begin{aligned} H_{\rm inv} &= c_1(A_1 - \frac{1}{3}A_2 - \frac{1}{36}A_6 - \frac{1}{60}A_7 + \frac{1}{180}A_8) \\ &\quad + c_3(A_3 - \frac{4}{3}A_4 - \frac{2}{3}A_6 + \frac{1}{3}A_8) + c_5(A_5 + A_6 + \frac{1}{5}A_7 - \frac{2}{5}A_8) \end{aligned} \tag{D.4}$$

The three combinations $\mathcal{O}_1$, $(\mathcal{O}_2 - 20\mathcal{O}_1)/12$, and $\mathcal{O}_3/3$ in Section 6.3 correspond, respectively, to $(c_1, c_3, c_5) = (3, 1/4, 1/4)$, $(0, 1, 5/6)$, and $(0, 1, 0)$.

D.2 Coefficients of the S-wave tree level amplitudes

This appendix gives the $\mathcal{D}_2$ and $\mathcal{D}_3$ matrices of the S-wave tree level meson-meson amplitudes in Eq. (6.21), for the various YIJ sectors (Tables D.1-D.38). Note that for the $Y = 0$ channels, G-parity is conserved, and that all $Y = 0$ states have well-defined G-parity except the $\bar{K}^*K$ and $K^*\bar{K}$ states, but the combinations $\left(\bar{K}K^* \pm K\bar{K}^*\right)/\sqrt{2}$ are actually G-parity eigenstates with eigenvalues ± 1. These states will be denoted $(\bar{K}K^*)_S$ and $(\bar{K}K^*)_A$, respectively.

$\mathcal{D}_2$ matrices

Table D.1: $(Y, I, J) = (0, 0, 0)$.

	$\pi\pi$	$\bar{K}K$	$\eta\eta$	$\rho\rho$	$\omega\omega$	$\omega\phi$	$\bar{K}^*K^*$	$\phi\phi$
	0	0	0	0	0	0	0	0
	0	0	0	0	0	0	0	0
	0	0	0	0	0	0	0	0
	0	0	0	$-\frac{208}{3}$	$\frac{80}{\sqrt{3}}$	0	$24\sqrt{3}$	0
	0	0	0	$\frac{80}{\sqrt{3}}$	$-\frac{80}{3}$	0	-24	0
	0	0	0	0	0	0	$\frac{16}{3}$	0
	0	0	0	$24\sqrt{3}$	-24	$\frac{16}{3}$	-72	-48
	0	0	0	0	0	0	-48	$-\frac{160}{3}$

Table D.2: $(Y, I, J) = (0, 0, 1)$.

G	$\eta\phi$	$\eta\omega$	$\pi\rho$	$(\bar{K}K^*)_A$	$\bar{K}^*K^*$	$\omega\phi$	$(\bar{K}K^*)_S$
$-$	0	0	0	0	0		
$-$	0	0	0	0	0		
$-$	0	0	0	0	0		
$-$	0	0	0	0	0		
$-$	0	0	0	0	-28		
$+$						0	0
$+$						0	0

Table D.3: $(Y, I, J) = (0, 0, 2)$.

	$\rho\rho$	$\omega\omega$	$\omega\phi$	$\bar{K}^*K^*$	$\phi\phi$
	$-\frac{16}{3}$	$\frac{32}{\sqrt{3}}$	0	$4\sqrt{3}$	0
	$\frac{32}{\sqrt{3}}$	$-\frac{32}{3}$	0	-4	0
	0	0	0	$\frac{40}{3}$	0
	$4\sqrt{3}$	-4	$\frac{40}{3}$	-12	-8
	0	0	0	-8	$-\frac{64}{3}$

Table D.4: $(Y, I, J) = (0, 1, 0)$.

	$\eta\pi$	$\bar{K}K$	$\omega\rho$	$\phi\rho$	$\bar{K}^*K^*$
	0	0	0	0	0
	0	0	0	0	0
	0	0	$-\frac{160}{3}$	0	$24\sqrt{2}$
	0	0	0	0	$-\frac{16}{3}$
	0	0	$24\sqrt{2}$	$-\frac{16}{3}$	-24

Table D.5: $(Y, I, J) = (0, 1, 1)$.

G	$\pi\phi$	$\pi\omega$	$\eta\rho$	$(\bar{K}K^*)_S$	$\rho\rho$	$\bar{K}^*K^*$	$\pi\rho$	$(\bar{K}K^*)_A$	$\omega\rho$	$\phi\rho$
+	0	0	0	0	0	0				
+	0	0	0	0	0	0				
+	0	0	0	0	0	0				
+	0	0	0	0	0	0				
+	0	0	0	0	$-\frac{56}{3}$	$\frac{28\sqrt{2}}{3}$				
+	0	0	0	0	$\frac{28\sqrt{2}}{3}$	$-\frac{28}{3}$				
−							0	0	0	0
−							0	0	0	0
−							0	0	0	0
−							0	0	0	0

Table D.6: $(Y, I, J) = (0, 1, 2)$.

	$\omega\rho$	$\phi\rho$	$\bar{K}^*K^*$
	$-\frac{64}{3}$	0	$4\sqrt{2}$
	0	0	$-\frac{40}{3}$
	$4\sqrt{2}$	$-\frac{40}{3}$	-4

Table D.7: $(Y, I, J) = (0, 2, 0)$.

	$\pi\pi$	$\rho\rho$
	0	0
	0	$-\frac{16}{3}$

Table D.8: $(Y, I, J) = (0, 2, 1)$.

	$\pi\rho$
	0

Table D.9: $(Y, I, J) = (0, 2, 2)$.

	$\rho\rho$
	$-\frac{40}{3}$

Table D.10: $(Y, I, J) = (1, 1/2, 0)$.

	$K\pi$	ηK	$K^*\rho$	$K^*\omega$	$K^*\phi$
	0	0	0	0	0
	0	0	0	0	0
	0	0	$-\frac{100}{3}$	$-\frac{44}{\sqrt{3}}$	$12\sqrt{6}$
	0	0	$-\frac{44}{\sqrt{3}}$	$-\frac{44}{3}$	$12\sqrt{2}$
	0	0	$12\sqrt{6}$	$12\sqrt{2}$	$-\frac{88}{3}$

Table D.11: $(Y, I, J) = (1, 1/2, 1)$.

	πK^*	$K\rho$	$K\omega$	ηK^*	$K\phi$	$K^*\rho$	$K^*\omega$	$K^*\phi$
	0	0	0	0	0	0	0	0
	0	0	0	0	0	0	0	0
	0	0	0	0	0	0	0	0
	0	0	0	0	0	0	0	0
	0	0	0	0	0	0	0	0
	0	0	0	0	0	-14	$-\frac{14}{\sqrt{3}}$	$-14\sqrt{\frac{2}{3}}$
	0	0	0	0	0	$-\frac{14}{\sqrt{3}}$	$-\frac{14}{3}$	$-\frac{14\sqrt{2}}{3}$
	0	0	0	0	0	$-14\sqrt{\frac{2}{3}}$	$-\frac{14\sqrt{2}}{3}$	$-\frac{28}{3}$

Table D.12: $(Y, I, J) = (1, 1/2, 2)$.

	$K^*\rho$	$K^*\omega$	$K^*\phi$
	$\frac{2}{3}$	$-\frac{26}{\sqrt{3}}$	$2\sqrt{6}$
	$-\frac{26}{\sqrt{3}}$	$-\frac{26}{3}$	$2\sqrt{2}$
	$2\sqrt{6}$	$2\sqrt{2}$	$-\frac{52}{3}$

Table D.13: $(Y, I, J) = (1, 3/2, 0)$.

	$K\pi$	$K^*\rho$
	0	0
	0	$-\frac{16}{3}$

Table D.14: $(Y, I, J) = (1, 3/2, 1)$.

	πK^*	$K\rho$	$K^*\rho$
	0	0	0
	0	0	0
	0	0	0

Table D.15: $(Y, I, J) = (1, 3/2, 2)$.

	$K^*\rho$
	$-\frac{40}{3}$

Table D.16: $(Y, I, J) = (2, 0, 1)$.

KK^*	K^*K^*
0	0
0	0

Table D.17: $(Y, I, J) = (2, 1, 0)$.

KK	K^*K^*
0	0
0	$-\frac{16}{3}$

Table D.18: $(Y, I, J) = (2, 1, 1)$.

KK^*
0

Table D.19: $(Y, I, J) = (2, 1, 2)$.

	K^*K^*
	$-\frac{40}{3}$

$\mathcal{D}_3$ matrices

Table D.20: $(Y, I, J) = (0, 0, 0)$.

	$\pi\pi$	$\bar{K}K$	$\eta\eta$	$\rho\rho$	$\omega\omega$	$\omega\phi$	$\bar{K}^*K^*$	$\phi\phi$
	0	0	0	0	0	0	0	0
	0	0	0	0	0	0	0	0
	0	0	0	0	0	0	0	0
	0	0	0	$-\frac{128}{3}$	0	0	$\frac{32}{\sqrt{3}}$	0
	0	0	0	0	0	0	$-\frac{32}{3}$	0
	0	0	0	0	0	0	$-\frac{64}{3}$	0
	0	0	0	$\frac{32}{\sqrt{3}}$	$-\frac{32}{3}$	$-\frac{64}{3}$	-32	$-\frac{64}{3}$
	0	0	0	0	0	0	$-\frac{64}{3}$	0

Table D.21: $(Y, I, J) = (0, 0, 1)$.

G	$\eta\phi$	$\eta\omega$	$\pi\rho$	$(\bar{K}K^*)_A$	$\bar{K}^*K^*$	$\omega\phi$	$(\bar{K}K^*)_S$
$-$	0	0	0	0	0		
$-$	0	0	0	0	0		
$-$	0	0	0	0	0		
$-$	0	0	0	0	0		
$-$	0	0	0	0	-48		
$+$						0	0
$+$						0	0

Table D.22: $(Y, I, J) = (0, 0, 2)$.

	$\rho\rho$	$\omega\omega$	$\omega\phi$	$\bar{K}^*K^*$	$\phi\phi$
	$\frac{64}{3}$	0	0	$-\frac{16}{\sqrt{3}}$	0
	0	0	0	$\frac{16}{3}$	0
	0	0	0	$\frac{32}{3}$	0
	$-\frac{16}{\sqrt{3}}$	$\frac{16}{3}$	$\frac{32}{3}$	16	$\frac{32}{3}$
	0	0	0	$\frac{32}{3}$	0

Table D.23: $(Y, I, J) = (0, 1, 0)$.

	$\eta\pi$	$\bar{K}K$	$\omega\rho$	$\phi\rho$	$\bar{K}^*K^*$
	0	0	0	0	0
	0	0	0	0	0
	0	0	0	0	$\frac{32\sqrt{2}}{3}$
	0	0	0	0	$\frac{64}{3}$
	0	0	$\frac{32\sqrt{2}}{3}$	$\frac{64}{3}$	$-\frac{32}{3}$

Table D.24: $(Y, I, J) = (0, 1, 1)$.

G	$\pi\phi$	$\pi\omega$	$\eta\rho$	$(\bar{K}K^*)_S$	$\rho\rho$	$\bar{K}^*K^*$	$\pi\rho$	$(\bar{K}K^*)_A$	$\omega\rho$	$\phi\rho$
+	0	0	0	0	0	0				
+	0	0	0	0	0	0				
+	0	0	0	0	0	0				
+	0	0	0	0	0	0				
+	0	0	0	0	-32	$16\sqrt{2}$				
+	0	0	0	0	$16\sqrt{2}$	-16				
−							0	0	0	0
−							0	0	0	0
−							0	0	0	0
−							0	0	0	0

Table D.25: $(Y, I, J) = (0, 1, 2)$.

	$\omega\rho$	$\phi\rho$	$\bar{K}^*K^*$
	0	0	$-\frac{16\sqrt{2}}{3}$
	0	0	$-\frac{32}{3}$
	$-\frac{16\sqrt{2}}{3}$	$-\frac{32}{3}$	$\frac{16}{3}$

Table D.26: $(Y, I, J) = (0, 2, 0)$.

	$\pi\pi$	$\rho\rho$
	0	0
	0	$\frac{64}{3}$

Table D.27: $(Y, I, J) = (0, 2, 1)$.

	$\pi\rho$
	0

Table D.28: $(Y, I, J) = (0, 2, 2)$.

	$\rho\rho$
	$-\frac{32}{3}$

Table D.29: $(Y, I, J) = (1, 1/2, 0)$.

	$K\pi$	ηK	$K^*\rho$	$K^*\omega$	$K^*\phi$
	0	0	0	0	0
	0	0	0	0	0
	0	0	$-\frac{80}{3}$	$\frac{16}{\sqrt{3}}$	$16\sqrt{\frac{2}{3}}$
	0	0	$\frac{16}{\sqrt{3}}$	$\frac{16}{3}$	$\frac{16\sqrt{2}}{3}$
	0	0	$16\sqrt{\frac{2}{3}}$	$\frac{16\sqrt{2}}{3}$	$\frac{32}{3}$

Table D.30: $(Y, I, J) = (1, 1/2, 1)$.

	πK^*	$K\rho$	$K\omega$	ηK^*	$K\phi$	$K^*\rho$	$K^*\omega$	$K^*\phi$
	0	0	0	0	0	0	0	0
	0	0	0	0	0	0	0	0
	0	0	0	0	0	0	0	0
	0	0	0	0	0	0	0	0
	0	0	0	0	0	0	0	0
	0	0	0	0	0	-24	$-8\sqrt{3}$	$-8\sqrt{6}$
	0	0	0	0	0	$-8\sqrt{3}$	-8	$-8\sqrt{2}$
	0	0	0	0	0	$-8\sqrt{6}$	$-8\sqrt{2}$	-16

Table D.31: $(Y, I, J) = (1, 1/2, 2)$.

	$K^*\rho$	$K^*\omega$	$K^*\phi$
	$\frac{40}{3}$	$-\frac{8}{\sqrt{3}}$	$-8\sqrt{\frac{2}{3}}$
	$-\frac{8}{\sqrt{3}}$	$-\frac{8}{3}$	$-\frac{8\sqrt{2}}{3}$
	$-8\sqrt{\frac{2}{3}}$	$-\frac{8\sqrt{2}}{3}$	$-\frac{16}{3}$

Table D.32: $(Y, I, J) = (1, 3/2, 0)$.

	$K\pi$	$K^*\rho$
	0	0
	0	$\frac{64}{3}$

Table D.33: $(Y, I, J) = (1, 3/2, 1)$.

	πK^*	$K\rho$	$K^*\rho$
	0	0	0
	0	0	0
	0	0	0

Table D.34: $(Y, I, J) = (1, 3/2, 2)$.

	$K^*\rho$
	$-\frac{32}{3}$

Table D.35: $(Y, I, J) = (2, 0, 1)$.

KK^*	K^*K^*
0	0
0	0

Table D.36: $(Y, I, J) = (2, 1, 0)$.

KK	K^*K^*
0	0
0	$\frac{64}{3}$

Table D.37: $(Y, I, J) = (2, 1, 1)$.

KK^*
0

Table D.38: $(Y, I, J) = (2, 1, 2)$.

	K^*K^*
	$-\frac{32}{3}$

Bibliography

[1] W. Pauli, "Dear radioactive ladies and gentlemen," *Phys.Today*, vol. 31N9, p. 27, 1978.

[2] C. Cowan, F. Reines, F. Harrison, H. Kruse, and A. McGuire, "Detection of the free neutrino: A confirmation," *Science*, vol. 124, pp. 103–104, 1956.

[3] K. Abe *et al.*, "The T2K Experiment," *Nucl.Instrum.Meth.*, vol. A659, pp. 106–135, 2011.

[4] D. Eichler, M. Livio, T. Piran, and D. N. Schramm, "Nucleosynthesis, Neutrino Bursts and Gamma-Rays from Coalescing Neutron Stars," *Nature*, vol. 340, pp. 126–128, 1989.

[5] T. Ohlsson, "Status of non-standard neutrino interactions," *Rept.Prog.Phys.*, vol. 76, p. 044201, 2013.

[6] A. Aguilar-Arevalo *et al.*, "First measurement of the muon neutrino charged current quasielastic double differential cross section," *Phys.Rev.*, vol. D81, p. 092005, 2010.

[7] A. Aguilar-Arevalo *et al.*, "Measurement of the neutrino neutral-current elastic differential cross section on mineral oil at $E_\nu \sim 1$ GeV," *Phys.Rev.*, vol. D82, p. 092005, 2010.

[8] A. Aguilar-Arevalo *et al.*, "First measurement of the muon antineutrino double-differential charged-current quasielastic cross section," *Phys.Rev.*, vol. D88, no. 3, p. 032001, 2013.

[9] L. Fields *et al.*, "Measurement of muon antineutrino quasielastic scattering on a hydrocarbon target at $E_\nu \sim 3.5$ GeV," *Phys.Rev.Lett.*, vol. 111, no. 2, p. 022501, 2013.

[10] G. Fiorentini *et al.*, "Measurement of muon neutrino quasielastic scattering on a hydrocarbon target at $E_\nu \sim 3.5$ GeV," *Phys.Rev.Lett.*, vol. 111, no. 2, p. 022502, 2013.

[11] V. Lyubushkin *et al.*, "A study of quasi-elastic muon neutrino and antineutrino scattering in the NOMAD experiment," *Eur.Phys.J.*, vol. C63, pp. 355–381, 2009.

[12] A. A. Aguilar-Arevalo *et al.*, "Measurement of ν_μ and $\bar{\nu}_\mu$ induced neutral current single π^0 production cross sections on mineral oil at $E_\nu \sim \mathcal{O}$ (1-GeV)," *Phys.Rev.*, vol. D81, p. 013005, 2010.

[13] A. Aguilar-Arevalo *et al.*, "Measurement of ν_μ-induced charged-current neutral pion production cross sections on mineral oil at $E_\nu \in 0.5 - 2.0$ GeV," *Phys.Rev.*, vol. D83, p. 052009, 2011.

[14] A. Aguilar-Arevalo *et al.*, "Measurement of neutrino-induced charged-current charged pion production cross sections on mineral oil at $\mathrm{E}_\nu \sim 1$ GeV," *Phys.Rev.*, vol. D83, p. 052007, 2011.

[15] K. Hiraide *et al.*, "Search for charged current coherent pion production on carbon in a few-GeV neutrino beam," *Phys.Rev.*, vol. D78, p. 112004, 2008.

[16] Y. Kurimoto *et al.*, "Improved measurement of neutral current coherent π^0 production on carbon in a few-GeV neutrino beam," *Phys.Rev.*, vol. D81, p. 111102, 2010.

[17] C. Kullenberg *et al.*, "A measurement of coherent neutral pion production in neutrino neutral current interactions in NOMAD," *Phys.Lett.*, vol. B682, pp. 177–184, 2009.

[18] K. Abe *et al.*, "Measurement of the inclusive ν_μ charged current cross section on carbon in the near detector of the T2K Experiment," *Phys.Rev.*, vol. D87, p. 092003, 2013.

[19] Y. Nakajima *et al.*, "Measurement of inclusive charged current interactions on carbon in a few-GeV neutrino beam," *Phys.Rev.*, vol. D83, p. 012005, 2011.

[20] P. Adamson *et al.*, "Neutrino and antineutrino inclusive charged-current cross section measurements with the MINOS near detector," *Phys.Rev.*, vol. D81, p. 072002, 2010.

[21] Q. Wu *et al.*, "A precise measurement of the muon neutrino-nucleon inclusive charged current cross-section off an isoscalar target in the energy range $2.5 < E_\nu < 40$ GeV by NOMAD," *Phys.Lett.*, vol. B660, pp. 19–25, 2008.

[22] J. G. Morfin, J. Nieves, and J. T. Sobczyk, "Recent developments in neutrino/antineutrino - nucleus interactions," *Adv.High Energy Phys.*, vol. 2012, p. 934597, 2012.

[23] K. M. Graczyk and J. T. Sobczyk, "The algebraic solution of RPA equations for the charged current quasielastic neutrino nucleus scattering," *Eur.Phys.J.*, vol. C31, pp. 177–185, 2003.

[24] J. Nieves, J. E. Amaro, and M. Valverde, "Inclusive quasi-elastic neutrino reactions," *Phys.Rev.*, vol. C70, p. 055503, 2004.

[25] M. S. Athar, S. Ahmad, and S. Singh, "Charged lepton production from iron induced by atmospheric neutrinos," *Eur.Phys.J.*, vol. A24, pp. 459–474, 2005.

[26] M. Martini, M. Ericson, G. Chanfray, and J. Marteau, "A unified approach for nucleon knock-out, coherent and incoherent pion production in neutrino interactions with nuclei," *Phys.Rev.*, vol. C80, p. 065501, 2009.

[27] O. Benhar, N. Farina, H. Nakamura, M. Sakuda, and R. Seki, "Electron- and neutrino-nucleus scattering in the impulse approximation regime," *Phys.Rev.*, vol. D72, p. 053005, 2005.

[28] A. M. Ankowski and J. T. Sobczyk, "Construction of spectral functions for medium-mass nuclei," *Phys.Rev.*, vol. C77, p. 044311, 2008.

[29] M. Martinez, P. Lava, N. Jachowicz, J. Ryckebusch, K. Vantournhout, *et al.*, "Relativistic models for quasi-elastic neutrino scattering," *Phys.Rev.*, vol. C73, p. 024607, 2006.

[30] A. Butkevich and S. A. Kulagin, "Quasi-elastic neutrino charged-current scattering cross sections on oxygen," *Phys.Rev.*, vol. C76, p. 045502, 2007.

[31] A. Meucci, M. Barbaro, J. Caballero, C. Giusti, and J. Udias, "Relativistic descriptions of final-state interactions in charged-current quasielastic neutrino-nucleus scattering at MiniBooNE kinematics," *Phys.Rev.Lett.*, vol. 107, p. 172501, 2011.

[32] J. Caballero, J. E. Amaro, M. Barbaro, T. Donnelly, C. Maieron, *et al.*, "Superscaling in charged current neutrino quasielastic scattering in the relativistic impulse approximation," *Phys.Rev.Lett.*, vol. 95, p. 252502, 2005.

[33] J. Amaro, M. Barbaro, J. Caballero, T. Donnelly, and C. Williamson, "Meson-exchange currents and quasielastic neutrino cross sections in the SuperScaling Approximation model," *Phys.Lett.*, vol. B696, pp. 151–155, 2011.

[34] J. Nieves, I. Ruiz Simo, and M. Vicente Vacas, "Inclusive charged–current neutrino–nucleus reactions," *Phys.Rev.*, vol. C83, p. 045501, 2011.

[35] M. Martini, M. Ericson, and G. Chanfray, "Neutrino energy reconstruction problems and neutrino oscillations," *Phys.Rev.*, vol. D85, p. 093012, 2012.

[36] J. Nieves, F. Sanchez, I. Ruiz Simo, and M. Vicente Vacas, "Neutrino energy reconstruction and the shape of the CCQE-like total cross section," *Phys.Rev.*, vol. D85, p. 113008, 2012.

[37] O. Lalakulich, U. Mosel, and K. Gallmeister, "Energy reconstruction in quasielastic scattering in the MiniBooNE and T2K experiments," *Phys.Rev.*, vol. C86, p. 054606, 2012.

[38] T. Sato, D. Uno, and T. Lee, "Dynamical model of weak pion production reactions," *Phys.Rev.*, vol. C67, p. 065201, 2003.

[39] E. Hernandez, J. Nieves, and M. Valverde, "Weak pion production off the nucleon," *Phys.Rev.*, vol. D76, p. 033005, 2007.

[40] E. Hernandez, J. Nieves, M. Valverde, and M. Vicente Vacas, "$N - \Delta(1232)$ axial form factors from weak pion production," *Phys.Rev.*, vol. D81, p. 085046, 2010.

[41] T. Leitner, O. Buss, L. Alvarez-Ruso, and U. Mosel, "Electron- and neutrino-nucleus scattering from the quasielastic to the resonance region," *Phys.Rev.*, vol. C79, p. 034601, 2009.

[42] B. D. Serot and X. Zhang, "Neutrinoproduction of photons and pions from nucleons in a chiral effective field theory for nuclei," *Phys.Rev.*, vol. C86, p. 015501, 2012.

[43] E. Hernández, J. Nieves, and M. J. V. Vacas, "Single π production in neutrino-nucleus scattering," *Phys.Rev.*, vol. D87, no. 11, p. 113009, 2013.

[44] S. Ahmad, M. Sajjad Athar, and S. Singh, "Neutrino induced charged current 1 π^+ production at intermediate energies," *Phys.Rev.*, vol. D74, p. 073008, 2006.

[45] T. Leitner, O. Buss, U. Mosel, and L. Alvarez-Ruso, "Neutrino induced pion production at MiniBooNE and K2K," *Phys.Rev.*, vol. C79, p. 038501, 2009.

[46] T. Golan, C. Juszczak, and J. T. Sobczyk, "Final state interactions effects in neutrino-nucleus interactions," *Phys.Rev.*, vol. C86, p. 015505, 2012.

[47] O. Lalakulich and U. Mosel, "Pion production in the MiniBooNE experiment," *Phys.Rev.*, vol. C87, p. 014602, 2013.

[48] S. Singh, M. Sajjad Athar, and S. Ahmad, "Nuclear effects in neutrino induced coherent pion production at K2K and MiniBooNE," *Phys.Rev.Lett.*, vol. 96, p. 241801, 2006.

[49] L. Alvarez-Ruso, L. Geng, S. Hirenzaki, and M. Vicente Vacas, "Charged current neutrino induced coherent pion production," *Phys.Rev.*, vol. C75, p. 055501, 2007.

[50] J. Amaro, E. Hernandez, J. Nieves, and M. Valverde, "Theoretical study of neutrino-induced coherent pion production off nuclei at T2K and MiniBooNE energies," *Phys.Rev.*, vol. D79, p. 013002, 2009.

[51] S. Nakamura, T. Sato, T.-S. Lee, B. Szczerbinska, and K. Kubodera, "Dynamical model of coherent pion production in neutrino-nucleus scattering," *Phys.Rev.*, vol. C81, p. 035502, 2010.

[52] X. Zhang and B. D. Serot, "Coherent neutrinoproduction of photons and pions in a chiral effective field theory for nuclei," *Phys.Rev.*, vol. C86, p. 035504, 2012.

[53] E. Paschos, A. Kartavtsev, and G. Gounaris, "Coherent pion production by neutrino scattering off nuclei," *Phys.Rev.*, vol. D74, p. 054007, 2006.

[54] C. Berger and L. Sehgal, "PCAC and coherent pion production by low energy neutrinos," *Phys.Rev.*, vol. D79, p. 053003, 2009.

[55] E. Hernandez, J. Nieves, and M. Vicente-Vacas, "Neutrino induced coherent pion production off nuclei and PCAC," *Phys.Rev.*, vol. D80, p. 013003, 2009.

[56] B. Kopeliovich, I. Schmidt, and M. Siddikov, "Diffractive neutrino-production of pions on nuclei: Adler relation within the color-dipole description," *Phys.Rev.*, vol. D85, p. 073003, 2012.

[57] C. Athanassopoulos *et al.*, "Evidence for $\bar{\nu}_\mu \to \bar{\nu}_e$ oscillations from the LSND experiment at LAMPF," *Phys.Rev.Lett.*, vol. 77, pp. 3082–3085, 1996.

[58] C. Athanassopoulos *et al.*, "Evidence for $\nu_\mu \to \nu_e$ neutrino oscillations from LSND," *Phys.Rev.Lett.*, vol. 81, pp. 1774–1777, 1998.

[59] A. Aguilar-Arevalo *et al.*, "Improved search for $\bar{\nu}_\mu \to \bar{\nu}_e$ oscillations in the MiniBooNE experiment," *Phys.Rev.Lett.*, vol. 110, no. 16, p. 161801, 2013.

[60] A. Aguilar-Arevalo *et al.*, "A search for electron neutrino appearance at the $\Delta m^2 \sim 1$ eV^2 scale," *Phys.Rev.Lett.*, vol. 98, p. 231801, 2007.

[61] A. Aguilar-Arevalo *et al.*, "Unexplained excess of electron-like events from a 1-GeV neutrino beam," *Phys.Rev.Lett.*, vol. 102, p. 101802, 2009.

[62] K. Abe *et al.*, "Evidence of electron neutrino appearance in a muon neutrino beam," *Phys.Rev.*, vol. D88, no. 3, p. 032002, 2013.

[63] J. Gasser and H. Leutwyler, "Chiral perturbation theory to one loop," *Annals Phys.*, vol. 158, p. 142, 1984.

[64] J. Oller, E. Oset, and J. Pelaez, "Nonperturbative approach to effective chiral Lagrangians and meson interactions," *Phys.Rev.Lett.*, vol. 80, pp. 3452–3455, 1998.

[65] J. Nieves and E. Ruiz Arriola, "Bethe-Salpeter approach for meson meson scattering in chiral perturbation theory," *Phys.Lett.*, vol. B455, pp. 30–38, 1999.

[66] N. Isgur and M. B. Wise, "Weak decays of heavy mesons in the static quark approximation," *Phys.Lett.*, vol. B232, p. 113, 1989.

[67] A. V. Manohar and M. B. Wise, "Heavy quark physics," *Camb.Monogr.Part.Phys.Nucl.Phys.Cosmol.*, vol. 10, pp. 1–191, 2000.

[68] C. Garcia-Recio, L. Geng, J. Nieves, and L. Salcedo, "Low-lying even parity meson resonances and spin-flavor symmetry," *Phys.Rev.*, vol. D83, p. 016007, 2011.

[69] E. Klempt and J.-M. Richard, "Baryon spectroscopy," *Rev.Mod.Phys.*, vol. 82, pp. 1095–1153, 2010.

[70] J. Beringer *et al.*, "Review of Particle Physics (RPP)," *Phys.Rev.*, vol. D86, p. 010001, 2012.

[71] S. Capstick and W. Roberts, "Quark models of baryon masses and decays," *Prog.Part.Nucl.Phys.*, vol. 45, pp. S241–S331, 2000.

[72] S. Sarkar, B.-X. Sun, E. Oset, and M. Vicente Vacas, "Dynamically generated resonances from the vector octet–baryon decuplet interaction," *Eur.Phys.J.*, vol. A44, pp. 431–443, 2010.

[73] E. Oset and A. Ramos, "Dynamically generated resonances from the vector octet-baryon octet interaction," *Eur.Phys.J.*, vol. A44, pp. 445–454, 2010.

[74] D. Gamermann, C. Garcia-Recio, J. Nieves, and L. Salcedo, "Odd parity light baryon resonances," *Phys.Rev.*, vol. D84, p. 056017, 2011.

[75] M. Pavon Valderrama, J.-J. Xie, and J. Nieves, "Are there three $\Xi(1950)$ states?," *Phys.Rev.*, vol. D85, p. 017502, 2012.

[76] B.-X. Sun, H.-X. Chen, and E. Oset, "$N\rho\rho$ and $\Delta\rho\rho$ molecules with $J^P = 5/2^+$ and $J^P = 7/2^+$," *Eur.Phys.J.*, vol. A47, p. 127, 2011.

[77] B. Zou, "Baryon resonances observed at BES," *eConf*, vol. C070910, p. 112, 2007.

[78] N. Muramatsu, J. Chen, W. Chang, D. Ahn, J. Ahn, *et al.*, "Near-threshold photoproduction of $\Lambda(1520)$ from protons and deuterons," *Phys.Rev.Lett.*, vol. 103, p. 012001, 2009.

[79] H. Kohri *et al.*, "Near-threshold $\Lambda(1520)$ production by the $\gamma p \to K^+\Lambda(1520)$ reaction at forward K^+ angles," *Phys.Rev.Lett.*, vol. 104, p. 172001, 2010.

[80] K. Moriya *et al.*, "Differential photoproduction cross sections of the $\Sigma^0(1385)$, $\Lambda(1405)$, and $\Lambda(1520)$," *Phys.Rev.*, vol. C88, p. 045201, 2013.

[81] A. W. Thomas and W. Weise, *The Structure of the Nucleon*. Berlin, Germany: Wiley-VCH, 2001.

[82] S. Weinberg, "A model of leptons," *Phys.Rev.Lett.*, vol. 19, pp. 1264–1266, 1967.

[83] A. Salam, "Weak and electromagnetic interactions," *Conf.Proc.*, vol. C680519, pp. 367–377, 1968.

[84] S. Glashow, J. Iliopoulos, and L. Maiani, "Weak interactions with lepton-hadron symmetry," *Phys.Rev.*, vol. D2, pp. 1285–1292, 1970.

[85] J. Formaggio and G. Zeller, "From eV to EeV: neutrino cross sections across energy scales," *Rev.Mod.Phys.*, vol. 84, p. 1307, 2012.

[86] R. J. Hill, "Low energy analysis of $\nu N \to \nu N \gamma$ in the Standard Model," *Phys.Rev.*, vol. D81, p. 013008, 2010.

[87] C. Barbero and A. Mariano, "Single photon production $\nu_l N \to \nu_l N \gamma$ in neutrino-nucleon scattering." [arXiv:1210.6940 [nucl-th]], 2012.

[88] X. Zhang and B. D. Serot, "Can neutrino-induced photon production explain the low energy excess in MiniBooNE," *Phys.Lett.*, vol. B719, pp. 409–414, 2013.

[89] A. M. Ankowski, O. Benhar, T. Mori, R. Yamaguchi, and M. Sakuda, "Analysis of γ-ray production in neutral-current neutrino-oxygen interactions at energies above 200 MeV," *Phys.Rev.Lett.*, vol. 108, p. 052505, 2012.

[90] R. J. Hill, "On the single photon background to ν_e appearance at MiniBooNE," *Phys.Rev.*, vol. D84, p. 017501, 2011.

[91] X. Zhang and B. D. Serot, "Incoherent neutrinoproduction of photons and pions in a chiral effective field theory for nuclei," *Phys.Rev.*, vol. C86, p. 035502, 2012.

[92] T. Leitner, O. Buss, U. Mosel, and L. Alvarez-Ruso, "Neutrino scattering with nuclei: Theory of low energy nuclear effects and its applications," *PoS*, vol. NUFACT08, p. 009, 2008.

[93] T. J. Leitner, "Neutrino-nucleus interactions in a coupled-channel hadronic transport model," *PhD Thesis, Giessen*, 2009.

[94] S. Gershtein, Y. Y. Komachenko, and M. Y. a. Khlopov, "Single photon production in exclusive neutrino process $\nu N \to \nu\gamma N$," *Sov.J.Nucl.Phys.*, vol. 33, p. 860, 1981.

[95] D. Rein and L. Sehgal, "Coherent production of photons by neutrinos," *Phys.Lett.*, vol. B104, pp. 394–398, 1981.

[96] L. Alvarez-Ruso, L. Geng, and M. Vicente Vacas, "Neutral current coherent pion production," *Phys.Rev.*, vol. C76, p. 068501, 2007.

[97] E. Oset, H. Toki, and W. Weise, "Pionic modes of excitation in nuclei," *Phys.Rept.*, vol. 83, pp. 281–380, 1982.

[98] J. Nieves, E. Oset, and C. Garcia-Recio, "Many body approach to low-energy pion nucleus scattering," *Nucl.Phys.*, vol. A554, pp. 554–579, 1993.

[99] R. Carrasco and E. Oset, "Interaction of real photons with nuclei from 100 MeV to 500 MeV," *Nucl.Phys.*, vol. A536, pp. 445–508, 1992.

[100] A. Gil, J. Nieves, and E. Oset, "Many body approach to the inclusive (e, e') reaction from the quasielastic to the Δ excitation region," *Nucl.Phys.*, vol. A627, pp. 543–598, 1997.

[101] A. Gil, J. Nieves, and E. Oset, "Inclusive $(e, e'N)$, $(e, e'NN)$, $(e, e'\pi)$: Reactions in nuclei," *Nucl.Phys.*, vol. A627, pp. 599–619, 1997.

[102] R. Carrasco, J. Nieves, and E. Oset, "Coherent $(\gamma,\ \pi^0)$ photoproduction in a local approximation to the Δ hole model," *Nucl.Phys.*, vol. A565, pp. 797–817, 1993.

[103] S. Hirenzaki, J. Nieves, E. Oset, and M. Vicente-Vacas, "Coherent π^0 electroproduction," *Phys.Lett.*, vol. B304, pp. 198–202, 1993.

[104] E. Wang, L. Alvarez-Ruso, and J. Nieves, "Photon emission in neutral current interactions at intermediate energies," *Phys.Rev.*, vol. C89, p. 015503, 2014.

[105] A. Krutov and V. Troitsky, "Extraction of the neutron charge form-factor from the charge form-factor of deuteron," *Eur.Phys.J.*, vol. A16, pp. 285–290, 2003.

[106] A. Bodek, S. Avvakumov, R. Bradford, and H. S. Budd, "Vector and axial nucleon form factors: A duality constrained parameterization," *Eur.Phys.J.*, vol. C53, pp. 349–354, 2008.

[107] S. Pate and D. Trujillo, "Strangeness vector and axial-vector form factors of the nucleon," 2013.

[108] J. Wess and B. Zumino, "Consequences of anomalous Ward identities," *Phys.Lett.*, vol. B37, p. 95, 1971.

[109] E. Witten, "Global aspects of current algebra," *Nucl.Phys.*, vol. B223, pp. 422–432, 1983.

[110] O. Lalakulich, E. A. Paschos, and G. Piranishvili, "Resonance production by neutrinos: The second resonance region," *Phys.Rev.*, vol. D74, p. 014009, 2006.

[111] D. Drechsel, S. Kamalov, and L. Tiator, "Unitary isobar model - MAID2007," *Eur.Phys.J.*, vol. A34, pp. 69–97, 2007.

[112] MAID. http://www.kph.uni-mainz.de/MAID.

[113] S. L. Adler, "Photoproduction, electroproduction and weak single pion production in the $(3,3)$ resonance region," *Annals Phys.*, vol. 50, pp. 189–311, 1968.

[114] J. Bijtebier, "A comparison between Salin's and Adler's models for $\nu_\mu N \to \mu N^*$ reactions," *Nucl.Phys.*, vol. B21, pp. 158–172, 1970.

[115] J. Nieves, M. Valverde, and M. Vicente Vacas, "Inclusive nucleon emission induced by quasi-elastic neutrino-nucleus interactions," *Phys.Rev.*, vol. C73, p. 025504, 2006.

[116] R. Carrasco, E. Oset, and L. Salcedo, "Inclusive (γ, π) reactions in nuclei," *Nucl.Phys.*, vol. A541, pp. 585–622, 1992.

[117] M. Hirata, J. Koch, E. Moniz, and F. Lenz, "Isobar hole doorway states and π^{16}O scattering," *Annals Phys.*, vol. 120, pp. 205–248, 1979.

[118] R. Freedman, G. Miller, and E. Henley, "Isobar dynamics and pion nucleus elastic scattering," *Nucl.Phys.*, vol. A389, pp. 457–491, 1982.

[119] E. Oset and L. Salcedo, "Δ Selfenergy in Nuclear Matter," *Nucl.Phys.*, vol. A468, pp. 631–652, 1987.

[120] J. Nieves, E. Oset, and C. Garcia-Recio, "A theoretical approach to pionic atoms and the problem of anomalies," *Nucl.Phys.*, vol. A554, pp. 509–553, 1993.

[121] S. Singh, M. Vicente-Vacas, and E. Oset, "Nuclear effects in neutrinoproduction of Δ at intermediate energies," *Phys.Lett.*, vol. B416, pp. 23–28, 1998.

[122] J. Lehr, M. Effenberger, and U. Mosel, "Electron and photon induced reactions on nuclei in the nucleon resonance region," *Nucl.Phys.*, vol. A671, pp. 503–531, 2000.

[123] E. Hernandez, J. Nieves, and M. Valverde, "Coherent pion production off nuclei at T2K and MiniBooNE energies revisited," *Phys.Rev.*, vol. D82, p. 077303, 2010.

[124] P. Fernandez de Cordoba, J. Nieves, E. Oset, and M. Vicente-Vacas, "Coherent pion production in the $(^3\mathrm{He}, t)$ reaction in nuclei," *Phys.Lett.*, vol. B319, pp. 416–420, 1993.

[125] P. Fernandez de Cordoba, Y. Ratis, E. Oset, J. Nieves, M. Vicente-Vacas, *et al.*, "Projectile Δ excitation in α-proton scattering," *Nucl.Phys.*, vol. A586, pp. 586–606, 1995.

[126] L. Alvarez-Ruso, J. Nieves, I. R. Simo, M. Valverde, and M. Vicente Vacas, "Charged kaon production by coherent scattering

of neutrinos and antineutrinos on nuclei," *Phys.Rev.*, vol. C87, p. 015503, 2013.

[127] R. Eramzhian, M. Gmitro, S. Kamalov, and R. Mach, "Nuclear pion photoproduction: a theory and the $^{16}O(\gamma, \pi^+)^{16}N$ (bound) example," *J.Phys.*, vol. G9, pp. 605–619, 1983.

[128] D. Drechsel, L. Tiator, S. Kamalov, and S. N. Yang, "Medium effects in coherent pion photoproduction and electroproduction on ^{4}He and ^{12}C," *Nucl.Phys.*, vol. A660, pp. 423–438, 1999.

[129] S. Boffi, L. Bracci, and P. Christillin, "Coherent (γ, π^0) on nuclei," *Nuovo Cim.*, vol. A104, pp. 843–854, 1991.

[130] T. Leitner, U. Mosel, and S. Winkelmann, "Neutrino-induced coherent pion production off nuclei reexamined," *Phys.Rev.*, vol. C79, p. 057601, 2009.

[131] C. Garcia-Recio, E. Oset, L. Salcedo, D. Strottman, and M. Lopez, "Pion nucleus elastic scattering in the microscopic local Δ hole model," *Nucl.Phys.*, vol. A526, pp. 685–702, 1991.

[132] E. Hernandez, J. Nieves, and M. J. Vicente Vacas. Private communication.

[133] A. Aguilar-Arevalo *et al.*, "Measurement of muon neutrino quasielastic scattering on carbon," *Phys.Rev.Lett.*, vol. 100, p. 032301, 2008.

[134] M. Martini, M. Ericson, and G. Chanfray, "Neutrino quasielastic interaction and nuclear dynamics," *Phys.Rev.*, vol. C84, p. 055502, 2011.

[135] J. Nieves, I. Ruiz Simo, and M. Vicente Vacas, "The nucleon axial mass and the MiniBooNE quasielastic neutrino-nucleus scattering problem," *Phys.Lett.*, vol. B707, pp. 72–75, 2012.

[136] S. Barish, M. Derrick, T. Dombeck, L. Hyman, K. Jaeger, *et al.*, "Study of neutrino interactions in hydrogen and deuterium: inelastic charged current reactions," *Phys.Rev.*, vol. D19, p. 2521, 1979.

[137] G. Radecky, V. Barnes, D. Carmony, A. Garfinkel, M. Derrick, *et al.*, "Study of single pion production by weak charged currents in low-energy neutrino d interactions," *Phys.Rev.*, vol. D25, pp. 1161–1173, 1982.

[138] T. Kitagaki, H. Yuta, S. Tanaka, A. Yamaguchi, K. Abe, *et al.*, "Charged current exclusive pion production in neutrino deuterium interactions," *Phys.Rev.*, vol. D34, pp. 2554–2565, 1986.

[139] T. Kitagaki, H. Yuta, S. Tanaka, A. Yamaguchi, K. Abe, *et al.*, "Study of $\nu d \to \mu^- p p_s$ and $\nu d \to \mu^- \Delta^{++}(1232) n_s$ using the BNL 7-foot deuterium filled bubble chamber," *Phys.Rev.*, vol. D42, pp. 1331–1338, 1990.

[140] C. De Jager, H. De Vries, and C. De Vries, "Nuclear charge and magnetization density distribution parameters from elastic electron scattering," *Atom.Data Nucl.Data Tabl.*, vol. 14, pp. 479–508, 1974.

[141] J. W. Negele and D. Vautherin, "Density-Matrix expansion for an effective nuclear hamiltonian," *Phys.Rev.*, vol. C5, pp. 1472–1493, 1972.

[142] C. Garcia-Recio, J. Nieves, and E. Oset, "Neutron distributions from pionic atoms," *Nucl.Phys.*, vol. A547, pp. 473–487, 1992.

[143] E. Oset, P. Fernandez de Cordoba, L. Salcedo, and R. Brockmann, "Decay modes of Σ and Λ hypernuclei," *Phys.Rept.*, vol. 188, p. 79, 1990.

[144] D. Forero, M. Tortola, and J. Valle, "Global status of neutrino oscillation parameters after Neutrino-2012," *Phys.Rev.*, vol. D86, p. 073012, 2012.

[145] T. Katori and J. Conrad, "Beyond standard model searches in the MiniBooNE experiment." [arXiv:1404.7759 [hep-ex]], 2014.

[146] A. Aguilar-Arevalo *et al.*, "Evidence for neutrino oscillations from the observation of anti-neutrino(electron) appearance in a anti-neutrino(muon) beam," *Phys.Rev.*, vol. D64, p. 112007, 2001.

[147] J. Conrad, C. Ignarra, G. Karagiorgi, M. Shaevitz, and J. Spitz, "Sterile neutrino fits to short baseline neutrino oscillation measurements," *Adv.High Energy Phys.*, vol. 2013, p. 163897, 2013.

[148] C. Giunti, M. Laveder, Y. Li, and H. Long, "Pragmatic view of short-baseline neutrino oscillations," *Phys.Rev.*, vol. D88, p. 073008, 2013.

[149] T. Katori, V. A. Kostelecky, and R. Tayloe, "Global three-parameter model for neutrino oscillations using Lorentz violation," *Phys.Rev.*, vol. D74, p. 105009, 2006.

[150] S. Gninenko, "The MiniBooNE anomaly and heavy neutrino decay," *Phys.Rev.Lett.*, vol. 103, p. 241802, 2009.

[151] A. Aguilar-Arevalo *et al.*, "The neutrino flux prediction at MiniBooNE," *Phys.Rev.*, vol. D79, p. 072002, 2009.

[152] MiniBooNE(2012). http://www-boone.fnal.gov/for_physicists/data_release/nue_nuebar_2012.

[153] E. Wang, L. Alvarez-Ruso, and J. Nieves, "Single photon events from neutral current interactions at MiniBooNE," [arXiv:1407.6060 [hep-ph]], 2014.

[154] S. Pate and D. Trujillo, "Strangeness vector and axial-vector form factors of the nucleon," *EPJ Web Conf.*, vol. 66, p. 06018, 2014.

[155] C. Llewellyn Smith, "Neutrino reactions at accelerator energies," *Phys.Rept.*, vol. 3, pp. 261–379, 1972.

[156] A. Aguilar-Arevalo *et al.*, "Measurement of the neutrino component of an anti-neutrino beam observed by a non-magnetized detector," *Phys.Rev.*, vol. D84, p. 072005, 2011.

[157] D. Rein and L. M. Sehgal, "Neutrino excitation of baryon resonances and single pion production," *Annals Phys.*, vol. 133, pp. 79–153, 1981.

[158] L. Alvarez-Ruso, Y. Hayato, and J. Nieves, "Progress and open questions in the physics of neutrino cross sections at intermediate energies," *New J.Phys.*, vol. 16, p. 075015, 2014.

[159] H. Chen *et al.*, "Proposal for a new experiment using the Booster and NuMI neutrino beamlines: MicroBooNE." Fermilab-Proposal-0974, 2007.

[160] K. Abe *et al.*, "Indication of Electron Neutrino Appearance from an Accelerator-produced Off-axis Muon Neutrino Beam," *Phys.Rev.Lett.*, vol. 107, p. 041801, 2011.

[161] F. An *et al.*, "Spectral measurement of electron antineutrino oscillation amplitude and frequency at Daya Bay," *Phys.Rev.Lett.*, vol. 112, p. 061801, 2014.

[162] J. Ahn *et al.*, "Observation of reactor electron antineutrino disappearance in the RENO experiment," *Phys.Rev.Lett.*, vol. 108, p. 191802, 2012.

[163] Y. Abe *et al.*, "Indication for the disappearance of reactor electron antineutrinos in the Double Chooz experiment," *Phys.Rev.Lett.*, vol. 108, p. 131801, 2012.

[164] K. Abe *et al.*, "Observation of electron neutrino appearance in a muon neutrino beam," *Phys.Rev.Lett.*, vol. 112, p. 061802, 2014.

[165] P. Adamson *et al.*, "Combined analysis of ν_μ disappearance and $\nu_\mu \to \nu_e$ appearance in MINOS using accelerator and atmospheric neutrinos," *Phys.Rev.Lett.*, vol. 112, p. 191801, 2014.

[166] J. A. Harvey, C. T. Hill, and R. J. Hill, "Anomaly mediated neutrino-photon interactions at finite baryon density," *Phys.Rev.Lett.*, vol. 99, p. 261601, 2007.

[167] M. Masip, P. Masjuan, and D. Meloni, "Heavy neutrino decays at MiniBooNE," *JHEP*, vol. 1301, p. 106, 2013.

[168] S. Toboyama and H. A. Tanaka, 2014. private communication.

[169] Y. Hayato, "A neutrino interaction simulation program library NEUT," *Acta Phys.Polon.*, vol. B40, pp. 2477–2489, 2009.

[170] K. Abe *et al.*, "The T2K neutrino flux prediction," *Phys.Rev.*, vol. D87, p. 012001, 2013.

[171] C. Kullenberg *et al.*, "A Search for Single Photon Events in Neutrino Interactions in NOMAD," *Phys.Lett.*, vol. B706, pp. 268–275, 2012.

[172] D. Casper, "The Nuance neutrino physics simulation, and the future," *Nucl.Phys.Proc.Suppl.*, vol. 112, pp. 161–170, 2002.

[173] K. Abe *et al.*, "Measurement of the intrinsic electron neutrino component in the T2K neutrino beam with the ND280 detector," *Phys.Rev.*, vol. D89, p. 092003, 2014.

[174] K. Abe *et al.*, "Measurement of the Inclusive Electron Neutrino Charged Current Cross Section on Carbon with the T2K Near Detector," 2014. [arXiv:1407.7389 [hep-ex]], 2014.

[175] A. Bondar *et al.*, "Observation of two charged bottomonium-like resonances in $Y(5S)$ decays," *Phys.Rev.Lett.*, vol. 108, p. 122001, 2012.

[176] S. Choi *et al.*, "Observation of a narrow charmonium-like state in exclusive $B^{\pm} \to K^{\pm}\pi^{+}\pi^{-}J/\psi$ decays," *Phys.Rev.Lett.*, vol. 91, p. 262001, 2003.

[177] J. Vijande, A. Valcarce, and J.-M. Richard, "Stability of multiquarks in a simple string model," *Phys.Rev.*, vol. D76, p. 114013, 2007.

[178] P. Ortega, J. Segovia, D. Entem, and F. Fernandez, "Coupled channel approach to the structure of the X(3872)," *Phys.Rev.*, vol. D81, p. 054023, 2010.

[179] S. Weinberg, "Phenomenological Lagrangians," *Physica*, vol. A96, p. 327, 1979.

[180] J. Gasser and H. Leutwyler, "Chiral perturbation theory: expansions in the mass of the strange quark," *Nucl.Phys.*, vol. B250, p. 465, 1985.

[181] M. Neubert, "Heavy quark symmetry," *Phys.Rept.*, vol. 245, pp. 259–396, 1994.

[182] T. N. Truong, "Chiral perturbation theory and final state theorem," *Phys.Rev.Lett.*, vol. 61, p. 2526, 1988.

[183] A. Dobado, M. J. Herrero, and T. N. Truong, "Unitarized chiral perturbation theory for elastic $\pi\pi$ scattering," *Phys.Lett.*, vol. B235, p. 134, 1990.

[184] A. Dobado and J. Pelaez, "A global fit of $\pi\pi$ and πK elastic scattering in ChPT with dispersion relations," *Phys.Rev.*, vol. D47, pp. 4883–4888, 1993.

[185] A. Dobado and J. Pelaez, "The inverse amplitude method in chiral perturbation theory," *Phys.Rev.*, vol. D56, pp. 3057–3073, 1997.

[186] T. Hannah, "The inverse amplitude method and chiral perturbation theory to two loops," *Phys.Rev.*, vol. D55, pp. 5613–5626, 1997.

[187] J. Oller and E. Oset, "Chiral symmetry amplitudes in the S wave isoscalar and isovector channels and the σ, $f_0(980)$, $a_0(980)$ scalar mesons," *Nucl.Phys.*, vol. A620, pp. 438–456, 1997.

[188] N. Kaiser, "$\pi\pi$ S wave phase shifts and nonperturbative chiral approach," *Eur.Phys.J.*, vol. A3, pp. 307–309, 1998.

[189] J. Oller, E. Oset, and J. Pelaez, "Meson meson interaction in a nonperturbative chiral approach," *Phys.Rev.*, vol. D59, p. 074001, 1999.

[190] J. Oller and E. Oset, "N/D description of two meson amplitudes and chiral symmetry," *Phys.Rev.*, vol. D60, p. 074023, 1999.

[191] J. Nieves and E. Ruiz Arriola, "Bethe-Salpeter approach for unitarized chiral perturbation theory," *Nucl.Phys.*, vol. A679, pp. 57–117, 2000.

[192] J. Nieves, M. Pavon Valderrama, and E. Ruiz Arriola, "The inverse amplitude method in $\pi\pi$ scattering in chiral perturbation theory to two loops," *Phys.Rev.*, vol. D65, p. 036002, 2002.

[193] A. Gomez Nicola and J. Pelaez, "Meson meson scattering within one loop chiral perturbation theory and its unitarization," *Phys.Rev.*, vol. D65, p. 054009, 2002.

[194] M. Lutz and E. Kolomeitsev, "On meson resonances and chiral symmetry," *Nucl.Phys.*, vol. A730, pp. 392–416, 2004.

[195] L. Roca, E. Oset, and J. Singh, "Low lying axial-vector mesons as dynamically generated resonances," *Phys.Rev.*, vol. D72, p. 014002, 2005.

[196] L. Geng, E. Oset, L. Roca, and J. Oller, "Clues for the existence of two $K_1(1270)$ resonances," *Phys.Rev.*, vol. D75, p. 014017, 2007.

[197] A. Gomez Nicola, J. Pelaez, and G. Rios, "The inverse amplitude method and adler zeros," *Phys.Rev.*, vol. D77, p. 056006, 2008.

[198] R. Molina, D. Nicmorus, and E. Oset, "The $\rho\rho$ interaction in the hidden gauge formalism and the $f_0(1370)$ and $f_2(1270)$ resonances," *Phys.Rev.*, vol. D78, p. 114018, 2008.

[199] L. Geng and E. Oset, "Vector meson–vector meson interaction in a hidden gauge unitary approach," *Phys.Rev.*, vol. D79, p. 074009, 2009.

[200] M. Albaladejo and J. Oller, "Identification of a scalar glueball," *Phys.Rev.Lett.*, vol. 101, p. 252002, 2008.

[201] P. C. Bruns, M. Mai, and U. G. Meissner, "Chiral dynamics of the $S_{11}(1535)$ and $S_{11}(1650)$ resonances revisited," *Phys.Lett.*, vol. B697, pp. 254–259, 2011.

[202] J. Pelaez, "On the nature of light scalar mesons from their large N_C behavior," *Phys.Rev.Lett.*, vol. 92, p. 102001, 2004.

[203] J. Pelaez and G. Rios, "Nature of the $f_0(600)$ from its N_C dependence at two loops in unitarized chiral perturbation theory," *Phys.Rev.Lett.*, vol. 97, p. 242002, 2006.

[204] L. Geng, E. Oset, J. Pelaez, and L. Roca, "Nature of the axial-vector mesons from their N_C behavior within the chiral unitary approach," *Eur.Phys.J.*, vol. A39, pp. 81–87, 2009.

[205] J. Nieves and E. Ruiz Arriola, "Properties of the ρ and σ mesons from unitary chiral dnamics," *Phys.Rev.*, vol. D80, p. 045023, 2009.

[206] J. Nieves and E. Ruiz Arriola, "Meson resonances at large N_C: complex poles versus Breit-Wigner masses," *Phys.Lett.*, vol. B679, pp. 449–453, 2009.

[207] J. Nieves, A. Pich, and E. Ruiz Arriola, "Large-N_C Properties of the ρ and $f_0(600)$ Mesons from Unitary Resonance Chiral Dynamics," *Phys.Rev.*, vol. D84, p. 096002, 2011.

[208] Z.-H. Guo and J. Oller, "Resonances from meson–meson scattering in U(3) CHPT," *Phys.Rev.*, vol. D84, p. 034005, 2011.

[209] C. Garcia-Recio, J. Nieves, and L. Salcedo, "SU(6) extension of the Weinberg-Tomozawa meson–baryon Lagrangian," *Phys.Rev.*, vol. D74, p. 034025, 2006.

[210] C. Garcia-Recio, J. Nieves, and L. Salcedo, "Large N_C Weinberg-Tomozawa interaction and negative parity s-wave baryon resonances," *Phys.Rev.*, vol. D74, p. 036004, 2006.

[211] S. Weinberg, "Pion scattering lengths," *Phys.Rev.Lett.*, vol. 17, pp. 616–621, 1966.

[212] Y. Tomozawa, "Axial vector coupling renormalization and the meson baryon scattering lengths," *Nuovo Cim.*, vol. A46, pp. 707–717, 1966.

[213] M. Bando, T. Kugo, S. Uehara, K. Yamawaki, and T. Yanagida, "Is ρ meson a dynamical gauge boson of hidden local symmetry," *Phys.Rev.Lett.*, vol. 54, p. 1215, 1985.

[214] M. Bando, T. Kugo, and K. Yamawaki, "Nonlinear realization and hidden local symmetries," *Phys.Rept.*, vol. 164, pp. 217–314, 1988.

[215] H. Nagahiro, L. Roca, A. Hosaka, and E. Oset, "Hidden gauge formalism for the radiative decays of axial-vector mesons," *Phys.Rev.*, vol. D79, p. 014015, 2009.

[216] G. Ecker, J. Gasser, H. Leutwyler, A. Pich, and E. de Rafael, "Chiral Lagrangians for massive spin 1 fields," *Phys.Lett.*, vol. B223, p. 425, 1989.

[217] C. García-Recio, L. Geng, J. Nieves, L. Salcedo, E. Wang, *et al.*, "Low-lying even parity meson resonances and spin-flavor symmetry revisited," *Phys.Rev.*, vol. D87, no. 9, p. 096006, 2013.

[218] J. Nieves and E. Ruiz Arriola, "The S_{11}-$N(1535)$ and -$N(1650)$ resonances in meson baryon unitarized coupled channel chiral perturbation theory," *Phys.Rev.*, vol. D64, p. 116008, 2001.

[219] G. 't Hooft, "A two-dimensional model for mesons," *Nucl.Phys.*, vol. B75, p. 461, 1974.

[220] E. Witten, "Baryons in the $1/n$ Expansion," *Nucl.Phys.*, vol. B160, p. 57, 1979.

[221] I. Caprini, G. Colangelo, and H. Leutwyler, "Mass and width of the lowest resonance in QCD," *Phys.Rev.Lett.*, vol. 96, p. 132001, 2006.

[222] R. Garcia-Martin, R. Kaminski, J. Pelaez, and J. Ruiz de Elvira, "Precise determination of the $f_0(600)$ and $f_0(980)$ pole parameters from a dispersive data analysis," *Phys.Rev.Lett.*, vol. 107, p. 072001, 2011.

[223] A. Filippi *et al.*, "An analysis of the contribution of isospin two $\pi\pi$ resonant states in the $\bar{n}p \to \pi^+\pi^+\pi^-$ annihilation reaction," *Phys.Lett.*, vol. B495, pp. 284–288, 2000.

[224] N. Mistry, S. Mori, D. Sober, and A. Sadoff, "Photoproduction of Y^{*0} resonant states ," *Physics Letters B*, vol. 24, no. 10, pp. 528 – 530, 1967.

[225] W. Blanpied, J. Greenberg, V. Hughes, P. Kitching, and D. Lu, "Evidence for the photoproduction of $Y = 0$ states with masses greater than 1900 MeV," *Phys.Rev.Lett.*, vol. 14, p. 741, 1965.

[226] A. Boyarski, R. E. Diebold, S. D. Ecklund, G. Fischer, Y. Murata, *et al.*, "Photoproduction of K^+ hyperon from hydrogen and deuterium at 11 GeV," *Phys.Lett.*, vol. B34, p. 547, 1971.

[227] D. Barber, J. Dainton, L. Lee, R. Marshall, J. Thompson, *et al.*, "Strangeness exchange in the photoproduction of $K^+\Lambda(1520)$ between 2.8-GeV and 4.8-GeV," *Z.Phys.*, vol. C7, p. 17, 1980.

[228] S. Barrow *et al.*, "Electroproduction of the $\Lambda(1520)$ hyperon," *Phys.Rev.*, vol. C64, p. 044601, 2001.

[229] F. Wieland, J. Barth, K. Glander, J. Hannappel, N. Jopen, *et al.*, "Study of the reaction $\gamma p \to K^+\Lambda(1520)$ at photon energies up to 2.65-GeV," *Eur.Phys.J.*, vol. A47, p. 47, 2011.

[230] S. Nam, A. Hosaka, and H. Kim, "Photoproduction of Θ baryon from the neutron," *Phys.Lett.*, vol. B579, pp. 43–51, 2004.

[231] S.-I. Nam, A. Hosaka, and H.-C. Kim, "$\Lambda(1520, 3/2^-)$ photoproduction reaction via $\gamma N \to K\Lambda(1520)$," *Phys.Rev.*, vol. D71, p. 114012, 2005.

[232] S.-I. Nam, A. Hosaka, and H.-C. Kim, "Suppression of $\Theta^+(J^P = 3/2^\pm)$ photoproduction from the proton," *Phys.Lett.*, vol. B633, pp. 483–487, 2006.

[233] S.-I. Nam, A. Hosaka, and H.-C. Kim, "Photoproduction of the pentaquark Θ^+ with positive and negative parities," *J.Korean Phys.Soc.*, vol. 49, p. 1928, 2006.

[234] S.-i. Nam, "Studies on the polarization transfer coefficients C_x and C_z in the $\gamma p \to K^+$ polarized $\Lambda(1520, 3/2^-)$ reaction process," *Phys.Rev.*, vol. C81, p. 015201, 2010.

[235] A. Titov, B. Kampfer, S. Date, and Y. Ohashi, "Θ^+ formation in inclusive $\gamma d \to pK^- X$," *Phys.Rev.*, vol. C74, p. 055206, 2006.

[236] H. Toki, C. Garcia-Recio, and J. Nieves, "Photon induced $\Lambda(1520)$ production and the role of the K^* exchange," *Phys.Rev.*, vol. D77, p. 034001, 2008.

[237] J.-J. Xie and J. Nieves, "The role of the $N^*(2080)$ resonance in the $\vec{\gamma} p \to K^+\Lambda(1520)$ reaction," *Phys.Rev.*, vol. C82, p. 045205, 2010.

[238] J. He and X.-R. Chen, "The roles of nucleon resonances in $\Lambda(1520)$ photoproduciton off proton," *Phys.Rev.*, vol. C86, p. 035204, 2012.

[239] S.-i. Nam and C.-W. Kao, "$\Lambda(1520)$ photoproduciton off the proton target with Regge contributions," *Phys.Rev.*, vol. C81, p. 055206, 2010.

[240] A. Anisovich, R. Beck, E. Klempt, V. Nikonov, A. Sarantsev, *et al.*, "Properties of baryon resonances from a multichannel partial wave analysis," *Eur.Phys.J.*, vol. A48, p. 15, 2012.

[241] S. Capstick and W. Roberts, "Strange decays of nonstrange baryons," *Phys.Rev.*, vol. D58, p. 074011, 1998.

[242] S.-i. Nam, "Electroproduction of $\Lambda(1520)$ off the nucleon target with nucleon resonances," *J.Phys.*, vol. G40, p. 115001, 2013.

[243] J.-J. Xie and B.-C. Liu, "Role of the $N^*(2080)$ in $pp \to pK^+\Lambda(1520)$ and $\pi^- p \to K^0\Lambda(1520)$ reactions," *Phys.Rev.*, vol. C87, no. 4, p. 045210, 2013.

[244] A. Ramos and E. Oset, "The role of vector-baryon channels and resonances in the $\gamma p \to K^0\Sigma^+$ and $\gamma n \to K^0\Sigma^0$ reactions near the $K^*\Lambda$ threshold," *Phys.Lett.*, vol. B727, pp. 287–292, 2013.

[245] R. Ewald, B. Bantes, O. Bartholomy, D. Bayadilov, R. Beck, *et al.*, "Anomaly in the $K^0_S\Sigma^+$ photoproduction cross section off the proton at the K^* threshold," *Phys.Lett.*, vol. B713, pp. 180–185, 2012.

[246] J.-J. Xie, E. Wang, and J. Nieves, "Re-analysis of the $\Lambda(1520)$ photoproduction reaction," *Phys.Rev.*, vol. C89, p. 015203, 2014.

[247] Y. Oh, C. M. Ko, and K. Nakayama, "Nucleon and Δ resonances in $K\Sigma(1385)$ photoproduction from nucleons," *Phys.Rev.*, vol. C77, p. 045204, 2008.

[248] J. de Swart, "The Octet model and its Clebsch-Gordan coefficients," *Rev.Mod.Phys.*, vol. 35, pp. 916–939, 1963.

[249] A. Reuber, K. Holinde, and J. Speth, "Meson exchange hyperon–nucleon interactions in free scattering and nuclear matter," *Nucl.Phys.*, vol. A570, pp. 543–579, 1994.

[250] A. Pich, "Chiral perturbation theory," *Rept.Prog.Phys.*, vol. 58, pp. 563–610, 1995.

[251] S. Scherer and M. R. Schindler, "Quantum chromodynamics and chiral symmetry," *Lect.Notes Phys.*, vol. 830, pp. 1–48, 2012.

[252] T. Mast, M. Alston-Garnjost, R. Bangerter, A. Barbaro-Galtieri, L. Gershwin, *et al.*, "Electromagnetic decay of the $Y^*_0(1520)$," *Phys.Rev.Lett.*, vol. 21, pp. 1715–1717, 1968.

[253] J. W. Darewych, M. Horbatsch, and R. Koniuk, "The photon decays of baryons with strangeness," *Phys.Rev.*, vol. D28, p. 1125, 1983.

[254] E. Kaxiras, E. Moniz, and M. Soyeur, "Hyperon radiative decay," *Phys.Rev.*, vol. D32, pp. 695–700, 1985.

[255] M. Warns, W. Pfeil, and H. Rollnik, "Electromagnetic properties of hyperons in a relativized quark model," *Phys.Lett.*, vol. B258, pp. 431–440, 1991.

[256] Y. Umino and F. Myhrer, "Electromagnetic decays of excited hyperons," *Nucl.Phys.*, vol. A529, pp. 713–726, 1991.

[257] R. Bijker, F. Iachello, and A. Leviatan, "Algebraic models of hadron structure: II. Strange baryons," *Annals Phys.*, vol. 284, pp. 89–133, 2000.

[258] T. Van Cauteren, J. Ryckebusch, B. Metsch, and H.-R. Petry, "Helicity amplitudes and electromagnetic decays of hyperon resonances," *Eur.Phys.J.*, vol. A26, pp. 339–359, 2005.

[259] L. Yu, X.-L. Chen, W.-Z. Deng, and S.-L. Zhu, "Radiative decays of decuplet baryons, $\Lambda(1405)$ and $\Lambda(1520)$ hyperons," *Phys.Rev.*, vol. D73, p. 114001, 2006.

[260] M. Doring, E. Oset, and S. Sarkar, "Radiative decay of the $\Lambda(1520)$," *Phys.Rev.*, vol. C74, p. 065204, 2006.

[261] N. Awaji, H. Hayashii, S. Iwata, R. Kajikawa, K. Makino, *et al.*, "Energy dependent partial wave analysis on single pion production," 1981.

[262] C. Amsler *et al.*, "Review of Particle Physics," *Phys.Lett.*, vol. B667, pp. 1–1340, 2008.

[263] L. Roca, S. Sarkar, V. Magas, and E. Oset, "Unitary coupled channel analysis of the $\Lambda(1520)$ resonance," *Phys.Rev.*, vol. C73, p. 045208, 2006.

[264] A. Sibirtsev, J. Haidenbauer, S. Krewald, U.-G. Meissner, and A. W. Thomas, "$K\bar{K}$ photoproduction from protons," *Eur.Phys.J.*, vol. A31, pp. 221–232, 2007.

[265] A. Donnachie and P. Landshoff, "Exclusive ρ production in deep inelastic scattering," *Phys.Lett.*, vol. B185, p. 403, 1987.

[266] V. Y. Grishina, L. Kondratyuk, W. Cassing, M. Mirazita, and P. Rossi, "Comparative Regge analysis of Λ, Σ^0, $\Lambda(1520)$ and Θ^+ production in γp, πp and pp reactions," *Eur.Phys.J.*, vol. A25, pp. 141–150, 2005.

[267] S. Weinberg, "Evidence that the deuteron is not an elementary particle," *Phys.Rev.*, vol. 137, pp. B672–B678, 1965.

[268] J. He, "Theoretical study of the $\Lambda(1520)$ photoproduction off proton target based on the new CLAS data," *Nucl.Phys.*, vol. A927, p. 24, 2014.

[269] S. Capstick, "Photoproduction and electroproduction of nonstrange baryon resonances in the relativized quark model," *Phys.Rev.*, vol. D46, pp. 2864–2881, 1992.

[270] E. Wang, J.-J. Xie, and J. Nieves, "Regge signatures from forward CLAS $\Lambda(1520)$ photoproduction data," [arXiv:1405.3142 [nucl-th]], 2014.

[271] H. Haberzettl, C. Bennhold, T. Mart, and T. Feuster, "Gauge invariant tree level photoproduction amplitudes with form-factors," *Phys.Rev.*, vol. C58, pp. 40–44, 1998.

[272] R. Davidson and R. Workman, "Form-factors and photoproduction amplitudes," *Phys.Rev.*, vol. C63, p. 025210, 2001.

[273] W. Cassing, L. Kondratyuk, G. Lykasov, and M. Rzjanin, "Open charm enhancement by secondary interactions in relativistic nucleus-nucleus collisions?," *Phys.Lett.*, vol. B513, pp. 1–8, 2001.

[274] M. Guidal, J. Laget, and M. Vanderhaeghen, "Pion and kaon photoproduction at high-energies: Forward and intermediate angles," *Nucl.Phys.*, vol. A627, pp. 645–678, 1997.

[275] T. Corthals, J. Ryckebusch, and T. Van Cauteren, "Forward-angle $K^+\Lambda$ photoproduction in a Regge-plus-resonance approach," *Phys.Rev.*, vol. C73, p. 045207, 2006.

[276] T. Corthals, D. Ireland, T. Van Cauteren, and J. Ryckebusch, "Regge-plus-resonance treatment of the $p(\gamma, K^+)\Sigma^0$ and $p(\gamma, K^0)\Sigma^+$ reactions at forward kaon angles," *Phys.Rev.*, vol. C75, p. 045204, 2007.

[277] T. Hyodo, S. Sarkar, A. Hosaka, and E. Oset, "The Coupling of $\bar{K}^*N$ to the $\Lambda(1520)$," *Phys.Rev.*, vol. C73, p. 035209, 2006.

[278] Y. Fukuda *et al.*, "Evidence for oscillation of atmospheric neutrinos," *Phys.Rev.Lett.*, vol. 81, pp. 1562–1567, 1998.

[279] M. Ahn *et al.*, "Indications of neutrino oscillation in a 250 km long baseline experiment," *Phys.Rev.Lett.*, vol. 90, p. 041801, 2003.

[280] O. Buss, "Photon- and pion-induced reactions in a transport approach," *PhD Thesis, Giessen*, 2008.